

UNIVERSITÀ DEGLI STUDI DI TRIESTE

XXXVIII CICLO DEL DOTTORATO DI RICERCA IN CHIMICA

Advanced TDDFT Computational Frameworks for Optical and Chiroptical Properties in Nanoscale Systems

Settore scientifico-disciplinare: **CHIM/02**

DOTTORANDO
PIERPAOLO D'ANTONI

COORDINATORE
PROF. ENZO ALESSIO

SUPERVISORE DI TESI
PROF. MAURO STENER

ANNO ACCADEMICO 2024/2025

Università degli Studi di Trieste
Dipartimento di Scienze Chimiche e Farmaceutiche

Advanced TDDFT Computational Frameworks for Optical and Chiroptical Properties in Nanoscale Systems

Pierpaolo D'Antoni

Relatore: Prof. Mauro Stener

A.A. 2024/2025

Contents

1 Introduction **1**

1.1 Spectroscopy 1
1.2 Computational absorption spectroscopy 3
1.3 Nanoscience and Metallic Nano Clusters 5
1.4 Chirality and Circular Dichroism in Nanostructures 7
1.5 Nanoplasmonics 9

2 Theoretical introduction **13**

2.1 Addressing quantum mechanics 13
2.1.1 Dirac notation 15
2.1.2 Matrix formulation 16
2.2 Time independent methods 18
2.2.1 Ab initio: Hartree–Fock 19
2.2.2 Density Functional Theory 21
2.3 The Kohn–Sham (KS) approach 23
2.4 Time-Dependent DFT 25
2.5 Linear response theory 27
2.5.1 The spectrum from the polarizability 31
2.6 Linear response KS time-dependent DFT 33
2.7 The Exchange–Correlation Energy, Potential and Kernel 35
2.7.1 Local Density Approximation (LDA) 37
2.7.2 Generalized Gradient Approximation (GGA) 38
2.7.3 Hybrid Functionals 38
2.7.4 Range-Separated Hybrid Functionals 40
2.7.5 The Adiabatic approximation 41

3 Computational Methods **43**

3.1 The Random Phase Approximation 43
3.2 The Casida Algorithm 47
3.3 PolTDDFT algorithm 51
3.3.1 PolTDDFT implementation 54
3.3.2 Unrestricted extension of PolTDDFT 57

3.4 Hybrid Diagonal Approximation (HDA) 60
3.5 Efficient HDA through Resolution of the Identity (RI) 62
3.6 Implementation of the Efficient HDA Scheme 64
3.7 Computational analysis tools 66
3.7.1 Fragment-projection analysis of absorption spectra 68
3.7.2 Independent component maps of oscillatory strength 69
3.8 Extension to Electronic Circular Dichroism 70

4 Publications **73**
4.1 Main Publications 73
4.1.1 RI TDDFT Hybrid Functionals 73
4.1.2 Photoabsorption of Pt-doped Clusters 88
4.1.3 Damped LR TDDFT RS 97
4.1.4 Dichroism of plasmonic chiral nanoalloys by rational design 109
4.2 Additional Publications 120
4.2.1 Time-dependent quantum/continuum modeling of plasmon-enhanced electronic circular dichroism 120
4.2.2 How Adsorption Geometry Dictates Chiroptical Properties: A Computational Study of L-Cysteine on Au(111) Cluster Models 135

5 Conclusions **147**

Bibliography **151**

List of Figures

1.1 The dimension of the nanoparticle affects the electron wavefunction thus changing its optical properties [52]. 6
1.2 possible sources of chirality at the nanoscale [105]. 9
1.3 schematic representation of the collective motion of electrons in two spherical nanoparticles (in gray) in response to an electro-magnetic perturbation (in red) . 10

2.1 Schematic location of the poles of the retarded response function in the complex frequency plane. 32

3.1 Discretization of the excitation energy axis with selected eigenvalue differences. 53

Abstract

Questo progetto di dottorato è stato dedicato allo sviluppo e all'applicazione di approcci computazionali per lo studio di proprietà ottiche e chiro-ottiche di sistemi molecolari nel range dei nanometri. L'obiettivo del lavoro è stato quello di estendere la teoria del funzionale densità dipendente dal tempo (TDDFT) a sistemi di grandi dimensioni, nei quali il compromesso tra accuratezza e costo computazionale rappresenta una sfida centrale.

In quest'ottica, l'attività di ricerca si è concentrata attorno al formalismo TDDFT basato sulla polarizzazione (polTDDFT), con particolare attenzione all'Hybrid Diagonal Approximation (HDA). L'introduzione di un algoritmo computazionale basato sulla Risoluzione dell'Identità (RI) ha permesso di accelerare in modo significativo il calcolo dei contributi HDA, rendendo agevoli descrizioni TDDFT con funzionali ibridi anche a sistemi costituiti da centinaia di atomi. Il formalismo RI–HDA così ottenuto è stato testato su sistemi metallici rappresentativi, mostrando un'elevato grado di accuratezza sia rispetto ad approcci computazionali più costosi che in confronto a dati sperimentali registrati a basse temperature.

Un ulteriore risultato è stata l'estensione dell'approccio RI–HDA ai funzionali ibridi Range-Separated, quali il CAMY-B3LYP. Tali funzionali risultano fondamentali per una corretta descrizione delle eccitazioni con trasferimento di carica e degli effetti elettronici a lungo raggio.

Parallelamente allo sviluppo metodologico, gli strumenti computazionali realizzati sono stati impiegati per affrontare diversi problemi di interesse chimico e fisico. In particolare, sono stati studiati i contributi plasmonici al dicroismo circolare elettronico (ECD) in nanotubi metallici chirali, evidenziando come l'interferenza distruttiva tra eccitazioni collettive possa portare alla soppressione del segnale plasmonico ECD. Sono stati inoltre analizzati i meccanismi di trasferimento di chiralità in cluster d'oro funzionalizzati con L-cisteina, mettendo in luce il ruolo dell'accoppiamento metallo–legante e dell'organizzazione molecolare all'interfaccia. Infine, è stato sviluppato un approccio multiscala in grado di combinare una descrizione quantistica TDDFT del sistema molecolare con un modello continuo per una nanoparticella metallica, consentendo lo studio di effetti chiro-ottici in sistemi ibridi molecola–nanoparticella.

Nel suo insieme, questo lavoro di dottorato integra sviluppo algoritmico e caratterizzazione di sistemi complessi, fornendo strumenti computazionali in grado di ampliare gli spazi di applicabilità delle simulazioni TDDFT e di offrire una miglior interpretazione dell'origine elettronica dei fenomeni osservati.

Abstract (English)

The aim of this PhD project has been the development and application of advanced computational approaches for the simulation of optical and chiroptical properties of complex molecular and nanoscale systems. In particular, this work focuses on extending the applicability of time-dependent density functional theory (TDDFT) to large systems, where both accuracy and computational efficiency represent critical challenges.

To this end, algorithmic developments have been carried out within the polarization–based TDDFT (polTDDFT) formalism, with special emphasis on the Hybrid Diagonal Approximation (HDA). A Resolution-of-Identity (RI) strategy has been implemented to accelerate the computation of HDA corrections, enabling hybrid TDDFT calculations for systems comprising hundreds of atoms. The resulting RI–HDA framework has been assessed on representative systems, showing excellent agreement with high resolution experimental data while achieving a substantial reduction in computational effort.

A further key aspect of this work is the extension of the RI–HDA approach to Range-Separated (RS)hybrid functionals, such as CAMY-B3LYP. This development allows for an improved description of charge-transfer excitations and long-range electronic effects, while retaining the scalability of the polTDDFT approach. As a result, the methodology developed in this thesis provides a general and efficient computational framework for the study of optical and chiroptical properties in large and complex systems.

Alongside these methodological developments, the computational tools have been applied to investigate a variety of physically relevant problems. These include the analysis of plasmon enhanced electronic circular dichroism in chiral gold and alloyed nanowires, where destructive interference among collective excitations was shown to suppress the ECD signal at the plasmon resonance; the study of chirality transfer mechanisms in L-cysteine–functionalized gold clusters, highlighting the role of metal–ligand coupling and molecular organization at the interface; and the development of a multiscale quantum/continuum approach to describe plasmon-enhanced chiroptical effects in hybrid molecular–nanoparticle systems.

Overall, this PhD project combines algorithmic development and physical interpretation, providing computational tools that extend the reach of TDDFT-based spectroscopy and offer insight into the electronic origins of chiroptical phenomena in complex systems.

Acknowledgments

I would like to sincerely thank my supervisor, Professor Mauro Stener, for his constant support, availability, and kindness throughout these years. His scientific guidance and intellectual integrity have been an invaluable source of inspiration, and his example has taught me what it truly means to conduct research as part of a scientific community.

I am also deeply grateful to all the researchers and scientists with whom I had the opportunity to collaborate during the development of the works presented in this thesis. Their expertise, generosity, and constructive discussions have significantly enriched both my research and my doctoral experience.

Finally, my warmest thanks go to my colleagues, whose companionship and collaboration made the many hours spent working together not only productive, but also genuinely pleasant.

1 Introduction

This work focuses on the theoretical characterization of the chiro-optical response of metallic Nanoparticles (NPs) and the development of computational methods, within the framework of Density Functional Theory, to simulate it. Because our main goal was the reliable reproduction of the UV-Vis absorption spectrum or Circular Dichroism signal for complex systems in this first chapter we briefly introduce:

- What a spectroscopy experiment is.
- The computational tools at our disposal.
- The key concepts of Nanoscience
- Chirality and CD signal
- The key concepts of Nanoplasmonics

1.1 Spectroscopy

The main object of interest of this work is to produce and study an "absorption spectrum". It is the response of a system to a probe as a function of the probe's energy. The science behind the measurement of such spectra is spectroscopy.

Spectroscopy is one of the most powerful and versatile experimental tools to investigate the structure and properties of matter[1, 2]. Its unique possibility to correlate microscopic features (such as electronic, vibrational, or rotational states) with macroscopic observables, made spectroscopy the ideal bridge between physics, chemistry, and materials science since its very origins.

As clearly reported by Jaan Laane in his introduction to *"Frontiers of molecular spectroscopy"*[3] the historical development of spectroscopy highlights its central role in modern science. Its origin could be ascribed to the first observations made by Newton about the dispersion of light through a prism (1666). In the nineteenth century, thanks to the connection between spectral lines and chemical composition established by Fraunhofer, Bunsen, and Kirchhoff, marked the starting point of elemental analysis. Spectroscopy was also instrumental to the emergence of quantum theory, from Planck's law of blackbody radiation and Bohr's

model of the hydrogen atom to Schrödinger's wave mechanics. In the twentieth century, technological advances such as lasers, Fourier transform infrared (FT-IR) spectrometers, and ultrafast techniques dramatically expanded its scope, making spectroscopy a cornerstone of molecular sciences. Not surprisingly, more than twenty Nobel Prizes have been directly or indirectly awarded for contributions related to spectroscopic discoveries.

Even now, although new advances in fundamental physics resulted mostly from work in high-energy physics, when the fundamental symmetries of physics and their violations are considered, spectroscopy could improve our fundamental knowledge [4].

Today, spectroscopic methods are widely used due to their accessibility, non-invasive character, and the richness of the information they provide. Techniques such as UV–Vis absorption, fluorescence, Raman and NMR allow one to probe not only the fundamental electronic and vibrational states of molecules but also their ultrafast dynamics, environmental effects, and nonlinear optical properties.

Nevertheless, the interpretation of experimental spectra is often far from trivial: thermal fluctuations, vibronic couplings, and solvent or solid-state environments complicate the direct assignment of spectral features [5]. The combination of experiment and theory thus has a dual role: it is *interpretative*, as it helps rationalize and disentangle complex spectroscopic signals, and *predictive*, since it allows the rational design of novel materials with tailored optical properties. This duality is particularly relevant for applications such as solar energy conversion, photonics, and optoelectronic devices, where a fine control of light–matter interactions is essential.

The more general description of a spectroscopy experiment would consider a probe interacting with the system under study and causing a transition from an initial state $|i\rangle$ to a final state $|f\rangle$ which describes both the system and the probe (although often times it is considered the two wavefunctions to be separated). The relative transition probability w is given by Fermi's golden rule:

$$w = \frac{2\pi}{\hbar} \left|\langle \psi_f | \hat{H}\mathrm{int} | \psi_i \rangle\right|^2 \delta!\big(E_f - E_i - \omega\big) \tag{1.1}$$

where $\hat{H}$int is the probe-system interacting term of the Hamiltonian.

Different spectra and spectroscopy techniques study different excitations caused by different kind of interaction. Typical excitations, sorted according to the energy range involved, are:

- Vibrational excitations or free-carrier absorption involve energies in the infrared (IR) range of the spectrum, typical techniques are IR absorption and high-resolution inelastic scattering techniques [6].

- Spin excitations and resonant inelastic X-ray scattering involve energies in the range 100–500 meV [7] and a typical probe are neutrons [8].

- Valence excitations are promoted by visible and ultraviolet (UV-vis) light absorption or Raman scattering and typical techniques are photoabsorption spectra and Electronic Circular Dichroism (ECD).

- The resonance energy of collective modes like Plasmons, depending on the dimension of the system, could range from few meV (in nanostructures [9]) to many eV (in bulk materials [10]).

- core excitations involving inner-shell electrons require energies up to hundreds of eV.

In summary, spectroscopy, originally born from the observation of light dispersed by a prism, has evolved into a central discipline for understanding the structure and dynamics of matter. The parallel development of increasingly sophisticated experimental techniques and accurate theoretical models continues to enhance its scope, confirming spectroscopy as one of the most indispensable tools of contemporary science.

1.2 Computational absorption spectroscopy

Absorption spectroscopy measures the amount of energy, in the form of electro-magnetic radiation (r.e.m.), absorbed by a sample at a given range of photon frequencies. The energy of the absorbed photons is used to promote neutral transitions of an electron (or more electrons) from an occupied to a virtual orbital thus creating an electron-hole pair. This means that the electron stays in the proximity of the newly created ion and feels the presence of the relative hole. Such interaction have to be explicitly taken into account when modeling this class of phenomena. Both for experimentalists and theoreticians, the hugely different energy ranges and regimes of interaction mean different measurement techniques and simulation tools. In this work we will focus our attention on UV-Visible absorption and Electronic Circular Dichroism (ECD).

In this context, *computational spectroscopy* has become an indispensable complement to experiment. The integration of quantum mechanical modeling and spectroscopy enables the assignment of spectral bands to specific transitions, the extraction of hidden information from band shapes and positions, and even the prediction of the optical properties of yet unknown molecules and materials.

Wavefunction-based ab initio methods (e.g., post–Hartree–Fock approaches such as Coupled Cluster) provide benchmark accuracy but are computationally feasible only for relatively small molecular systems. Density Functional Theory (DFT) and its time-dependent extension (TDDFT) [11] have revolutionized the field, offering a practical balance between accuracy and computational cost.

In particular, the quality of TDDFT calculations depends strongly on the choice of the functional and the introduction of hybrid exchange-correlational (xc) functionals as B3LYP [12–14], and range-separated (RS) ones as CAM-B3LYP [15, 16], drastically increased their accuracy. However, the cost of the calculation increases together with the accuracy of the xc functional, e.g. the inclusion of the exact Hartree-Fock (HF) non-local exchange, hence its choice is strongly related to the system size.

The most popular TDDFT formalism was proposed by Casida [17], whose equations are usually solved by means of the Davidson iterative algorithm [**Davidson**] in quantum-chemical codes like Amsterdam Modeling Suite (AMS) [18–21] and TURBOMOLE [22]. Such approach is efficient when a relatively small number of low excitation energies is extracted but becomes unaffordable for large systems when a larger number of excitation is needed. Therefore, the Casida's formulation and its computational implementation work fine mostly for small or medium-size molecules and large systems where only very few excited states are studied.

When dealing with larger molecules various strategies to reduce the computational cost of the simulation are possible: neglecting terms (like in Tamm-Dancoff approximation [23]), partitioning into subsystems [24, 25], truncating the single orbital transition space [26] and approximating integrals.

In this last category falls the approximation developed by Niehaus et al. called time dependent density functional theory based tight binding (TD-DFTB) [27–29]. It starts from a ground state DFTB calculation (cheaper because of the optimized minimum valence orbital basis set and the approximated two-centered integrals) [30, 31] and recasts Casida's linear response approach in the tight binding framework. It has been used in several applications and proved to yield good results for $\pi \rightarrow \pi*$ transitions [27] but it inherits limitations from the DFTB ground state calculation (limited accuracy with respect to DFT and needs careful parametrization for different elements and systems).

The so called simplified Tamm Dancoff Approximation (sTDA) [32] and TD-DFT (sTDDFT) [33] methods, proposed by Grimme, start from a DFT ground state calculation and approximates two-electron integrals using short-range damped Coulomb interactions of transition density monopoles in the TDA/TD-DFT scheme.

A similar approach, denoted TDDFT+TB, is inspired by sTDA and sTDDFT but it employs only local functionals for the calculation of the excited states [34, 35].

Other alternative TDDFT strategies try to solve the limitation over the energy range of the spectrum in different ways. It is possible to treat the time-propagation of the system explicitly, as proposed by Yabana and Bertsch [36] and implemented, over a real space grid, in OCTOPUS code [37] to simulate the optical response of large biomolecules [38] and metal clusters up to 236 atoms [39].

A different approach is based on a superoperator formulation of TDDFT; the spectrum is

extracted from the dynamical polarizability of the system by efficiently exploiting the Lanczos method [40]. This idea has been implemented using plain waves basis set and applied to study systems like C_{60}, C_{70} [41] together with organic molecules like chlorophyll a [42]. This approach is quite appealing for large systems because it allows for the simulation of the whole spectrum at once without, at least in theory, intrinsic limitations over the energy range, as it is for the Davidson diagonalization procedure. A similar idea lies at the core of PolTDDFT [43, 44], the main algorithm used in this thesis work, but a more detailed description of it will be offered in future chapters.

Other possibilities to study large metallic systems are the TDDFT time-propagation with Transition Contribution Map (TCM) [45] by H"akkinen and the Nobusada's massively parallel implementation of TDDFT based on real time and real-space [46, 47]. In particular the TCM is able to extract information regarding the nature of the transitions involved in the spectral feature at a similar level as what granted by more Casida inspired procedures. Of course, the availability of massively parallel supercomputers represents a strong stimulus for the development of highly parallel ab initio and DFT codes like NWCHEM [48].

Thus, for small to medium-sized molecules, theoretical predictions can nowadays reach the accuracy of state-of-the-art experimental measurements, while continuous methodological and computational advances extend their applicability to increasingly large and complex systems.

1.3 Nanoscience and Metallic Nano Clusters

Nanoscience examines materials structured or patterned below ~100 nm, a regime where size is not a mere geometric attribute but a control knob for quantum and collective phenomena.

To understand the importance and central role of this field of research: the wavelength of visible light, the de Broglie wavelength of charge carriers, characteristic plasmonic length scales, and even the dimensions of large biomolecules all lie inside this dimension range. As a result, at this scale, materials acquire *size-dependent* properties that are neither purely molecular nor bulk-like [49].

So, we can interpret nanostructures and nanomaterials as belonging to a separate class of matter: although they share the same atomic composition of the parent solid, their properties can be tuned through a single, intuitive, parameter: their size. Maybe, the most known example of this is provided by quantum dots, whose band gap and hence optical absorption/emission can be shifted across the visible by reducing the particle radius, in line with particle-in-a-box quantization where the level spacing scales as $\Delta E \propto 1/L^2$ [50, 51].

Similar size control extends to redox potentials, melting points, and phase behavior.

Historically, the notion that macroscopic dimensions influence electronic properties emerged early: Fr"ohlich argued that a free-electron metal [53] confined to small particles would

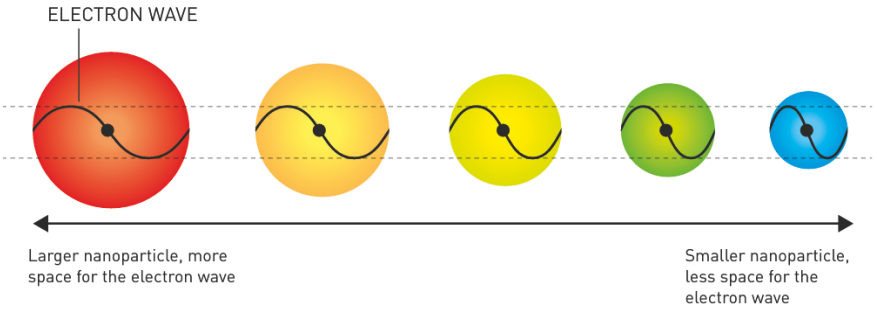


Figure 1.1: The dimension of the nanoparticle affects the electron wavefunction thus changing its optical properties [52].

exhibit measurable deviations (e.g., in specific heat) from bulk behavior [54]. Experimental hints were long indirect e.g., the colors of colloidal glasses [55, 56], until controlled syntheses allowed systematic study of truly nanoscale, discrete systems [57–60].

Nowadays nanoscience represents a milestone at the crossroad of chemistry, physics, and materials science and its applications span from catalysis and sensing [61] to photonics [62, 63], medicine [64, 65], and quantum technologies. As a consequence of this, chemistry, among other disciplines, has a pivotal role: precise, bottom-up synthesis, purification, and passivation translate quantum ideas into real, stable materials.

Among nanoscale objects, *monolayer-protected metal nanoclusters* (MPCs) occupy a unique niche. These compounds comprise a metal core (often Au, Ag, or bimetallic alloys) of well-defined atom count, *protected* by an organic monolayer, typically thiolates, but also phosphines and related ligands, to prevent aggregation and to stabilize discrete stoichiometries. Thanks to advances in wet-chemistry protocols, many MPCs can now be prepared with *atomic precision* and fully characterized by high-resolution mass spectrometry and single-crystal X-ray crystallography [61, 66–69]. This atomic-level knowledge has been instrumental in establishing rigorous cross-validation between experiment and computation, enabling reliable structure–property studies and the rational selection of quantum-mechanical (QM) methods with controlled accuracy/cost trade-offs [70].

In this work we focus primarily on *thiolate-protected gold nanoclusters* (often denoted RS–AuNCs)[71–78], while keeping an eye on closely related metallic systems and on extended, yet still nanoscale, architectures such as nanowires [79–84]. The first predicted structure of $Au_{25}(SR)^{-}_{18}$ (later became a standard in the field) was reported by H"akkinen and Gr"onback *et al.* in 2008 [72] and confirmed experimentally by two groups at the same time [66, 85]. Over the last two decades, synthesis, total structural determination, and optical characterization of RS–AuNCs have progressed hand in hand with theory, revealing rich trends as a function of metal composition, ligand identity, and “staple” motif geometry at the metal–ligand interface [70, 85–88].

The optical absorption of MPCs is a stringent benchmark for electronic-structure theory and,

although a qualitative agreement between theory and experiment is generally obtained[89, 90], a quantitative match has rarely been achieved [91–93] because it reflects a subtle interplay among three electronically distinct moieties: (i) a low-oxidation-state metallic core, (ii) a metal–ligand interfacial shell comprising staple motifs, and (iii) the organic ligands themselves. Accurate predictions therefore demand a *balanced* treatment across chemically heterogeneous regions [91]. Time-dependent density functional theory (TDDFT) has become the workhorse for simulating the photoabsorption of MPCs. Several lessons have emerged from systematic validation studies. First, the *geometry* matters: using experimentally resolved structures (when available) avoids error accumulation from geometry predictions [91]. Second, for the *low-energy* spectral region—where metal–ligand and interfacial transitions dominate—*hybrid* exchange–correlation (xc) functionals (e.g., B3LYP in both ground-state Kohn–Sham equations and response kernel) are generally required to achieve near-quantitative agreement with experiment [94]. Semilocal GGAs tend to underestimate transition energies in this window, while asymptotically corrected models (e.g., LB94, SAOP) often improve higher-energy ligand-centered excitations yet still struggle at low energy without hybrid exchange [92]. The broader implication is methodological: once a protocol is validated on reference MPCs—accurate experimental geometry; hybrid xc functional and kernel; careful basis/pseudopotential and environment choices—it can be *predictively* applied when experimental spectra are unavailable, guiding materials design for sensing, photocatalysis, and plasmon-assisted chemistry [95]. In this spirit, extending validation to families with varied metal composition and ligands (e.g., M_{25} cores with Au/Ag/Pt admixtures and DMBT or *n*-butyl thiolates) is essential to assess transferability and to map how metal–ligand cooperativity sculpts optical features.

While atomically precise MPCs epitomize zero-dimensional confinement, one-dimensional nanowires (and related anisotropic nanostructures) introduce directional quantization and distinct surface plasmon modes [96]. Chemically, many of the same principles apply: ligand passivation governs stability, charge transfer, and interfacial screening; composition and cross-section tune resonant energies; and atomic-scale morphology can break symmetries, enabling chiroptical activity [97]. From a simulation standpoint, these systems challenge theory across length scales: TDDFT remains the gold standard at the tens–hundreds of atoms scale, while efficient formulations (e.g., polarization-based TDDFT or real-time approaches) help access broader spectral windows and larger electron counts without sacrificing essential physics.

1.4 Chirality and Circular Dichroism in Nanostructures

One of the most interesting and studied properties in nature is chirality. It is the geometrical property possessed by an object, or a system in general, that cannot be superimposed onto its

mirror image. In symmetry terms this statement is equivalent to say the object lacks improper symmetry elements S_n, such as mirror planes or an inversion center. Chirality is an intrinsic property of a system which could manifest itself at any scale: from the single stereogenic centre of a single molecule, then coiling of DNA helices, to viruses and macroscopic systems such as human hands or even galaxies [98–100]. One of the most distinctive physical consequences of chirality is *optical activity* the presence of a *Circular Dichroism* (CD) signal. CD measures the difference in absorption between left- and right-circularly polarized light. Conceptually, a CD experiment is very similar to a conventional absorption measurement, except that the incident beam is circularly polarized and the transmitted intensity is recorded separately for the two polarizations. The CD signal corresponds to the differential absorption of these components and thus provides a direct signature of the chiral nature of the system. Depending on the type of light–matter interaction involved, different spectroscopic regimes can be explored: *electronic CD (ECD)* in the UV–Vis region, *vibrational CD (VCD)* in the infrared, and *circularly polarized luminescence (CPL)* in emission experiments [101–103]. These techniques are routinely employed to obtain conformational and three-dimensional structural information about molecules and materials in various electronic or excited states [104]. In the present work, we focus on *electronic CD*, which probes the electronic transitions of chiral molecular systems and metal-based nanostructures. Within the Rosenfeld formalism, the ECD intensity is proportional to the imaginary part of the scalar product between the electric and magnetic transition dipole moments:

$$\mathrm{CD} \propto \frac{4}{3}\,\gamma\ \mathrm{Im}(\langle 0|\mu|n\rangle \cdot \langle n|m|0\rangle) \tag{1.2}$$

where μ and m are the electric and magnetic transition moments between the ground ($|0\rangle$) and excited ($|n\rangle$) states [105]. Chirality at molecular level is a well understood phenomena but its extension to metallic, semiconducting, or hybrid nanostructures remains an active field of research. Chiral nanomaterials occupy a unique position between molecular and macroscopic systems, providing both practical applications and fundamental insights into the origins of chirality. They have attracted growing attention for their roles in biomedicine [106], enantioselective catalysis [107], and optical and photonic devices [108], thanks to their tunable properties determined by *size, shape, and composition* [109–111]. In general, a nanoparticle (NP) refers to a structure with dimensions between approximately 0.5 and 100 nm. Chirality in such nanostructures can arise from several mechanisms [112–114]:

(i) Chiral shape: inherent asymmetry in the morphology of the nanostructure, as in twisted nanorods, helical nanowires, or chiral metal clusters;

(ii) Chiral assembly: collective arrangements of otherwise achiral nanoparticles into a chiral superstructure, often leading to plasmon coupling effects;

(iii) Molecule–nanoparticle interactions: where chirality is transferred from chiral ligands or adsorbed molecules to an initially achiral metallic core, or even induced by achiral ligands forming chiral patterns on the surface.

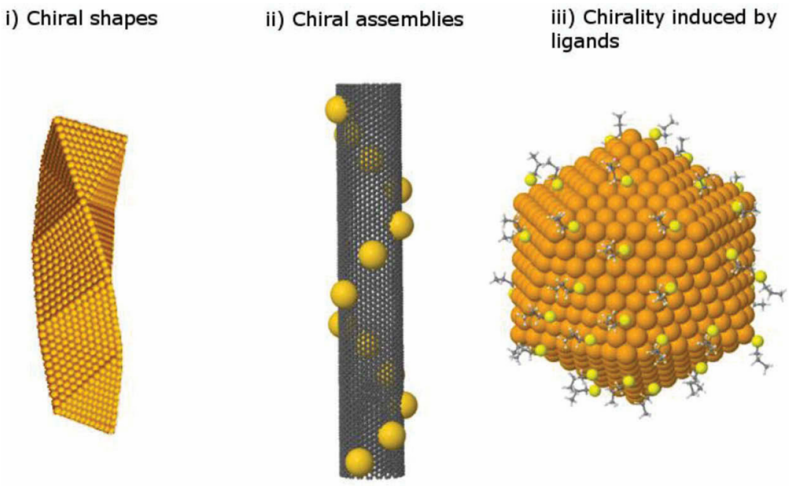


Figure 1.2: possible sources of chirality at the nanoscale [105].

Examples of the first case of chirality are twisted gold clusters [115], helical ribbons [116], and spiraled nanowires of Au, SiO_2, or TiO_2 [117–119]. The plasmonic origin of the CD signal for such systems is confirmed by the fact that their optical activity does not depend on the temperature[120, 121]. The second case often involve the assembly of achiral Nanoparticle guided by biomolecules or polymers; of course, being the source of chirality in the spatial arrangement of the Nanoparticles, their optical response is particularly sensitive to inter-particle distance and orientation [122–125]. The third scenario, *chirality transfer* — observed by Whetten *et al.* for the first time in 1998 [126] — represents a connection between chirality at the nanoscale and at the molecular level; a typical example are achiral ligands disposed in a chiral pattern at the surface of a Nanoparticle [127]. In summary, *chiral nanostructures* are at the cross-section of geometrical complexity and quantum effects, and their optical phenomena needs the integration of both to be fully appreciated. Circular Dichroism thus provides a fundamental spectroscopic probe to understand the nature of these complex systems — from molecular transitions to collective plasmonic modes — providing fundamental insight into how chirality manifests, transfers, and amplifies at the nanoscale.

1.5 Nanoplasmonics

One of the most dominant phenomena shaping the chemical and optical activity of metallic nanostructures is the collective oscillation of valence electrons. This collective motion, known as plasmon, have the ability to dramatically focus the electromagnetic field within a small

region of space, thus obtaining a high electromagnetic energy density that could be exploited to drive new chemical pathways or augment the intensity of otherwise weak signals [128]. The energy released upon their decay could lead to even more interesting phenomena like the creation of energetic carriers or a local heating through scattering processes (electron-electron or electron-photon scattering)[129].

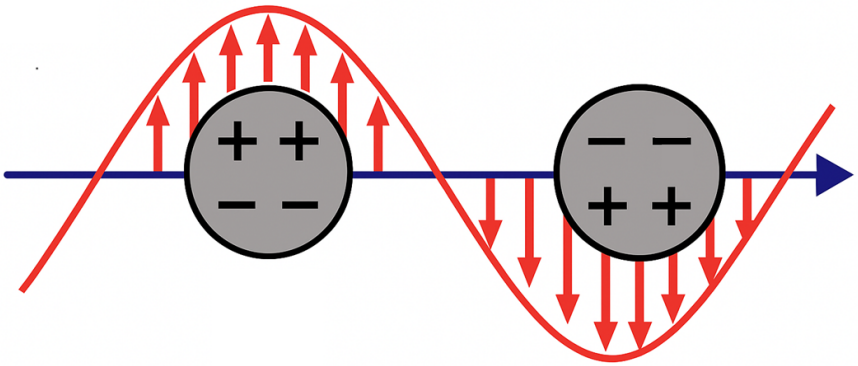


Figure 1.3: schematic representation of the collective motion of electrons in two spherical nanoparticles (in gray) in response to an electro-magnetic perturbation (in red) .

These plasmon-mediated effects form the foundation of plasmonic chemistry [130, 131] where such collective excitations are used to drive and regulate chemical transformations in potentially more efficient and sustainable ways [132]. When the plasmonic motion involved electrons localized at the surface of the system we talk about localized surface plasmon resonance (LSPR)[130].

Perhaps the most important thing about plasmons is that, being a collective motion, they span a wider region then the normal, single electron excitation, for this reason its specifics are strongly dependent on the shape, morphology and overall structure of the plasmonic system. This dependence is strikingly manifested in metallic nanoparticles where, the conceptual and practical tools of nanoscience can be used to optimally tailor such materials.

Over the last decade, the interaction between plasmonic modes and molecular excitations has specialized into a research area referred to as molecular nanoplasmonics [133]. In broad terms, molecular nanoplasmonics exploits the intense, spatially localized fields generated by a plasmonic nanostructures to reshape the properties of a closely molecular system [134–136]. This field brings together a wide spectrum of light–matter phenomena, including surface-enhanced Raman scattering [134, 137], modulation of fluorescence by plasmonic environments [138, 139], generation of high harmonics [140–143], plasmon-induced circular dichroism [144, 145], and a variety of plasmon-driven photochemical processes [146, 147].

As mentioned at the incipit of this section, plasmonic influence could amplify inherently weak molecular signals. A typical application example is the Surface-enhanced Raman spectroscopy. Also the circular dichroism of chiral molecules, which would be inherently

weaker than conventional absorption (because of the magnetic dipole contribution) can increase several orders of magnitude under the influence of a plasmon, enabling detection at extremely low concentrations [148–151].

As said before, the plasmon is a collective behavior that span the entirety, or at least a larger section of the nanoparticle, this means its effect on nearby molecular systems strongly depends on the morphological and structural details of the nanoparticle: size, shape and chemical composition determine both the intensity and the character of the interaction. By deliberately shaping these features, is it possible to tune the response of the molecular system; which explains the ongoing effort in designing nanoparticles with tailored optical behaviour. Central to this control is the excitation of localized surface plasmon resonances (LSPRs) [152–154].

2 Theoretical introduction

This chapter aims to provide the theoretical framework underlying the computational protocols employed in this thesis. After an introductory section, where a common vocabulary for discussing quantum phenomena is established, we review the theoretical foundations of the most relevant time-independent electronic-structure methods, namely Hartree–Fock and Density Functional Theory. Finally, we provide the theoretical justification for extending Density Functional Theory to the treatment of time-dependent phenomena.

The following sections are elaborated starting from well-established literature [155–159].

2.1 Addressing quantum mechanics

In Quantum Mechanics (QM), the time evolution of the state of a particle is governed by the time-dependent Schrödinger equation:

$$\mathrm{i}\,\frac{\partial}{\partial t}\,\Psi(\mathbf{r},t) = \hat{H}\,\Psi(\mathbf{r},t), \tag{2.1}$$

where $\hat{H}$ denotes the Hamiltonian operator. If $\hat{H}$ is time independent, the solution takes the separable form

$$\Psi(\mathbf{r},t) = \Phi(\mathbf{r})\,\mathrm{e}^{-\mathrm{i}Et}, \tag{2.2}$$

and Eq. (2.1) reduces to the time-independent eigenvalue problem:

$$\hat{H}\,\Phi_k(\mathbf{r}) = E_k\,\Phi_k(\mathbf{r}), \tag{2.3}$$

where $\Phi_k(\mathbf{r})$ and E_k are the k-th eigenstate and eigenvalue, respectively. Since multiple stationary states are possible, k represents a set of quantum numbers characterizing each state.

The wavefunction is an abstract object and is not directly observable. Its physical meaning is given by the probability density

$$|\Phi_k(\mathbf{r})|^2, \tag{2.4}$$

which describes the likelihood of finding the particle at position $\mathbf{r}$ when in state k.

Let us now recall some basic properties:

- The probability density must be normalizable:

$$\int \mathrm{d}^3\mathbf{r}\,|\Phi_k(\mathbf{r})|^2 = 1. \tag{2.5}$$

  Throughout this thesis, the notation $\mathrm{d}^3\mathbf{r}$ denotes the volume element in three-dimensional real space.

- Any linear combination of time-dependent solutions is itself a solution:

$$\Psi(\mathbf{r},\mathbf{t}) = C_1\,\Psi_1(\mathbf{r},\mathbf{t}) + C_2\,\Psi_2(\mathbf{r},\mathbf{t}), \tag{2.6}$$

  where C_1 and C_2 are arbitrary complex coefficients.

All measurable properties of a quantum system are encoded in its wavefunction, and the value of any observable is obtained by applying the corresponding operator. The experimentally accessible quantity associated with an operator $\hat{A}$ is its *expectation value*:

$$\langle\hat{A}\rangle(t) = \int \mathrm{d}^3r\,\Psi^*(\mathbf{r},t)\,\hat{A}\,\Psi(\mathbf{r},t). \tag{2.7}$$

In general, $\langle\hat{A}\rangle$ is time dependent.

Operators act on the right:

$$\Phi' = \hat{A}\,\Phi, \tag{2.8}$$

where Φ' is the resulting state. The Hermitian adjoint $\hat{A}^\dagger$ is defined through

$$\int \mathrm{d}^3r\,\Phi^*(\hat{A}\Psi) = \int \mathrm{d}^3r\,(\hat{A}^\dagger\Phi)^*\Psi, \tag{2.9}$$

and observables correspond to Hermitian operators:

$$\hat{A} = \hat{A}^\dagger. \tag{2.10}$$

Many-particle systems often involve operators that can be decomposed into sums of independent contributions. If

$$\hat{C}(\mathbf{r_1},\mathbf{r_2}) = \hat{A}(\mathbf{r_1}) + \hat{B}(\mathbf{r_2}), \tag{2.11}$$

with eigenvalue equations

$$\hat{A}\,\Phi_\alpha(\mathbf{r}_1) = A_\alpha\,\Phi_\alpha(\mathbf{r}_1), \qquad \hat{B}\,\Phi_\beta(\mathbf{r}_2) = B_\beta\,\Phi_\beta(\mathbf{r}_2), \tag{2.12}$$

then the eigenstates of $\hat{C}$ are direct products:

$$\Psi_{\alpha\beta}(\mathbf{r}_1, \mathbf{r}_2) = \Phi_\alpha(\mathbf{r}_1)\, \Phi_\beta(\mathbf{r}_2), \tag{2.13}$$

$$C_{\alpha\beta} = A_\alpha + B_\beta. \tag{2.14}$$

This separability property will be pivotal when treating non-interacting electron systems.

2.1.1 Dirac notation

In Dirac notation, a state function $\Phi(\mathbf{r})$ is represented as a vector in Hilbert space, denoted by a *ket*:

$$\Phi(\mathbf{r}) \longrightarrow |\Phi\rangle, \qquad \Phi^*(\mathbf{r}) \longrightarrow \langle\Phi|, \tag{2.15}$$

where $\langle\Phi|$ is the corresponding *bra*, i.e., the complex conjugate transpose of the ket.

A general state can be written as a linear combination of basis states,

$$|\Phi\rangle = c_1\, |\Phi_1\rangle + c_2\, |\Phi_2\rangle, \tag{2.16}$$

with c_1 and c_2 complex coefficients. The scalar product between two states is defined as

$$\langle\Phi_1|\Phi_2\rangle = \int \mathrm{d}^3 r\, \Phi_1^*(\mathbf{r})\, \Phi_2(\mathbf{r}). \tag{2.17}$$

An operator acting on a state, written in coordinate representation as

$$\Psi(\mathbf{r}) = \hat{O}\, \Phi(\mathbf{r}), \tag{2.18}$$

corresponds in Dirac notation to

$$|\Psi\rangle = \hat{O}\, |\Phi\rangle = |\hat{O}\Phi\rangle. \tag{2.19}$$

Taking the Hermitian conjugate of this expression yields

$$\langle\Psi| = \langle\Phi|\, \hat{O}^\dagger = \langle\hat{O}\Phi|. \tag{2.20}$$

More generally, for two states $|\Phi_1\rangle$ and $|\Phi_2\rangle$ and an operator $\hat{A}$, the following relation holds:

$$\left(\langle\Phi_1|\hat{A}|\Phi_2\rangle\right)^* = \langle\Phi_2|\hat{A}^\dagger|\Phi_1\rangle. \tag{2.21}$$

Since vectors in Hilbert space are not necessarily normalized, the expectation value of an operator $\hat{O}$ is defined as

$$\langle\hat{O}\rangle = \frac{\langle\Phi|\, \hat{O}\, |\Phi\rangle}{\langle\Phi|\Phi\rangle}. \tag{2.22}$$

If the state is normalized, $\langle\Phi|\Phi\rangle = 1$, and the denominator reduces to unity.

2.1.2 Matrix formulation

Quantum Mechanics can equivalently be formulated in terms of matrix analysis, as first established by Heisenberg [160–162]. The key steps of this correspondence are summarized below.

- **Diagonal representation of an operator.**

  Consider an Hermitian operator $\hat{A}$ with eigenvalue equation

  $$\hat{A}\,\Phi_k = A_k\,\Phi_k, \tag{2.23}$$

  where $\{\Phi_k\}_{k=1,2,\ldots,M}$ is an orthonormal set of eigenfunctions (possibly with $M = \infty$). In Dirac notation this becomes

  $$\hat{A}\,|k\rangle = A_k\,|k\rangle, \tag{2.24}$$

  where each eigenstate is represented as

  $$|k\rangle \longrightarrow \begin{pmatrix} 0 \\ \vdots \\ 1 \\ \vdots \\ 0 \end{pmatrix}, \qquad \langle k| \longrightarrow (0,\ldots,1,\ldots,0). \tag{2.25}$$

  In this basis, the operator $\hat{A}$ is represented by the diagonal matrix

  $$\hat{A} \longrightarrow \begin{pmatrix} A_1 & 0 & \cdots & 0 \\ 0 & A_2 & \cdots & 0 \\ \vdots & \vdots & \ddots & \vdots \\ 0 & 0 & \cdots & A_M \end{pmatrix}. \tag{2.26}$$

  The set $\{|k\rangle\}$ is referred to as the *basis set*.

- **Expansion of arbitrary states.**

By completeness, any state $|\Psi\rangle$ can be expanded as

$$|\Psi\rangle = \sum_{k=1}^{M} c_k \, |k\rangle \;\longrightarrow\; \begin{pmatrix} c_1 \\ c_2 \\ \vdots \\ c_M \end{pmatrix} = C, \tag{2.27}$$

and similarly,

$$\langle\Psi| = \sum_{k=1}^{M} c_k^* \, \langle k| \;\longrightarrow\; \begin{pmatrix} c_1^* & c_2^* & \cdots & c_M^* \end{pmatrix} = C^\dagger. \tag{2.28}$$

The coefficient c_k represents the projection of $|\Psi\rangle$ onto the k-th basis vector.

- **Matrix representation of an operator.**

Let $\hat{B}$ be an operator acting on a state:

$$\hat{B}\,|\Psi\rangle = |\Omega\rangle. \tag{2.29}$$

Both states may be expanded in the chosen basis:

$$|\Psi\rangle = \sum_{k=1}^{M} c_k |k\rangle \;\longrightarrow\; C, \qquad |\Omega\rangle = \sum_{k=1}^{M} d_k |k\rangle \;\longrightarrow\; D. \tag{2.30}$$

Projecting the relation $\hat{B}|\Psi\rangle = |\Omega\rangle$ onto $\langle k'|$ gives

$$\sum_{k=1}^{M} B_{k'k}\, c_k = d_{k'}, \qquad k' = 1, \ldots, M, \tag{2.31}$$

where the matrix elements of $\hat{B}$ are

$$B_{k'k} \equiv \langle k'|\hat{B}|k\rangle = \int \mathrm{d}^3 r \, \Phi_{k'}^*(\mathbf{r})\, \hat{B}\, \Phi_k(\mathbf{r}). \tag{2.32}$$

In matrix notation this becomes the linear system

$$B\,C = D. \tag{2.33}$$

Thus $\hat{B}$ is represented by the square matrix

$$\hat{B} \longrightarrow B = \begin{pmatrix} B_{11} & B_{12} & \cdots & B_{1M} \\ B_{21} & B_{22} & \cdots & B_{2M} \\ \vdots & \vdots & \ddots & \vdots \\ B_{M1} & B_{M2} & \cdots & B_{MM} \end{pmatrix}, \tag{2.34}$$

which depends only on the choice of basis, not on the state $|\Psi\rangle$.

- **Diagonalization and eigenvalue problem.**

  Let $|\lambda\rangle$ be an eigenstate of $\hat{B}$ with eigenvalue λ:

$$\hat{B}\,|\lambda\rangle = \lambda\,|\lambda\rangle. \tag{2.35}$$

  Expanding in the basis,

$$|\lambda\rangle = \sum_{k=1}^{M} b_k\,|k\rangle \longrightarrow \begin{pmatrix} b_1 \\ b_2 \\ \vdots \\ b_M \end{pmatrix}, \tag{2.36}$$

  the eigenvalue equation becomes

$$B \begin{pmatrix} b_1 \\ b_2 \\ \vdots \\ b_M \end{pmatrix} = \lambda \begin{pmatrix} b_1 \\ b_2 \\ \vdots \\ b_M \end{pmatrix}. \tag{2.37}$$

  The corresponding secular equation reads

$$\det \begin{pmatrix} B_{11} - \lambda & B_{12} & \cdots & B_{1M} \\ B_{21} & B_{22} - \lambda & \cdots & B_{2M} \\ \vdots & \vdots & \ddots & \vdots \\ B_{M1} & B_{M2} & \cdots & B_{MM} - \lambda \end{pmatrix} = 0. \tag{2.38}$$

2.2 Time independent methods

Before examining the time-dependent response of a system it is appropriate to introduce how we could describe the static problem. Two main possibilities are available: *ab initio* methods

and DFT.

2.2.1 Ab initio: Hartree–Fock

In the Hartree–Fock (HF) method, the ground-state wavefunction of an N-electron system (described within the Born–Oppenheimer approximation) is approximated by a single Slater determinant composed of the "best" Molecular Orbitals (MOs), determined through a variational principle.

We consider a trial wavefunction in the form of an antisymmetrized Slater determinant:

$$\Psi(\mathbf{x}_1, \ldots, \mathbf{x}_N) = \frac{1}{\sqrt{N!}} \begin{vmatrix} \psi_1(\mathbf{x}_1) & \psi_2(\mathbf{x}_1) & \cdots & \psi_N(\mathbf{x}_1) \\ \psi_1(\mathbf{x}_2) & \psi_2(\mathbf{x}_2) & \cdots & \psi_N(\mathbf{x}_2) \\ \vdots & \vdots & \ddots & \vdots \\ \psi_1(\mathbf{x}_N) & \psi_2(\mathbf{x}_N) & \cdots & \psi_N(\mathbf{x}_N) \end{vmatrix}, \tag{2.39}$$

where ψ_i denotes the i-th occupied MO.

We will show that the optimal set of orbitals for describing the ground state Ψ_0 is obtained as the first N solutions of the one-electron eigenvalue equation

$$\hat{F}\,\psi = \epsilon\,\psi, \tag{2.40}$$

which is known as the *Hartree–Fock equation*. To derive it, we impose stationarity of the electronic energy

$$E = \langle \Psi_0 | \hat{H} | \Psi_0 \rangle, \qquad \delta E = 0. \tag{2.41}$$

Using Slater rules, the HF variational energy for a single determinant reads

$$E_0 = \sum_i^N \langle i | \hat{h} | i \rangle + \frac{1}{2} \sum_i^N \sum_j^N \langle ij \| ij \rangle, \tag{2.42}$$

where $\hat{h}$ is the one-electron Hamiltonian and

$$\langle ij \| ij \rangle = \langle ij | ij \rangle - \langle ij | ji \rangle \tag{2.43}$$

is the antisymmetrized two-electron integral. The general two-electron integral is defined as

$$\langle ij | kl \rangle = \iint \psi_i^*(\mathbf{x}_1)\, \psi_j^*(\mathbf{x}_2)\, \frac{1}{|\mathbf{r}_1 - \mathbf{r}_2|}\, \psi_k(\mathbf{x}_1)\, \psi_l(\mathbf{x}_2)\, \mathrm{d}\mathbf{x}_1\, \mathrm{d}\mathbf{x}_2. \tag{2.44}$$

The first contribution represents the *Coulomb* interaction; the second the *exchange* contribution arising from fermionic antisymmetry.

The above expression holds only for orthonormal orbitals $\langle i | j \rangle = \delta_{ij}$. We therefore

introduce Lagrange multipliers ϵ_{ij} and define the Lagrangian

$$\mathcal{L} = E_0 - \sum_{i}^{\text{occ.}} \sum_{j}^{\text{occ.}} \epsilon_{ji} \left(\langle i|j\rangle - \delta_{ij} \right). \tag{2.45}$$

Since $\mathcal{L}$ is real, the matrix ϵ must be Hermitian:

$$\epsilon_{ij} = \epsilon_{ji}^{*}. \tag{2.46}$$

Computing the first-order variation yields

$$\begin{aligned} \delta\mathcal{L} = &\sum_{i}^{\text{occ.}} \left(\langle \delta i|\hat{h}|i\rangle + \langle i|\hat{h}|\delta i\rangle \right) \\ &+ \frac{1}{2} \sum_{i}^{\text{occ.}} \sum_{j}^{\text{occ.}} \left(\langle \delta i j \| i j\rangle + \langle i \delta j \| i j\rangle + \langle i j \| \delta i j\rangle + \langle i j \| i \delta j\rangle \right) \\ &- \sum_{i}^{\text{occ.}} \sum_{j}^{\text{occ.}} \left(\langle \delta i|j\rangle + \langle i|\delta j\rangle \right) \epsilon_{ja} = 0. \end{aligned} \tag{2.47}$$

Collecting all terms depending on $\langle \delta i|$, and adding their complex conjugates (CC), leads to

$$\delta\mathcal{L} = \sum_{i}^{\text{occ.}} \left\langle \delta i \middle| \hat{h}\,|i\rangle + \sum_{j}^{\text{occ.}} \hat{J}_j|i\rangle - \sum_{j}^{\text{occ.}} \hat{K}_j|i\rangle - \sum_{j}^{\text{occ.}} |j\rangle\, \epsilon_{ja} \right\rangle + \text{CC} = 0. \tag{2.48}$$

Since the variations $\langle \delta i|$ are arbitrary, the bracketed term must vanish:

$$\hat{h}\,|i\rangle + \sum_{j}^{\text{occ.}} \hat{J}_j\,|i\rangle - \sum_{j}^{\text{occ.}} \hat{K}_j\,|i\rangle - \sum_{j}^{\text{occ.}} |j\rangle\, \epsilon_{ji} = 0. \tag{2.49}$$

The Coulomb operator associated with orbital ψ_j is

$$\hat{J}_j\, \psi_i(\mathbf{x}_1) = \int \frac{|\psi_j(\mathbf{x}_2)|^2}{|\mathbf{r}_1 - \mathbf{r}_2|}\, \psi_i(\mathbf{x}_1)\, \mathrm{d}\mathbf{x}_2. \tag{2.50}$$

The exchange operator is non-local:

$$\hat{K}_j\, \psi_i(\mathbf{x}_1) = \int \frac{\psi_j^{*}(\mathbf{x}_2)\, \psi_i(\mathbf{x}_2)}{|\mathbf{r}_1 - \mathbf{r}_2|}\, \psi_j(\mathbf{x}_1)\, \mathrm{d}\mathbf{x}_2. \tag{2.51}$$

Summing over occupied orbitals we obtain:

$$\hat{J} = \sum_{j}^{\text{occ.}} \hat{J}_j, \qquad \hat{K} = \sum_{j}^{\text{occ.}} \hat{K}_j. \tag{2.52}$$

We define the Fock operator as:

$$\hat{F} = \hat{h} + \hat{J} - \hat{K}. \tag{2.53}$$

It represents an effective one-electron Hamiltonian describing motion in the external potential of the nuclei plus the Coulomb–exchange field generated by the other electrons.

The previous result becomes

$$\hat{F}\,\psi_i = \sum_{j}^{\text{occ.}} \psi_j\,\epsilon_{ji}. \tag{2.54}$$

Since ϵ is Hermitian, it can be diagonalized by a unitary transformation. Because a Slater determinant is invariant under unitary rotations of the occupied MOs, we may choose a basis where ϵ is diagonal, yielding the *canonical* HF equations:

$$\hat{F}\,\psi_i = \epsilon_i\,\psi_i. \tag{2.55}$$

In practice, HF equations are solved via a Self-Consistent Field (SCF) procedure. Each MO is expanded over a finite basis of Atomic Orbitals (AOs), turning the HF eigenvalue problem into a matrix equation:

$$\mathbf{F}\,\mathbf{C} = \mathbf{S}\,\mathbf{C}\,\mathbf{E}, \tag{2.56}$$

known as the *Roothaan–Hall equations*, where:

- $\mathbf{C}$ is the matrix of MO coefficients in the AO basis,
- $\mathbf{S}$ is the AO overlap matrix,
- $\mathbf{F}$ is the matrix representation of the Fock operator,
- $\mathbf{E}$ is the diagonal matrix of orbital energies.

Since the Fock matrix depends on the orbitals themselves (via $\hat{J}$ and $\hat{K}$), the procedure is iterative: a guess density is used to build $\mathbf{F}$, the generalized eigenvalue problem is solved, new orbitals are obtained, and the procedure is repeated until self-consistency is achieved.

2.2.2 Density Functional Theory

Density Functional Theory (DFT) provides a formally exact alternative to *ab initio* approaches such as Hartree–Fock and post-HF methods. Its computational appeal lies in the use of the electron density as the basic quantity from which all observables of the N-electron system (ground-state energy, dipole moment, polarizability, etc.) are derived.

Working with the electron density $\rho(\mathbf{r})$, a function of only three spatial coordinates, rather than the full many-body wavefunction $\Psi(\mathbf{x}_1, \ldots, \mathbf{x}_N)$ depending on $3N$ coordinates, allows the treatment of much larger and more complex systems.

DFT relies on two foundational results: the *Hohenberg–Kohn theorems*. The first theorem states:

Theorem 1 (Hohenberg–Kohn Theorem)**.** *For a finite, interacting N-electron system with a given particle–particle interaction, there exists a one-to-one correspondence between the external potential V_{ext} and the ground-state density ρ_0. Therefore, V_{ext} is a unique functional of ρ_0, up to an arbitrary additive constant.*

In the nonrelativistic Born–Oppenheimer approximation, the electronic Hamiltonian is

$$\hat{H} = \hat{T} + \hat{V}_{ee} + \hat{V}_{\text{ext}}, \tag{2.57}$$

or, in atomic units,

$$\hat{H} = -\frac{1}{2}\sum_{i=1}^{N}\nabla_i^2 + \sum_{i<j}\frac{1}{r_{ij}} + \sum_{i=1}^{N}V_{\text{ext}}(\mathbf{r}_i). \tag{2.58}$$

The expectation value of $\hat{V}_{\text{ext}}$ is

$$\begin{aligned}\langle\Psi|\hat{V}_{\text{ext}}|\Psi\rangle &= \int \Psi^* \sum_{i=1}^{N} V_{\text{ext}}(\mathbf{r}_i)\,\Psi\,\mathrm{d}\mathbf{x}_1\cdots\mathrm{d}\mathbf{x}_N \\ &= \int \rho(\mathbf{r})\,V_{\text{ext}}(\mathbf{r})\,\mathrm{d}\mathbf{r},\end{aligned} \tag{2.59}$$

where we used the definition of the electron density:

$$\rho(\mathbf{r}) = N\int |\Psi(\mathbf{x}_1,\mathbf{x}_2,\ldots,\mathbf{x}_N)|^2\,\mathrm{d}\omega_1\mathrm{d}\mathbf{x}_2\cdots\mathrm{d}\mathbf{x}_N. \tag{2.60}$$

This relation is key to the proof of Theorem 1 (see Ref. [158]).

It is now necessary we specify what is a *functional*. It is a mapping that assigns a scalar value to a function. In DFT, energy expressions are functionals of the electron density:

$$F[\rho] : \rho(\mathbf{r}) \longrightarrow \mathbb{R}. \tag{2.61}$$

The total-energy functional is defined as

$$E[\rho] = \min_{\Psi\to\rho}\langle\Psi|\hat{T} + \hat{V}_{ee} + \hat{V}_{\text{ext}}|\Psi\rangle = F[\rho] + \int \rho(\mathbf{r})\,V_{\text{ext}}(\mathbf{r})\,\mathrm{d}\mathbf{r}, \tag{2.62}$$

where

$$F[\rho] = \min_{\Psi\to\rho}\langle\Psi|\hat{T} + \hat{V}_{ee}|\Psi\rangle \tag{2.63}$$

is a universal functional, independent of the external potential.

The second theorem by Hohenberg–Kohn is the following.

Theorem 2 (Variational Theorem)**.** *Let ρ_{GS} be the exact ground-state density and E_{GS} its energy. Then:*

$$E[\rho] \geq E_{\mathrm{GS}} \qquad \forall\, \rho, \tag{2.64}$$

$$E[\rho_{\mathrm{GS}}] = E_{\mathrm{GS}}. \tag{2.65}$$

Thus the ground-state density is obtained by minimizing $E[\rho]$:

$$\frac{\delta}{\delta\rho(\mathbf{r})}\left[E[\rho] - \mu \int \rho(\mathbf{r}')\,\mathrm{d}\mathbf{r}'\right] = 0, \tag{2.66}$$

where the Lagrange multiplier μ enforces particle-number conservation.

Using the decomposition

$$E[\rho] = F[\rho] + \int \rho(\mathbf{r})\, V_{\mathrm{ext}}(\mathbf{r})\,\mathrm{d}\mathbf{r}, \tag{2.67}$$

the Euler equation becomes

$$\frac{\delta F[\rho]}{\delta\rho(\mathbf{r})} + V_{\mathrm{ext}}(\mathbf{r}) = \mu. \tag{2.68}$$

This provides a reformulation of the electronic many-body problem in which the wavefunction Ψ is replaced by the ground-state density ρ_{GS}. The difficulty is that the exact universal functional $F[\rho]$ is unknown and must be approximated.

There are two principal ways to minimize $E[\rho]$:

- *Direct methods*, such as the Thomas–Fermi approach, in which the density is varied directly.
- *Indirect methods*, such as the Kohn–Sham approach, in which the density is parametrized through molecular orbitals.

2.3 The Kohn–Sham (KS) approach

In the Kohn–Sham (KS) approach, a reference system of non-interacting electrons is introduced in place of the interacting many-electron system. The electron density of this fictitious system is constrained to equal the density of the real interacting system through an effective, local, one-electron potential $V_{\mathrm{KS}}(\mathbf{r})$, which must be determined self-consistently.

The Hamiltonian of the KS non-interacting system is

$$\hat{H}_{\mathrm{KS}} = \hat{T} + \hat{V}_{\mathrm{KS}} = \sum_{i=1}^{N}\left(-\frac{1}{2}\nabla_i^2 + V_{\mathrm{KS}}(\mathbf{r}_i)\right), \tag{2.69}$$

and, by the Hohenberg–Kohn theorem, there is a one-to-one correspondence between $V_{\mathrm{KS}}(\mathbf{r})$ and the density $\rho_{\mathrm{KS}}(\mathbf{r})$ of this non-interacting system.

The associated energy functional is

$$E_{\mathrm{KS}}[\rho] = T_{\mathrm{KS}}[\rho] + \int \rho(\mathbf{r})\, V_{\mathrm{KS}}(\mathbf{r})\, \mathrm{d}\mathbf{r}, \tag{2.70}$$

and the Euler equation takes the form

$$\frac{\delta T_{\mathrm{KS}}[\rho]}{\delta \rho(\mathbf{r})} + V_{\mathrm{KS}}(\mathbf{r}) = \mu. \tag{2.71}$$

However, the explicit functional form of $T_{\mathrm{KS}}[\rho]$ is unknown.

For a non-interacting system, the ground-state wavefunction is (up to degeneracy) a single Slater determinant:

$$\Psi_{\mathrm{KS}} = \frac{1}{\sqrt{N!}} \det[\chi_1\ \chi_2\ \ldots\ \chi_N], \tag{2.72}$$

where the spin-orbitals χ_i satisfy the one-electron KS equations:

$$\left(-\frac{1}{2}\nabla^2 + V_{\mathrm{KS}}(\mathbf{r})\right)\chi_i(\mathbf{r}) = \epsilon_i \chi_i(\mathbf{r}), \qquad i = 1, 2, \ldots, N. \tag{2.73}$$

Expanding the orbitals on a finite basis leads to the matrix equation

$$\mathbf{H}_{\mathrm{KS}}\,\mathbf{C} = \mathbf{S}\,\mathbf{C}\,\mathbf{E}, \tag{2.74}$$

analogous to the Roothaan–Hall equations of Hartree–Fock theory. The electron density is then reconstructed as

$$\rho_{\mathrm{KS}}(\mathbf{r}) = \sum_{i=1}^{N} |\varphi_i(\mathbf{r})|^2. \tag{2.75}$$

A self-consistent-field (SCF) procedure is used: a trial density generates a V_{KS}, the KS equations are solved, a new density is computed, and the cycle is repeated until convergence. In practice, damping or mixing schemes are often introduced to avoid oscillations.

The key idea of KS theory is to choose $V_{\mathrm{KS}}(\mathbf{r})$ so that the Euler equation for the non-interacting system reproduces the density of the real, interacting system. To this end, the total energy of the real system is written as

$$E[\rho] = T[\rho] + V_{ee}[\rho] + \int \rho(\mathbf{r})\, V_{\mathrm{ext}}(\mathbf{r})\, \mathrm{d}\mathbf{r}. \tag{2.76}$$

It is convenient to decompose the electron–electron interaction term into:

- the classical Coulomb (Hartree) energy

$$J[\rho] = \frac{1}{2} \iint \frac{\rho(\mathbf{r})\,\rho(\mathbf{r}')}{|\mathbf{r} - \mathbf{r}'|}\,\mathrm{d}\mathbf{r}\,\mathrm{d}\mathbf{r}', \tag{2.77}$$

- an exchange–correlation (xc) functional defined as

$$E_{\mathrm{xc}}[\rho] = T_{\mathrm{KS}}[\rho] - T[\rho] + V_{ee}[\rho] - J[\rho]. \tag{2.78}$$

The total energy functional becomes

$$E[\rho] = T_{\mathrm{KS}}[\rho] + J[\rho] + E_{\mathrm{xc}}[\rho] + \int \rho(\mathbf{r})\,V_{\mathrm{ext}}(\mathbf{r})\,\mathrm{d}\mathbf{r}, \tag{2.79}$$

where the only unknown quantity is $E_{\mathrm{xc}}[\rho]$. Although unknown, it is typically much smaller than the other contributions and can be approximated.

With this expression for the energy functional, taking the functional derivative yields

$$\frac{\delta T_{\mathrm{KS}}[\rho]}{\delta\rho(\mathbf{r})} + \int \frac{\rho(\mathbf{r}')}{|\mathbf{r} - \mathbf{r}'|}\,\mathrm{d}\mathbf{r}' + \frac{\delta E_{\mathrm{xc}}[\rho]}{\delta\rho(\mathbf{r})} + V_{\mathrm{ext}}(\mathbf{r}) = \mu. \tag{2.80}$$

Comparing this with the Euler equation for the non-interacting system shows that they coincide if we define the KS potential as

$$V_{\mathrm{KS}}(\mathbf{r}) = \int \frac{\rho(\mathbf{r}')}{|\mathbf{r} - \mathbf{r}'|}\,\mathrm{d}\mathbf{r}' + V_{\mathrm{xc}}(\mathbf{r}) + V_{\mathrm{ext}}(\mathbf{r}), \tag{2.81}$$

where the exchange–correlation potential is

$$V_{\mathrm{xc}}[\rho](\mathbf{r}) = \frac{\delta E_{\mathrm{xc}}[\rho]}{\delta\rho(\mathbf{r})}. \tag{2.82}$$

Once the KS orbitals are obtained, the non-interacting kinetic energy $T_{\mathrm{KS}}[\rho]$ is computed exactly, the dominant part of the electron–electron interaction is captured by the Hartree energy $J[\rho]$, and all remaining many-body effects are collected into the xc functional $E_{\mathrm{xc}}[\rho]$. Although E_{xc} is unknown, numerous accurate approximations exist.

2.4 Time-Dependent DFT

Because we are interested in time-dependent phenomena such as optical absorption, we now extend Density Functional Theory to the time-dependent domain. The dynamics of an N-electron interacting system evolving under a time-dependent external potential $V_{\mathrm{ext}}(\mathbf{r}, t)$ is

governed by the time-dependent Schrödinger equation:

$$\mathrm{i}\,\frac{\partial}{\partial t}\Psi(\mathbf{x}_1,\ldots,\mathbf{x}_N,t) = \hat{H}(t)\,\Psi(\mathbf{x}_1,\ldots,\mathbf{x}_N,t). \tag{2.83}$$

This equation defines a mapping from the external potential to the full time-dependent wavefunction, and therefore to the time-dependent electron density:

$$V_{\mathrm{ext}}(\mathbf{r},t) \;\longrightarrow\; \Psi(t) \;\longrightarrow\; \rho(\mathbf{r},t). \tag{2.84}$$

To build a time-dependent analogue of DFT, we need to invert this relation: we must prove the existence of a one-to-one correspondence between time-dependent densities and time-dependent external potentials. This was established in the seminal work of Runge and Gross (1984), which forms the foundation of Time-Dependent Density Functional Theory (TDDFT).

Theorem 3 (Runge–Gross Theorem)**.** *Two densities $\rho(\mathbf{r},t)$ and $\rho'(\mathbf{r},t)$ evolving from the same initial state Ψ_0 under two external potentials $V_{\mathrm{ext}}(\mathbf{r},t)$ and $V'_{\mathrm{ext}}(\mathbf{r},t)$, which may differ only by a purely time-dependent additive function $c(t)$, and which are both Taylor-expandable around t_0, will begin to differ infinitesimally after t_0. Therefore, for any fixed initial state, there exists a one-to-one correspondence between densities and external potentials.*

Consequently, the potential, and therefore the Hamiltonian and wavefunction, become functionals of the time-dependent density. This establishes the density as the central quantity from which all time-dependent observables can, in principle, be obtained:

$$O(t) = \langle\Psi[\rho](t)|\hat{O}(t)|\Psi[\rho](t)\rangle = O[\rho](t). \tag{2.85}$$

In order to exploit a non-interacting system like we did for the time-independent case, now we ask whether two many-body systems with different particle–particle interactions and different external potentials can nevertheless reproduce the same time-dependent density. Van Leeuwen (1999) proved that the answer is yes.

Theorem 4 (van Leeuwen Theorem)**.** *Given a time-dependent density $\rho(\mathbf{r},t)$ generated by an interacting system with interaction $w(|\mathbf{r}-\mathbf{r}'|)$, external potential V_{ext}, and initial state Ψ_0, there exists another many-body system with a different interaction $w'(|\mathbf{r}-\mathbf{r}'|)$ and a different potential $V'_{\mathrm{ext}}(\mathbf{r},t)$ (up to a purely time-dependent constant), which reproduces the same density. The corresponding initial state Ψ'_0 must be chosen so as to reproduce both the density and its first time derivative at t_0.*

This theorem provides the formal foundation for the time-dependent Kohn–Sham (TD-KS) method.

Like we did before, we introduce a non-interacting reference system with density constrained to equal that of the interacting system by means of a KS potential $V_{\mathrm{KS}}[\rho](\mathbf{r}, t)$. For systems initially in their ground state, this potential can be written as:

$$V_{\mathrm{KS}}(\mathbf{r}, t) = V_0(\mathbf{r}) + V'(\mathbf{r}, t)\,\theta(t - t_0), \tag{2.86}$$

where θ is the Heaviside step function.

At $t = t_0$ the usual static KS-DFT scheme applies. Infinitesimally after t_0 the density is

$$\rho(\mathbf{r}, t) = \sum_{j=1}^{N} |\psi_j(\mathbf{r}, t)|^2, \tag{2.87}$$

and the orbitals evolve according to the time-dependent KS equations:

$$\left(-\frac{1}{2}\nabla^2 + V_{\mathrm{KS}}[\rho](\mathbf{r}, t)\right)\psi_j(\mathbf{r}, t) = \mathrm{i}\,\frac{\partial}{\partial t}\psi_j(\mathbf{r}, t). \tag{2.88}$$

The KS potential now contains three contributions:

$$V_{\mathrm{KS}}[\rho](\mathbf{r}, t) = V_{\mathrm{ext}}(\mathbf{r}, t) + \int \frac{\rho(\mathbf{r}', t)}{|\mathbf{r} - \mathbf{r}'|}\,\mathrm{d}\mathbf{r}' + V_{\mathrm{xc}}[\rho](\mathbf{r}, t), \tag{2.89}$$

where the time-dependent xc potential is defined by

$$V_{\mathrm{xc}}[\rho](\mathbf{r}, t) = \frac{\delta E_{\mathrm{xc}}[\rho]}{\delta \rho(\mathbf{r}, t)}. \tag{2.90}$$

In practice, solving the static KS equations already requires an approximation to the ground-state exchange–correlation functional. TD-KS propagation also requires an approximation to the time-dependent xc potential, which enters the evolution of the orbitals $\psi_j(\mathbf{r}, t)$. The most widely used approximation is the *adiabatic* one, in particular the Adiabatic Local Density Approximation (ALDA), which will be introduced later.

2.5 Linear response theory

Linear–response (LR) theory is a fundamental framework which, when combined with TDDFT, allows the computation of excitation energies and optical spectra. LR theory applies when a system—whose ground-state properties are fully characterized—is subjected to a sufficiently weak external perturbation. In this regime, one does not need to solve the full time-dependent Schrödinger or TDKS equations: to obtain information about the excitation spectrum it is enough to analyse how a weak external field induces a small change in the ground-state observables or in the density.

The central quantity of LR theory is the *susceptibility* (or response function) χ_{AB}, which describes how the expectation value of an observable A at time t responds to a perturbation coupling to an observable B at time t'. Once χ_{AB} is known, the induced variation of A follows from a time convolution, or, equivalently, from a product in frequency space:

$$\delta A(t) = \int \mathrm{d}t'\, \chi_{AB}(t - t')\, F(t'), \qquad \delta A(\omega) = \chi_{AB}(\omega)\, F(\omega), \tag{2.91}$$

where $F(t)$ is the time-dependent perturbing field.

We should now provide a definition for the linear response of property A. Let $\hat{A}$ be a quantum-mechanical observable. Its ground-state expectation value is

$$A_0 = \langle \Psi_0 | \hat{A} | \Psi_0 \rangle, \tag{2.92}$$

where $|\Psi_0\rangle$ is the ground state of the unperturbed Hamiltonian $\hat{H}_0$.

From time t_0 onward, the system is subjected to a weak perturbation:

$$\hat{H}(t) = \hat{H}_0 + \hat{H}'(t), \qquad \hat{H}'(t) = -F(t)\, \hat{B}, \tag{2.93}$$

where $F(t)$ couples to the operator $\hat{B}$. The wavefunction becomes time dependent and the expectation value of $\hat{A}$ evolves as

$$A(t) = \langle \Psi(t) | \hat{A} | \Psi(t) \rangle. \tag{2.94}$$

The response of the observable is defined as

$$\delta A(t) = A(t) - A_0. \tag{2.95}$$

In LR theory we expand this in powers of the external field:

$$\delta A(t) = A^{(1)}(t) + \cancel{A^{(2)}(t) + A^{(3)}(t) + \cdots}, \tag{2.96}$$

and retain only the linear term.

To derive the expression for the linear response we need to recall some basic ideas about the time-dependent evolution of many-body system of electrons. It is governed by the TDSE:

$$\mathrm{i}\, \frac{\partial}{\partial t} |\Psi(t)\rangle = \hat{H}(t)\, |\Psi(t)\rangle, \qquad |\Psi(t_0)\rangle = |\Psi_0\rangle. \tag{2.97}$$

which propagates an initial state $\Psi(\mathbf{x}_1, \ldots, \mathbf{x}_N, t_0) = \Psi_0$ over a time period $[t_0, t]$. Formally,

the solution is written in terms of the evolution operator:

$$|\Psi(t)\rangle = \hat{U}(t, t_0)\,|\Psi_0\rangle. \tag{2.98}$$

To simplify the treatment in the presence of a weak perturbation, it is convenient to move to the *interaction picture*. In this framework operators evolve according only to the unperturbed Hamiltonian $\hat{H}_0$ while states evolve only under the perturbation.

Operators in the interaction picture are defined as

$$\hat{O}_I(t) = e^{i\hat{H}_0(t-t_0)}\hat{O}\,e^{-i\hat{H}_0(t-t_0)}, \tag{2.99}$$

while states are defined as

$$|\Psi_I(t)\rangle = e^{i\hat{H}_0(t-t_0)}|\Psi(t)\rangle. \tag{2.100}$$

In this picture the Schrödinger equation becomes

$$i\frac{\partial}{\partial t}|\Psi_I(t)\rangle = \hat{H}_I(t)\,|\Psi_I(t)\rangle \tag{2.101}$$

where the interaction Hamiltonian is

$$\hat{H}_I(t) = e^{i\hat{H}_0(t-t_0)}\hat{H}'(t)\,e^{-i\hat{H}_0(t-t_0)} = -F(t)\,\hat{B}_I(t). \tag{2.102}$$

The formal solution is

$$|\Psi_I(t)\rangle = \hat{U}_I(t, t_0)\,|\Psi_I(t_0)\rangle, \tag{2.103}$$

where the interaction–picture evolution operator is

$$\hat{U}_I(t, t_0) = \hat{\tau}\exp\left[-i\int_{t_0}^{t} dt'\,\hat{H}_I(t')\right], \tag{2.104}$$

Here $\hat{\tau}$ is a time–ordering operator. It enforces causal time evolution by rearrainging products of time-dependent operators so that operators evaluated at later times appear to the left of those evaluated at earlier times.

To first order in the perturbation we expand the exponential:

$$\hat{U}_I(t, t_0) \simeq 1 - i\int_{t_0}^{t} dt'\,\hat{H}_I(t') = 1 + i\int_{t_0}^{t} dt'\,F(t')\,\hat{B}_I(t'). \tag{2.105}$$

The adjoint operator is therefore

$$\hat{U}_I^{\dagger}(t, t_0) \simeq 1 - i\int_{t_0}^{t} dt'\,F(t')\,\hat{B}_I(t'). \tag{2.106}$$

Using the interaction picture, the expectation value of $\hat{A}$ is

$$A(t) = \langle \Psi_I(t)|\hat{A}_I(t)|\Psi_I(t)\rangle = \langle \Psi_I(t_0)|\hat{U}_I^\dagger(t,t_0)\,\hat{A}_I(t)\,\hat{U}_I(t,t_0)|\Psi_I(t_0)\rangle. \tag{2.107}$$

Substituting the first–order expansions of $\hat{U}_I$ and $\hat{U}_I^\dagger$ and retaining only the linear terms in $F(t)$, we obtain

$$\begin{aligned} A(t) &\simeq \langle \Psi_I(t_0)|\hat{A}_I(t)|\Psi_I(t_0)\rangle \\ &\simeq -i\int_{t_0}^{t} dt'\,F(t')\,\langle \Psi_I(t_0)|\hat{A}_I(t)\,\hat{B}_I(t')|\Psi_I(t_0)\rangle \\ &\quad + i\int_{t_0}^{t} dt'\,F(t')\,\langle \Psi_I(t_0)|\hat{B}_I(t')\,\hat{A}_I(t)|\Psi_I(t_0)\rangle. \end{aligned} \tag{2.108}$$

Subtracting the ground–state expectation value we obtain the first–order response:

$$A^{(1)}(t) = -i\int_{t_0}^{t} dt'\,F(t')\,\left\langle \Psi_I(t_0)\left|[\,\hat{A}_I(t),\hat{B}_I(t')\,]\right|\Psi_I(t_0)\right\rangle. \tag{2.109}$$

Since $\hat{H}_0$ is time–independent, the commutator depends only on the time difference, and we introduce the *retarded response function*:

$$\chi_{AB}(t-t') = -i\,\theta(t-t')\,\langle \Psi_I(t_0)\,|[A_I(t-t'),B_I]|\,\Psi_I(t_0)\rangle\,. \tag{2.110}$$

The linear response is then

$$A^{(1)}(t) = \int_{-\infty}^{\infty} dt'\,\chi_{AB}(t-t')F(t'). \tag{2.111}$$

Using the Fourier transform

$$f(\omega) = \int_{-\infty}^{\infty} dt\,f(t)\,e^{i\omega t}, \tag{2.112}$$

the retarded susceptibility becomes

$$\chi_{AB}(\omega) = -i\int_{-\infty}^{\infty} dt\,\theta(t)\,\left\langle \Psi_I(t_0)\left|[\hat{A}_I(t),\hat{B}_I]\right|\Psi_I(t_0)\right\rangle e^{i\omega t}. \tag{2.113}$$

Finally, in the frequency domain the linear response takes the simple form

$$A^{(1)}(\omega) = \chi_{AB}(\omega)F(\omega). \tag{2.114}$$

If we apply this to study the response of the density we can derive the expression for the

frequency-dependent density response

$$\rho^1(\vec{r},\omega) = \int d^3r\, \chi_{\rho\rho}(\vec{r},\vec{r}',\omega) V_{ext}(\vec{r}',\omega) \tag{2.115}$$

where $\chi_{\rho\rho}(\vec{r},\vec{r}',\omega)$ is the density-density response function in the Lehmann representation (its expression will be derived in the next section).

2.5.1 The spectrum from the polarizability

One of the main applications of LR theory is the calculation of excitation spectra. To make this connection explicit, we analyse the frequency–dependent susceptibility $\chi_{AB}(\omega)$ derived in the previous section.

Let $\{\Psi_n\}_{n=0,1,2,\ldots}$ be the complete set of eigenfunctions of the unperturbed Hamiltonian $\hat{H}_0$, with excitation energies

$$\Omega_n = E_n - E_0, \qquad n = 1, 2, \ldots, \tag{2.116}$$

where E_0 is the ground–state energy.

Inserting the completeness relation

$$\sum_{n=0}^{\infty} |\Psi_n\rangle\langle\Psi_n| = 1 \tag{2.117}$$

into the expression for the retarded response function, we obtain

$$\chi_{AB}(\omega) = -\,\mathrm{i} \sum_{n=1}^{\infty} \int_{-\infty}^{\infty} \mathrm{d}t\, \theta(t)\, \mathrm{e}^{\mathrm{i}\omega t} \Big[\langle\Psi_0|A|\Psi_n\rangle\langle\Psi_n|B|\Psi_0\rangle\, \mathrm{e}^{-\mathrm{i}\Omega_n t} - \langle\Psi_0|B|\Psi_n\rangle\langle\Psi_n|A|\Psi_0\rangle\, \mathrm{e}^{\mathrm{i}\Omega_n t} \Big]. \tag{2.118}$$

Using the integral representation of the Heaviside function,

$$\theta(t) = \lim_{\eta\to 0^+} \frac{\mathrm{i}}{2\pi} \int_{-\infty}^{\infty} \mathrm{d}\omega'\, \frac{\mathrm{e}^{-\mathrm{i}\omega' t}}{\omega' + \mathrm{i}\eta}, \tag{2.119}$$

and performing the time integration, one obtains the *Lehmann representation* of the linear response function:

$$\chi_{AB}(\omega) = \lim_{\eta\to 0^+} \sum_{n=1}^{\infty} \left[\frac{\langle\Psi_0|A|\Psi_n\rangle\langle\Psi_n|B|\Psi_0\rangle}{\omega - \Omega_n + \mathrm{i}\eta} - \frac{\langle\Psi_0|B|\Psi_n\rangle\langle\Psi_n|A|\Psi_0\rangle}{\omega + \Omega_n + \mathrm{i}\eta} \right]. \tag{2.120}$$

This expression is central in LR theory because it shows that the poles of $\chi_{AB}(\omega)$ occur

exactly at the excitation energies $\pm\Omega_n$. The infinitesimal imaginary term $i\eta$ shifts the poles just below the real axis, enforcing causality. The residues of these poles encode the transition strengths through the matrix elements of A and B.

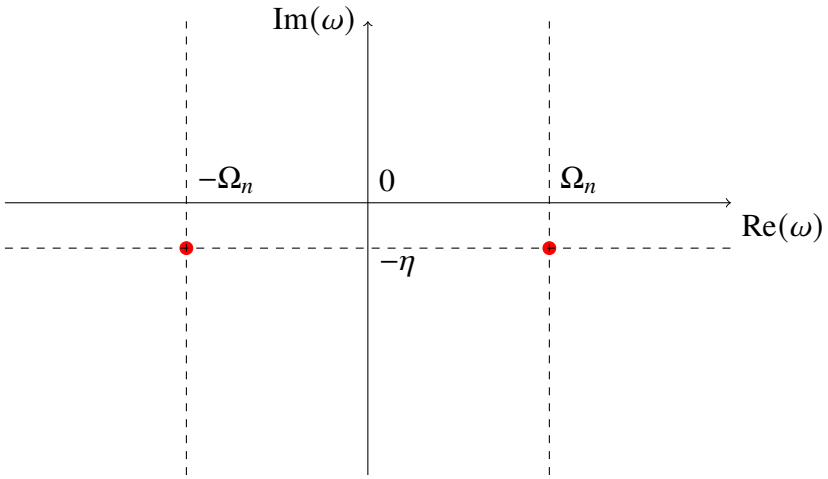


Figure 2.1: Schematic location of the poles of the retarded response function in the complex frequency plane.

We now specialise to the physically important case where both A and B are dipole operators:

$$\hat{A} = \hat{x}, \hat{y}, \hat{z}, \qquad \hat{B} = \hat{x}, \hat{y}, \hat{z}. \tag{2.121}$$

In this case, the response function becomes the *dynamical polarizability tensor* $\alpha_{\alpha\beta}(\omega)$. For a single component, e.g. $\hat{A} = \hat{B} = \hat{z}$, hermiticity implies

$$\langle\Psi_0|\hat{z}|\Psi_n\rangle\langle\Psi_n|\hat{z}|\Psi_0\rangle = |\langle\Psi_0|\hat{z}|\Psi_n\rangle|^2 . \tag{2.122}$$

Near a resonance ($\omega \approx \Omega_n$), the counter–rotating contribution $(\omega + \Omega_n + i\eta)^{-1}$ is negligible, yielding the standard approximation:

$$\alpha_{zz}(\omega) \simeq \frac{|\langle\Psi_0|\hat{z}|\Psi_n\rangle|^2}{i\eta}. \tag{2.123}$$

Thus, the poles of $\chi_{AB}(\omega)$ manifest as resonances in the polarizability.

The imaginary part of the polarizability determines the absorption cross section:

$$\sigma(\omega) \propto \omega \ \mathrm{Im}\left[\sum_\alpha \alpha_{\alpha\alpha}(\omega)\right]. \tag{2.124}$$

Using

$$\mathrm{Im}\left[\frac{1}{\omega - \Omega_n + i\eta}\right] = \frac{\eta}{(\Omega_n - \omega)^2 + \eta^2}, \tag{2.125}$$

we see that each excitation produces a Lorentzian peak centered at Ω_n. As $\eta \to 0^+$, the integral of each peak approaches π, and the strength of the peak is proportional to the transition dipole moment:

$$\mathrm{Im}[\alpha_{zz}(\omega)] \propto -\pi \sum_{n>0} |\langle \Psi_0 | \hat{z} | \Psi_n \rangle|^2 . \tag{2.126}$$

Thus, the imaginary part of the dynamical polarizability provides direct access to the *transition probabilities* between ground and excited states, in accordance with Fermi's golden rule.

2.6 Linear response KS time-dependent DFT

From TDDFT we know that the exact time-dependent density of an interacting many-electron system, evolving under an external potential $V_{\mathrm{ext}}(\mathbf{r}, t)$, can be reproduced by a non-interacting KS system evolving under the effective KS potential

$$V_{\mathrm{KS}}[\rho](\mathbf{r}, t) = V_{\mathrm{ext}}(\mathbf{r}, t) + \int \mathrm{d}^3 r' \, \frac{\rho(\mathbf{r}', t)}{|\mathbf{r} - \mathbf{r}'|} + V_{\mathrm{xc}}[\rho](\mathbf{r}, t). \tag{2.127}$$

This relation can be inverted, so that the time-dependent density may be written as a functional of the KS potential:

$$\rho(\mathbf{r}, t) = \rho[V_{\mathrm{KS}}](\mathbf{r}, t). \tag{2.128}$$

In the linear–response (LR) regime we expand the density around its ground-state value. The first-order variation of the density is

$$\rho^{(1)}(\mathbf{r}, t) = \int \mathrm{d}t' \int \mathrm{d}^3 r' \, \chi_{KS}(\mathbf{r}, t; \mathbf{r}', t') \, V_{\mathrm{KS}}^{(1)}(\mathbf{r}', t'), \tag{2.129}$$

where χ_{KS} is the KS density–density response function and $V_{\mathrm{KS}}^{(1)}(\mathbf{r}, t)$ is the linear variation of the KS potential.

Linearizing Eq. (2.127) we obtain:

$$V_{\mathrm{KS}}^{(1)}(\mathbf{r}, t) = V_{\mathrm{ext}}^{(1)}(\mathbf{r}, t) + \int \mathrm{d}^3 r' \, \frac{\rho_1(\mathbf{r}', t)}{|\mathbf{r} - \mathbf{r}'|} + V_{\mathrm{xc}}^{(1)}(\mathbf{r}, t), \tag{2.130}$$

where $V_{\mathrm{ext}}^{(1)}$ is the linearized external perturbation, the second term is the linearized Hartree potential, and $V_{\mathrm{xc}}^{(1)}$ is the first-order variation of the xc potential:

$$V_{\mathrm{xc}}^{(1)}(\mathbf{r}, t) = \int \mathrm{d}t' \int \mathrm{d}^3 r' \, \left. \frac{\delta V_{\mathrm{xc}}[\rho](\mathbf{r}, t)}{\delta \rho(\mathbf{r}', t')} \right|_{\rho_0} \rho_1(\mathbf{r}', t'). \tag{2.131}$$

This defines the xc kernel of LR–TDDFT:

$$f_{\mathrm{xc}}(\mathbf{r},t;\mathbf{r}',t') = \left.\frac{\delta V_{\mathrm{xc}}[\rho](\mathbf{r},t)}{\delta\rho(\mathbf{r}',t')}\right|_{\rho_0}. \tag{2.132}$$

Now, by substituting the expression of $V_{\mathrm{KS},1}$ into Eq. (2.129) yields:

$$\begin{aligned}\rho^{(1)}(\mathbf{r},t) = \int \mathrm{d}t' \int \mathrm{d}^3r'\, \chi_s(\mathbf{r},t;\mathbf{r}',t') \Bigg[& V_{\mathrm{ext},1}(\mathbf{r}',t') \\ & + \int \mathrm{d}\tau \int \mathrm{d}^3x \left(\frac{\delta(t'-\tau)}{|\mathbf{r}'-\mathbf{x}|} + f_{\mathrm{xc}}(\mathbf{r}',t';\mathbf{x},\tau) \right) \rho_1(\mathbf{x},\tau) \Bigg].\end{aligned} \tag{2.133}$$

Because the unknown $\rho^{(1)}$ appears on both sides, this is a self-consistent integral equation.

After Fourier transform, we obtain the standard Dyson-like LR–TDDFT equation:

$$\begin{aligned}\rho^{(1)}(\mathbf{r},\omega) = \int \mathrm{d}^3r'\, \chi_s(\mathbf{r},\mathbf{r}',\omega) \Bigg[& V^{(1)}_{\mathrm{ext}}(\mathbf{r}',\omega) \\ & + \int \mathrm{d}^3x \left(\frac{1}{|\mathbf{r}'-\mathbf{x}|} + f_{\mathrm{xc}}(\mathbf{r}',\mathbf{x},\omega) \right) \rho^{(1)}(\mathbf{x},\omega) \Bigg].\end{aligned} \tag{2.134}$$

From LR theory, the KS response function reads:

$$\chi_{KS}(\mathbf{r},\mathbf{r}',\omega) = \sum_{j,k} (f_k - f_j) \frac{\varphi^0_j(\mathbf{r})\,\varphi^{0*}_k(\mathbf{r})\,\varphi^{0*}_j(\mathbf{r}')\,\varphi^0_k(\mathbf{r}')}{\omega - \omega_{jk} + \mathrm{i}\eta}, \tag{2.135}$$

where φ^0_j are the KS orbitals, f_j their occupation numbers, and $\omega_{jk} = \epsilon_k - \epsilon_j$ the KS orbital energy differences.

Equation (2.134) contains both the KS response function χ_{KS} and the full interacting response χ. This might seem problematic, because χ_{KS} has poles at the KS transition energies ω_{jk}, whereas the physical response of the interacting system has poles at the true excitation energies Ω_n.

The apparent inconsistency is resolved by the self-consistency of the Dyson-like equation and, crucially, by the presence of the exchange–correlation kernel f_{xc}. Together, the Hartree term and f_{xc} shift the poles of the KS susceptibility, replacing the unphysical single-particle transitions ω_{jk} with the physical, many-body excitation energies Ω_n.

This is the essential mechanism by which LR–TDDFT restores the correct excitation spectrum of the interacting system.

2.7 The Exchange–Correlation Energy, Potential and Kernel

In Kohn–Sham Density Functional Theory the exchange–correlation (XC) energy

$$E_{\mathrm{xc}}[\rho] \tag{2.136}$$

acts as a *placeholder* for all the many-body effects that the auxiliary non-interacting Kohn–Sham (KS) system cannot reproduce. By construction, the KS system yields the exact ground-state density of the interacting electrons, but it lacks both the true many-body kinetic effects and the full electron–electron interaction. For this reason, the XC energy collects two distinct contributions:

$$E_{\mathrm{xc}}[\rho] = (T - T_{KS}) + (\langle V_{ee}\rangle - J[\rho])\,, \tag{2.137}$$

where T is the kinetic energy of the interacting system, T_{KS} the kinetic energy of the KS system, $\langle V_{ee}\rangle$ the expectation value of the true electron–electron repulsion and $J[\rho]$ the classical Hartree term.

The name "exchange–correlation" can be explained as follows:

- *Exchange.* Is a purely quantum-mechanical effect arising from the antisymmetry of the electronic wavefunction. Because of the Pauli exclusion principle, two electrons with the same spin cannot occupy the same region of space. As a consequance their joint probability distribution contains a node when their positions coincide, thereby reducing the effective Coulomb repulsion compared to the classical Hartree description. This reduction can be visualised through the *exchange hole*, which represents the depletion of same-spin probability density around each electron. Exchange does not correspond to a physical force: it emerges solely from the sign structure and symmetry of the fermionic wavefunction.

- *Correlation.* It describes the dynamical adjustment of the electronic motion due to their mutual Coulomb repulsion. It includes both quantum (fluctuational) correlation and classical correlation arising from instantaneous electrostatic avoidance. Correlation include both kinetic correlation and Coulomb (dynamic) correlation energy. These effects are absent in the Hartree term, which describes only a static density–density interaction. Correlation further reduces the effective repulsion relative to the Hartree picture. Similarly to the exchange, the Coulomb (dynamic) correlation can be visualised through the *correlation hole*, describing the suppression of electronic probability around a reference electron beyond the exchange-only effect.

The qualitative picture above can be formalised using the *pair density*. For an N-electron system, the pair density is defined as

$$\rho_2(\mathbf{x}_1, \mathbf{x}_2) = N(N-1) \int |\Psi(\mathbf{x}_1, \mathbf{x}_2, \ldots, \mathbf{x}_N)|^2 \, d\mathbf{x}_3 \ldots d\mathbf{x}_N, \tag{2.138}$$

where $\mathbf{x} = (\mathbf{r}, s)$ collects spatial and spin coordinates. It represents the probability of finding one electron in $d\mathbf{x}_1$ and another in $d\mathbf{x}_2$ simultaneously. It is symmetric under particle exchange and integrates to $N(N-1)$.

It is convenient to introduce the conditional probability density of finding an electron at $\mathbf{x}_2$ given that one electron is already at $\mathbf{x}_1$:

$$g(\mathbf{x}_2|\mathbf{x}_1) = \frac{\rho_2(\mathbf{x}_1, \mathbf{x}_2)}{\rho(\mathbf{x}_1)}, \qquad \int g(\mathbf{x}_2|\mathbf{x}_1) \, d\mathbf{x}_2 = N - 1. \tag{2.139}$$

The deviation of this conditional probability from the unconditional density defines the *exchange–correlation hole*:

$$h_{\mathrm{xc}}(\mathbf{x}_1, \mathbf{x}_2) = g(\mathbf{x}_2|\mathbf{x}_1) - \rho(\mathbf{x}_2), \tag{2.140}$$

which obeys the exact sum rule

$$\int h_{\mathrm{xc}}(\mathbf{x}_1, \mathbf{x}_2) \, d\mathbf{x}_2 = -1. \tag{2.141}$$

After integrating over the spin variables, the spinless pair density may be written as

$$\rho_2(\mathbf{r}_1, \mathbf{r}_2) = \rho(\mathbf{r}_1)\rho(\mathbf{r}_2) + \rho(\mathbf{r}_1) h_{\mathrm{xc}}(\mathbf{r}_1, \mathbf{r}_2). \tag{2.142}$$

Using this identity, the expectation value of the electron–electron repulsion becomes

$$\langle V_{ee} \rangle = \frac{1}{2} \iint \frac{\rho_2(\mathbf{r}_1, \mathbf{r}_2)}{r_{12}} \, d\mathbf{r}_1 d\mathbf{r}_2 = J[\rho] + \frac{1}{2} \iint \frac{\rho(\mathbf{r}_1) h_{\mathrm{xc}}(\mathbf{r}_1, \mathbf{r}_2)}{r_{12}} \, d\mathbf{r}_1 d\mathbf{r}_2. \tag{2.143}$$

The first term is the classical Hartree contribution. The second term describes the interaction between the density and the XC hole and corresponds precisely to the quantity $\langle V_{ee} \rangle - J[\rho]$ appearing in the definition of E_{xc}. For conceptual purposes, the XC hole is often separated into an exchange (Fermi) and a correlation (Coulomb) part:

$$h_{\mathrm{xc}}(\mathbf{r}_1, \mathbf{r}_2) = h_X(\mathbf{r}_1, \mathbf{r}_2) + h_C(\mathbf{r}_1, \mathbf{r}_2), \tag{2.144}$$

where h_X integrates to -1 and affects only same-spin electrons, while h_C integrates to zero and affects all electrons. Only their sum has a strict physical meaning.

Once the exchange–correlation energy is defined, its first functional derivative with respect

to the density yields the XC potential and, in LR-TDDFT, the response of the XC potential to infinitesimal variations of the density defines the XC kernel

Together, the hierarchy

$$E_{\mathrm{xc}}[\rho] \longrightarrow V_{\mathrm{xc}}(\mathbf{r}) \longrightarrow f_{\mathrm{xc}}(\mathbf{r}, \mathbf{r}') \tag{2.145}$$

provides the conceptual and mathematical link between DFT, TDDFT and linear-response theory.

Within Density Functional Theory, several approximate expressions exist for $E_{\mathrm{xc}}[\rho]$, ranging from simple local models to highly sophisticated non-local formulations. In the following sections an overview of the most widely used exchange–correlation approximations is presented.

2.7.1 Local Density Approximation (LDA)

In the Local Density Approximation the exchange–correlation energy functional is written as

$$E_{\mathrm{xc}}^{\mathrm{LDA}}[\rho] = \int \rho(\mathbf{r})\, \varepsilon_{\mathrm{xc}}^{\mathrm{LDA}}(\rho(\mathbf{r}))\, d\mathbf{r}, \tag{2.146}$$

where $\varepsilon_{\mathrm{xc}}$ is the exchange–correlation energy *per particle* of a homogeneous electron gas of density ρ.

LDA is therefore rooted in the uniform electron gas model: an idealized metal characterized by an infinite system of valence electrons embedded in a uniform, neutralizing positive background. Within this model, the exchange energy density has the exact analytical expression

$$\varepsilon_x^{\mathrm{LDA}}(\rho) = -\frac{3}{4}\left(\frac{3}{\pi}\right)^{1/3} \rho^{1/3}, \tag{2.147}$$

which however, not being free from self-interaction, displays the wrong asymptotic decay for finite systems. The correlation energy density, $\varepsilon_c^{\mathrm{LDA}}(\rho)$, is obtained from accurate Quantum Monte Carlo calculations of the homogeneous electron gas and parametrized accordingly [163, 164].

LDA works remarkably well for systems with slowly varying electron densities, such as solids and metallic systems, and it typically provides good structural properties. These good results are probably a consequance of the fact that LDA is based on a real physical system (thus it satisfy a number of exact conditions) and error cancellations are also involved. However, it becomes less accurate for systems where the density is highly inhomogeneous, such as atoms and molecules. In such cases LDA tends to overbind, underestimates band gaps, and yields poor energetics despite reasonably good geometries.

2.7.2 Generalized Gradient Approximation (GGA)

The Local Density Approximation assumes that the exchange–correlation energy density at a point depends only on the value of the electron density at thet point $\rho(\mathbf{r})$. In real systems, however, the density is highly inhomogeneous. To account for this effect, Generalized Gradient Approximations introduce an explicit dependence on the local density gradient:

$$E_{\mathrm{xc}}^{\mathrm{GGA}}[\rho] = \int \rho(\mathbf{r})\, \varepsilon_{\mathrm{xc}}^{\mathrm{GGA}}\big(\rho(\mathbf{r}), \nabla\rho(\mathbf{r})\big)\, d\mathbf{r}. \tag{2.148}$$

In this sense, GGAs go beyond LDA by incorporating information about the *local inhomogeneity* of the electronic density. Early GGAs were initially motivated by the idea of treating LDA as the leading term in an expansion around the homogeneous electron gas, with gradient corrections representing higher-order terms. Although this interpretation is conceptually useful, modern GGAs are no longer derived from a formal Taylor expansion, but are instead constructed to satisfy exact physical constraints and sum rules for the exchange–correlation hole.

Unfortunately gradient corrections did not consistently improve the accuracy of LDA. The associated exchange–correlation holes often violated essential physical conditions—such as normalization, negativity, and the correct short- and long-range behaviour—leading to poor energetics and incorrect asymptotic decay of the resulting Kohn–Sham potentials.

Modern GGA functionals, such as B88 [165], LYP [166], (the combination of the two, BLYP [12], its widly used) and especially PBE [167], address these issues by enforcing exact constraints on the exchange–correlation hole. There have been also attemps to directly build GGA functionals with the correct asymptotic behaviour like LB94 [168]. As a result, GGAs typically reduce the strong overbinding of LDA, improve reaction energies and molecular energetics, and provide more realistic electron densities, while still remaining computationally inexpensive.

2.7.3 Hybrid Functionals

Exchange effects are generally larger in magnitude than correlation effects, and their accurate description is essential for obtaining high-quality DFT results. The exact exchange energy of a Slater determinant is known analytically and can be written as an interaction between the density and the exchange hole:

$$E_x^{\mathrm{exact}} = \frac{1}{2} \iint \frac{\rho(\mathbf{r}_1)\, h_x^{\mathrm{exact}}(\mathbf{r}_1, \mathbf{r}_2)}{r_{12}}\, d\mathbf{r}_1 d\mathbf{r}_2. \tag{2.149}$$

A natural question arises: why not combine exact exchange with an approximate correlation

functional?

$$E_{\mathrm{xc}} = E_x^{\mathrm{exact}} + E_c^{\mathrm{DFT}} \tag{2.150}$$

In practice, this "exact-exchange + DFT-correlation" approach fails for molecular systems and for chemically relevant situations such as bond dissociation. The reason lies in the properties of the exchange–correlation hole. In strongly inhomogeneous regions (for instance in stretched chemical bonds) the exact exchange hole is highly delocalized, while the exact correlation hole is delocalized in an opposite and compensating manner. Only their sum—the total XC hole—is physically meaningful and remains properly localized. Combining a delocalized exact exchange hole with a localized semilocal (DFT) correlation hole produces an unphysical total hole and leads to poor energetics.

However, a rigorous framework for introducing exact exchange into density-functional approximations is provided by the adiabatic-connection formalism. In the Kohn–Sham scheme, the exchange–correlation energy can be written as

$$E_{\mathrm{xc}}[\rho] = \int_0^1 W_{\mathrm{xc}}^{\lambda}[\rho]\, d\lambda, \tag{2.151}$$

where $W_{\mathrm{xc}}^{\lambda}$ is the non-classical part of the electron–electron interaction at coupling strength λ. The limits of the integration have a clear physical interpretation:

- at $\lambda = 0$, the system reduces to the non-interacting KS reference and $W_{\mathrm{xc}}^{\lambda=0}$ contains *only exact exchange*;
- at $\lambda = 1$, the fully interacting system is recovered and $W_{\mathrm{xc}}^{\lambda=1}$ contains both exchange and correlation, which must be approximated by a density functional.

To evaluate the integral, an explicit form of $W_{\mathrm{xc}}^{\lambda}$ is needed for intermediate λ, but this quantity is not known. Becke proposed to interpolate between the $\lambda = 0$ and $\lambda = 1$ limits by mixing a fraction of exact exchange with semilocal exchange, while retaining a DFT description for correlation. Functionals that include a percentage of exact exchange are called *hybrid functionals*. They represent a compromise between pure DFT exchange and Hartree–Fock exact exchange and significantly improve thermochemistry, barrier heights and reaction energetics.

The most widely used hybrid functional is B3LYP, introduced by Stephens *et al.* in 1994 [14]. Its exchange–correlation energy is given by

$$E_{\mathrm{xc}}^{\mathrm{B3LYP}} = (1-a)\, E_x^{\mathrm{LDA}} + a\, E_x^{\mathrm{exact}} + b\, E_x^{\mathrm{B88}} + c\, E_c^{\mathrm{LYP}} + (1-c)\, E_c^{\mathrm{LDA}}, \tag{2.152}$$

where the parameters a, b and c control the fraction of exact exchange and the magnitude of the gradient corrections. Their values are chosen to best reproduce experimental thermochemistry, making B3LYP a semi-empirical hybrid functional.

2.7.4 Range-Separated Hybrid Functionals

Global hybrid functionals, such as B3LYP or PBE0 [169], mix a fixed fraction of Hartree–Fock (HF) exchange with semilocal DFT exchange. This improves upon LDA and GGA, especially for thermochemistry and molecular elastic properties. However, a *constant* amount of exact exchange is not sufficient to describe phenomena that depend critically on the long-range behaviour of the exchange potential, such as Rydberg excitations, charge-transfer (CT) excitations, and long-range non-covalent interactions.

In particular, semilocal functionals and global hybrids share the same fundamental limitation: their Kohn–Sham exchange–correlation potential decays too rapidly (exponentially) with distance, instead of following the correct Coulombic asymptotic form $-1/r$. As a consequence, the virtual orbital manifold is too low in energy, and excitations where the electron is promoted to a spatially distant region (e.g., from a donor to an acceptor fragment, or to diffuse Rydberg orbitals) are severely underestimated.

To overcome this issue, range-separated (RS) hybrid functionals introduce a distance-dependent partitioning of the Coulomb operator:

$$\frac{1}{r_{12}} = \frac{1-\omega(\gamma r_{12})}{r_{12}} + \frac{\omega(\gamma r_{12})}{r_{12}}, \tag{2.153}$$

where ω is a continuous switching function that varies smoothly from 0 at short inter-electronic distances to 1 in the long-range limit, and γ controls the separation between the two regimes. This splitting allows HF exchange and DFT exchange to be applied selectively in the short-range (SR) and long-range (LR) regions of the electron–electron interaction.

For molecular systems, it is advantageous to employ semilocal DFT exchange at short range, where electrons are highly correlated and the exchange hole is compact, while enforcing the exact HF exchange in the long-range limit, where the correct asymptotic behaviour is essential. This ensures:

- the correct $-1/r$ decay of the exchange potential,
- accurate orbital energy gaps,
- recovery of the $-1/R$ electron–hole interaction for CT excitations,
- a physically correct virtual orbital spectrum, crucial for Rydberg states.

A widely used example is CAM-B3LYP [15, 16], where the short-range and long-range exchange contributions are controlled by parameters α, β, and γ:

$$\frac{1}{r_{12}} = \frac{1-[\alpha+\beta\,\mathrm{erf}(\gamma r_{12})]}{r_{12}} + \frac{\alpha+\beta\,\mathrm{erf}(\gamma r_{12})}{r_{12}}. \tag{2.154}$$

Another popular functional, ωB97X-D [170], employs approximately 22% short-range and 100% long-range exact exchange and includes empirical dispersion corrections, making it particularly suitable for describing non-covalent interactions and solute–solvent effects.

Range-separated hybrids are therefore a natural choice when studying excited states involving substantial electron displacement, such as the charge-transfer and Rydberg excitations that are central in this thesis. By enforcing the correct asymptotic form of the exchange potential, RS Hybrid functionals overcome fundamental limitations of semilocal kernels and global hybrids and provide a more reliable foundation for linear-response TDDFT.

2.7.5 The Adiabatic approximation

As stated in the section dedicated to TDDFT, the time-dependent exchange–correlation (XC) potential is a fundamental ingredient of the theory. Within the adiabatic approximation, one exploits the wide variety of ground-state XC functionals by evaluating them at the instantaneous time-dependent density:

$$V_{\mathrm{xc}}^{A}(\mathbf{r},t) = V_{\mathrm{xc}}^{\mathrm{static}}[\rho(0)](\mathbf{r})\big|_{\rho_0(\mathbf{r})\longrightarrow\rho(\mathbf{r},t)} \tag{2.155}$$

Here $V_{\mathrm{xc}}^{\mathrm{static}}$ denotes any ground-state approximation introduced in the previous sections (LDA, GGA, hybrid, range-separated hybrid), and the approximation consists in replacing the ground-state density with the instantaneous time-dependent one, $\rho(\mathbf{r},t)$, neglecting all history-dependent (memory) effects.

The most widely used time-dependent XC potential is the Adiabatic Local-Density Approximation (ALDA). In ALDA, the XC potential at time t is obtained by taking the functional derivative of the LDA XC energy with respect to the density:

$$V_{\mathrm{xc}}^{\mathrm{ALDA}}(\mathbf{r},t) = \left.\frac{d\,\varepsilon_{\mathrm{xc}}^{\mathrm{LDA}}(\rho)}{d\rho}\right|_{\rho=\rho(\mathbf{r},t)}, \tag{2.156}$$

where $\varepsilon_{\mathrm{xc}}^{\mathrm{LDA}}(\rho)$ is the XC energy per particle of the homogeneous electron gas.

Moving to LR-TDDFT the key quantity of interest is the xc-kernel $f_{\mathrm{xc}}(\mathbf{r},\mathbf{r}',\omega)$. Also in this case we need suitable approximations and, the most widely used is, again, the adiabatic approximation

$$f_{\mathrm{xc}}^{\mathrm{A}}(\mathbf{r},\mathbf{r}') = \frac{\partial V_{\mathrm{xc}}^{0}[\rho_0](\mathbf{r})}{\partial\rho_0(\mathbf{r}')} \tag{2.157}$$

It is frequency-independent and purely real. It can be interpreted as replacing the xc kernel at each frequency with its static limit (it follows directly from a linearization of the KS equation for a system under the influence of a static perturbation). Similarly to what we described before, any approximate static xc potential will automatically give the corresponding Adiabatic

xc kernel. We report here the expression for the ALDA xc kernel:

$$f_{\mathrm{xc}}^{\mathrm{ALDA}}(\mathbf{r},\mathbf{r}') = \left.\frac{d^2\,\varepsilon_{\mathrm{xc}}^{\mathrm{LDA}}(\rho)}{d\rho^2}\right|_{\rho=\rho_0(\mathbf{r})} \delta(\mathbf{r}-\mathbf{r}') \tag{2.158}$$

Thus, ALDA is both *local in space* (it depends only on the density at the same point $\mathbf{r}$) and *local in time* (it responds only to the density at the same instant t). These properties make ALDA computationally efficient and remarkably successful for describing valence excitations where occupied and virtual orbitals strongly overlap.

However, the spatial and temporal locality of ALDA introduces well-known limitations. In particular, ALDA fails to describe:

- long-range charge-transfer (CT) excitations, where donor and acceptor densities do not overlap;
- Rydberg excitations, due to the incorrect asymptotic decay of the KS potential inherited from semilocal DFT;
- double excitations, which require a frequency-dependent (non-adiabatic) kernel.

These failures motivate the use of more sophisticated XC approximations, including hybrid and range-separated hybrid functionals, which provide the correct long-range behaviour required for CT and Rydberg excited states.

3 Computational Methods

This chapter is dedicated to the description of the computational protocols and tools used to study and characterize the optical response of the system under study in the works presented in the next chapter.

3.1 The Random Phase Approximation

In order to introduce the Casida formalism and Hybrid Diagonal Approximation, it is useful to first recall how linear response theory is formulated at the Hartree–Fock (HF) level. The resulting working equations are known as the Random Phase Approximation (RPA). RPA describes the response of the single-particle HF orbitals to an external time-dependent perturbation.

Throughout this section we assume a closed-shell HF reference. Indices $i, j, \ldots$ denote *occupied* spin–orbitals, and indices $a, b, \ldots$ denote *virtual* (unoccupied) orbitals and atomic units are used unless otherwise stated.

Let us assume to have solved the stationary HF problem

$$F^{(0)}\,\chi_i^{(0)} = \varepsilon_i\,\chi_i^{(0)}, \tag{3.1}$$

where $F^{(0)}$ is the unperturbed Fock operator and ε_i are the orbital energies. The corresponding time-dependent orbitals are

$$\psi_i^{(0)}(t) = \chi_i^{(0)}\,e^{-i\varepsilon_i t}. \tag{3.2}$$

We now consider how the HF solution evolves in the presence of a weak external perturbation

$$F(t)\,\psi_i(t) = i\frac{\partial}{\partial t}\psi_i(t). \tag{3.3}$$

In particular, we consider an external pertubation of frequency ω and, because the HF potential depends on the electron density, and the density depends on the orbitals, the external perturbation induces a self-consistent variation of the Fock operator. For this reason we express the perturbed Fock operator as

$$F(t) = F^{(0)} + \lambda\left(A_\omega e^{-i\omega t} + A_{-\omega}e^{i\omega t}\right) + \lambda\left(F_\omega^{(1)}e^{-i\omega t} + F_{-\omega}^{(1)}e^{i\omega t}\right), \tag{3.4}$$

where:

- $A_{\pm\omega}$ describe the external perturbation,
- $F^{(1)}_{\pm\omega}$ account for the self-consistent change of the HF potential.

Note that, although we refer to the perturbation as oscillating at frequency ω, a real time-dependent field must contain both complex Fourier components $e^{-i\omega t}$ and $e^{+i\omega t}$. Indeed, any real oscillating function such as $\cos(\omega t)$ can be written as

$$\cos(\omega t) = \tfrac{1}{2}\left(e^{-i\omega t} + e^{+i\omega t}\right).$$

For this reason, and in order for the Fock operator and the density to remain Hermitian at all times, the response of the system must include contributions at both $+\omega$ and $-\omega$. This leads naturally to the appearance of the two exponential terms in the expansion of $F(t)$.

Since the frequency of the response must be the same as that of the perturbation, we write the perturbed occupied orbitals as

$$\psi_i(t) = \chi_i^{(0)} e^{-i\varepsilon_i t} + \lambda\left[\chi_i^{(1,+)} e^{-i(\varepsilon_i+\omega)t} + \chi_i^{(1,-)} e^{-i(\varepsilon_i-\omega)t}\right]. \tag{3.5}$$

Using these expressions for the wavefunction and the Fock operators leads to:

$$\begin{aligned} &e^{-i(\varepsilon_i+\omega)t}\left[F^{(0)}\chi_i^{(1,+)} - (\varepsilon_i+\omega)\,\chi_i^{(1,+)} + \left(A_\omega + F_\omega^{(1)}\right)\chi_i^{(0)}\right] \\ &+ e^{-i(\varepsilon_i-\omega)t}\left[F^{(0)}\chi_i^{(1,-)} - (\varepsilon_i-\omega)\,\chi_i^{(1,-)} + \left(A_{-\omega} + F_{-\omega}^{(1)}\right)\chi_i^{(0)}\right] = 0. \end{aligned} \tag{3.6}$$

from which it follows that each term multiplying the exponential factors must vanish. Thus:

$$\begin{cases} \left(F^{(0)} - \varepsilon_i - \omega\right)\chi_i^{(1,+)} = -\left(A_\omega + F_\omega^{(1)}\right)\chi_i^{(0)}, \\ \left(F^{(0)} - \varepsilon_i + \omega\right)\chi_i^{(1,-)} = -\left(A_{-\omega} + F_{-\omega}^{(1)}\right)\chi_i^{(0)}. \end{cases} \tag{3.7}$$

What we need now are operative expressions for the first-order perturbed orbitals and, consequently, for the Fock operator.

In order to preserve the first order orthonormality of the occupied orbitals, we express their variation as a linear combination of the virtual ones:

$$\chi_i^{(1,+)} = \sum_a^{\text{virt}} X_{ia}\,|a\rangle, \qquad \chi_i^{(1,-)} = \sum_a^{\text{virt}} Y_{ia}^*\,|a\rangle. \tag{3.8}$$

doing so we can interpret X_{ia} and Y_{ia} as response amplitudes i.e. how much the occupied orbital χ_i mixes with virtual orbital χ_a at frequencies $(\varepsilon_i + \omega)$ and $(\varepsilon_i - \omega)$ respectively.

The HF Fock operator has the standard form

$$F = h + \sum_{j \in \text{occ}} \langle \cdot j \| \cdot j \rangle, \tag{3.9}$$

where $\langle pq \| rs \rangle$ denote antisymmetrized electron–repulsion integrals. Differentiating with respect to the orbital variations yields

$$\delta F = \sum_{j}^{\text{occ}} \left(\langle \cdot \, \delta j \| \cdot j \rangle + \langle \cdot j \| \cdot \, \delta j \rangle \right). \tag{3.10}$$

Since the first–order variation of an occupied orbital is

$$\delta j \equiv \chi_j^{(1)} = \chi_j^{(1,+)} \, e^{-i(\varepsilon_j + \omega)t} + \chi_j^{(1,-)} \, e^{-i(\varepsilon_j - \omega)t} \equiv \delta j^+ + \delta j^-, \tag{3.11}$$

we can write the corresponding variation of the Fock operator as

$$\begin{aligned} \delta F = \sum_{j \in \text{occ}} \Big(& \langle \cdot \, \chi_j^{(1,+)} \| \cdot j \rangle \, e^{i(\varepsilon_j + \omega)t} + \langle \cdot j \| \cdot \, \chi_j^{(1,+)} \rangle \, e^{-i(\varepsilon_j + \omega)t} \\ & + \langle \cdot \, \chi_j^{(1,-)} \| \cdot j \rangle \, e^{i(\varepsilon_j - \omega)t} + \langle \cdot j \| \cdot \, \chi_j^{(1,-)} \rangle \, e^{-i(\varepsilon_j - \omega)t} \Big). \end{aligned} \tag{3.12}$$

and, by comparison with the definition of the perturbed Fock operator, we identify the coefficients of $e^{-i\omega t}$ and $e^{+i\omega t}$, obtaining

$$F_{\omega}^{(1)} = \sum_{j \in \text{occ}} \left(\langle \cdot \, \chi_j^{(1,-)} \| \cdot j \rangle + \langle \cdot j \| \cdot \, \chi_j^{(1,+)} \rangle \right), \tag{3.13}$$

$$F_{-\omega}^{(1)} = \sum_{j \in \text{occ}} \left(\langle \cdot \, \chi_j^{(1,+)} \| \cdot j \rangle + \langle \cdot j \| \cdot \, \chi_j^{(1,-)} \rangle \right). \tag{3.14}$$

Substituting the operative expression just defined into equation 3.7, we obtain:

$$\begin{cases} \sum_a^{\text{virt}} \left(F^{(0)} - \varepsilon_i - \omega \right) X_{ia} |a\rangle = - \left[A_{\omega} + \sum_j^{\text{occ}} \sum_b^{\text{virt}} \left(Y_{jb} \langle \cdot b \| \cdot j \rangle + X_{jb} \langle \cdot j \| \cdot b \rangle \right) \right] |i\rangle \\ \sum_a^{\text{virt}} \left(F^{(0)} - \varepsilon_i + \omega \right) Y_{ia}^* |a\rangle = - \left[A_{-\omega} + \sum_j^{\text{occ}} \sum_b^{\text{virt}} \left(X_{jb}^* \langle \cdot b \| \cdot j \rangle + Y_{jb}^* \langle \cdot j \| \cdot b \rangle \right) \right] |i\rangle \end{cases} \tag{3.15}$$

and projecting onto a virtual orbital $\langle c|$ yields the coupled equations

$$\begin{cases} X_{ic}(\varepsilon_c - \varepsilon_i - \omega) + \sum_{jb} X_{bs} \langle cj \| ib \rangle + \sum_{jb} Y_{jb} \langle cb \| ij \rangle = -\langle c | A_{\omega} | i \rangle, \\ Y_{ic}(\varepsilon_c - \varepsilon_i + \omega) + \sum_{jb} X_{jb} \langle ij \| cb \rangle + \sum_{jb} Y_{jb} \langle ib \| cj \rangle = -\langle i | A_{\omega} | c \rangle. \end{cases} \tag{3.16}$$

We now introduce two square matrices A and B, each of dimension $(N_{\text{occ}}N_{\text{virt}})$:

$$A_{ic,jb} = \langle cj \| ib \rangle + (\varepsilon_c - \varepsilon_i)\, \delta_{ij}\delta_{cb}, \tag{3.17}$$

$$B_{ic,jb} = \langle cb \| ij \rangle. \tag{3.18}$$

Allowing us to express the coupled equations above in compact form

$$\begin{pmatrix} A & B \\ B^* & A^* \end{pmatrix} \begin{pmatrix} X \\ Y \end{pmatrix} = \omega \begin{pmatrix} I & 0 \\ 0 & -I \end{pmatrix} \begin{pmatrix} X \\ Y \end{pmatrix} + \begin{pmatrix} -\langle c|A_\omega|i\rangle \\ -\langle i|A_\omega|c\rangle \end{pmatrix}, \tag{3.19}$$

where I is the identity matrix and the column vectors:

$$\begin{pmatrix} X \\ Y \end{pmatrix} \quad ; \quad \begin{pmatrix} -\langle c|A_\omega|i\rangle \\ -\langle i|A_\omega|c\rangle \end{pmatrix}$$

have dimension $2 \times (N_{\text{occ}}N_{\text{virt}})$ and are obtained, respectively, by attaching a vector X containing the X_{ic} coefficients to a vector Y containing the Y_{ic} coefficients and by considering all the possible ic pairs.

The above expression describe the forced oscillation of the electronic density to an external perturbation. Solving it for a given driving frequency ω yields the coefficients $X(\omega)$ and $Y(\omega)$. Whenever the driving frequency approaches a true excitation energy of the system, the response formally diverges. This reflects the fact that the excitation energies correspond to the poles of the linear response function.

To make this connection explicit, consider the variation of the expectation value of a one-body operator B, such as the electric dipole:

$$\delta\langle B(t)\rangle = \sum_{i\in\text{occ}} \left(\langle \delta\phi_i | B | \phi_i \rangle + \langle \phi_i | B | \delta\phi_i \rangle \right).$$

As shown previously, the first-order variation of the occupied orbitals can be expanded in the virtual space. Substituting this expansion gives

$$\begin{aligned} \delta\langle B(t)\rangle = &\sum_{i\in\text{occ}} \sum_{a\in\text{virt}} e^{-i\omega t} \left(Y_{ia}\langle a|B|i\rangle + X_{ia}\langle i|B|a\rangle \right) \\ &+ \sum_{i\in\text{occ}} \sum_{a\in\text{virt}} e^{+i\omega t} \left(X^*_{ia}\langle a|B|i\rangle + Y^*_{ia}\langle i|B|a\rangle \right). \end{aligned} \tag{3.20}$$

By comparing this with the form of the linear response function we derived in the section dedicated to Linear Response (for the special case where a monochromatic perturbation of

frequency ω_0 is considered) one identifies the quantity

$$\chi_{BA}(\omega) = \sum_{i\in\mathrm{occ}} \sum_{a\in\mathrm{virt}} \left(Y_{ia}(\omega)\langle\phi_a|B|\phi_i\rangle + X_{ia}(\omega)\langle\phi_i|B|\phi_a\rangle\right),$$

whose poles determine the excitation energies.

Therefore, absorption occurs when the amplitudes X and Y satisfy the homogeneous system

$$\begin{pmatrix} A & B \\ B^* & A^* \end{pmatrix} \begin{pmatrix} X \\ Y \end{pmatrix} = \omega \begin{pmatrix} I & 0 \\ 0 & -I \end{pmatrix} \begin{pmatrix} X \\ Y \end{pmatrix}, \tag{3.21}$$

which is the well-known Random Phase Approximation (RPA) and the eigenvectors satisfy the normalization condition

$$X^\dagger X - Y^\dagger Y = 1. \tag{3.22}$$

The positive roots ω correspond to excitation energies, and the vectors X and Y encode the forward and backward transition amplitudes, respectively. .

This problem simplifies in two common cases: (i) when the molecular orbitals are real, so that $A = A^*$ and $B = B^*$; (ii) when the coupling matrix B is neglected, leading to the more familiar eigenvalue equation

$$AX = \omega X, \tag{3.23}$$

known as the Tamm–Dancoff approximation (TDA) [23].

3.2 The Casida Algorithm

The Casida [17] formulation of linear-response TDDFT can be derived in close analogy with the Random Phase Approximation (RPA) equations introduced for Hartree–Fock theory. In the HF case, the response matrix is built from the Coulomb and exact exchange contributions of the Fock operator. In a DFT framework, the situation changes because the Kohn–Sham Hamiltonian contains no exact exchange. Instead, the electron–electron interaction enters through the Hartree potential and the exchange–correlation kernel f_{xc}. In this section we start from the RPA structure and adapt it to the Kohn–Sham setting in order to derive the standard Casida equation.

In RPA matrices A and B contain antisymmetrized two-electron integrals like:

$$\langle aj\|ib\rangle = \langle aj \mid ib\rangle - \langle aj \mid bi\rangle, \tag{3.24}$$

where the first term originates from the Coulomb interaction and the second from the exact exchange.

In TDDFT, the starting point is the Kohn–Sham reference system. The KS Hamiltonian

contains the Coulomb interaction but not the exact exchange. Correlation and exchange effects are instead included through an effective exchange–correlation kernel f_{xc}. Assuming a local kernel in the adiabatic approximation, the RPA-like coupling matrices become

$$A_{ia,jb} = (\varepsilon_a - \varepsilon_i)\,\delta_{ij}\delta_{ab} + \langle aj \mid ib\rangle + \left\langle aj \left| f_{\mathrm{xc}}^{A} \right| ib \right\rangle, \tag{3.25}$$

$$B_{ia,jb} = \langle ab \mid ij\rangle + \left\langle ab \left| f_{\mathrm{xc}}^{A} \right| ij \right\rangle. \tag{3.26}$$

Because KS orbitals of a closed-shell system can be chosen real, the matrices A and B are real and symmetric.

The linear-response problem for the vectors X and Y takes the form

$$\begin{cases} AX + BY = \omega X, \\ BX + AY = -\omega Y. \end{cases} \tag{3.27}$$

ans now, by forming symmetric and antisymmetric combinations of the amplitudes, these equations can be rewritten as

$$\begin{cases} (A+B)(X+Y) = \omega(X-Y), \\ (A-B)(X-Y) = \omega(X+Y). \end{cases} \tag{3.28}$$

At this point, it is useful to examine the expression for matrix $(A-B)$,

$$(A-B)_{ia,jb} = (\varepsilon_a - \varepsilon_i)\,\delta_{aj}\delta_{ab} + \langle aj \mid ib\rangle - \langle ab \mid ij\rangle. \tag{3.29}$$

For real closed-shell Kohn–Sham orbitals the two-electron Coulomb-like integrals satisfy

$$\langle aj \mid ib\rangle = \langle ab \mid ij\rangle,$$

so that the last two terms in Eq. (3.29) cancel. Thus matrix

$$\varepsilon \equiv A - B$$

is diagonal, with elements

$$\varepsilon_{ia,jb} = (\varepsilon_a - \varepsilon_i)\,\delta_{ij}\delta_{ab}. \tag{3.30}$$

From the second equation of (3.28) we immediately obtain

$$X - Y = \omega\,\varepsilon^{-1}(X+Y). \tag{3.31}$$

Substituting Eq. (3.31) into the first line of (3.28) leads to

$$(A + B)(X + Y) = \omega^2 \, \varepsilon^{-1}(X + Y). \tag{3.32}$$

Because ε is diagonal, we may define its matrix square roots,

$$\varepsilon_{ij}^{1/2} = \delta_{ij}\sqrt{\varepsilon_{ij}}, \qquad \varepsilon_{ij}^{-1/2} = \delta_{ij}\sqrt{\varepsilon_{ij}}.$$

Multiplying Eq. (3.32) on the left by $\varepsilon^{1/2}$ gives

$$\varepsilon^{1/2}(A + B)\, \varepsilon^{1/2}\, \varepsilon^{-1/2}(X + Y) = \omega^2 \, \varepsilon^{-1/2}(X + Y). \tag{3.33}$$

This shows that the vector

$$F = \varepsilon^{-1/2}(X + Y) \tag{3.34}$$

is an eigenvector of the matrix

$$\Omega = \varepsilon^{1/2}(A + B)\, \varepsilon^{1/2}, \tag{3.35}$$

with eigenvalue ω^2.

We thus arrive at the celebrated *Casida equation*:

$$\Omega F = \omega^2 F. \tag{3.36}$$

The eigenvalues ω are the true excitation energies of the interacting system (within the adiabatic approximation), while from the eigenvectors F the corresponding excitation amplitudes can be derived.

In practical implementations, Casida's equation is solved by explicitly diagonalizing the matrix Ω defined in Eq. (3.36). This matrix lives in the space of single particle–hole (1h–1p) transitions and therefore carries four indices: two for occupied orbitals and two for virtual orbitals, with an additional spin index when necessary. The dimension of Ω is thus

$$N_{\text{occ}} \times N_{\text{virt}},$$

corresponding to the total number of KS transitions $i \to a$. In a spin-resolved formulation, the matrix elements take the form

$$\Omega_{ia\sigma,\, jb\tau} = \delta_{\sigma\tau}\, \delta_{ij}\, \delta_{ab}\, (\varepsilon_a - \varepsilon_i)^2 + 2\, \sqrt{\varepsilon_a - \varepsilon_i}\, K_{ia\sigma,\, jb\tau}\, \sqrt{\varepsilon_b - \varepsilon_j}, \tag{3.37}$$

where i, j run over occupied orbitals, a, b over virtual orbitals, and σ, τ denote spin.

The matrix K appearing in (3.37) is the *coupling matrix*, which contains contributions from

the Coulomb interaction, the exchange–correlation potential, and the exchange–correlation kernel. In the adiabatic local-density approximation (ALDA), it reads

$$K_{ia\sigma,\,jb\tau} = \iint \phi_{i\sigma}(r)\,\phi_{a\sigma}(r)\left[\frac{1}{|r-r'|} + f_{\mathrm{xc}}^{\mathrm{ALDA}}(r)\,\delta(r-r')\right]\phi_{j\tau}(r')\,\phi_{b\tau}(r')\,dr\,dr'. \tag{3.38}$$

This kernel couples different transitions and is responsible for redistributing oscillator strengths and generating collective excitations.

Once the eigenvalue problem

$$\Omega F_{n0} = \omega_{n0}^2\,F_{n0}$$

is solved, the eigenvectors F_{n0} contain all the information needed to compute transition properties. For example, the oscillator strength associated with the transition from the ground state $|0\rangle$ to the excited state $|n\rangle$ is given by

$$f_{n0} = \frac{2}{3}\,\omega_{n0}\left(|\langle n|x|0\rangle|^2 + |\langle n|y|0\rangle|^2 + |\langle n|z|0\rangle|^2\right). \tag{3.39}$$

Within the Casida formalism, these transition dipoles can be written directly in terms of the eigenvector F_{n0}. Using the connection between the RPA amplitudes and the Casida's eigenvectors derived previously we obtain the compact expression

$$f_{n0} = \frac{2}{3}\left(x^\dagger\,\varepsilon^{1/2}F_{n0} + y^\dagger\,\varepsilon^{1/2}F_{n0} + z^\dagger\,\varepsilon^{1/2}F_{n0}\right), \tag{3.40}$$

where x, y, z denote the dipole transition vectors in the particle–hole basis. Hence, both the excitation energies ω_{n0} and the corresponding intensities are obtained consistently from Casida's eigenvectors.

Although Eqs. (3.36) and (3.37) give a formally exact (within the adiabatic approximation) representation of the TDDFT excitation problem, the direct diagonalization of Ω is rarely feasible.

In practice, the Casida eigenvalue problem is solved using iterative subspace algorithms, most commonly the Davidson method [171, 172], which efficiently extracts only the lowest excitation energies and corresponding eigenvectors. Davidson's method performs very well for both small and large molecules, but it is limited to the extraction of a small number of low energy excitations; it becomes inefficient or numerically unstable when:

- many excited states are required,
- the spectrum is dense,
- strong coupling between transitions makes convergence slow.

For such systems, alternative approaches to solving TDDFT response equations have been

developed, including real-time propagation schemes, density-matrix based formulations, and iterative methods exploiting sparsity or locality. These approaches are particularly advantageous for large-scale systems such as metallic nanoclusters.

3.3 PolTDDFT algorithm

An alternative formulation of TDDFT exists which avoids the explicit solution of Casida's eigenvalue equation and instead works directly with the frequency–dependent induced density. When a time–dependent external perturbation $V_{\text{ext}}(\mathbf{r}, \omega)$ acts on a system, it induces a first–order density variation $\rho^{(1)}(\mathbf{r}, \omega)$ witch can be expressed using the dielectric susceptibility χ of the system

$$\rho^{(1)}(\mathbf{r}, \omega) = \int \mathrm{d}^3 r' \, \chi(\mathbf{r}, \mathbf{r}', \omega) \, V_{\text{ext}}(\mathbf{r}', \omega). \tag{3.41}$$

The interacting susceptibility χ is, however, not directly accessible in practice. Instead, the same induced density may be equivalently obtained using the Kohn–Sham susceptibility χ_{KS} of a non–interacting reference system, provided that the external field is replaced by an effective field V_{SCF}. The advantage is that χ_{KS} has a simple explicit expression in terms of KS orbitals and energies:

$$\chi_{KS}(\mathbf{r}, \mathbf{r}', \omega) = \sum_{i}^{\text{occ}} \sum_{a}^{\text{virt}} \frac{\varphi_i(\mathbf{r}) \varphi_a(\mathbf{r}) \varphi_a(\mathbf{r}') \varphi_i(\mathbf{r}') (\epsilon_a - \epsilon_i)}{\omega^2 - (\epsilon_a - \epsilon_i)^2}. \tag{3.42}$$

The self–consistent effective field consists of the external perturbation plus the linearized Coulomb and xc contributions:

$$V_{\text{SCF}}(\mathbf{r}, \omega) = V_{\text{ext}}(\mathbf{r}, \omega) + \int \frac{\rho^{(1)}(\mathbf{r}', \omega)}{|\mathbf{r} - \mathbf{r}'|} \, \mathrm{d}^3 r' + \int f_{\text{xc}}(\mathbf{r}, \mathbf{r}', \omega) \, \rho^{(1)}(\mathbf{r}', \omega) \, \mathrm{d}^3 r', \tag{3.43}$$

where f_{xc} is the TDDFT xc kernel. Thus the induced density satisfies the self–consistent relation

$$\rho^{(1)}(\mathbf{r}, \omega) = \int \mathrm{d}^3 r' \, \chi_{KS}(\mathbf{r}, \mathbf{r}', \omega) \, V_{\text{SCF}}(\mathbf{r}', \omega). \tag{3.44}$$

From $\rho^{(1)}$ one obtains the dynamical polarizability; for example, the zz component reads

$$\alpha_{zz}(\omega) = \int z \, \rho_z^{(1)}(\mathbf{r}, \omega) \, \mathrm{d}^3 r. \tag{3.45}$$

We mentioned before how the Casida equation involves the diagonalization of the large matrix Ω, which becomes computationally prohibitive when:

- one needs a wide energy window for the absorption spectrum;

- large systems with dense manifolds of excitations are considered.

To overcome these limitations, the Trieste theoretical chemistry group developed an alternative algorithm, named PolTDDFT [43, 44, 173], which extracts the spectrum point–by–point from the imaginary part of the complex dynamical polarizability $\alpha(\omega)$.

The photoabsorption spectrum is obtained through

$$\sigma(\omega) = \frac{4\pi\omega}{c} \text{ Im } \alpha(\omega), \tag{3.46}$$

where $\alpha(\omega)$ is the isotropic polarizability (its trace divided by 3). Accordingly to this algorithm the polarizability must be evaluated at complex frequencies $\omega = \omega_r + i\omega_i$, where ω_r is the photon energy and ω_i introduces a physical line broadening that mimics the finite lifetime of excited states.

Equations (3.44)–(3.43) can be written in compact operator form:

$$\rho^{(1)} = \chi_{KS} V_{\text{SCF}}, \tag{3.47}$$

$$V_{\text{SCF}} = V_{\text{ext}} + K\,\rho^{(1)}, \tag{3.48}$$

where K is the full Coulomb+xc coupling operator. Exploiting the linearity to eliminate V_{SCF} we derive the TDDFT response equation:

$$\left[1 - \chi_{KS} K\right] \rho^{(1)} = \chi_{KS} V_{\text{ext}}. \tag{3.49}$$

To solve Eq. (3.49), we expand the induced density in an auxiliary density–fitting basis $\{f_\mu(\mathbf{r})\}$,

$$\rho^{(1)}(\mathbf{r}, \omega) = \sum_\mu f_\mu(\mathbf{r})\, b_\mu(\omega), \tag{3.50}$$

restricting the fitting space to functions relevant for the valence region only. Projecting Eq. (3.49) onto the auxiliary basis leads to a non–homogeneous linear system. In matrix form it reads:

$$\left[S - M(\omega)\right] b = d, \tag{3.51}$$

where:

- $S_{\mu\nu} = \langle f_\mu | f_\nu \rangle$ is the fitting functions overlap matrix,
- b contains the coefficients of the expansion $b_\mu(\omega)$,
- $d_\mu = \langle f_\mu | \chi_{KS}(\omega) | z \rangle$ are the known non-homogeneous terms,
- $M_{\mu\nu} = \langle f_\mu | \chi_{KS}(\omega) K | f_\nu \rangle$.

The computational cost is dominated by the construction of the frequency–dependent matrix $M(\omega)$, which requires a double sum over occupied and virtual orbitals for each frequency.

A central feature of PolTDDFT is a controlled approximation that rewrites $M(\omega)$ as a linear combination of frequency–independent matrices with frequency–dependent coefficients. By inspecting the explicit expression of the KS susceptibility,

$$\chi_{KS}(\mathbf{r},\mathbf{r}',\omega) = \sum_{i}^{\text{occ}} \sum_{a}^{\text{virt}} \varphi_i(\mathbf{r})\varphi_a(\mathbf{r}) \frac{4\epsilon_{ia}}{\omega^2 - \epsilon_{ia}^2} \varphi_a(\mathbf{r}')\varphi_i(\mathbf{r}') \tag{3.52}$$

$$= \sum_{i,a} \Theta_{ia}(\mathbf{r})\, \lambda_{ia}(\omega)\, \Theta_{ia}(\mathbf{r}'), \tag{3.53}$$

where

$$\epsilon_{ia} = \epsilon_a - \epsilon_i, \qquad \Theta_{ia}(\mathbf{r}) = \varphi_i(\mathbf{r})\varphi_a(\mathbf{r}), \qquad \lambda_{ia}(\omega) = \frac{4\epsilon_{ia}}{\omega^2 - \epsilon_{ia}^2}.$$

we see that the frequency dependence appears only in $\lambda_{ia}(\omega)$, which varies smoothly for transitions with similar ϵ_{ia}.

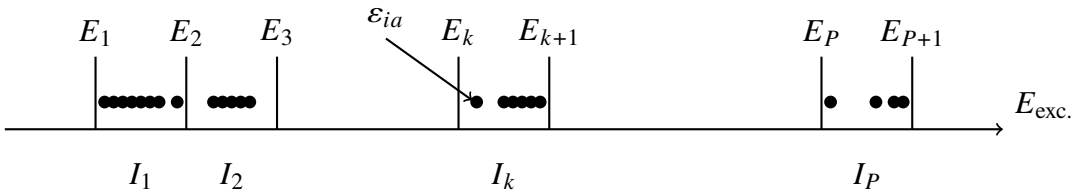


Figure 3.1: Discretization of the excitation energy axis with selected eigenvalue differences.

Thus, the energy axis spanned by the set of excitation energies $\{\epsilon_{ia}\}$ is partitioned into P intervals I_k. Within each interval the ϵ_{ia} values are approximated by the midpoint energy

$$\bar{E}_k = \frac{E_k + E_{k+1}}{2},$$

so that $\lambda_{ia}(\omega)$ may be replaced by

$$s_k(\omega) = \frac{4\bar{E}_k}{\omega^2 - \bar{E}_k^2}.$$

With this approximation, the susceptibility becomes

$$\chi_{KS}(\mathbf{r},\mathbf{r}',\omega) = \sum_{k=1}^{P} s_k(\omega) \sum_{\epsilon_{ia}\in I_k} \Theta_{ia}(\mathbf{r})\, \Theta_{ia}(\mathbf{r}'), \tag{3.54}$$

and inserting Eq. (3.54) into the definition of $M_{\mu\nu}$ yields

$$M_{\mu\nu}(\omega) = \sum_{k=1}^{P} s_k(\omega)\, G^k_{\mu\nu}, \tag{3.55}$$

where the frequency–independent matrices G^k collect all orbital–dependent terms:

$$G^k_{\mu\nu} = \sum_{\epsilon_{ia}\in I_k} \langle f_\mu|\Theta_{ia}\rangle\, \langle\Theta_{ia}|K|f_\nu\rangle. \tag{3.56}$$

A similar decomposition holds for the non–homogeneous term:

$$d_\mu(\omega) = \sum_{k=1}^{P} s_k(\omega) \sum_{\epsilon_{ia}\in I_k} \langle f_\mu|\Theta_{ia}\rangle\langle\Theta_{ia}|z\rangle. \tag{3.57}$$

Thus the computationally expensive orbital–dependent quantities are evaluated once at the beginning of the calculation. At each new frequency, assembling $M(\omega)$ requires only forming the linear combination with the scalar coefficients $s_k(\omega)$.

Solving Eq. (3.51) for $b(\omega)$ provides the expansion coefficients of the induced density. The dynamical polarizability follows from

$$\alpha_{zz}(\omega) = \int z\, \rho^{(1)}(\mathbf{r},\omega)\, \mathrm{d}^3r = \sum_\mu b_\mu(\omega) \int z\, f_\mu(\mathbf{r})\, \mathrm{d}^3r. \tag{3.58}$$

Its imaginary part yields the absorption spectrum, and the use of complex frequencies introduces a physically meaningful broadening without diagonalizing any excitation matrix.

PolTDDFT therefore provides a numerically efficient and scalable frequency–domain alternative to the Casida approach, particularly well–suited for large systems and wide spectral windows.

3.3.1 PolTDDFT implementation

In a later chapter, a new efficient evaluation of the diagonal correction within the Hybrid Diagonal Approximation (HDA) for TDDFT will be presented. Its implementation relies heavily on the infrastructure developed for the PolTDDFT algorithm; for this reason, it is useful to analyse in detail the computational realization of the PolTDDFT scheme.

The algorithm was originally developed within the ADF code and is currently available in its successor package, AMS. The AMS framework provides several analytical integrals and precomputed quantities essential to the PolTDDFT implementation. Among them:

- Density–fitting overlap matrix

$$S_{\mu\nu} = \langle f_\mu|f_\nu\rangle; \tag{3.59}$$

- Density–fitting Coulomb matrix

$$F_{\mu\nu} = \left\langle f_\mu \left| \frac{1}{|\mathbf{r} - \mathbf{r}'|} \right| f_\nu \right\rangle; \tag{3.60}$$

- Pair–fitting integrals, involving two basis basis functions and one fitting function:

$$\langle f_\mu | \sigma\tau \rangle; \tag{3.61}$$

- Dipole integrals between basis functions

$$\langle \sigma | z | \tau \rangle; \tag{3.62}$$

- Molecular orbital energies and coefficients: $\{\epsilon_p\}$ and $\{c_{\sigma p}\}$.

The implementation proceeds as follows. First, the excitation–energy grid is constructed and the KS energy differences $\epsilon_{ia} = \epsilon_a - \epsilon_i$ are assigned to the corresponding intervals I_k. Next, the fitting functions are selected and the matrices needed to assemble the PolTDDFT linear system are built.

The contribution of interval k to the matrix $M(\omega)$ is:

$$G^k_{\mu\nu} = \sum_{\epsilon_{ia} \in I_k} \langle f_\mu | \Theta_{ia} \rangle \langle \Theta_{ia} | K | f_\nu \rangle = \sum_{\epsilon_{ia} \in I_k} A^k_{\mu,ia} \, B^k_{ia,\nu}, \tag{3.63}$$

where:

$$A^k_{\mu,ia} = \langle f_\mu | \Theta_{ia}(\mathbf{r}) \rangle, \tag{3.64}$$

$$B^k_{ia,\nu} = \langle \Theta_{ia}(\mathbf{r}') | K | f_\nu \rangle = \left\langle \Theta_{ia} \left| \frac{1}{|\mathbf{r} - \mathbf{r}'|} \right| f_\nu \right\rangle + \langle \Theta_{ia} | f_{\mathrm{xc}} | f_\nu \rangle. \tag{3.65}$$

By taking advantage of the AMS pair–fitting integrals, A^k is written as:

$$A^k_{\mu,ia} = \langle f_\mu | \varphi_i \varphi_a \rangle = \sum_{\sigma\tau} \langle f_\mu | \sigma\tau \rangle \, c_{\sigma i} c_{\tau a}. \tag{3.66}$$

This is the most computationally demanding step of the algorithm, because it scales over all AO pairs contributing to the KS transition densities Θ_{ia}.

The first contribution in Eq. (3.65) is handled using the resolution of the identity in the

fitting basis:

$$\left\langle \Theta_{ia}(\mathbf{r}') \left| \frac{1}{|\mathbf{r}-\mathbf{r}'|} \right| f_\nu \right\rangle = \sum_{\gamma\eta} \langle \Theta_{ia}|f_\gamma\rangle \, S^{-1}_{\gamma\eta} \, \langle f_\eta | \frac{1}{|\mathbf{r}-\mathbf{r}'|} | f_\nu \rangle$$
$$= \left((A^k)^\dagger S^{-1} F\right)_{ia,\nu}, \tag{3.67}$$

where $(A^k)^\dagger$ denotes the conjugate transpose.

The xc contribution to B^k takes an analogous form:

$$\langle \Theta_{ia}|f_{\mathrm{xc}}|f_\nu\rangle = \sum_{\gamma\eta} \langle \Theta_{ia}|f_\gamma\rangle S^{-1}_{\gamma\eta} \langle f_\eta|f_{\mathrm{xc}}|f_\nu\rangle$$
$$= \left((A^k)^\dagger S^{-1} Z\right)_{ia,\nu}, \tag{3.68}$$

where:

$$Z_{\mu\nu} = \langle f_\mu | f_{\mathrm{xc}} | f_\nu \rangle \tag{3.69}$$

is the matrix of xc-kernel integrals in the fitting basis (computed once).

Putting the Coulomb and xc contributions together:

$$B^k_{ia,\nu} = \left((A^k)^\dagger S^{-1}(F+Z)\right)_{ia,\nu}. \tag{3.70}$$

It is now convenient to introduce:

$$D^k = A^k (A^k)^\dagger, \tag{3.71}$$
$$L = S^{-1}(F+Z), \tag{3.72}$$

so that each interval contribution assumes the compact form:

$$G^k = D^k \, L. \tag{3.73}$$

This avoids explicitly constructing B^k for each k. Only A^k and L must be computed, and the remaining operations reduce to matrix multiplications.

Thus the PolTDDFT matrix $M(\omega)$ becomes:

$$M(\omega) = \sum_{k=1}^{P} s_k(\omega) G^k = \sum_{k=1}^{P} s_k(\omega) D^k L = \left(\sum_{k=1}^{P} s_k(\omega) D^k \right) L. \tag{3.74}$$

Finally, the linear term in the TDDFT equation, $d_\mu = \langle f_\mu | \chi_{KS}(\omega) | z \rangle$, is obtained directly

from the previously constructed A^k:

$$\begin{aligned} d_\mu &= \sum_{k=1}^{P} s_k(\omega) \sum_{\epsilon_{ia} \in I_k} A^k_{\mu,ia} \langle \varphi_i | z | \varphi_a \rangle \\ &= \sum_{k=1}^{P} s_k(\omega) \sum_{\epsilon_{ia} \in I_k} A^k_{\mu,ia} \sum_{\sigma\tau} \langle \sigma | z | \tau \rangle c_{\sigma i} c_{\tau a}. \end{aligned} \tag{3.75}$$

Once $M(\omega)$ and $d(\omega)$ are available, the solution of the linear system from Eq. (3.51) yields the induced-density expansion coefficients for each complex frequency ω.

3.3.2 Unrestricted extension of PolTDDFT

In this section we propose an extension of the PolTDDFT algorithm to Open-Shell systems. An open-shell system is a quantum system whose electronic ground state contains one or more unpaired electrons, i.e. at least one molecular (or atomic) orbital is singly occupied. These systems are not properly described by a restricted formalism if only one determinant is employed in the description of the groun state. They require an unrestricted (spin-polarized) treatment, where α and β electrons are allowed to occupy different spatial orbitals. The TDDFT treatment of open-shell molecular excitations has been an open question since the first works by Hirata and Head-Gordon [174], where they calculated the lowest two excitation energies for open-shell diatomic and organic radicals, to nowadays, where complex relativistic spin-orbit coupling effects are introduces perturbativly on top on top of a restricted open-shell Kohn–Sham (ROKS) TDDFT-TDA calculation [175]. To see how it would be possible to describe such systems within the PolTDDFT algorithm, let us now relax the restricted closed-shell condition and consider an unrestricted formalism. Accordingly, all quantities become spin-dependent, including molecular orbitals, induced densities, susceptibilities, and response kernels.

In practice, our proposed implementation relies on an unrestricted single-determinant description of the ground state, and spin–flip effects are not included. Within such a scheme, the Slater determinant is not a spin eigenfunction; this condition could in principle be restored by adopting a multi-determinant wavefunction, which we do not pursue here.

The operatorial equations for the induced density and the effective self-consistent field potential, witch we described before, are generalized to the spin-resolved case as

$$\rho^{(1)}_\alpha(\omega) = \chi^{\mathrm{KS}}_\alpha(\omega)\, V^{\mathrm{SCF}}_\alpha(\omega), \tag{3.76}$$

$$\rho^{(1)}_\beta(\omega) = \chi^{\mathrm{KS}}_\beta(\omega)\, V^{\mathrm{SCF}}_\beta(\omega), \tag{3.77}$$

with the corresponding effective potentials

$$V_\alpha^{\mathrm{SCF}}(\omega) = V^{\mathrm{ext}}(\omega) + K_C\big(\rho_\alpha^{(1)}(\omega) + \rho_\beta^{(1)}(\omega)\big) + K_{\alpha\alpha}^{XC}\rho_\alpha^{(1)}(\omega) + K_{\alpha\beta}^{XC}\rho_\beta^{(1)}(\omega), \tag{3.78}$$

$$V_\beta^{\mathrm{SCF}}(\omega) = V^{\mathrm{ext}}(\omega) + K_C\big(\rho_\alpha^{(1)}(\omega) + \rho_\beta^{(1)}(\omega)\big) + K_{\beta\beta}\rho_\beta^{(1)}(\omega) + K_{\beta\alpha}\rho_\alpha^{(1)}(\omega). \tag{3.79}$$

In this formulation the KS susceptibilities $\chi_\alpha^{\mathrm{KS}}$ and χ_β^{KS} differ, as they are built from distinct occupied–virtual manifolds for α and β spins. Explicitly, the KS dielectric susceptibility is decomposed into two contributions arising from α and β spin channels:

$$\begin{aligned}
\chi_{\mathrm{KS}}(\mathbf{r},\mathbf{r}',\omega) &= \sum_{i,a} \Theta_{ia}(\mathbf{r})\,\lambda_{ia}(\omega)\,\Theta_{ia}(\mathbf{r}') && (3.80)\\
&= \sum_{i\in\alpha}\sum_{a\in\alpha} \Theta_{ia}^{\alpha}(\mathbf{r})\,\lambda_{ia}^{\alpha}(\omega)\,\Theta_{ia}^{\alpha}(\mathbf{r}') + \sum_{i\in\beta}\sum_{a\in\beta} \Theta_{ia}^{\beta}(\mathbf{r})\,\lambda_{ia}^{\beta}(\omega)\,\Theta_{ia}^{\beta}(\mathbf{r}') && (3.81)\\
&= \chi_\alpha^{\mathrm{KS}}(\mathbf{r},\mathbf{r}',\omega) + \chi_\beta^{\mathrm{KS}}(\mathbf{r},\mathbf{r}',\omega). && (3.82)
\end{aligned}$$

where each term involves only occupied–virtual pairs of the same spin.

The effective potentials are also spin-dependent: the exchange–correlation kernel K^{XC} couples the different spin channels, whereas the Coulomb interaction is spin-independent.

Eliminating the self-consistent potentials from Eqs. (3.76)–(3.79) leads to a coupled system of linear equations for the spin-resolved induced densities:

$$\begin{aligned}
\left[1 - \chi_\alpha^{\mathrm{KS}}\left(K_C + K_{\alpha\alpha}\right)\right]\rho_\alpha^{(1)} - \chi_\alpha^{\mathrm{KS}}\left(K_C + K_{\alpha\beta}\right)\rho_\beta^{(1)} &= \chi_\alpha^{\mathrm{KS}} V^{\mathrm{ext}}, && (3.83)\\
\left[1 - \chi_\beta^{\mathrm{KS}}\left(K_C + K_{\beta\beta}\right)\right]\rho_\beta^{(1)} - \chi_\beta^{\mathrm{KS}}\left(K_C + K_{\beta\alpha}\right)\rho_\alpha^{(1)} &= \chi_\beta^{\mathrm{KS}} V^{\mathrm{ext}}, && (3.84)
\end{aligned}$$

Projecting the induced densities onto an auxiliary density-fitting basis $\{f_p\}$ yields the matrix formulation:

$$\begin{pmatrix} \mathbf{S} + \mathbf{M}_{\alpha\alpha}(\omega) & \mathbf{M}_{\alpha\beta}(\omega) \\ \mathbf{M}_{\beta\alpha}(\omega) & \mathbf{S} + \mathbf{M}_{\beta\beta}(\omega) \end{pmatrix} \begin{pmatrix} \mathbf{b}_\alpha(\omega) \\ \mathbf{b}_\beta(\omega) \end{pmatrix} = \begin{pmatrix} \mathbf{d}_\alpha(\omega) \\ \mathbf{d}_\beta(\omega) \end{pmatrix}, \tag{3.85}$$

where:

- $S_{\mu\nu} = \langle f_\mu | f_\nu \rangle$ is the fitting functions overlap matrix,
- b^σ contains the coefficients of the expansion of the induced density due to the σ channel,
- $d_\mu^\sigma = \langle f_\mu | \chi_{KS}^\sigma(\omega) | z \rangle$ are the known non-homogeneous terms,
- $M_{\mu\nu}^{\sigma\gamma} = \langle f_\mu | \chi_{KS}^\sigma(\omega)(K_C + K_{\sigma\gamma}^{XC}) | f_\nu \rangle$.

here σ and γ stand for the possible spin variable.

In the closed-shell limit, the unrestricted formulation reduces to the restricted one: spin-dependent densities and susceptibilities become equal, each being one half of the restricted quantity, and the exchange–correlation kernel coincides with its restricted counterpart

$$\frac{1}{2}\left(K^{XC}_{\alpha\alpha} + K^{XC}_{\alpha\beta}\right) = \frac{1}{2}\left(K^{XC}_{\beta\beta} + K^{XC}_{\beta\alpha}\right) = K_{XC} \tag{3.86}$$

The construction of the frequency-dependent matrices $\mathbf{M}_{\gamma\sigma}(\omega)$ follows the same strategy introduced for the restricted case. Exploiting the high density of KS excitation energies, the KS susceptibility is expressed as a linear combination of frequency-independent matrices weighted by frequency-dependent coefficients, allowing the matrix in Eq. (3.85) to be assembled efficiently at each photon energy.

In practice, in order to calculate the frequency-independent matrices $G_k^{\sigma\gamma}$ we could follow closely what is already done for the restricted case:

$$G_k^{\sigma\gamma} = D_k^{\sigma} L_{\sigma\gamma} \tag{3.87}$$

where

$$D_k^{\sigma} = A_k^{\sigma}\left(A_k^{\sigma}\right)^{\dagger} \quad , \quad L_{\sigma\gamma} = S^{-1}(F + Z^{\sigma\gamma}) \tag{3.88}$$

and the non-homogeneous term would be written as:

$$\begin{aligned} d_\mu^\sigma &= \langle f_\mu | \chi^\sigma_{\mathrm{KS}}(\omega) | z \rangle \\ &= \sum_{k=1}^{P} s_k(\omega) \sum_{\varepsilon^\sigma_{ia} \in I_k} \langle f_\mu | \Theta^\sigma_{ia}(\mathbf{r}) \rangle \langle \Theta^\sigma_{ia}(\mathbf{r}) | z \rangle \\ &= \sum_{k=1}^{P} s_k(\omega) \sum_{\varepsilon^\sigma_{ia} \in I_k} A^{k,\sigma}_{\mu,ia} \, \langle \varphi^\sigma_i | z | \varphi^\sigma_a \rangle . \end{aligned} \tag{3.89}$$

To do so we would need to build the spin-dependent matrices:

$$A^{k,\sigma}_{\mu,ia} = \langle f_\mu | \varphi^\sigma_i \, \varphi^\sigma_a \rangle = \sum_{\eta,\tau} \langle f_\mu | \eta\tau \rangle \, c^\sigma_{\eta i} \, c^\sigma_{\tau a} \tag{3.90}$$

$$Z^{\sigma\gamma}_{\mu\nu} = \left\langle f_\mu \left| \frac{\partial V^\sigma_{\mathrm{XC}}}{\partial \rho_\gamma} \right| f_\nu \right\rangle \tag{3.91}$$

The proposed unrestricted formulation retains the computational efficiency of the complex polarizability approach, while extending its applicability to spin-polarized open-shell systems. The implementation of the present theoretical scheme is currently ongoing

3.4 Hybrid Diagonal Approximation (HDA)

As discussed earlier, the most widely adopted formulation of TDDFT in quantum chemistry is the Casida approach. Hybrid exchange–correlation functionals such as B3LYP often yield improved excitation energies with respect to semi–local functionals. However, the use of hybrid kernels in TDDFT introduces severe numerical difficulties due to the non–local Hartree–Fock (HF) exchange operator.

With Gaussian–type orbitals (GTOs), analytic expressions for the four–center HF exchange integrals are available, making hybrid TDDFT computationally feasible. In contrast, the Slater–type orbitals (STOs) used in AMS/ADF do not have analytic solutions for products of orbitals on different centers. In this case, the HF exchange contributions must be evaluated through density fitting techniques by expanding the orbital product in an auxiliary basis. While this keeps hybrid DFT ground–state calculations tractable, the HF contribution to the TDDFT kernel becomes prohibitively expensive due to its unfavorable scaling with the number of occupied–virtual pairs.

A natural workaround could be to use a hybrid functional only at the DFT KS level, and to evaluate the TDDFT kernel within the Adiabatic Local Density Approximation (ALDA). However, this leads to a well–known inconsistency: the inclusion of HF exchange in the KS equations shifts virtual orbitals upward, whereas a full hybrid kernel would produce a compensating downward shift via the diagonal elements of the Casida matrix. Since ALDA lacks this corrective contribution, excitation energies become systematically overestimated by toolarge amount.

This imbalance is most transparent when TDDFT is written in its RPA–like form:

$$\begin{pmatrix} A & B \\ B^* & A^* \end{pmatrix} \begin{pmatrix} X \\ Y \end{pmatrix} = \omega \begin{pmatrix} I & 0 \\ 0 & -I \end{pmatrix} \begin{pmatrix} X \\ Y \end{pmatrix}, \tag{3.92}$$

For hybrid TDDFT, the matrix elements read:

$$A_{ia,jb} = \delta_{ij}\delta_{ab}(\epsilon_a - \epsilon_i) + \langle \varphi_a \varphi_j | \varphi_i \varphi_b \rangle - \alpha \langle \varphi_a \varphi_j | \varphi_b \varphi_i \rangle + (1-\alpha) \left\langle \varphi_a \left| \frac{\partial V_{\mathrm{xc}}}{\partial \rho} \varphi_j^* \varphi_b \right| \varphi_i \right\rangle, \tag{3.93}$$

$$B_{ia,jb} = \langle \varphi_a \varphi_b | \varphi_i \varphi_j \rangle - \alpha \langle \varphi_a \varphi_b | \varphi_j \varphi_i \rangle + (1-\alpha) \left\langle \varphi_a \left| \frac{\partial V_{\mathrm{xc}}}{\partial \rho} \varphi_b^* \varphi_j \right| \varphi_i \right\rangle. \tag{3.94}$$

where α is the fraction of HF exchange and ALDA is used for the last term in both equations. The diagonal elements of A highlight the origin of the problem:

$$A_{ia,ia} = (\epsilon_a - \epsilon_i) + \langle \varphi_a \varphi_i | \varphi_i \varphi_a \rangle - \alpha \langle \varphi_a \varphi_i | \varphi_a \varphi_i \rangle + (1-\alpha) \left\langle \varphi_a \left| \frac{\partial V_{\mathrm{xc}}}{\partial \rho} \varphi_i^* \varphi_a \right| \varphi_i \right\rangle. \tag{3.95}$$

The third term, arising from non–local HF exchange, provides the crucial negative shift

that counterbalances the KS overestimation of the virtual–occupied gap. If this contribution is omitted from the kernel, the imbalance between the KS reference and the response kernel leads to overly large excitation energies.

This consideration motivated the development of the *Hybrid Diagonal Approximation* (HDA) [176], introduced by the Trieste group. The central idea is to keep the HF exchange only in the expression for the diagonal elements of the A matrix, while evaluating all its off–diagonal elements and the entire B matrix at the ALDA level. This preserves the essential energetic correction while avoiding the expensive evaluation of the full HF–exchange kernel.

Under this approximation:

$$A_{ia,jb} = \delta_{ij}\delta_{ab}(\epsilon_a - \epsilon_i - \Delta_{ia}) + \langle \varphi_a \varphi_j | \varphi_i \varphi_b \rangle + \left\langle \varphi_a \left| \frac{\partial V_{\mathrm{xc}}}{\partial \rho}\, \varphi_j^* \varphi_b \right| \varphi_i \right\rangle, \tag{3.96}$$

$$B_{ia,jb} = \langle \varphi_a \varphi_b | \varphi_i \varphi_j \rangle + \left\langle \varphi_a \left| \frac{\partial V_{\mathrm{xc}}}{\partial \rho}\, \varphi_b^* \varphi_j \right| \varphi_i \right\rangle. \tag{3.97}$$

The corrective shift Δ_{ia} entering Eq. (3.96) is:

$$\Delta_{ia} = \alpha \langle \varphi_a \varphi_i | \varphi_a \varphi_i \rangle + \alpha \left\langle \varphi_a \left| \frac{\partial V_{\mathrm{xc}}}{\partial \rho}\, \varphi_i^* \varphi_a \right| \varphi_i \right\rangle, \tag{3.98}$$

where the second term is generally much smaller and often neglected in practice. With this new expression for the A and B matrices their difference is still diagonal, as it is customary for TDDFT with local kernel, so it is possible to solve the RPA-like equation and obtain the standard Casida expression for the Ω matrix. The only difference is the diagonal term Δ_{ia}

A key advantage of HDA is the dramatic reduction in computational cost: the number of HF–exchange integrals decreases from the full $(N_{\mathrm{occ}}N_{\mathrm{virt}})^2$ elements of the Casida matrix to the $N_{\mathrm{occ}}N_{\mathrm{virt}}$ diagonal terms only. Additional savings are obtained by applying an energy cutoff so that Δ_{ia} is computed only for transitions lying within the spectral region of interest.

The implementation is straightforward in both TDDFT frameworks:

- Casida formulation: all matrix elements are evaluated at ALDA level except for the diagonal elements of A, which are corrected by Δ_{ia}.

- PolTDDFT formulation: the KS energy differences $\epsilon_a - \epsilon_i$ are replaced by $(\epsilon_a - \epsilon_i - \Delta_{ia})$, which modifies the distribution of the occupied-virtual energy differences along the excitation energy axis.

Finally, HDA is a general acceleration scheme and can be effectively applied also to large hybrid TDDFT calculations in GTO-based codes, where density fitting of HF exchange may become a bottleneck for very large systems.

3.5 Efficient HDA through Resolution of the Identity (RI)

HDA reduces drastically the cost of an hybrid calculation but the numerical calcultation of the first term of equation (3.98) is still time-consuming. It is therefore highly desirable to develop a more efficient strategy for evaluating these integrals.

A viable and efficient approach is to express the two–electron integral in Eq. (3.98) as a sum of analytical integrals by exploiting the Resolution of the Identity (RI) [177, 178]. In RI-HDA, the electron density of each molecular orbital is expanded in an auxiliary basis of density–fitting functions, allowing the Coulomb interaction to be evaluated analytically even for STOs on different centers.

This idea was explored and implemented within the AMS code.

We begin by rewriting the corrective diagonal integral, noting that the KS orbitals are real-valued:

$$\langle \varphi_a \varphi_i | \varphi_a \varphi_i \rangle = \iint \frac{\varphi_a(\mathbf{r}_1)\varphi_a(\mathbf{r}_1)\,\varphi_i(\mathbf{r}_2)\varphi_i(\mathbf{r}_2)}{|\mathbf{r}_1 - \mathbf{r}_2|}\, d\mathbf{r}_1\, d\mathbf{r}_2. \tag{3.99}$$

The numerator is simply the product of the orbital densities:

$$\rho_a(\mathbf{r}_1) = \varphi_a(\mathbf{r}_1)^2, \tag{3.100}$$

$$\rho_i(\mathbf{r}_2) = \varphi_i(\mathbf{r}_2)^2. \tag{3.101}$$

Both densities can be approximated in the auxiliary fitting basis $\{f_k\}_{k=1}^{N_F}$:

$$\rho_a(\mathbf{r}_1) \approx \sum_{k=1}^{N_F} f_k(\mathbf{r}_1)\, C_{ka}, \tag{3.102}$$

$$\rho_i(\mathbf{r}_2) \approx \sum_{m=1}^{N_F} f_m(\mathbf{r}_2)\, C_{mi}. \tag{3.103}$$

Inserting these expressions into Eq. (3.99) yields

$$\langle \varphi_a \varphi_i | \varphi_a \varphi_i \rangle \approx \sum_{k=1}^{N_F} \sum_{m=1}^{N_F} C_{ka} \left[\iint \frac{f_k(\mathbf{r}_1) f_m(\mathbf{r}_2)}{|\mathbf{r}_1 - \mathbf{r}_2|} d\mathbf{r}_1 d\mathbf{r}_2 \right] C_{mi}. \tag{3.104}$$

We define the Coulomb matrix in the fitting basis:

$$V_{km} = \iint \frac{f_k(\mathbf{r}_1) f_m(\mathbf{r}_2)}{|\mathbf{r}_1 - \mathbf{r}_2|} d\mathbf{r}_1 d\mathbf{r}_2, \tag{3.105}$$

which is *analytically* computable in AMS even for STOs on different centers.

Thus,

$$\langle \varphi_a \varphi_i | \varphi_a \varphi_i \rangle \approx \sum_{k=1}^{N_F} \sum_{m=1}^{N_F} C_{ka}^{\dagger}\, V_{km}\, C_{mi}. \tag{3.106}$$

What we need now are the coefficients C_{ka}. By taking the scalar product of Eq. (3.100) with another fitting function f_p we obtain:

$$\langle f_p|\rho_a\rangle = \sum_{k=1}^{N_F}\langle f_p|f_k\rangle\, C_{ka} = \sum_{k=1}^{N_F} S^f_{pk}\, C_{ka}, \tag{3.107}$$

where S^f is the overlap matrix of the fitting basis.

For each virtual orbital φ_a we define a vector d_a with elements

$$d_{pa} = \langle f_p|\rho_a\rangle.$$

Equation (3.107) then becomes a linear system:

$$\sum_{k=1}^{N_f} S^f_{pk} C_{ka} = d_{pa},$$

whose solution is

$$C_{ka} = \sum_{k=1}^{N_f} (S^f_{kp})^{-1} d_{pa}.$$

An analogous expression holds for the occupied orbital φ_i.

Substituting these expressions for the coefficients into Eq. (3.106) gives:

$$\langle \varphi_a\varphi_i|\varphi_a\varphi_i\rangle \approx \sum_{n}^{N_f}\sum_{p}^{N_f}\sum_{k}^{N_f}\sum_{m}^{N_f} d^\dagger_{an}\,(S^f)^{-1}_{nk} V_{km} (S^f)^{-1}_{mp}\, d_{pi}. \tag{3.108}$$

It is therefore convenient to define the matrix

$$Q = (S^f)^{-1} V (S^f)^{-1}, \tag{3.109}$$

so that the diagonal correction becomes simply:

$$\langle \varphi_a\varphi_i|\varphi_a\varphi_i\rangle \approx d^\dagger_a Q\, d_i. \tag{3.110}$$

This formulation transforms a numerically expensive two–electron integral into a sequence of matrix multiplications involving precomputed analytical matrices, thus drastically reducing the cost of hybrid TDDFT calculations using the HDA scheme.

3.6 Implementation of the Efficient HDA Scheme

As discussed in Section 3.3.1, the AMS framework already computes and stores several matrices and integrals essential for the PolTDDFT implementation. These pre–existing objects can be reused to efficiently implement the HDA correction introduced in the previous section. We first describe the construction of the matrix Q, and then the evaluation of the vectors d_a and d_i entering the diagonal HDA term.

Within the PolTDDFT module of AMS, routine `CalcMatrixL.f90` defines the matrix

$$Z = (S^f)^{-1}V, \tag{3.111}$$

where S^f is the density–fitting overlap matrix and V collects the kernel–related integrals. The matrix Z is obtained by solving the linear system

$$S^f Z = V, \tag{3.112}$$

using ScaLAPACK routines designed for distributed linear algebra.

The HDA scheme requires the matrix

$$Q = Z(S^f)^{-1}. \tag{3.113}$$

To compute it we can multiply from the right by S^f

$$QS^f = Z. \tag{3.114}$$

by taking the transpose matrix and using the fact that both S^f and Q are real symmetric matrices,

$$(S^f)Q = Z^t. \tag{3.115}$$

Thus, Q is obtained as the solution of the linear system

$$S^f Q = Z^t. \tag{3.116}$$

This is formally identical to the system used to compute Z, meaning that the same numerical routines can be reused. In practice, the Z^t matrix must first be constructed and stored.

The final evaluation of Q is implemented directly inside `CalcMatrixL.f90`.

A new routine, `Calcdpadqi.f90`, has been created to evaluate the vectors d_a and d_i entering the diagonal HDA correction. The implementation closely follows that of `CalcAk.f90`, which constructs the matrices A^k used in PolTDDFT (see Section 3.3.1). The analogy emerges by comparing the definitions of the matrix elements.

The matrix A^k contains the density–fitting representation of the KS transition density:

$$A^k_{\mu,ia} = \langle f_\mu | \varphi_i(\mathbf{r})\varphi_a(\mathbf{r}) \rangle,$$

On the other hand, the HDA diagonal term requires integrals of the form:

$$d_{pa} = \langle f_p | \rho_a(\mathbf{r}) \rangle = \langle f_p | \varphi_a(\mathbf{r})\varphi_a(\mathbf{r}) \rangle.$$

Thus, the structure of d_{pa} is identical to that of $A^k_{\mu,ia}$ except for the substitution of the occupied orbital index i with the virtual orbital index a. This observation makes it possible to reuse the efficient density–fitting machinery already implemented in AMS for PolTDDFT.

By exploiting the Resolution of the Identity (RI), the numerical evaluation of the diagonal corrective term becomes a sum of analytical density–fitting integrals, dramatically accelerating the computation compared to a brute–force approach.

An additional modification concerns the normalization of the orbital densities when they are represented in the auxiliary density–fitting basis. While the exact orbital products $\varphi_i(\mathbf{r})\varphi_i(\mathbf{r})$ are properly normalized, the corresponding fitted densities obtained through the expansion over the fitting basis set do not automatically preserve this normalization. To recover the correct integral, a constraint must be imposed so that the fitted density integrates to unity.

Following the strategy adopted in the present implementation, the normalization is enforced via a standard Lagrange–multiplier approach. In matrix form, this corresponds to "bordering" the density–fitting overlap matrix S^f: an extra row and column are added, containing the normalization integrals

$$w_\mu = \int f_\mu(\mathbf{r})\, d^3r,$$

thus the overlap matrix S is augmented as

$$S \longrightarrow \begin{pmatrix} S & w \\ w^T & 0 \end{pmatrix}, \tag{3.117}$$

and each vector $d^{(p)}$ is augmented with the normalization constant (unity in this case) accordingly as

$$d^{(p)} \longrightarrow \begin{pmatrix} d^{(p)} \\ 1 \end{pmatrix}, \tag{3.118}$$

thereby enforcing the normalization condition on the fitted orbital density.

This modification stabilizes the solution of the fitting equations and ensures that the reconstructed orbital densities retain the correct integral even in the presence of numerical approximations intrinsic to the RI procedure. The usefulness of this constraint has long been recognized in the context of efficient Hartree–potential evaluation during SCF cycles, and it

is now adopted as a standard component of the PolTDDFT/HDA infrastructure.

3.7 Computational analysis tools

The analysis and interpretation of optical absorption spectra of complex systems, such as hybrid metal–organic nanostructures or ligand-protected metal clusters, often require more than the direct inspection of excitation energies and spectral intensities. In these systems, the optical response typically arises from the interplay of multiple electronic subsystems and a large number of single-particle excitations, making a straightforward assignment of spectral features difficult. For this reason, additional analysis tools are essential to rationalize the microscopic origin of the absorption spectrum and to disentangle the contributions associated with different electronic degrees of freedom.

For this purpose, PolTDDFT algorithm adopt the Modified Sternheimer Approach (MSA) formulation [179] of linear response. The first-order perturbation of the Kohn–Sham orbitals can be found as the solution of the following inhomogeneous equations:

$$\begin{aligned} \left(\hat{H}^0_{\mathrm{KS}} - \varepsilon_i - \omega\right) \phi_i^{(1,-)} &= -\hat{V}_{\mathrm{SCF}}\, \phi_i, \\ \left(\hat{H}^0_{\mathrm{KS}} - \varepsilon_i + \omega\right) \phi_i^{(1,+)\,*} &= -\hat{V}_{\mathrm{SCF}}\, \phi_i. \end{aligned} \tag{3.119}$$

and consequently, the first-order perturbed electron density can be expressed as

$$\rho^{(1)}(\mathbf{r}) = 2 \sum_{i}^{\mathrm{occ}} \phi_i(\mathbf{r}) \left[\phi_i^{(1,-)}(\mathbf{r}) + \phi_i^{(1,+)\,*}(\mathbf{r}) \right]. \tag{3.120}$$

Equations (3.119) and (3.120) are used to obtain a direct analysis in terms of one-electron excited configurations.

This is possible because, if the perturbed orbitals are expanded over the virtual Kohn–Sham orbitals, the operator in brackets in Eq. (3.119) becomes diagonal.

$$\phi_i^{(1,\pm)}(\mathbf{r}) = \sum_{a}^{\mathrm{virt}} c_i^{a\pm}\, \phi_a(\mathbf{r}), \tag{3.121}$$

Moreover $\hat{V}_{\mathrm{SCF}}$ has been already calculated from the linear system (3.51) and so, the following expressions for the expansion coefficients are obtained:

$$\begin{aligned} (\varepsilon_a - \varepsilon_i - \omega)\, c_i^{a-} &= -\langle \phi_a | \hat{V}_{\mathrm{SCF}} | \phi_i \rangle, \\ (\varepsilon_a - \varepsilon_i + \omega)\, c_i^{a+\,*} &= -\langle \phi_a | \hat{V}_{\mathrm{SCF}} | \phi_i \rangle. \end{aligned} \tag{3.122}$$

The dynamical polarizability is now written as

$$\alpha_{zz}(\omega) = 2\sum_{i}^{\text{occ}}\sum_{a}^{\text{virt}}\langle\phi_i|z|\phi_a\rangle\left(c_i^{a-} + c_i^{a+*}\right) = \sum_{i}^{\text{occ}}\sum_{a}^{\text{virt}}\langle\phi_i|z|\phi_a\rangle\, P_i^a, \tag{3.123}$$

It is convenient now to introduce the density-matrix elements (dipole amplitudes)

$$P_i^a = 2\left(c_i^{a-} + c_i^{a+*}\right) \tag{3.124}$$

The above expression for the polarizability thus becomes

$$\alpha_{zz}(\omega) = \sum_{i}^{\text{occ}}\sum_{a}^{\text{virt}}\langle\phi_i|z|\phi_a\rangle\, P_i^a \tag{3.125}$$

If we use Eq. (3.122) to derive an expression for the expansion coefficients:

$$c_i^{a-} = -\frac{\langle\phi_i|\hat{V}|\phi_a\rangle}{E_k - \omega} \quad , \quad c_i^{a+*} = -\frac{\langle\phi_i|\hat{V}|\phi_a\rangle}{E_k + \omega} \tag{3.126}$$

where, in a PolTDDFT faschion we approximated the occupied-virtual energy difference to E_k. Substituing in the expression of the density matrix and using the definition of $s_k(\omega)$, one obtains

$$\begin{aligned}
P_i^a &= 2\left(c_i^{a-} + c_i^{a+*}\right) && (3.127)\\
&= 2\left[-\frac{\langle\phi_i|\hat{V}|\phi_a\rangle}{E_k - \omega} - \frac{\langle\phi_i|\hat{V}|\phi_a\rangle}{E_k + \omega}\right] && (3.128)\\
&= 2\left[-\langle\phi_i|\hat{V}|\phi_a\rangle\frac{(E_k + \omega) + (E_k - \omega)}{E_k^2 - \omega^2}\right] && (3.129)\\
&= 2\left[-\langle\phi_i|\hat{V}|\phi_a\rangle\frac{2E_k}{E_k^2 - \omega^2}\right] && (3.130)\\
&= \frac{4E_k}{\omega^2 - E_k^2}\,\langle\phi_i|\hat{V}|\phi_a\rangle && (3.131)\\
&= s_k(\omega)\,\langle\phi_i|\hat{V}|\phi_a\rangle && (3.132)
\end{aligned}$$

Eq. (3.123) represents an expression for the polarizability analogous to eq. (3.58) and has proven to be more accurate. For this reason, in the actual implementation of the code, the spectrum is extracted from this formulation.

From an implementation point of view, exploiting already available objects, the density

matrix can be calculated as follow:

$$P_i^a = s_k(\omega) \left[\langle \phi_i | z | \phi_a \rangle + \sum_{\mu\tau} A_{ia,\mu}^{k,+} L_{\mu\tau} b_\tau \right]. \tag{3.133}$$

In the present work, two complementary analysis tools derived within the TDDFT linear-response framework are employed to investigate the absorption spectra: (i) a fragment-projection analysis of oscillator strength, and (ii) independent component maps of oscillatory strength (ICM-OS). Together, these approaches provide both a real-space and an energy-resolved description of the electronic excitations underlying the optical response.

3.7.1 Fragment-projection analysis of absorption spectra

The fragment-projection analysis [180] is aimed at clarifying the role played by different parts of a complex system in shaping its optical absorption spectrum. The basic idea consists in partitioning the system into a set of fragments and decomposing the absorption intensity according to electronic transitions occurring within or between these fragments.

According to TDDFT formalism, an excited state is described as a linear combination of one-electron excited configurations, where an electron is excited from an occupied Kohn–Sham orbital to a virtual one

$$|\Psi_K\rangle = \sum_i^{\text{occ}} \sum_a^{\text{virt}} c_i^a(K) \left| \Phi_i^a \right\rangle, \tag{3.134}$$

The $|c_i^a(K)|^2$, already tell us how much each Slater determinant Φ_i^a weight in the description of the excited state Ψ_K.

Let us now subdivide our system into chemically relevant fragments. We want to investigate, within each of these electronic configurations, at which fragment the occupied and virtual molecular orbitals involved in the corresponding transition belong to. This can be done by performing a Mulliken population analysis of the molecular orbitals. Starting from the normalization condition for a molecular orbital and expanding it over the basis set of atomic orbitals we get:

$$1 = \langle \phi_i | \phi_i \rangle = \sum_{\mu\lambda} C_{i\lambda}^+ S_{\lambda\mu} C_{\mu i} \tag{3.135}$$

$$= \sum_\mu M_{\mu i} = \sum_F \sum_{\mu \in F} M_{\mu i} \tag{3.136}$$

$$= \sum_F M_{Fi} \tag{3.137}$$

where we defined

$$M_{\mu i} = \sum_{lambda} C_{i\lambda}^+ S_{\mu\lambda} C_{\mu i} \quad , \quad M_{Fi} = \sum_{\mu \in F} M_{\mu i} \tag{3.138}$$

here F is an index running over the fragments we created.

Now, because the coefficients c_i^a are normalized too, it is possible to write

$$1 = \sum_{ia} |c_i^a|^2 \sum_F M_{Fi} \sum_G M_{Ga} = \sum_F \sum_G M_{FG} \tag{3.139}$$

where we defined

$$M_{FG} = \sum_{ia} |c_i^a|^2 M_{Fi} M_{Ga} \tag{3.140}$$

The fragment contributions of eq.3.140 are used to split the absorption spectrum.

To implement the fragment projection analysis within the complex polarizability algorithm we can compare the expressions for the diagonal elements of the complex dynamical polarizability (see eq. —) to that of the oscillator strength (witch is proportional to the imaginary part of the polarizability and to the squared modulus of the dipole transition moment between the ground and the excited states):

$$f_z(\omega) = K \sum_{ia} \mathrm{Im}\left[P_i^a\right] \, \langle \phi_i \,|\, z \,|\, \phi_a \rangle == K' \left|\langle \Psi_0 | z | \Psi_I \rangle\right|^2 = K' \, \langle \Psi_0 | z | \Psi_I \rangle \sum_{i,a} \langle i | z | a \rangle \, c_i^a \tag{3.141}$$

it appears reasonable to consider the coefficient c_i^a proportional to the density matrix elements under the condition that they must be normalized:

$$c_i^a = \frac{\mathrm{Im}\left[P_i^a\right]}{\sum_{i,a} \left|\mathrm{Im}\left[P_i^a\right]\right|^2} \tag{3.142}$$

This provides the expression for the coefficients to be used in the above equations

This fragment-projection analysis provides an intuitive and chemically meaningful interpretation of the absorption spectrum, enabling the identification of metal-centered excitations, ligand-localized transitions, and charge-transfer processes between different subsystems. While the present implementation relies on a Mulliken-based projection scheme, the general strategy is not restricted to a specific population analysis and can be extended to alternative fragmentation approaches.

3.7.2 Independent component maps of oscillatory strength

A complementary and more detailed insight into the nature of the electronic excitations contributing to the absorption spectrum is provided by Independent Component Maps of Oscillatory Strength (ICM-OS) [181]. This analysis tool allows one to resolve the absorption intensity in terms of individual single-particle excitations characterized by specific occupied and virtual molecular orbitals energy difference.

The ICM-OS approach is based on the expression of the oscillator strength as the imaginary part of the dynamical polarizability tensor

$$\alpha_{zz}(\omega) = \sum_{i}^{\text{occ}} \sum_{a}^{\text{virt}} \langle \phi_i | z | \phi_a \rangle \, P_i^a \tag{3.143}$$

Within this formulation, the absorption intensity at a given photon energy can be written as a sum of contributions involving products of dipole matrix elements and induced density-matrix elements between occupied and virtual orbitals.

In an ICM-OS plot, these individual contributions are represented as a function of the energies of the occupied (ε_i) and virtual (ε_a) orbitals involved in the excitation and the optical absorption intensity at each given energy is proportional to the integral of ICM-OS at the given energy over the $(\varepsilon_i, \varepsilon_a)$ plane. For a fixed photon energy, the resulting map highlights which regions of the occupied–virtual energy space dominate the optical response. To enhance the readability of the maps, the discrete contributions are typically broadened using a Gaussian smearing.

An important feature of ICM-OS plots is that they preserve the sign of the individual contributions, allowing one to identify constructive and destructive interference effects between different single-particle excitations. This makes the ICM-OS analysis particularly well suited for the investigation of collective excitations, such as plasmon-like modes, where the absorption intensity arises from the coherent superposition of many electronic transitions.

3.8 Extension to Electronic Circular Dichroism

The PolTDDFT formalism described in the previous chapter provides the photoabsorption spectrum by extracting it from the complex dynamical polarizability tensor. The same machinery has been extended by Baseggio et al. [182] to the simulation of electronic circular dichroism (CD) spectra. In this implementation, like in the original work of Autschbach and Ziegler [183], the dependence on the current density of the xc functionals is neglected.

For a transition from the ground state $|0\rangle$ to an excited state $|n\rangle$, we already introduced in Section 1.4 the Rosenfeld equation:

$$\text{CD}(\omega) \propto \text{Im}[\langle 0|\hat{\mu}|n\rangle \cdot \langle n|\hat{\mathbf{m}}|0\rangle] \,, \tag{3.144}$$

which defines the rotatory strength as

$$R_{0n} = \text{Im}[\langle 0|\hat{\mu}|n\rangle \cdot \langle n|\hat{\mathbf{m}}|0\rangle] \,. \tag{3.145}$$

Within the complex–polarizability framework, the CD response is extracted from the

optical rotation tensor $\beta(\omega)$, which appears in the expression of the dipole moment induced by an electromagnetic field

$$\mu_u^{'} = \sum_v \alpha_{uv}(\omega)\, E_v - \sum_v \beta_{uv}(\omega)\, \frac{1}{c} \frac{\partial B_v}{\partial t}, \tag{3.146}$$

where $\alpha(\omega)$ is the dynamical polarizability tensor, E_v and B_v are the electric and magnetic field components, and c is the speed of light. $\beta(\omega)$ is related to the rotatory strengths via the sum–over–states relation

$$\bar{\beta}(\omega) = \frac{2c}{3} \sum_n \frac{R_{0n}}{\omega_{0n}^2 - \omega^2}. \tag{3.147}$$

where ω is the photon energy and ω_{0n} corresponds to the excitation energy from the ground state to the n-th excited state.

In the PolTDDFT implementation, following the same MSA [179] adopted for the conventional photoabsorption spectrum, the $\beta_{zz}(\omega)$ component can be written as

$$\beta_{zz}(\omega) = -\frac{i\,c}{\omega} \sum_i^{\text{occ}} \sum_a^{\text{virt}} \langle \varphi_i | \hat{m}_z | \varphi_a \rangle\, \overline{P}_i^a(\omega), \tag{3.148}$$

where $\langle \varphi_i | \hat{m}_z | \varphi_a \rangle$ are the magnetic dipole moments and $P_i^a(\omega)$ are expressed as:

$$\overline{P}_i^a = t_k(\omega) \left[\langle \phi_a | \mu_z | \phi_i \rangle + \sum_{\mu\tau}^{\text{fit}} \left(A^k \right)_{ia,\mu}^{+} L_{\mu\tau}\, b_\tau \right]$$

here we recognise many objects we already calculated for the simulation of the absorption spectrum: A^k and L matrices, the electric dipole moments $\langle \phi_a | \mu_z | \phi_i \rangle$ and b_τ coefficients solutions of the linear system $\left[S - M(\omega) \right] b = d$.

The only new objects needed for the evaluation of the optical rotation tensor are therefore:

- the magnetic dipole moments $\langle \varphi_i | \hat{m}_z | \varphi_a \rangle$
- the frequency-dependent coefficients $t_k(\omega)$ (analogous to the $s_k(\omega)$ coefficients from photoabsorption)

$$t_k(\omega) = \frac{1}{\omega - \omega_{0n} + i\varepsilon} + \frac{1}{\omega + \omega_{0n} + i\varepsilon}$$

As a consequence, the evaluation of $\beta(\omega)$ is achieved at essentially no additional computational cost, since it only requires post-processing the frequency-domain response already available from the photoabsorption calculation.

Finally the expression of the rotatory strength as calculated with the complex polarizability algorithm is

$$R = \frac{3\varepsilon\omega}{2c}\, \mathrm{Im}\left(\bar{\beta}\right) \tag{3.149}$$

where ω is the photon energy, c is the speed of light, ε is the HWHM of the electronic transition, which corresponds to the imaginary part of the frequency, and $\bar{\beta}$ stands for the averaged optical rotation tensor.

The ECD response obtained with the PolTDDFT algorithm can be interpreted and rationalised in terms of Independent Component Maps of Rotatory Strength (ICM-RS) [184] and Fragment-projection analysis [105] in an analogous way to what we did for conventional photoabsorption.

4 Publications

Optical absorption spectroscopy is a powerful and widely used tool to probe the electronic structure of molecular and nanoscale systems. In this context, time-dependent density functional theory (TDDFT) represents one of the most successful theoretical frameworks, offering a favorable compromise between accuracy and computational cost. However, achieving quantitative accuracy for complex systems often requires the use of hybrid exchange–correlation functionals, whose application at the TDDFT level remains computationally demanding, especially for large systems described with non-Gaussian basis sets.

The main focus of my research work during this PhD was to address this limitation by efficiently treating the hybrid exchange by combining the Hybrid Diagonal Approximation (HDA) with the Resolution of Identity (RI) technique. The following three papers described the method, its implementation, its accuracy and extension to include different kind of hybrid functionals.

4.1 Main Publications

4.1.1 A Resolution of Identity Technique to Speed up TDDFT with Hybrid Functionals: Implementation and Application to the Magic Cluster Series $Au_{8n+4}(SC_6H_5)_{4n+8}(n = 3 - 6)$

In this first work the RI approach is employed to avoid the numerical evaluation of the diagonal nonlocal exchange contributions, which constituted the main bottleneck of earlier HDA implementations. The method is implemented within the polTDDFT framework, a damped linear-response formulation particularly well suited for large-scale applications, as available in the AMS/ADF software package.

The resulting approach retains the accuracy of hybrid TDDFT while dramatically reducing the computational cost, yielding speedups of approximately one order of magnitude compared to previous numerical schemes. The performance and reliability of the method are assessed through a systematic comparison with experimental photoabsorption spectra of ligand-protected gold clusters, as well as with more approximate TDDFT-based methods. Overall, the proposed RI-accelerated HDA scheme provides an efficient and predictive strategy for the simulation of optical spectra of metal clusters comprising several hundreds of atoms.

THE JOURNAL OF PHYSICAL CHEMISTRY A
A JOURNAL OF THE AMERICAN CHEMICAL SOCIETY

Open Access
This article is licensed under CC-BY 4.0

pubs.acs.org/JPCA
Article

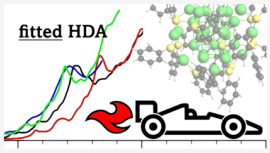
A Resolution of Identity Technique to Speed up TDDFT with Hybrid Functionals: Implementation and Application to the Magic Cluster Series $Au_{8n+4}(SC_6H_5)_{4n+8}$ (n = 3−6)

Pierpaolo D'Antoni, Marco Medves, Daniele Toffoli, Alessandro Fortunelli, Mauro Stener,* and Lucas Visscher*

Cite This: J. Phys. Chem. A 2023, 127, 9244−9257
Read Online

ACCESS | Metrics & More | Article Recommendations | Supporting Information

ABSTRACT: The Resolution of Identity (RI) technique has been employed to speed up the use of hybrid exchange-correlation (xc) functionals at the TDDFT level using the Hybrid Diagonal Approximation. The RI has been implemented within the polTDDFT algorithm (a complex damped polarization method) in the AMS/ADF suite of programs. A speedup factor of 30 has been obtained with respect to a previous numerical implementation, albeit with the same level of accuracy. Comparison of TDDFT simulations with the experimental photoabsorption spectra of the cluster series $Au_{8n+4}(SR)_{4n+8}$(n = 3−6; R = C_6H_5) showed the excellent accuracy and efficiency of the method. Results were compared with those obtained via the more simplified and computationally cheaper TDDFT+TB and sTDDFT methods. The present method represents an accurate as well as computationally affordable approach to predict photoabsorption spectra of complex species, realizing an optimal compromise between accuracy and computational efficiency, and is suitable for applications to large metal clusters with sizes up to several hundreds of atoms.



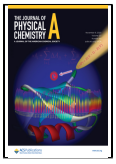
1. INTRODUCTION

Optical spectroscopies are among the most powerful investigation techniques in chemistry due to their direct applicability, easily accessible instrumentation, and ability to provide relevant information regarding the electronic structure of the studied system. However, it is often difficult to rationalize and assign the observed spectral features on the basis of purely experimental information. The availability of reliable models and accurate computational protocols therefore represents a formidable tool not only to rationalize the experiment but also to extract all the information, which is actually included in the experimental data but cannot be understood by a simple analysis of the spectrum.[1] Moreover, if the computational protocol is able to reach quantitative accuracy, theory can be predictive, thus opening the way to the rational design, for example, of new materials with a required optical response. In this scenario, the best compromise between accuracy and computational economy is often the time-dependent density functional theory (TDDFT), which at the moment allows the calculation of systems containing up to 1000 of atoms. In quantum chemistry, the most popular implementation of TDDFT has been formulated by Casida.[2] In the Casida formulation, an eigenvalue equation on the space of single-particle excitations, whose number is the product between the number of occupied and unoccupied orbitals, is solved. Besides the Casida approach, other TDDFT formulations and implementations are available.[3−11] More recently, a complex polarizability algorithm for TDDFT[12−14] (also known as polTDDFT) has proven particularly suitable for application to very large systems and will be employed also in the present work.[15]

In both DFT and TDDFT, accuracy represents a challenging issue, since it is intimately connected with the choice of the exchange-correlation (xc) functional in DFT to solve Kohn−Sham equations, and in the response kernel of TDDFT when solving the TDDFT equations.[16] The search for more and more accurate xc functionals and kernels is a very active, widely spread, and highly demanded research activity.[17,18] Hybrid xc functionals for DFT and hybrid kernels for TDDFT, i.e., functionals containing a variable fraction of the exact (Hartree−Fock, HF) nonlocal exchange, often represent the best choice in terms of accuracy, at least with respect to simpler local density approximation (LDA) and generalized gradient approximation (GGA). Among hybrid xc functionals, B3LYP[19,20] is the most popular.

It is worth noting that in hybrid functionals, the HF nonlocal exchange can be problematic to handle when evaluating the matrix elements needed for the Casida equations. More precisely, matrix elements can be treated efficiently when Gaussian-type orbital (GTO) basis sets are employed but become problematic with other basis sets, such as slater-type

Received: August 8, 2023
Revised: October 6, 2023
Accepted: October 9, 2023
Published: October 31, 2023



Downloaded via UNIVERSITA STUDI TRIESTE on September 30, 2025 at 09:06:04 (UTC).
See https://pubs.acs.org/sharingguidelines for options on how to legitimately share published articles.

ACS Publications
© 2023 The Authors. Published by American Chemical Society

https://doi.org/10.1021/acs.jpca.3c05368
J. Phys. Chem. A 2023, 127, 9244−9257

orbitals (STO) or plane waves (PW). To solve these technical issues and get a still efficient TDDFT approach employing hybrid xc functionals, recently a new approximate scheme has been suggested for the TDDFT kernel, called Hybrid Diagonal Approximation (HDA).[21] The HDA consists in employing the nonlocal exchange only for the diagonal terms in the response equations: this allows one to limit the computational cost of the TDDFT simulation while keeping almost the same accuracy as in the full TDDFT scheme using hybrid xc functionals.

The first HDA implementation, although much more efficient than the full-kernel one, was not fully optimized since the integrals needed to calculate the diagonal correction were calculated numerically. In the present work, we describe a much more efficient computational scheme to calculate such terms according to a procedure that avoids the numerical integration, by means of a density fitting auxiliary basis set and the Resolution of Identity (RI) technique. It is worth noting that auxiliary Gaussian−Hermite functions (named GEN-An GEN-An*)[22] have proven to be generally useful as fitting functions; in fact, the same set is able to fit (1) the SCF Coulomb potential, (2) the SCF nonlocal exchange for hybrid functionals, and (3) the TDDFT-perturbed density.[23−26] Use of STO functions for fitting is typically combined with the pair-fitting approximation[27,28] since global fitting requires evaluation of three-center integrals for which for STOs, in contrast to GTOs, no analytical expressions are available.

In general, the RI technique has been introduced in modern quantum chemistry methods roughly 50 years ago in DFT[27] and much later it started to be routinely employed in wave function theory (WFT) methods as well.[25,26,29−34] In the RI approach, integrals are either approximated by a predetermined fit set or by an on-the-fly factorization procedure such as Cholesky decomposition.[35] This reduces the computational scaling of computing multicenter integral contributions from a formal n^4 to n^3 or even lower depending on the approximations and distance screening techniques that are used. In the present work, since STO basis sets are employed, RI allows to avoid the numerical integration, which proved to be the bottleneck of the previous HDA implementation.[21]

The article is organized as follows. First we provide a short review of the HDA approximation in both the Casida and polTDDFT implementation. Then, we give the details of the RI method to calculate the HDA integrals as well as its implementation within the AMS-ADF program. In order to assess the performances of the method, we applied it to a series of four well-characterized gold clusters protected by aromatic thiolic ligands, with sizes between 268 and 460 atoms.[36] Finally, a complete assessment of the RI method is given in terms of accuracy and computational efficiency, with respect to the numerical approach. A comparison with respect to photoabsorption experimental data as well as to the more approximate sTDDFT[7] and TDDFT+TB[37] approaches allows to assess the merits of the suggested approach.

2. THEORETICAL METHOD AND IMPLEMENTATION

2.1. HDA. In order to briefly recall the HDA scheme,[21] the most convenient way is to start with the random phase approximation (RPA) formulation of the linear response TDDFT approach:

$$\begin{pmatrix} A & B \\ B^* & A^* \end{pmatrix}\begin{pmatrix} X \\ Y \end{pmatrix} = \omega\begin{pmatrix} 1 & 0 \\ 0 & -1 \end{pmatrix}\begin{pmatrix} X \\ Y \end{pmatrix} \tag{1}$$

where the submatrices A and B take the following general form for hybrid kernels:

$$A_{ia,jb} = \delta_{ij}\delta_{ab}(\varepsilon_a - \varepsilon_i) + \langle aj|ib\rangle - \alpha\langle aj|bi\rangle + (1-\alpha)\langle a|\frac{\partial V_{XC}}{\partial\rho}j^*b|i\rangle \tag{2}$$

$$B_{ia,jb} = \langle ab|ij\rangle - \alpha\langle ab|ji\rangle + (1-\alpha)\langle a|\frac{\partial V_{XC}}{\partial\rho}b^*j|i\rangle \tag{3}$$

where in equations 2 and 3, we employ i and j for occupied orbitals and a and b for the virtual ones. α represents the fraction of nonlocal HF exchange in the xc kernel, and the adiabatic local density approximation (ALDA) is assumed in the last terms of both equations. With STOs, it is very time-consuming to calculate the terms with the nonlocal exchange, namely, the third term in the rhs of equation 2 and the second term in the rhs of equation 3.

Now let us consider the diagonal elements of the RPA matrix, which correspond to the diagonal elements of matrix A:

$$A_{ia,ia} = (\varepsilon_a - \varepsilon_i) + \langle ai|ia\rangle - \alpha\langle ai|ai\rangle + (1-\alpha)\langle a|\frac{\partial V_{XC}}{\partial\rho}i^*a|i\rangle \tag{4}$$

The third element in the right-hand side of equation 4 is the key ingredient to recover the too high occupied-virtual energy difference obtained from the KS equation when a hybrid xc functional, containing a fraction of HF exchange, is used. This simple observation suggests that a possible strategy is to employ the nonlocal HF exchange of the kernel only for the diagonal elements of the A matrix, while treating at the simpler ALDA level (no HF exchange) all the off-diagonal elements of the A matrix and the full B matrix. With this choice, which we named HDA,[21] the matrices A and B take the following equations:

$$A_{ia,jb} = \delta_{ij}\delta_{ab}(\varepsilon_a - \varepsilon_i - \Delta_{ia}) + \langle aj|ib\rangle + \langle a|\frac{\partial V_{XC}}{\partial\rho}j^*b|i\rangle \tag{5}$$

$$B_{ia,jb} = \langle ab|ij\rangle + \langle a|\frac{\partial V_{XC}}{\partial\rho}b^*j|i\rangle \tag{6}$$

where in eq 5, we have introduced a diagonal corrective term:

$$\Delta_{ia} = \alpha\langle ai|ai\rangle + \alpha\langle a|\frac{\partial V_{XC}}{\partial\rho}i^*a|i\rangle \tag{7}$$

In eq 7, the second term is much smaller than the first term and can be safely neglected. With eq 5 and eq 6 for the A and B matrices, the difference $A-B$ is still diagonal as it is customary in TDDFT with local kernels. Therefore, it becomes possible to solve the RPA-like equation with respect to Y and obtain again the conventional Casida equation for the Ω matrix, with the only difference occurring in the eigenvalue differences, which must be corrected by eq 7.

Importantly, following this approach, the number of required exchange integrals is only (Nocc × Nvirt) instead of (Nocc × Nvirt)^2, i.e., it is greatly reduced. In the previous

https://doi.org/10.1021/acs.jpca.3c05368
J. Phys. Chem. A 2023, 127, 9244−9257

implementations of eq 7, the first term was calculated numerically while the second term is neglected.

2.2. Extension of HDA to the Complex Polarizability TDDFT Formulation. Despite the efficiency of numerical diagonalization techniques such as the Davidson one, it becomes hard to calculate valence photoabsorption spectra over a wide excitation energy range when large systems are considered. The Davidson iterative algorithm, generally employed in all the TDDFT codes that use the Casida method, is efficient on large Ω matrices but is limited to extracting a relatively small number of lowest eigenvalues and eigenvectors. In order to overcome this problem, we have recently proposed the complex polarizability TDDFT (polTDDFT) algorithm.[12] This approach avoids the diagonalization bottleneck via a direct solution of the response equations and thereby allows for the treatment of very large systems. The reader is referred to the original work for a detailed description of the algorithm,[12] together with its implementation in the ADF program.[13]

In polTDDFT, the photoabsorption spectrum $\sigma(\omega)$ is discretized and computed in a limited number of points from the imaginary part of the dynamical polarizability $\alpha(\omega)$:

$$\sigma(\omega) = \frac{4\pi\omega}{c}\mathrm{Im}[\alpha(\omega)] \tag{8}$$

The polarizability is calculated for complex frequencies, i.e., $\omega = \omega_r + i\omega_i$, where the real part ω_r is the scanned photon frequency (energy) and ω_i is the imaginary part, which corresponds to a broadening of the discrete lines and can be interpreted as a pragmatic inclusion of the excited-state finite lifetime. The complex dynamical polarizability is calculated by solving the following nonhomogeneous linear system:

$$[\mathbf{S} - \mathbf{M}(\omega)]\mathbf{b} = \mathbf{d} \tag{9}$$

In eq 9, $\mathbf{S}$ is the overlap matrix between fitting functions, $\mathbf{b}$ is the unknown vector with the expansion coefficients $b_\mu(\omega)$ of the induced density $\rho_z^{(1)}$, $\mathbf{d}$ is the frequency-dependent vector corresponding to the known nonhomogeneous term, and finally the elements of the frequency-dependent matrix $\mathbf{M}$ are

$$M_{\mu\nu} = \langle f_\mu | \chi_{\mathrm{KS}}(\omega) K | f_\nu \rangle \tag{10}$$

In eq 10, χ_{KS} refers to the Kohn−Sham frequency-dependent dielectric susceptibility and K to the kernel. The original characteristic of the polTDDFT method is the introduction of a simple approximation, which enables the construction of $\mathbf{M}(\omega)$ as a linear combination of *frequency-independent* matrices $\mathbf{G}^k$ with frequency-dependent coefficients $s_k(\omega)$, with the following equation:

$$\mathbf{M}(\omega) = \sum_k s_k(\omega)\mathbf{G}^k \tag{11}$$

With this idea, a set of matrices $\{\mathbf{G}^k\}$ is calculated and stored only once at the beginning and then the matrix $\mathbf{M}(\omega)$ is calculated very rapidly at each photon energy ω, as a linear combination of the $\{\mathbf{G}^k\}$ matrices with the following coefficients:

$$s_k(\omega) = \frac{4\overline{E}_k}{\omega^2 - \overline{E}_k^2} \tag{12}$$

where in equation 12, $\overline{E}_k$ refers to the center of the interval, which discretizes the excitation energy variable and in the original formulation corresponds to the difference between virtual and occupied orbital energies: $\varepsilon_a - \varepsilon_i$.

In order to apply within the polTDDFT algorithm the HDA approach already discussed for the RPA procedure, it is sufficient to correct the orbital energy differences with the same correction term (7) as already done for equation 5: $\varepsilon_a - \varepsilon_i - \Delta_{ia}$.

2.3. Resolution of Identity implementation (Fitted HDA). As mentioned in the previous section, in the previous HDA implementation, the first term of the diagonal correction (7) was calculated numerically, which is accurate but still time-consuming although much less demanding than the complete nonlocal kernel. Finding a cheaper way to get equation 7 that avoids the time-consuming numerical integration is therefore desirable. We can do so by expressing the two-electron integral of eq 7 as a sum of analytical integrals through the RI technique in which the density of each molecular orbital is expressed as a linear combination of auxiliary density fitting functions. We start by rewriting the corrective diagonal integral as follows, taking into account that the molecular orbitals are real so that complex conjugation of the bra functions can be omitted:

$$\langle ai|ai\rangle = \iint \frac{\phi_a(\vec{r}_1)\phi_a(\vec{r}_1)\phi_i(\vec{r}_2)\phi_i(\vec{r}_2)}{|\vec{r}_1 - \vec{r}_2|}\mathrm{d}\vec{r}_1\mathrm{d}\vec{r}_2 \tag{13}$$

The numerator of the integrand is just the product of the electron densities of orbitals ϕ_a and ϕ_i:

$$\rho_a(\vec{r}_1) = \phi_a(\vec{r}_1)\phi_a(\vec{r}_1) \tag{14}$$

$$\rho_i(\vec{r}_2) = \phi_i(\vec{r}_2)\phi_i(\vec{r}_2) \tag{15}$$

Both densities can be approximated as a sum of density fit functions as

$$\rho_a(\vec{r}_1) \cong \sum_{k=1}^{N_F} f_k(\vec{r}_1)C_{ka}\rho_i(\vec{r}_2) \cong \sum_{m=1}^{N_F} f_m(\vec{r}_2)C_{mi} \tag{16}$$

Using the above equations to rewrite eq 13, we get:

$$\langle ai|ai\rangle \cong \sum_{k=1}^{N_F}\sum_{m=1}^{N_F}\iint \frac{f_k(\vec{r}_1)C_{ka}f_m(\vec{r}_2)C_{mi}}{|\vec{r}_1 - \vec{r}_2|}\mathrm{d}\vec{r}_1\mathrm{d}\vec{r}_2 \tag{17}$$

For convenience, we define a matrix F, with dimension of the auxiliary density fitting basis set, whose elements are

$$F_{km} = \iint \frac{f_k(\vec{r}_1)f_m(\vec{r}_2)}{|\vec{r}_1 - \vec{r}_2|}\mathrm{d}\vec{r}_1\mathrm{d}\vec{r}_2 \tag{18}$$

The key step feature of this RI approach is that an analytical expression can be found for the integral (18) even for STO functions located at different centers. After computing F, the corrective diagonal integrals can be easily calculated via the matrix transform:

$$\langle ai|ai\rangle \cong \sum_{k=1}^{N_F}\sum_{m=1}^{N_F} C_{ak}^{+}F_{km}C_{mi} \tag{19}$$

once the C coefficients have been determined. These follow from the projection of the orbital density $\rho_a(\vec{r}_1)$ on the set of fit functions f_p:

$$\langle f_p|\rho_a\rangle = \sum_{k=1}^{N_F}\langle f_p|f_k\rangle C_{ka} = \sum_{k=1}^{N_F} S_{pk}^{\mathrm{f}}C_{ka} = d_{pa} \tag{20}$$

where S^{f} is the overlap matrix between fitting functions pairs. In this work, we follow the standard choice of using the overlap metric in the determination of fit coefficients; an alternative is to use robust fitting in which the Coulomb metric is used to

https://doi.org/10.1021/acs.jpca.3c05368
J. Phys. Chem. A 2023, 127, 9244−9257

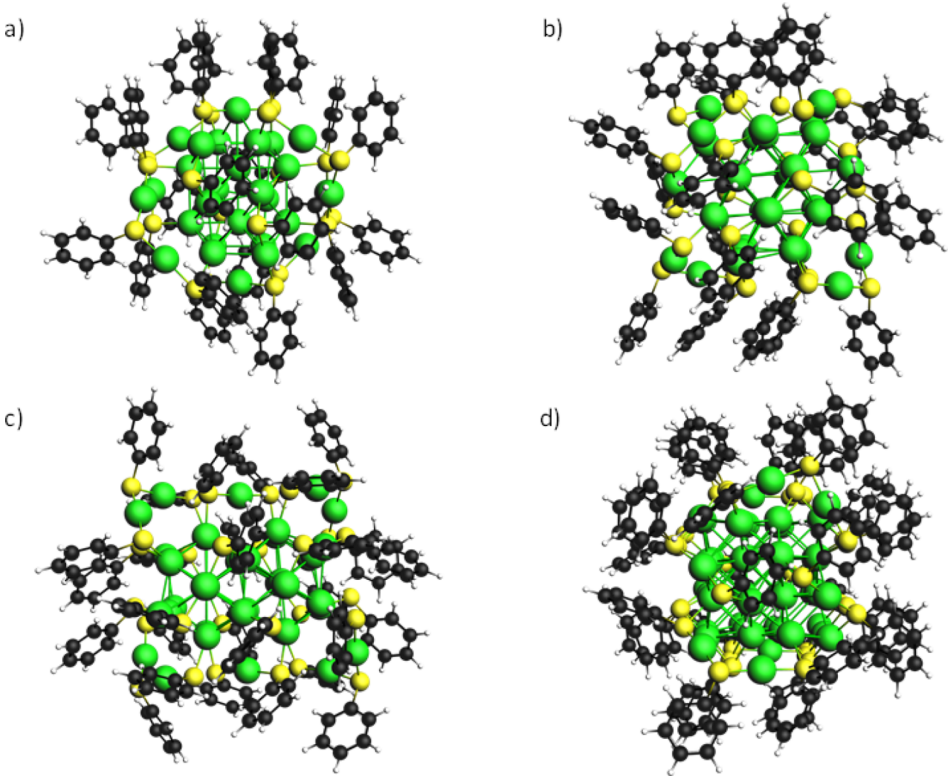


Figure 1. Cluster series experimental geometries with simplified ligands: (a) $Au_{28}(SC_6H_5)_{20}$, (b) $Au_{36}(SC_6H_5)_{24}$, (c) $Au_{44}(SC_6H_5)_{28}$, and (d) $Au_{52}(SC_6H_5)_{32}$.

define the scalar product $\langle f_p \mid \rho_a \rangle$. An extensive discussion of different fit procedures for STOs and their accuracy can be found in ref 28. Solving the linear set of eq 20 yields the fit coefficients for the virtual orbital densities, and a similar procedure is followed for the occupied orbitals φ_i as well. We have

$$\sum_{n=1}^{N_F} (S^f)^{-1}_{kn} d_{na} = C_{ka}, \sum_{p=1}^{N_F} (S^f)^{-1}_{mp} d_{pi} = C_{mi} \tag{21}$$

so that we can rewrite eq 19:

$$\langle ai|ai\rangle \cong \sum_{n=1}^{N_F} \sum_{p=1}^{N_F} \sum_{k=1}^{N_F} \sum_{m=1}^{N_F} d^{\dagger}_{an} (S^f)^{-1}_{nk} F_{km} (S^f)^{-1}_{mp} d_{pi} \tag{22}$$

The RI approach makes it possible to build and store a new matrix Q, to also include the second correction term of equation 7, which was neglected in the previous numerical implementation. In Section 4.1, we analyze the effect of the second term, which actually gives negligible contribution, justifying the previous choice, in the numerical implementation of HDA, to neglect this term. In fact, now it can be easily included since the matrix of the ALDA kernel over the auxiliary density fitting basis is already available since is needed by the polTDDFT (see matrix **Z** in ref 12):

$$\mathbf{Q} = (\mathbf{S}^f)^{-1}(\mathbf{F} + \mathbf{Z})(\mathbf{S}^f)^{-1} \tag{23}$$

Finally, the correction for the diagonal term is obtained as

$$\langle ai|ai\rangle + \langle a|\frac{\partial V_{XC}}{\partial \rho} i^* a|i\rangle \cong \boldsymbol{d}_a^{+} \mathbf{Q} \boldsymbol{d}_i \tag{24}$$

2.4. Implementation of Efficient HDA. In the AMS implementation, many of the required matrices and integrals needed for this purpose are already available. We first consider the calculation of the Q matrix. The auxiliary **L** matrix is defined as

$$\boldsymbol{L} = (\boldsymbol{S}^f)^{-1}(\boldsymbol{F} + \boldsymbol{Z}) \tag{25}$$

and computed, taking advantage of Scalable Linear Algebra PACKage (ScaLAPACK), by solving the following linear system

$$\boldsymbol{S}^f \boldsymbol{L} = \boldsymbol{F} + \boldsymbol{Z} \tag{26}$$

Thus, taking advantage of the already existing **L** and **S** matrices, we can express **Q** as

$$\mathbf{Q} = \boldsymbol{L}(\boldsymbol{S}^f)^{-1} \tag{27}$$

To compute it, we can multiply the above equation by $\boldsymbol{S}^f$ on the right side and then take the transpose of both sides. Then, considering that both **Q** and **S** are real symmetric matrices, we thus obtain the following linear system whose formal solution is the **Q** matrix; to solve it, we just use the same routines used before in the code to obtain the **L** matrix.

$$\boldsymbol{S}^f \mathbf{Q} = \boldsymbol{L}^t \tag{28}$$

This implementation could be realized directly inside a pre-existing (CalcMatrixL.f90) subroutine. We needed to transpose and store the **L** matrix. Regarding the calculation of d_a and d_i vectors, this is done in a new, appositely created, routine. This new routine has been built starting from an already existent one, which calculates the integrals between a fit function and a product of a pair of occupied−virtual molecular orbitals. This was modified, changing the occupied−virtual products with occupied−occupied and virtual−virtual products.

https://doi.org/10.1021/acs.jpca.3c05368
J. Phys. Chem. A 2023, 127, 9244−9257

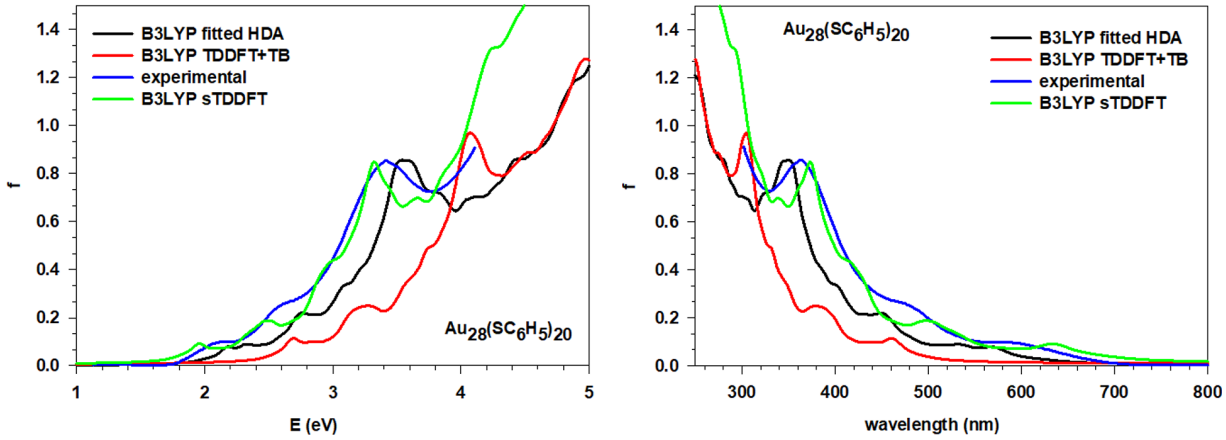


Figure 2. Comparison of the experiment with the simulated spectra using fitted HDA, sTDDFT, and TDDFT+TB for the $Au_{28}(SC_6H_5)_{20}$ cluster, both energy (eV), above, and wavelength (nm), below, plots are reported.

Regarding the representation of the matrices, the matrices of the polTDDFT method (eqs 9-12) are in the density fitting basis as well as matrix F (eq 18) as well as the matrices in eqs 25-28. The RPA matrices are well-known and are in the basis of the MO products occupied*virtual (the so-called 1h1p space in the Configuration Interaction method).

As an outcome of this section, we conclude that we have been able to exploit in AMS the efficient RI technique and convert the numerical calculation of diagonal corrective term (eq 7) to a sum of analytical integrals.

3. COMPUTATIONAL DETAILS

All the DFT KS calculations reported in this work were performed employing a TZP basis of STO functions (included in the ADF database) and the B3LYP hybrid xc functional.[19,20] The auxiliary density fitting basis STO functions are taken from the POLTDDFT basis set database included in the AMS program.[38] The TDDFT calculations were performed with the polTDDFT algorithm.[12,13] The HDA-B3LYP density functional approxiamtion[21] is the only available scheme for hybrid functional within polTDDFT. The HDA has been implemented by exploiting the parallelization at the general Message Passing Interface (MPI) level. The imaginary part of the photon energy (see ω_i after eq 8) has been set to 0.075 eV during the calculation of the polTDDFT spectra. All of the calculations were performed with a local version of the ADF code, which will be distributed in a forthcoming ADF release. The calculations for the gold cluster in Section 4 were performed employing the zero-order regular approximation (ZORA)[39] in order to include relativistic effects at the scalar level. In order to have a comparison with an alternative, much cheaper computational scheme, we have also performed sTDDFT[7] and TDDFT+TB calculations[37] on the same metal clusters. All the calculations have been performed on an HPE ProLiant DL580 Gen10 server (with four processors each with an 18-core Intel Xeon Gold 6140 CPU at 2.30 GHz, in total 72 cores and 728 GB of RAM), on which the present calculations were run using 24 cores. The coordinates of the clusters were taken from the experiment, but ligands have been simplified to benzene thiol instead of *tert*-butylbenzene thiol. The coordinates of the four clusters are reported in Tables S1 and S4 of the Supporting Information.

4. RESULTS AND DISCUSSION

In order to test the performance and assess the accuracy of the RI-fitted HDA algorithm, the photoabsorption spectra of a gold cluster series[36] have been simulated and compared with the available experimental data. Moreover, the results obtained with the new RI algorithm were also compared with those simulated using the already available numerical-integration HDA,[21] the sTDDFT,[7] and the more simplified and cheaper TDDFT+TB[37] methods. This cluster series is of particular interest because it represents a typical "magic series" with formula $Au_{8n+4}(SR)_{4n+8}$(n = 3−6; R = C_6H_5). Figure 1 shows the geometries of the clusters, which were taken from the X-ray diffraction experiment[36] but have been simplified using benzene instead of *tert*-butylbenzene residues in the thiols. This simplification has no impact on the photoabsorption spectra and allows to lighten the computational cost of the simulation, as proved by previous work.[40] Moreover, the same simplification of the ligands has been already employed previously to simulate the same magic series.[41]

From Figure 1, it is possible to appreciate how the organic layer tends to reduce its conformational energy by maximizing the stabilizing interactions; for example, phenyl groups are disposed face to face to allow the $\pi-\pi$ stacking interaction between delocalized aromatic electrons.

4.1. $Au_{28}(SC_6H_5)_{20}$. In the following, we will focus on the smaller cluster of this series, $Au_{28}(SC_6H_5)_{20}$. The comparison between the experimental and the simulated spectra, obtained using fitted HDA, TDDFT+TB, and sTDDFT schemes, for this cluster is reported in Figure 2. It is clear that fitted HDA is able to reproduce very nicely the experimental data on the whole energy range available (up to 4.25 eV). In particular, the strong peak at 3.4 eV of the experiment is well reproduced by the fitted HDA scheme with a limited overestimation in the excitation energy of only 0.14 eV. The performance is similar for the other spectral features, which are less intense and occur at lower energy values: their excitation energies and relative intensities with respect to the experiment are also nicely reproduced. On the other hand, the TDDFT+TB method reproduces correctly the spectral shape but yields strong overestimation of the excitation energy, by almost 1 eV. It is worth noting, however, that above 4 eV the TDDFT+TB and fitted HDA profile are in excellent match. This suggests that TDDFT+TB is able to reproduce correctly the high energy part of the spectrum, a spectral region in which the ligands play

https://doi.org/10.1021/acs.jpca.3c05368
J. Phys. Chem. A 2023, 127, 9244−9257

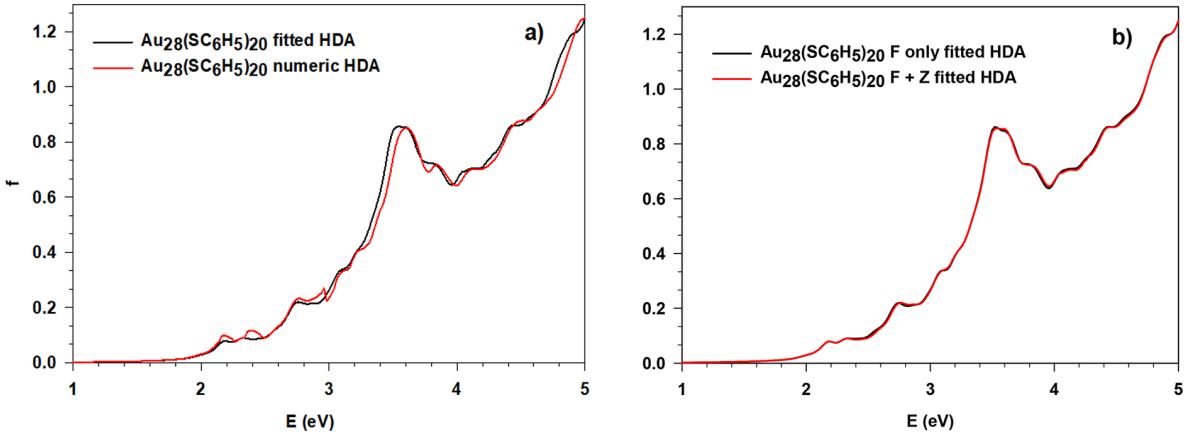


Figure 3. Comparison of the photoabsorption spectra for the $Au_{28}(SC_6H_5)_{20}$ cluster with polTDDFT. (a) Numeric HDA and new fitted HDA. (b) New fitted HDA with only *F* and complete *F*+*Z* kernel (see eq 23).

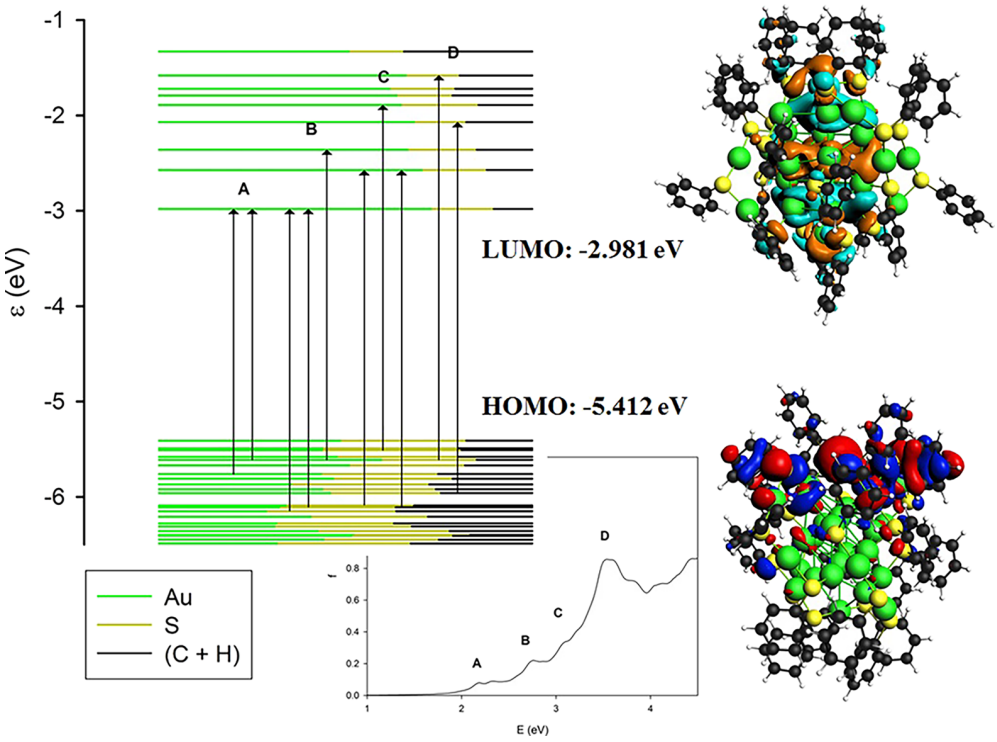


Figure 4. On the left, the molecular orbital energy plot for the $Au_{28}(SC_6H_5)_{20}$ cluster with arrows indicating the major transitions involved in each spectral feature (A, B, C, and D), on the right, HOMO and LUMO energies, and orbital plots. The contribution of different fragments (the metal core of Au atoms, the ligand's polar heads S, and their spacers C+H) to each molecular orbital considered is depicted through the ratio of the associated colors.

a major role. At lower energies, where the metal excitations dominate, the tight-binding approximation is not as good and the more accurate fitted HDA scheme performs much better with a predictive quantitative accuracy. On the other hand, the sTDDFT scheme is in fairly nice agreement with the experiment, with an accuracy superior to that of the fitted HDA with regard to the shape of the profile reported in Figure 2. The energy of the maximum of the experimental absorption falls at 3.43 eV, while it is calculated at 3.32 and 3.56 eV with sTDDFT and fitted HDA, respectively, with a discrepancy around 0.1 eV for both methods.

The accuracy of numeric HDA has been already tested in a previous work[21] so, to demonstrate the benefit of using the new fitted approach in HDA, in terms of both accuracy and computational economy, the numeric HDA calculation for this smallest cluster has been performed as well. The spectra obtained with the two different approaches to HDA are reported in Figure 3a, and it is clear how both methods lead to the same simulated spectrum with negligible differences. We employed this cluster also to verify if the approximation previously introduced in the numerical HDA, namely, to neglect the fraction of the XC ALDA kernel in the diagonal correction, is justified. With the fitted HDA, this task is trivial; it consists of using only the *F* matrix instead of *F*+*Z* in eq 23. The comparison is reported in Figure 3b, and the two profiles

https://doi.org/10.1021/acs.jpca.3c05368
J. Phys. Chem. A 2023, 127, 9244−9257

Table 1. Principal Contributions in Terms of One-Electron Excited Configurations to the Main Spectral Features of $Au_{28}(SC_6H_5)_{20}$ Calculated at PolTDDFT Level with the B3LYP XC Functional and TZP Basis Set and Using Fitted HDA

excitation	excitation E (eV)	f	assignment
A	2.34	0.0898	62.53% HOMO−6 (21% S 3p, 8% Au 5d, 5% C 2p)→ LUMO (25% Au 6p, 22% Au 6s, 2% S 3p); 18.25% HOMO−4 (20% Au 6s, 13% S 3p, 6% Au 5d) → LUMO
B	2.76	0.2206	21.5% HOMO−14 (25% S 3p, 4% C 2p, 1% Au 6s) → LUMO; 18.21% HOMO−13 (14% S 3p, 11% C 2p, 5% Au 5d) → LUMO; 10.97% HOMO−4 → LUMO+2 (17% Au 6p, 16% Au 6s, 7% S 3p)
C	3.10	0.3383	21.23% HOMO−11 (22% S 3p, 4% Au 6s, 4% C 2p) → LUMO+1 (21% Au 6p, 19% Au 6s); 15.85% HOMO−2 (28% S 3p, 16% Au 5d, 3% Au 6s) → LUMO+4 (21% Au 6p, 14% Au 6s, 3% S 3p); 10.97% HOMO−13 → LUMO+1
D	3.54	0.8568	10.94% HOMO−4 → LUMO+7 (25% Au 6p, 8% Au 6s, 1% C 2p); 10.59% HOMO−10 (15% S 3p, 8% Au 6s, 4% Au 5d) → LUMO+3 (24% Au 6p, 18% Au 6s, 2% S 3p)

are almost superimposed so the role of the Z matrix is marginal and the previous approximation is justified.

The accuracy of fitted HDA in comparison with standard numeric HDA, Figure 3, and with experiment, Figure 2, takes on even greater significance when considering the times needed for the simulations. For this smaller cluster, $Au_{28}(SC_6H_5)_{20}$, of "only" 268 atoms, it takes 83 h using numeric HDA and 3 h using the new fitted approach. In other words, fitted HDA allows to obtain the same photoabsorption spectrum as numeric HDA but 28 times faster. For comparison, the sTDDFT calculation on the same cluster took 55 h while TDDFT+TB only 11 min. From this analysis, it is evident that TDDFT+TB is 1 order of magnitude faster than fitted HDA but much less accurate; on the other hand, sTDDFT displays a comparable accuracy as fitted HDA but is less efficient by one order of magnitude. Similar relative behaviors between the method timings have been obtained for the larger clusters as well; however, since the timings are somehow dependent on the machine load, we do not report their values. From this simple analysis, it seems that a still more efficient scheme could be obtained integrating sTDDFT with polTDDFT: for example, using the very efficient sTDDFT method to build the matrix elements but employing the polTDDFT algorithm to solve the TDDFT equations.

This is a remarkable speedup, which enabled us to simulate and study the remaining, larger clusters of the series using the polTDDFT-HDA scheme in a reasonable amount of CPU time (less than 1 week). The simulations for each cluster of the series were then characterized by analyzing the most prominent spectral features in terms of one-electron-excited configurations, i.e., in pairs of occupied−virtual molecular orbitals. Moreover, the nature of the molecular orbitals involved in the electronic transitions was also analyzed via Mulliken population analysis and direct inspection of the plotted orbitals.

Let us continue to consider the $Au_{28}(SC_6H_5)_{20}$ cluster. From the analysis of the molecular orbital energy levels, we find that the HOMO lies at −5.412 eV while the LUMO lies at −2.981 eV leading to an energy gap of 2.431 eV. This band gap is quite large, confirming that this system has a closed-shell electronic structure and is particularly stable, as expected for a member of a magic series. The major spectral features are the four peaks labeled A, B, C, and D in the side panel of Figure 4 and whose main contributions in terms of one-electron excited configurations are reported in Table 1. It is worth noting that feature A displays a strong contribution for the most relevant one-electron excited configuration (62% HOMO−6 → LUMO) and can be qualitatively described with only one excited configuration. In contrast, the following transitions at higher energies (A, B, and C) cannot be described with only one configuration, since the maximum contribution is around 21% for B and C and even 11% for D, indicating that they must be described as a mixing of several configurations. From the analysis of the orbital contributions, it is worth noting that the occupied orbitals close to the HOMO have a very mixed character with both the metal atoms and ligands contributing, while virtual orbitals show a more pronounced metal contribution (as apparent from the different proportions of each color in the molecular orbitals energy plot of Figure 4). A visual representation of this behavior is in the HOMO and LUMO plots of Figure 4, while the plots of all the most relevant molecular orbitals are provided in the Supporting Information in Figures S3 and S4.

It is worth noting that the intensities of the spectral features increase with energy. This is a quite general behavior for these systems, and it is due to the increasing density of excited states with energy. In the specific case, it can be attributed to the manifold of empty orbitals that accept the excited electron. In fact, from Figure 4, it is well apparent that the set of occupied orbitals from which the transitions originate for the different spectral features A, B, C, and D are roughly the same while the virtual "arrival" orbitals cover a wider energy range. From this analysis, it is possible to attribute all these features to transitions from Au−S bonding orbitals to orbitals belonging mainly to the cluster metal core, so that these transitions have a partial character of ligand-to-metal charge transfer. In particular, the D feature is rather intense. This can also be related to the aromatic nature of the ligands; in fact, we have previously shown[40] that aromatic ligands can amplify the transition intensity by an electronic coupling mechanism between the metal cluster and the ligand through a conjugation effect.

The induced density and independent component mapping of oscillator strength (ICM-OS) plots were also inspected in order to identify possible plasmonic behaviors and the connection between absorption and single-particle excitations.[42] However, no such collective behavior has been detected. The plots are available in Supporting Information in Figure S1. The absence of collective behavior follows from the absence of contributions (spots), which lie far from the white straight line corresponding to occupied−virtual orbital pairs whose energy difference equals the photon energy in the

https://doi.org/10.1021/acs.jpca.3c05368
J. Phys. Chem. A 2023, 127, 9244−9257

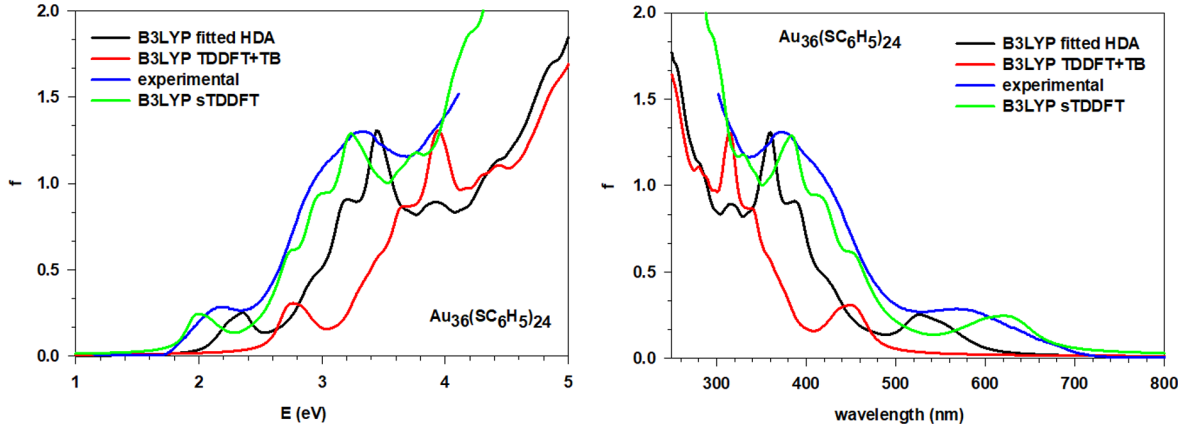


Figure 5. Comparison of the experiment with the simulated spectra using fitted HDA, sTDDFT, and TDDFT+TB for the $Au_{36}(SC_6H_5)_{24}$ cluster; both energy (eV), left, and wavelength (nm), right, plots are reported.

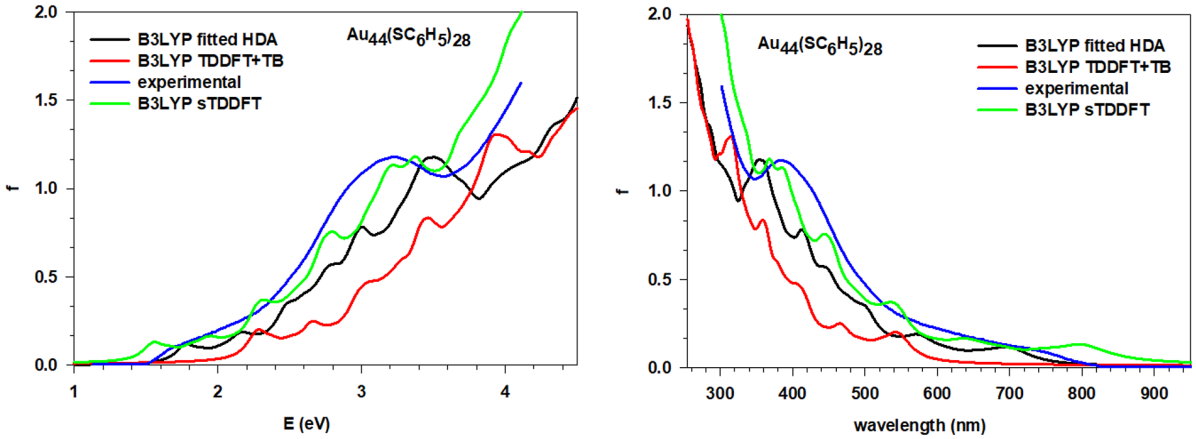


Figure 6. Comparison of the experiment with the simulated spectra using fitted HDA, sTDDFT, and TDDFT+TB for the $Au_{44}(SC_6H_5)_{28}$ cluster; both energy (eV), left, and wavelength (nm), right, plots are reported.

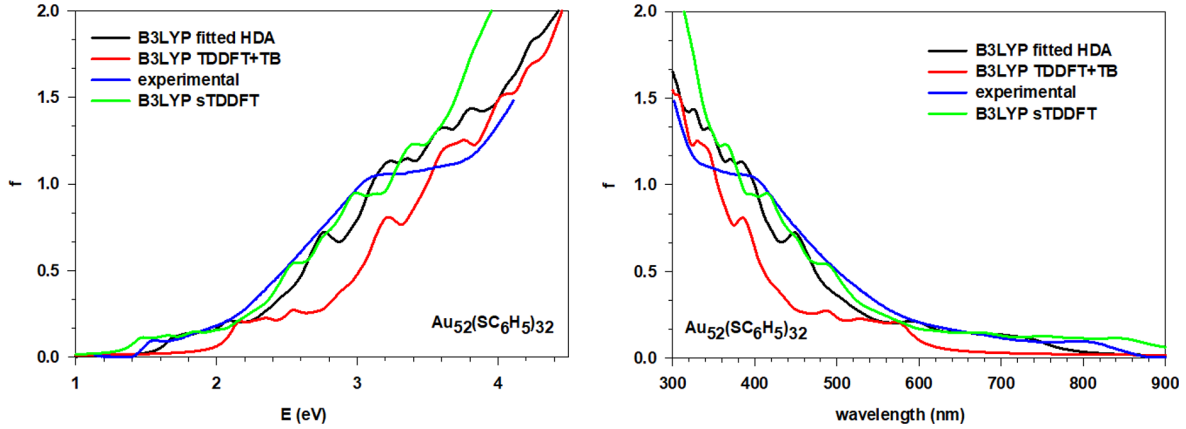


Figure 7. Comparison of the experiment with the simulated spectra using fitted HDA, sTDDFT, and TDDFT+TB for the $Au_{52}(SC_6H_5)_{32}$ cluster; both energy (eV), left, and wavelength (nm), right, plots are reported.

ICM-OS plots. The corresponding induced densities are reported in Figure S2, and also in this case one can observe that there is no indication of a plasmonic behavior. Indeed, plasmons usually give induced densities with an evident dipolar shape whereas the plots reported in Figure S2 display very irregular shapes, which cannot be ascribed to dipolar shapes at all.

4.2. $Au_{36}(SC_6H_5)_{24}$, $Au_{44}(SC_6H_5)_{28}$, and $Au_{52}(SC_6H_5)_{32}$.

The same analysis has been performed for all of the remaining clusters of the series with analogous results. For each member of the series, we have considered the comparison between the photoabsorption spectra simulated using fitted HDA, sTDDFT, and TDDFT+TB with respect to the experimental data (Figures 5, 6, and 7), the molecular orbital energy plots (Figures 8, 9, and 10), and the analysis in terms of one-

https://doi.org/10.1021/acs.jpca.3c05368
J. Phys. Chem. A 2023, 127, 9244−9257

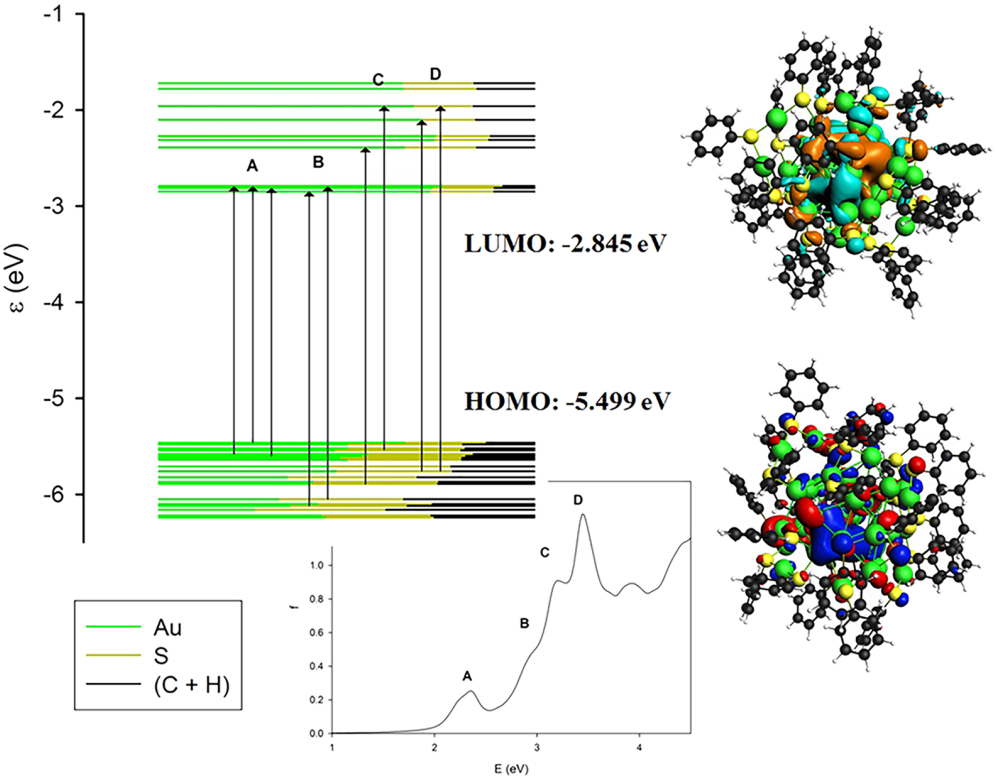


Figure 8. On the left, the molecular orbital energy plot for the $Au_{36}(SC_6H_5)_{24}$ cluster with arrows indicating the major transitions involved in each spectral feature (A, B, C, and D), on the right, HOMO and LUMO energies and orbital plots. The contribution of different fragments (the metal core of Au atoms, the ligand's polar heads S, and their spacers C+H) to each molecular orbital considered is depicted through the ratio of the associated colors.

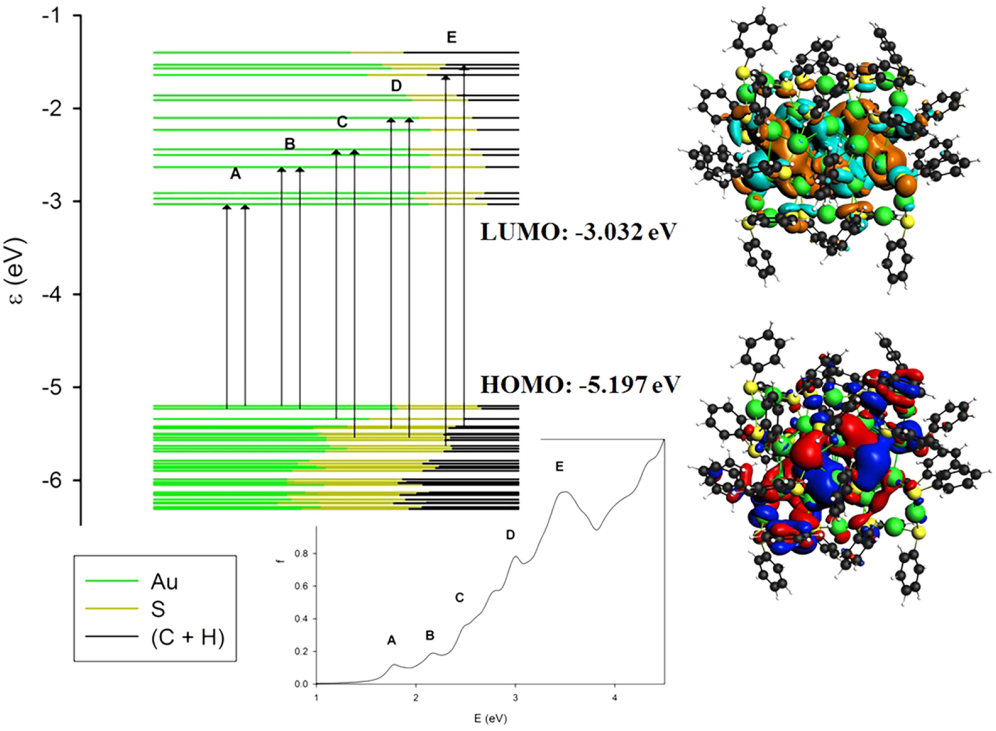


Figure 9. On the left, the molecular orbital energy plot for the $Au_{44}(SC_6H_5)_{28}$ cluster with arrows indicating the major transitions involved in each spectral feature (A, B, C, D, and E), on the right, HOMO and LUMO energies and orbital plots. The contribution of different fragments (the metal core of Au atoms, the ligand's polar heads S, and their spacers C+H) to each molecular orbital considered is depicted through the ratio of the associated colors.

https://doi.org/10.1021/acs.jpca.3c05368
J. Phys. Chem. A 2023, 127, 9244−9257

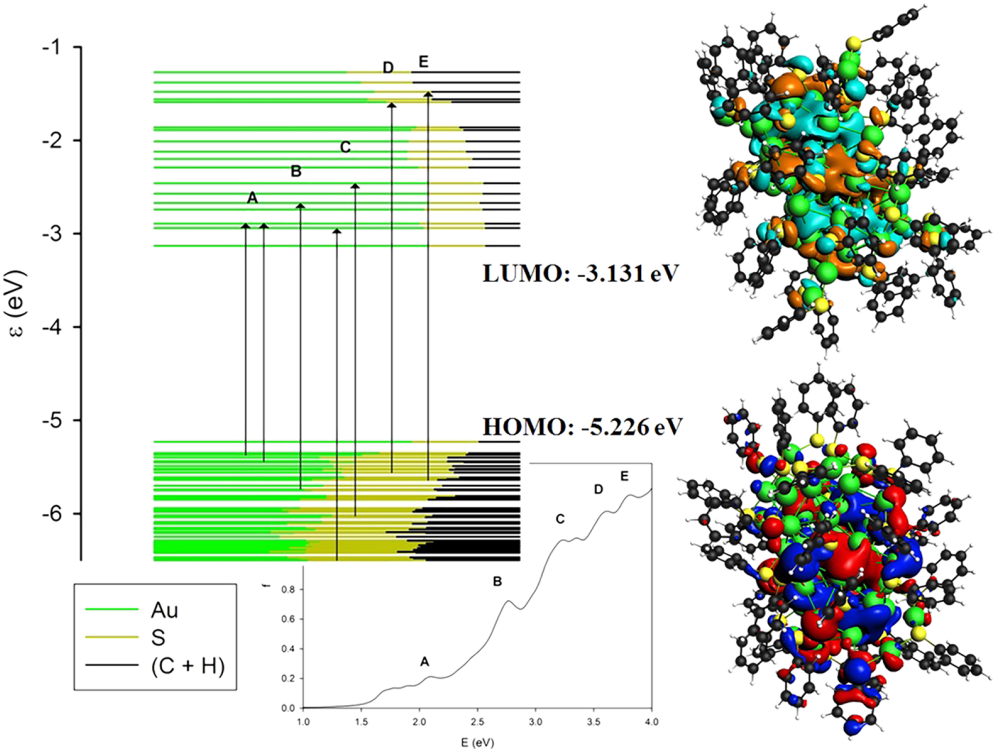


Figure 10. On the left, the molecular orbital energy plot for the $Au_{52}(SC_6H_5)_{32}$ cluster with arrows indicating the major transitions involved in each spectral feature (A, B, C, D, and E), on the right, HOMO and LUMO energies and orbital plots. The contribution of different fragments (the metal core of Au atoms, the ligand's polar heads S, and their spacers C+H) to each molecular orbital considered is depicted through the ratio of the associated colors.

Table 2. Principal Contributions in Terms of One-Electron Excited Configurations to the Main Spectral Features of $Au_{36}(SC_6H_5)_{24}$ Calculated at the PolTDDFT Level with the B3LYP XC Functional, TZP Basis Set, and Using Fitted HDA

excitation	excitation *E* (eV)	*f*	assignment
A	2.36	0.2533	17.51% HOMO−4 (16% S 3p, 8% Au 6s, 6% Au 5d)→ LUMO+2 (21% Au 6s, 19% Au 6p, 3% S 3p); 12.02% HOMO (15% Au 6s, 7% S 3p, 3% Au 5d) → LUMO+2; 10.30% HOMO−5 (14% S 3p, 8% Au 6s, 4% Au 5d) → LUMO+1 (19% Au 6p, 16% Au 6s, 4% S 3p)
B	2.92	0.4508	10.29% HOMO−15 (15% S 3p, 1% C 2p)→ LUMO (20% Au 6p, 12% Au 6s, 3% S 3p); 8.30% HOMO−13 (18% S 3p, 1% Au 6s, 1% Au 5d)→ LUMO+2
C	3.20	0.9101	9.43% HOMO−12 (20% S 3p, 1% Au 5d) → LUMO+3 (20% Au 6s, 11% Au 6p, 9% S 3p); 8.15% HOMO−3 (25% S 3p, 7% Au 5d, 3% C 2p) → LUMO+7 (22% Au 6s, 10% Au 6p, 1% S 3p)
D	3.44	1.3064	8.96% HOMO−9 (18% S 3p, 3% Au 6s, 1% Au 5d) → LUMO+6 (19% Au 6s, 18% Au 6p, 1% S 3p); 5.76% HOMO−9 → LUMO+7

electron excited configurations of the main spectral features (Tables 2, 3, and 4). Considering each cluster separately, it is clear how the simulations using fitted HDA are in better agreement with the experiment when compared to the simulations using TDDFT+TB, while sTDDFT displays an accuracy comparable to fitted HDA. The location of the absorption peaks retraces almost perfectly that of the experiment with minor discrepancies of few tenths of eV. The general profile is also well reproduced with the correct trend for the absorption intensities and its peculiarities, like the two more pronounced peaks of $Au_{36}(SC_6H_5)_{24}$ (Figure 5) near 2.25 and 3.5 eV. The simulations obtained with the TDDFT +TB scheme all show a positive energy shift of ∼0.5 eV. Although we observe a smooth trend along the series of the spectra, there are some interesting discontinuities such as, for example, the just noted feature of $Au_{36}(SC_6H_5)_{24}$ at 2.25 eV. This effect resembles the previously observed "rebirth of the plasmon" in $Au_{30}(SR)_{18}$,[40] which was ascribed to a strong electronic conjugation between the metal core and the aromatic ligands. Therefore, we are led to conclude that in present series such conjugation is maximized in the $Au_{36}(SC_6H_5)_{24}$ cluster, $Au_{28}(SC_6H_5)_{20}$ being too small while $Au_{44}(SC_6H_5)_{28}$ and $Au_{52}(SC_6H_5)_{32}$ probably are too congested (due to their larger radius), and therefore, their structures do not allow proper conjugation between the ligands and the metal core. Another peculiarity of $Au_{36}(SC_6H_5)_{24}$, which can be correlated with the strong feature at 2.25 eV, is the presence of many virtual orbitals almost degenerate with the LUMO

https://doi.org/10.1021/acs.jpca.3c05368
J. Phys. Chem. A 2023, 127, 9244−9257

Table 3. Principal Contributions in Terms of One-Electron Excited Configurations to the Main Spectral Features of $Au_{44}(SC_6H_5)_{28}$ Calculated at the PolTDDFT Level with the B3LYP XC Functional and TZP Basis Set and Using Fitted HDA

excitation	excitation E (eV)	f	assignment
A	1.78	0.1199	42.97% HOMO−1 (14% Au 6s, 13% S 3p, 3% Au 6p) → LUMO (15% Au 6p, 13% Au 6s); 35.09% HOMO (13% Au 6s, 11% S 3p, 2% Au 6p) → LUMO
B	2.18	0.1902	35.71% HOMO → LUMO+3 (21% Au 6s, 8% Au 6p, 5% S 3p); 19.25% HOMO−1 → LUMO+3
C	2.48	0.3526	41.99% HOMO−2 (15% S 3p, 5% Au 6s, 3% Au 5d) → LUMO+5 (16% Au 6s, 13% Au 6p, 2% S 3p); 12.62% HOMO−7 (28% S 3p, 9% Au 5d) → LUMO+3
D	3.0	0.7835	14.33% HOMO−4 (23% S 3p, 2% Au 5d) → LUMO+7 (22% Au 6s, 11% Au 6p); 7.57% HOMO−7 → LUMO+7
E	3.44	1.1661	12.60% HOMO−9 (18% S 3p, 4% Au 5d, 2% Au 6s) → LUMO+10 (13% Au 6p, 7% Au 6s, 3% S 3p); 10.55% HOMO−3 (19% S 3p, 8% Au 5d) → LUMO+12 (13% Au 6p, 8% Au 6s)

Table 4. Principal Contributions in Terms of One-Electron Excited Configurations to the Main Spectral Features of $Au_{52}(SC_6H_5)_{32}$ Calculated at the PolTDDFT Level with the B3LYP XC Functional and TZP Basis Set and Using Fitted HDA

excitation	excitation E (eV)	f	assignment
A	2.10	0.2127	17.92% HOMO−2 (13% S 3p, 6% Au 6s, 2% Au 6p)→ LUMO+2 (10% Au 6p, 7% Au 6s); 14.30% HOMO−4 (21% S 3p, 1% Au 5d) → LUMO+2
B	2.76	0.7238	6.10% HOMO−14 (18% S 3p, 3% Au 5d, 2% C 2p) → LUMO+4 (8% Au 6p, 6% Au 7s, 4% Au 6s)
C	3.24	1.1340	4.57% HOMO−46 (13% S 3p, 1% Au 5d, 1% Au 6s) → LUMO+1 (14% Au 6s, 9% Au 6p); 4.54% HOMO−22 (15% S 3p, 9% Au 5d, 8% Au 6s) → LUMO+6 (14% Au 6s, 13% Au 6p, 1% Au 7s)
D	3.62	1.3275	3.55% HOMO−9 (15% S 3p, 6% Au 5d, 3% Au 6s) → LUMO+13 (13% Au 6p, 12% Au 6s, 3% S 3p)
E	3.82	1.4371	3.85% HOMO−12 (15% S 3p) → LUMO+15 (10% Au 6s, 6% Au 6p)

(see Figure 8). By comparison with Figures 3, 9, and 10, it is well apparent that while in the other clusters the virtual orbitals are distributed rather uniformly above the LUMO, whereas for $Au_{36}(SC_6H_5)_{24}$ such distribution is much less homogeneous.

It is interesting, at this point, to consider the cluster series as a whole and look at how the properties of the cluster evolve along it. The optical absorption spectra of the four clusters exhibit similar profiles (Figure 11), featuring an intense peak at ∼3.25 eV and less intense features moving to lower energy region. With increasing the cluster dimension, the density of the molecular orbitals near the HOMO and LUMO energy levels increases while the HOMO−LUMO energy gap decreases, with the exception of $Au_{36}(SC_6H_5)_{32}$. These observations provide an explanation for other two general features of the cluster series. First is the fact that the spectral profiles appear smoother and smoother moving to larger clusters, because far more features are present close to each other in energy. Second, the absorption intensities increase with energy and the cluster size. This is connected with the fact that the occupied molecular orbitals, due to their more pronounced ligand character, have a better overlap with the higher energy virtual molecular orbitals, since the lowest virtual ones have mainly metal character. Therefore, the associated transitions gain intensity going at higher energies.

Looking at Figure 11, it is possible to notice, with increasing cluster size, a redshift in the energy of the main absorption peaks. The same shift is more pronounced looking at the onset of the absorption profiles. Both the fitted HDA and sTDDFT simulations and experiment agree, at least qualitatively, about the order in which the absorptions for the different clusters begin: the lower absorption energy is that of $Au_{52}(SC_6H_5)_{32}$ followed by $Au_{44}(SC_6H_5)_{28}$ and, with a non-negligible energy difference, $Au_{36}(SC_6H_5)_{24}$ and $Au_{28}(SC_6H_5)_{20}$, which are practically overlapping. The onset of the absorption peak depends on the optical gap of the system, which is the energy gap plus the exciton binding energy, and indeed, it reflects the trend of the HOMO−LUMO energy difference obtained from the fitted HDA simulations. Such a similarity and uniform evolution in the UV−vis spectra of the "magic series" can be ascribed to the identical structure type (fcc) and protecting ligand used that make it similar to other, well-defined, quantum systems, like quantum dots or conjugated alkenes, with a clear quantum confinement nature.

It is worthwhile to note that besides these general trends, the present calculations are able to reproduce even minor details of the experiment. For example from Figure 11, in the experiment, the intensity profile of $Au_{36}(SC_6H_5)_{24}$ is always greater than that of $Au_{28}(SC_6H_5)_{20}$, but they touch each other around 2.6 eV. The theory reproduces fairly well this behavior, with a minimal shift of only 0.1 eV at higher energy. Another remarkable result is the behavior above 3.5 eV, where the three smaller clusters display a shallow minimum followed by an intensity increase, a feature not present in $Au_{52}(SC_6H_5)_{32}$; also, such effect is properly reproduced by theory.

In summary, the polTDDFT with B3LYP and fitted HDA has proven to be a very efficient and quantitative method to

https://doi.org/10.1021/acs.jpca.3c05368
J. Phys. Chem. A 2023, 127, 9244−9257

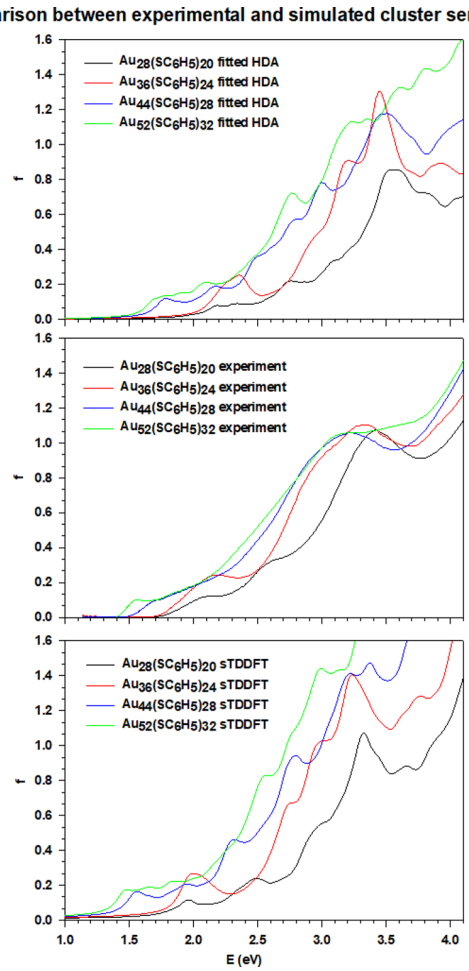


Figure 11. Comparison of the photoabsorption spectra for the cluster series: fitted HDA within the polTDDFT computational scheme (upper panel), experiment (central panel), and sTDDFT (lower panel).

describe the optical properties of the investigated series. It must be also considered that the available experimental data have been all recorded at room temperature, so further experiment at low temperature[43] would be extremely useful to better assess the performance of the present theoretical approach as well as to better understand the optical properties of these fascinating and intriguing systems. Although the topic of the present work is focused on the series of thiolate-protected gold metal clusters, the fitted HDA method is completely general and it is expected to keep its accuracy and computational efficiency in general. In fact, we compared the numerical and fitted HDA for a completely different system, namely, a decapeptide with explicit solvent consisting of 40 water molecules $(GVGVP)_2$ $(H2O)_{40}$, and obtained a very good match (see Figure S11 in the Supporting Information). This suggests that the conclusions of this work are general and are not restricted to the systems here considered.

5. CONCLUSIONS

In this work, we have implemented an RI technique to speed up the use of the hybrid xc functionals within the HDA approximation at the TDDFT theory level, solving the equations with the polTDDFT algorithm. In practice, the diagonal matrix elements of the nonlocal HF exchange kernel are calculated exploiting the RI instead of using the numerical integration as in the previous version of the code. The use of RI produced a speedup of almost a factor of 30 with respect to the previous numerical implementation, keeping the same level of accuracy, so that eventually the prediction of the optical photoabsorption spectrum via TDDFT/HDA requires essentially the same level of computational effort as a DFT SCF single-point calculation with a hybrid functional. Comparison with respect to the experimental photoabsorption spectra of the cluster series $Au_{8n+4}(SR)_{4n+8}$(n = 3−6; R = C_6H_5) demonstrated the high accuracy and efficiency of the method. The method has proven quantitatively accurate in both the high energy part of the spectrum, dominated by ligand contribution, and the lowest part of the spectrum, dominated by the metal-core absorption. Even minor spectral features and trends are well reproduced by theory. For comparison, we also employed sTDDFT and the much cheaper TDDFT+TB method to calculate the spectra, finding that it gives qualitatively correct results in the overall spectrum but with quantitative agreement with experiment only in the highest-energy part of the spectrum, dominated by the ligands, whereas the more accurate fitted HDA scheme performs much better with a predictive quantitative accuracy on the whole optical region. On the other hand, the sTDDFT method has proven to furnish absorption profiles with better agreement with respect to the experiment than the fitted HDA, although the discrepancy between the experimental maximum and the sTDDFT and fitted HDA is about 0.1 eV for both methods. Moreover, the sTDDFT is more computationally demanding than the fitted HDA. This finding suggests that the polTDDFT with the RI technique and hybrid xc functionals represents an accurate as well as computationally cheap approach, with optimal compromise between accuracy and computational efficiency, for applications to large metal clusters with sizes up to several hundreds of atoms.

■ ASSOCIATED CONTENT

Data Availability Statement

The data that support the findings of this study are available from the corresponding author upon reasonable request.

Supporting Information

The Supporting Information is available free of charge at https://pubs.acs.org/doi/10.1021/acs.jpca.3c05368.

The ICM-OS plots, the induced density plots, the plots of occupied and virtual orbitals involved in the salient transitions, the photoabsorption profiles calculated by numerical and fitted HDA for $(GVGVP)_2$ $(H_2O)_{40}$, and the geometries of all the gold clusters considered in this work (PDF)

■ AUTHOR INFORMATION

Corresponding Authors

Mauro Stener − *Dipartimento di Scienze Chimiche e Farmaceutiche, Università di Trieste, Trieste 34127, Italy;* orcid.org/0000-0003-3700-7903; Email: stener@units.it

Lucas Visscher − *Department of Chemistry and Pharmaceutical Sciences, Vrije Universiteit Amsterdam, Amsterdam 1081 HV, The Netherlands;* orcid.org/0000-0002-7748-6243; Email: l.visscher@vu.nl

Authors

Pierpaolo D'Antoni − *Dipartimento di Scienze Chimiche e Farmaceutiche, Università di Trieste, Trieste 34127, Italy*

Marco Medves − *Dipartimento di Scienze Chimiche e Farmaceutiche, Università di Trieste, Trieste 34127, Italy*

Daniele Toffoli − *Dipartimento di Scienze Chimiche e Farmaceutiche, Università di Trieste, Trieste 34127, Italy;* orcid.org/0000-0002-8225-6119

Alessandro Fortunelli − *CNR-ICCOM, Consiglio Nazionale delle Ricerche, Pisa 56124, Italy;* orcid.org/0000-0001-5337-4450

Complete contact information is available at: https://pubs.acs.org/10.1021/acs.jpca.3c05368

Notes

The authors declare no competing financial interest.

■ ACKNOWLEDGMENTS

P.D.A. and M.S. are grateful to Erik van Lenthe and Stan van Gisbergen of SCM (Amsterdam) for fruitful discussions and technical assistance during the implementation within the AMS/ADF program. Computational support from the CINECA supercomputing center within the ISCRA program is gratefully acknowledged. The authors are grateful to the Stiftung Beneficentia for a generous grant employed to set up a computational server. Support from Trieste University within the FRA program is gratefully acknowledged. Financial support from ICSC − Centro Nazionale di Ricerca in High Performance Computing, Big Data and Quantum Computing, funded by European Union − NextGenerationEU is gratefully acknowledged. Networking within the COST Action CA21101 "Confined molecular systems: from a new generation of materials to the stars" (COSY) supported by COST (European Cooperation in Science and Technology) is gratefully acknowledged.

■ REFERENCES

(1) Barone, V. The Virtual Multifrequency Spectrometer: A New Paradigm for Spectroscopy. *WIREs Comput. Mol. Sci.* **2016**, *6*, 86−110.

(2) Casida, M. E. In *Recent Advances in Density Functional Methods*; Chong, D. P.; World Scientific: Singapore, 1995; p 155.

(3) Yabana, K.; Bertsch, G. F. Time-Dependent Local-Density Approximation in Real Time. *Phys. Rev. A* **1996**, *54*, 4484−4487.

(4) Marques, M. A. L.; Castro, A.; Bertsch, G. F.; Rubio, A. Octopus: A First-Principles Tool for Excited Electron−Ion Dynamics. *Comput. Phys. Commun.* **2003**, *151*, 60−78.

(5) Walker, B.; Saitta, A. M.; Gebauer, R.; Baroni, S. Efficient Approach to Time-Dependent Density-Functional Perturbation Theory for Optical Spectroscopy. *Phys. Rev. Lett.* **2006**, *96*, No. 113001.

(6) Grimme, S. A Simplified Tamm-Dancoff Density Functional Approach for the Electronic Excitation Spectra of Very Large Molecules. *J. Chem. Phys.* **2013**, *138*, 244104.

(7) Bannwarth, C.; Grimme, S. A Simplified Time-Dependent Density Functional Theory Approach for Electronic Ultraviolet and Circular Dichroism Spectra of Very Large Molecules. *Comput. Theor. Chem.* **2014**, *1040−1041*, 45−53.

(8) Zuehlsdorff, T. J.; Hine, N. D. M.; Spencer, J. S.; Harrison, N. M.; Riley, D. J.; Haynes, P. D. Linear-Scaling Time-Dependent Density-Functional Theory in the Linear Response Formalism. *J. Chem. Phys.* **2013**, *139*, No. 064104.

(9) Malola, S.; Lehtovaara, L.; Enkovaara, J.; Häkkinen, H. Birth of the Localized Surface Plasmon Resonance in Monolayer-Protected Gold Nanoclusters. *ACS Nano* **2013**, *7*, 10263−10270.

(10) Noda, M.; Ishimura, K.; Nobusada, K.; Yabana, K.; Boku, T. Massively-Parallel Electron Dynamics Calculations in Real-Time and Real-Space: Toward Applications to Nanostructures of More than Ten-Nanometers in Size. *J. Comput. Phys.* **2014**, *265*, 145−155.

(11) Iida, K.; Noda, M.; Ishimura, K.; Nobusada, K. First-Principles Computational Visualization of Localized Surface Plasmon Resonance in Gold Nanoclusters. *J. Phys. Chem. A* **2014**, *118*, 11317−11322.

(12) Baseggio, O.; Fronzoni, G.; Stener, M. A New Time Dependent Density Functional Algorithm for Large Systems and plasmons in Metal Clusters. *J. Chem. Phys.* **2015**, *143*, No. 024106.

(13) Baseggio, O.; De Vetta, M.; Fronzoni, G.; Stener, M.; Fortunelli, A. A New Time-Dependent Density-Functional Method for Molecular Plasmonics: Formalism, Implementation, and the $Au_{144}(SH)_{60}$Case Study. *Int. J. Quantum Chem.* **2016**, *116*, 1603−1611.

(14) Baseggio, O.; Toffoli, D.; Fronzoni, G.; Stener, M.; Sementa, L.; Fortunelli, A. Extension of the Time-Dependent Density Functional Complex Polarizability Algorithm to Circular Dichroism: Implementation and Applications to Ag_8 and $Au_{38}(SC_2H_4c_6H_5)_{24}$. *J. Phys. Chem. C* **2016**, *120*, 24335−24345.

(15) Baseggio, O.; De Vetta, M.; Fronzoni, G.; Stener, M.; Sementa, L.; Fortunelli, A.; Calzolari, A. photoabsorption of Icosahedral Noble Metal Clusters: An Efficient TDDFT Approach to Large-Scale Systems. *J. Phys. Chem. C* **2016**, *120*, 12773−12782.

(16) Kaur, J.; Ospadov, E.; Staroverov, V. N. What Is the Accuracy Limit of Adiabatic Linear-Response TDDFT Using Exact Exchange−Correlation Potentials and Approximate Kernels? *J. Chem. Theory Comput.* **2019**, *15*, 4956−4964.

(17) Becke, A. D. Perspective: Fifty Years of Density-Functional Theory in Chemical Physics. *J. Chem. Phys.* **2014**, *140*, 18A301.

(18) Mardirossian, N.; Head-Gordon, M. Thirty Years of Density Functional Theory in Computational Chemistry: An Overview and Extensive Assessment of 200 Density functionals. *Mol. Phys.* **2017**, *115*, 2315−2372.

(19) Becke, A. D. Density - Functional Thermochemistry III. The Role of Exact Exchange. *J. Chem. Phys.* **1993**, *98*, 5648−5652.

(20) Stephens, P. J.; Devlin, F. J.; Chabalowski, C. F.; Frisch, M. J. Ab Initio Calculation of Vibrational Absorption and Circular Dichroism Spectra Using Density Functional Force Fields. *J. Phys. Chem.* **1994**, *98*, 11623−11627.

(21) Medves, M.; Sementa, L.; Toffoli, D.; Fronzoni, G.; Fortunelli, A.; Stener, M. An Efficient Hybrid Scheme for Time Dependent Density Functional Theory. *J. Chem. Phys.* **2020**, *152*, 184104−184104.

(22) Andzelm, J.; Radzio, E.; Salahub, D. R. Compact Basis Sets for LCAO-LSD Calculations. Part I: Method and Bases for Sc to Zn. *J. Comput. Chem.* **1985**, *6*, 520−532.

(23) Delesma, F. A.; Delgado-Venegas, R. I.; Salahub, D. R.; del Campo, J. M.; Pedroza-Montero, J. N.; Calaminici, P.; Köster, A. M. Self-Consistent Auxiliary Density Perturbation Theory. *J. Chem. Theory Comput.* **2021**, *17*, 6934−6946.

(24) Dunlap, B. I.; Rösch, N. The Gaussian-Type Orbitals Density-Functional Approach to Finite Systems. *Adv. Quantum Chem.* **1990**, *21*, 317−339.

(25) Fortunelli, A.; Salvetti, O. A simplified representation of the potential produced by Gaussian charge distributions. *J. Comput. Chem.* **1991**, *12*, 36−41.

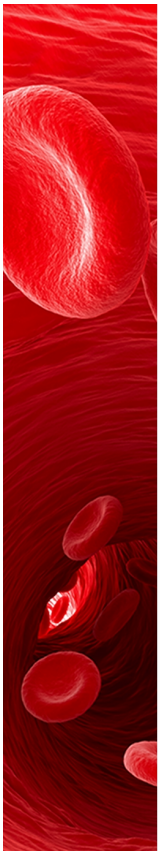
(26) Fortunelli, A.; Salvetti, O. Overlapping and non-overlapping integrals in molecular calculations. *Chem. Phys. Lett.* **1991**, *186*, 372−378.

(27) Baerends, E. J.; Ellis, D. E.; Ros, P. Self-consistent molecular Hartree—Fock—Slater calculations I. The computational procedure. *Chem. Phys.* **1973**, *2*, 41−51.

(28) Spadetto, E.; Philipsen, P. H. T.; Förster, A.; Visscher, L. Toward Pair Atomic Density Fitting for Correlation Energies with Benchmark Accuracy. *J. Chem. Theory Comput.* **2023**, *19*, 1499−1516.

(29) Feyereisen, M.; Fitzgerald, G.; Komornicki, A. Use of Approximate Integrals in Ab Initio Theory. An Application in MP2 Energy Calculations. *Chem. Phys. Lett.* **1993**, *208*, 359−363.

(30) Vahtras, O.; Almlöf, J.; Feyereisen, M. W. Integral Approximations for LCAO-SCF Calculations. *Chem. Phys. Lett.* **1993**, *213*, 514−518.
(31) Kendall, R. A.; Früchtl, H. A. The impact of the resolution of the identity approximate integral method on modern ab initio algorithm development. *Theor. Chem. Acc.* **1997**, *97*, 158−163.
(32) Hamel, S.; Casida, M. E.; Salahub, D. R. Assessment of the quality of orbital energies in resolution-of-the-identity Hartree−Fock calculations using deMon auxiliary basis sets. *J. Chem. Phys.* **2001**, *114*, 7342−7350.
(33) Weigend, F. A Fully Direct RI-HF Algorithm: Implementation, Optimised Auxiliary Basis Sets, Demonstration of Accuracy and Efficiency. *Phys. Chem. Chem. Phys.* **2002**, *4*, 4285−4291.
(34) Sodt, A.; Head-Gordon, M. Hartree-Fock Exchange Computed Using the Atomic Resolution of the Identity Approximation. *J. Chem. Phys.* **2008**, *128*, 104106.
(35) Aquilante, F.; Lindh, R.; Pedersen, T. B. Unbiased auxiliary basis sets for accurate two-electron integral approximations. *J. Chem. Phys.* **2007**, *127*, 114107.
(36) Zeng, C.; Chen, Y.; Iida, K.; Nobusada, K.; Kirschbaum, K.; Lambright, K. J.; Jin, R. Gold Quantum Boxes: On the Periodicities and the Quantum Confinement in the Au_{28}, Au_{36}, Au_{44}, and Au_{52} Magic Series. *J. Am. Chem. Soc.* **2016**, *138*, 3950−3953.
(37) Rüger, R.; van Lenthe, E.; Heine, T.; Visscher, L. Tight-Binding Approximations to Time-Dependent Density Functional Theory — a Fast Approach for the Calculation of Electronically Excited States. *J. Chem. Phys.* **2016**, *144*, 184103.
(38) Medves, M.; Fronzoni, G.; Stener, M. Optimization of Density Fitting Auxiliary Slater-Type Basis Functions for Time-Dependent Density Functional Theory. *J. Comput. Chem.* **2022**, *43*, 1923−1935.
(39) van Lenthe, E.; Baerends, E. J.; Snijders, J. G. Relativistic Regular Two-Component Hamiltonians. *J. Chem. Phys.* **1993**, *99*, 4597−4610.
(40) Sementa, L.; Barcaro, G.; Baseggio, O.; De Vetta, M.; Dass, A.; Aprà, E.; Stener, M.; Fortunelli, A. Ligand-Enhanced Optical Response of Gold Nanomolecules and Its Fragment Projection Analysis: The Case of $Au_{30}(SR)_{18}$. *J. Phys. Chem. C* **2017**, *121*, 10832−10842.
(41) Pelayo, J. J.; Valencia, I.; García, A. P.; Chang, L.; López, M.; Toffoli, D.; Stener, M.; Fortunelli, A.; Garzón, I. L. Chirality in bare and ligand-protected metal nanoclusters. *Adv. Phys.: X* **2018**, *3*, 1509727.
(42) Theivendran, S.; Chang, L.; Mukherjee, A.; Sementa, L.; Stener, M.; Fortunelli, A.; Dass, A. Principles of Optical Spectroscopy of Aromatic Alloy Nanomolecules: $Au_{36-x}Ag_x(SPh\text{-}tBu)_{24}$. *J. Phys. Chem. C* **2018**, *122*, 4524−4531.
(43) Medves, M.; Sementa, L.; Toffoli, D.; Fronzoni, G.; Krishnadas, K. R.; Bürgi, T.; Bonacchi, S.; Dainese, T.; Maran, F.; Fortunelli, A.; et al. Predictive Optical photoabsorption of $Ag_{24}Au(DMBT)_{18}^-$ via Efficient TDDFT Simulations. *J. Chem. Phys.* **2021**, *155*, No. 084103.


CAS BIOFINDER DISCOVERY PLATFORM™
CAS BIOFINDER HELPS YOU FIND YOUR NEXT BREAKTHROUGH FASTER
Navigate pathways, targets, and diseases with precision
Explore CAS BioFinder
CAS
A division of the American Chemical Society

https://doi.org/10.1021/acs.jpca.3c05368
J. Phys. Chem. A 2023, 127, 9244−9257

4.1.2 Combined experimental and computational study of the photoabsorption of the monodoped and nondoped nanoclusters $Au_{24}Pt(SR)_{18}$, $Ag_{24}Pt(SR)_{18}$, and $Ag_{25}(SR)_{18}$

Following the methodological developments presented in the previous work, this article aims at providing a stringent and independent validation of the RI-accelerated Hybrid Diagonal Approximation (RI/HDA) within TDDFT by comparing theoretical simulations with high-resolution experimental photoabsorption spectra. While the first study focused on efficiency and large-scale applicability, the present work offers the opportunity to critically assess the quantitative accuracy of the proposed computational framework against low-temperature experimental data, thereby strengthening its reliability for predictive applications.

The study addresses a set of atomically precise monolayer-protected metal nanoclusters with different metal compositions and ligand environments, including both doped and undoped systems. Low-temperature absorption spectra were measured to enhance spectral resolution and enable a detailed one-to-one comparison with TDDFT calculations performed using hybrid exchange–correlation functionals and experimentally derived geometries. This combination represents a particularly demanding benchmark, as the optical response of such systems arises from the intricate interplay between metal cores, metal–ligand interfaces, and organic ligands.

The excellent agreement observed between theory and experiment, with typical deviations well below 0.1 eV, provides a strong validation of the RI/HDA TDDFT approach previously introduced. Beyond reproducing peak positions and overall spectral profiles, the calculations allow for a consistent assignment of the main spectral features in terms of specific occupied–virtual orbital transitions. In this context, the effect of metal doping on the electronic structure and optical response of the nanoclusters is also characterized, demonstrating the capability of the method to capture subtle but chemically relevant modifications of the excitation spectrum.

Overall, this work confirms that the RI/HDA formulation of hybrid TDDFT is not only computationally efficient but also quantitatively accurate when applied to experimentally well-characterized real systems. The results therefore establish the method as a reliable tool for the interpretation of optical spectra of complex metal nanoclusters and support its use in future studies aimed at understanding and predicting structure–property relationships in doped and functionalized nanoscale materials.

PCCP

ROYAL SOCIETY OF CHEMISTRY

PAPER

View Article Online
View Journal | View Issue

Check for updates

Cite this: *Phys. Chem. Chem. Phys.*, 2024, **26**, 17569

Combined experimental and computational study of the photoabsorption of the monodoped and nondoped nanoclusters $Au_{24}Pt(SR)_{18}$, $Ag_{24}Pt(SR)_{18}$, and $Ag_{25}(SR)_{18}$†

Pierpaolo D'Antoni,[a] Luca Sementa,[b] Sara Bonacchi,[c] Mattia Reato,[c] Flavio Maran,*[cd] Alessandro Fortunelli*[b] and Mauro Stener*[a]

Received 23rd February 2024,
Accepted 28th May 2024

DOI: 10.1039/d4cp00789a

rsc.li/pccp

Assessing the accuracy of first-principles computational approaches is instrumental to predict electronic excitations in metal nanoclusters with quantitative confidence. Here we describe a validation study on the optical response of a set of monolayer-protected clusters (MPC). The photoabsorption spectra of $Ag_{25}(DMBT)_{18}^-$, $Ag_{24}Pt(DMBT)_{18}^{2-}$ and $Au_{24}Pt(SC_4H_9)_{18}$, where DMBT is 2,4-dimethylbenzenethiolate and SC_4H_9 is *n*-butylthiolate, have been obtained at low temperature and compared with accurate TDDFT calculations. An excellent match between theory and experiment, with typical deviations of less than 0.1 eV, was obtained, thereby validating the accuracy and reliability of the proposed computational framework. Moreover, an analysis of the TDDFT simulations allowed us to ascribe all relevant spectral features to specific transitions between occupied/virtual orbital pairs. The doping effect of Pt on the optical response of these ultrasmall MPC systems was identified and discussed.

Open Access Article. Published on 07 June 2024. Downloaded on 9/30/2025 10:07:30 AM.
This article is licensed under a Creative Commons Attribution-NonCommercial 3.0 Unported Licence.

1. Introduction

Metal nanoclusters protected by a layer of coating ligands with well-defined stoichiometry and chemical structure, often referred to as monolayer-protected clusters (MPC), are compounds that exhibit peculiar physicochemical properties and have emerged as a very important class of nanomaterials for both fundamental studies and potential applications.[1–31]

Thanks to the versatility of properly devised bottom-up wet-chemistry synthesis and purification procedures, many MPC have been successfully characterized with atomic precision *via* mass spectrometry and single-crystal X-ray crystallography, thereby achieving a level of information that surpasses by far the more elusive bare 'naked' metal clusters originally investigated and characterized in, *e.g.*, molecular beams and inert dielectric matrices. Knowledge of the crystal geometry and composition has been also instrumental to devise experimental and computational characterization procedures, and this provided the chance of cross-validating methods and results in a rigorous and robust framework. Cross-validation is especially important to develop and refine computational methods aimed to be quantitatively predictive in the study of the MPCs' structure/property relationships, such as first-principles quantum mechanics (QM) methods. For example, although several different theoretical methods are available and have been employed to study MPCs with various degrees of accuracy and computational cost, it is very important to assess their performances and shortcomings in view of choosing the most suitable method for a specific investigation, while keeping the expected error and computational effort under control. Once validated, computational approaches can then be employed with confidence to obtain accurate and predictive information also when experimental information is not available, and ultimately, design new materials with desired properties.

The optical response, particularly the photoabsorption spectrum of MPCs, is one of the those properties for which accurate validation studies are desirable.[32,33] Indeed, whereas a qualitative agreement between theory and experiment has been generally obtained,[34–36] a quantitative match is much more challenging and has rarely been achieved.[37–39] In this context, one of the first quantitatively accurate optical-response calculations for an MPC system was carried out for $Au_{30}(S\text{–}t\text{Bu})_{18}$.[37]

[a] *Dipartimento di Scienze Chimiche e Farmaceutiche, Università di Trieste, Via Giorgieri 1, I-34127 Trieste, Italy. E-mail: stener@units.it*
[b] *CNR-ICCOM & IPCF, Consiglio Nazionale delle Ricerche, Via Giuseppe Moruzzi 1, I-56124 Pisa, Italy. E-mail: alessandro.fortunelli@cnr.it*
[c] *Department of Chemistry, University of Padova, Via Marzolo 1, I-35131 Padova, Italy. E-mail: flavio.maran@unipd.it*
[d] *Department of Chemistry, University of Connecticut, 55 North Eagleville Road, Storrs, Connecticut 06269, USA*

† Electronic supplementary information (ESI) available: Syntheses' details and further spectra, molecular orbitals of the clusters with large contributions to the relevant spectral features, atomic coordinates employed in the calculations. See DOI: https://doi.org/10.1039/d4cp00789a

Open Access Article. Published on 07 June 2024. Downloaded on 9/30/2025 10:07:30 AM. This article is licensed under a Creative Commons Attribution-NonCommercial 3.0 Unported Licence.

The conclusions of that study were that the necessary conditions for a quantitative match between theory and experiment are: (i) use an accurate MPC geometry, *e.g.*, employing the experimental geometry (from X-ray diffraction) in the calculation to avoid inaccuracies due to QM structure prediction; (ii) employ a time dependent density functional theory (TDDFT) method that uses hybrid exchange–correlation (xc-) functionals (such as the B3LYP[40,41] xc-functional in both the Kohn–Sham equation and the response kernel).

More recently,[42] some of us have considered an even more stringent comparison regarding the hybrid B3LYP TDDFT scheme calculation and the low temperature (77 K) absorption spectrum of the $Ag_{24}Au(DMBT)_{18}^{-}$ anion. In that work an almost quantitative agreement was attained across the entire energy interval considered in the experimental spectral analysis. In particular, it was confirmed that the use of a hybrid xc-functional is mandatory to properly describe the low energy optical spectral region, where electronic transitions involving metal–ligand bonds play a major role. In contrast, GGA xc-functionals such as PBE[43] or even asymptotically correct xc-functionals such as LB94[44] gave a significantly worse agreement with experiment in the low energy region of the spectrum, although performing better at higher energies, which are dominated by ligand excitations. A previous complete study regarding the choice of the exchange–correlation functional[38] (as well the basis set and the geometry) has allowed to assess which are the principal requirements of TDDFT for the calculation of photoabsorption of MPCs. In general it was concluded that asymptotically corrected functionals like LB94 and SAOP perform much better than standard GGA, but the low energy region remains difficult to predict and can be properly described only by hybrid functionals like B3LYP. The accurate prediction of the optical response of MPCs represents a real challenge to theory, due the co-existence and, thus, coupling of three moieties with quite different electronic properties: (1) a metal core in a low-oxidation state; (2) the metal shell of the "staple" motifs that interacts with both metal core and ligands, (3) the ligands (thiolates, *etc.*). Indeed, it has been shown that the B3LYP hybrid xc-functional and kernel enable one to obtain a balanced description of the electronic structure of regions with such a different chemical nature.[37,38] It is worth stressing that a quantitative prediction of optical excitations in MPCs is particularly important for understanding properties and exploiting these compounds in view of applications, such as sensing and photocatalysis.[45]

The present work develops within this research framework. Our main goal consists in testing and extending the validation of the B3LYP scheme to a larger and more diverse set of clusters than previously investigated. The present study, where we vary the nature of the metal and the ligands, is particularly relevant to assess the predictivity of the previously proposed B3LYP scheme, as it is known[37] that the optical properties of MPC are affected by both the metal and the ligand components. We selected three metal clusters that share the same M_{25} metallic core structure but have different metal composition and ligands: $Ag_{25}(DMBT)_{18}^{-}$, $Ag_{24}Pt(DMBT)_{18}^{2-}$ and $Au_{24}Pt(SC_4H_9)_{18}$ where DMBT is 2,4-dimethylbenzenethiolate and SC_4H_9 is *n*-butylthiolate. These nanoclusters can be prepared with atomic precision and offer a diverse set of MPC compounds on which to test and validate our theoretical approach.

2. Theoretical method

To predict optical spectra, we employ the complex polarizability TDDFT (polTDDFT) algorithm.[46] This approach is able to treat very large systems by avoiding the bottleneck of the more traditional Casida diagonalization *via* a direct solution of the response equations, while still providing a very good accuracy when compared with the exact Casida solution.[38,47] The reader is referred to the original work for a detailed description of the algorithm[46] and its implementation in the AMS/ADF program.[48]

In practice, the photoabsorption spectrum $\sigma(\omega)$ is calculated point by point, from the imaginary part of the dynamical polarizability $\alpha(\omega)$:

$$\sigma(\omega) = \frac{4\pi\omega}{c}\mathrm{Im}[\alpha(\omega)] \quad (1)$$

This expression is of practical interest when the polarizability is calculated for complex frequency, *i.e.* $\omega = \omega_r + i\omega_i$, where the real part ω_r is the scanned photon frequency (energy) and ω_i is the imaginary part which corresponds to a Lorentzian broadening of the discrete lines and can be interpreted as a pragmatic inclusion of the excited states finite lifetime. The complex dynamical polarizability is calculated by solving the following non-homogeneous linear system, working with a basis set of density-fitting functions:

$$[\mathbf{S} - \mathbf{M}(\omega)]\mathbf{b} = \mathbf{d} \quad (2)$$

In eqn (2) **S** is the overlap matrix between fitting functions, **b** is the unknown vector with the expansion coefficients $b_\mu(\omega)$ of the time-dependent electron density $\rho_z^{(1)}$ induced by the electromagnetic field, **d** is the frequency dependent vector corresponding to the known non-homogeneous term, and finally the elements of the frequency dependent matrix **M** are:

$$M_{\mu\nu} = \langle f_\mu | \chi_{KS}(\omega) K | f_\nu \rangle \quad (3)$$

In eqn (3) χ_{KS} is the Kohn–Sham frequency-dependent dielectric function, K is the kernel, and f_μ and f_ν are the elements of the basis set of density-fitting functions. Note that the matrix element in eqn (3) is between density fitting functions, and therefore the present implementation of the algorithm allows one to employ only density-dependent kernels. For this reason, the density-matrix-dependent Hartree–Fock exchange kernel, which is an ingredient of hybrid xc-functionals, cannot directly be employed in polTDDFT. However, it is still possible to employ hybrid kernels with nonlocal Hartree–Fock exchange components if the hybrid diagonal approximation (HDA) is employed. The HDA method, which we have recently proposed,[49] to which we refer for further details is a very efficient and robust approximation to TDDFT: by correcting only the diagonal matrix elements for the non-local exchange, while including local-density exchange–correlation terms of the kernel in the off-diagonal elements, the computational complexity is drastically reduced while keeping an excellent accuracy.[49]

 This journal is © the Owner Societies 2024

Open Access Article. Published on 07 June 2024. Downloaded on 9/30/2025 10:07:30 AM. This article is licensed under a Creative Commons Attribution-NonCommercial 3.0 Unported Licence.

3. Experimental and computational details

[*n*-Oct$_4$N$^+$][Ag$_{25}$(DMBT)$_{18}^-$], [*n*-Oct$_4$N$^+$]$_2$[Ag$_{24}$Pt(DMBT)$_{18}^{2-}$], and Au$_{24}$Pt(SC$_4$H$_9$)$_{18}$ were synthetized according to known procedures,[50–52] with minor modifications (see ESI†).

Photoabsorption measurements were carried out with a near-infrared VARIAN Cary 60 spectrophotometer with a spectral resolution of 0.5 nm. The spectra were collected over a range of 250–900 nm. [*n*-Oct$_4$N$^+$][Ag$_{25}$(DMBT)$_{18}^-$] and [*n*-Oct$_4$N$^+$]$_2$[Ag$_{24}$Pt(DMBT)$_{18}^{2-}$] were dissolved in a 5 : 4 : 2 vol butyronitrile/propionitrile/dichloromethane solution, whereas Au$_{24}$Pt(SC$_4$H$_9$)$_{18}$ was dissolved in a 1 : 1 vol tetrahydrofuran/toluene solution; we verified that both solvent combinations form clear glasses at low temperatures. The solutions were adjusted to obtain an absorbance of 0.2 at 400 nm, using a 1 mm optical-path quartz cuvette. The temperature was controlled with an OptistatDN cryostat equipped with a MercuryiTC temperature controller (Oxford Instrument). A HiCube 80 Eco, DN 63 ISO-K turbo pumping station (PFEIFFER Vacuum) was used to generate a high vacuum inside the outer vacuum chamber of the cryostat. Before experiment, the sample holder was purged with high-purity helium, which was used as the temperature-exchange gas.

The cluster geometries used to perform TDDFT simulations were taken from the corresponding experimental X-ray structures.[51] The geometries were partially optimized in the ligand coordinates, while freezing the metal and sulfur atoms at their experimental geometry.

Geometry relaxations were performed using the CP2K package[53] at the DFT/PBE level[43] with the addition of the Grimme-D3 dispersion terms.[54] DFT simulations, based on the hybrid Gaussian/plane-wave scheme (GPW),[55] employed double-zeta-valence-plus polarization (DZVP) basis sets[56] to represent the DFT Kohn–Sham orbitals, GTH pseudopotentials for describing the core-electrons of all the atomic species,[57] and an auxiliary set of plane-waves whose cut-off was set to 300 Ry.

From these geometries, optical-response TDDFT calculations were performed with the version 2023.01 of the Amsterdam modeling suite (AMS)[58] set of programs,[59,60] employing a basis set of Slater type orbitals (STO) functions of Triple Zeta plus polarization (TZP) quality and optimized density fitting functions.[61] Scalar relativistic effects were included *via* the Zero order regular approximation[62] (ZORA). The hybrid B3LYP xc-functional was employed, which includes a portion of Hartree–Fock non-local exchange and provides consistently the most accurate predictions among DFT approaches. In this work, we employed the resolution of the identity (RI) technique to calculate the B3LYP HDA exchange integrals, as recently implemented in version 2023.01 of AMS.[63] Such implementation, known as 'fitted HDA', allows a speedup up to a factor of 30 in the calculation of integrals with respect to the previous version that used numerical quadrature. The polTDDFT results were broadened by a Lorentzian function to obtain 0.150 eV of FWHM. An imaginary frequency ω_i of 0.075 eV was employed in eqn (1).

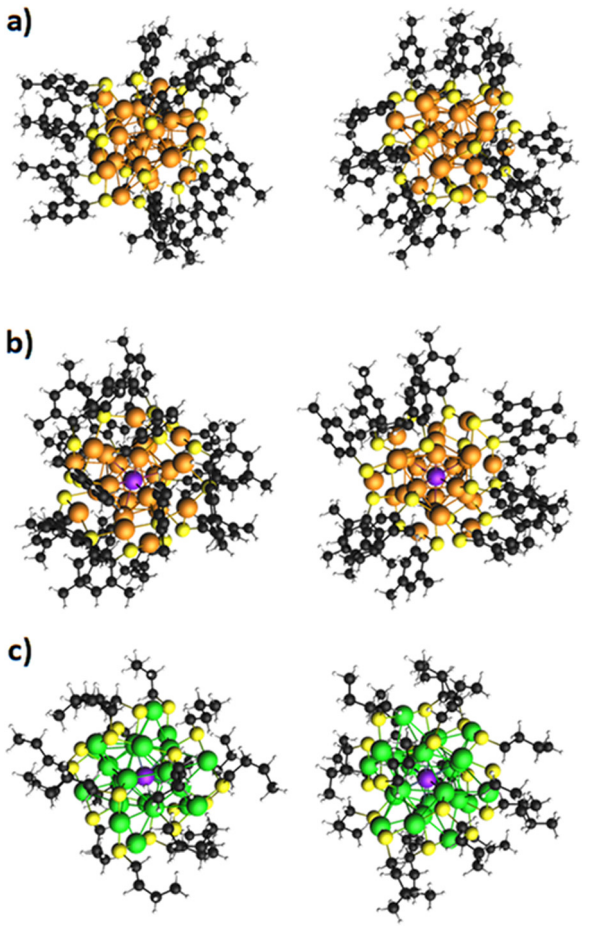


Fig. 1 Geometries of the clusters (a) Ag$_{25}$(DMBT)$_{18}^-$, (b) Ag$_{24}$Pt(DMBT)$_{18}^{2-}$, and (c) Au$_{24}$Pt(SC$_4$H$_9$)$_{18}$.

4. Results and discussion

4.1. Cluster structures

Fig. 1 shows a schematic depiction of the structures of the three clusters, each one taken from two different points of view. The systems are characterized by the typical M_{25} structure which can be briefly described as follows:[64] (1) one metal atom is in the center of the cluster; (2) 12 metal atoms form an icosahedron around the central atom; (c) a shell of ligands consisting of six 'staple' units -SR-M-SR-M-SR- protects the inner metal core. In the cluster series here considered: Ag$_{25}$(DMBT)$_{18}^-$, Ag$_{24}$Pt(DMBT)$_{18}^{2-}$ and Au$_{24}$Pt(SC$_4$H$_9$)$_{18}$, the first compound is a monometallic silver cluster, while the next terms correspond to monodoped silver and gold clusters respectively, where the central Au or Ag atom is replaced by a Pt atom. As to the ligand, whereas the first two clusters are protected by the typical aromatic DMBT ligand, SC$_4$H$_9$, is aliphatic and this may have effects on the optical properties. Indeed, it has been shown[65] that aromatic thiolates can promote a plasmon 'rebirth' already at cluster sizes that would not yet be plasmonic. Although the first cluster is anionic, the second is dianionic, and the last one is neutral, they all display a closed-shell electronic structure.

Open Access Article. Published on 07 June 2024. Downloaded on 9/30/2025 10:07:30 AM.
This article is licensed under a Creative Commons Attribution-NonCommercial 3.0 Unported Licence.

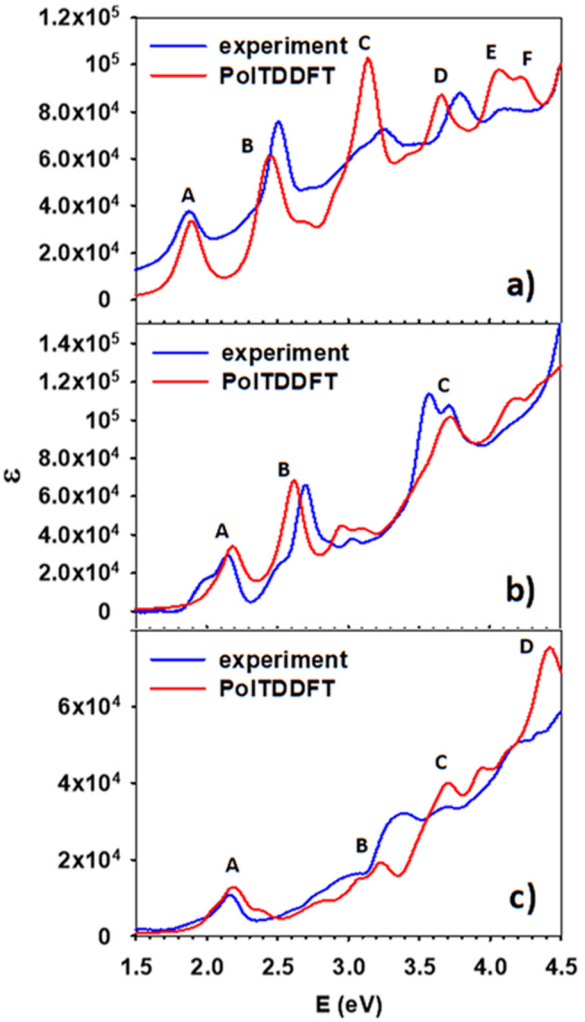


Fig. 2 Comparison between experimental and calculated photoabsorption of the clusters (a) $Ag_{25}(DMBT)_{18}^-$, (b) $Ag_{24}Pt(DMBT)_{18}^{2-}$, and (c) $Au_{24}Pt(SC_4H_9)_{18}$.

4.2. Cluster selection and comparison with experiment

Fig. 2 shows the calculated photoabsorption of the three clusters calculated at the TDDFT level, as described in Sections 2 and 3, and the experimental spectra obtained at 77 K. The intensity scale is absolute for the calculated profiles, whereas the experimental profile intensity has been rescaled to achieve a best match with the calculated profile and compare the intensity of the calculated profile across different clusters. To have a more general perspective, we start by discussing the whole series, and defer the discussion of the single terms of the series to the following sections.

First, we observe that for all three clusters a fairly nice agreement between theory and experiment holds. All the experimental features are properly reproduced by theory, with modest energy shifts of few tenth of eV and a rather accurate distribution of intensities, with only occasional deterioration. These finding provide a strict validation of our theory approach, demonstrating that the fitted HDA B3LYP polTDDFT scheme can attain quantitative accuracy even with

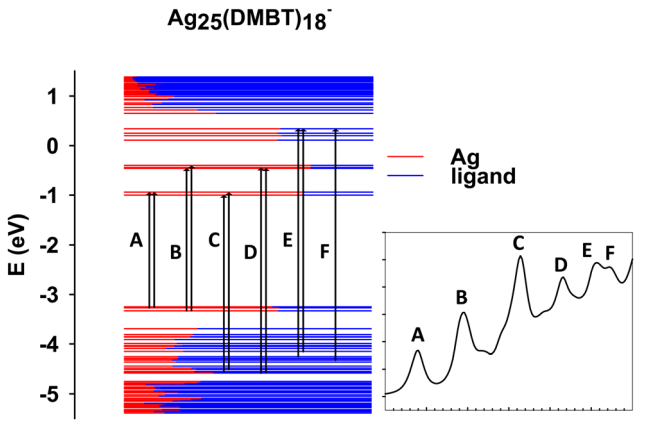


Fig. 3 Scheme with the most important occupied-virtual configurations involved in the transitions in $Ag_{25}(DMBT)_{18}^-$. The labels refer to specific features as reported in the inset. The color of the levels represents the nature of the molecular orbitals in terms of fragments (see legend).

metal doping and with different ligand nature and electronic effects.

Considering the trend of the spectra along the series, we notice that whereas $Ag_{25}(DMBT)_{18}^-$ and $Ag_{24}Pt(DMBT)_{18}^{2-}$ display a photoabsorption spectrum very rich of spectral features, with many well resolved bands and maxima, the spectrum of $Au_{24}Pt(SC_4H_9)_{18}$, aside from the region at low energy, is much less structured, consisting mainly of weak shoulders superimposed to a background smoothly increasing with energy.

4.3. $Ag_{25}(DMBT)_{18}^-$

In this section we focus on the specific analysis of the photoabsorption of $Ag_{25}(DMBT)_{18}^-$. Fig. 3 shows a schematic picture of the main features (designated by the same capital letters from A to F as in Fig. 2a, as described in the inset), whereas Table 1 provides for each spectral feature the main contributions in terms of electronic configurations. From Fig. 2a it appears that the theory generally underestimates the experimental absorption energy: for the features A, E and F the difference is less than 0.1 eV, whereas a slightly larger disagreement is found for the other features, the largest deviation of 0.13 eV being found for feature D. The shape of the peaks is very well reproduced by theory, but for peak C where a quite sharper shape is predicted: this difference could be attributed to vibrational broadening or to a deficiency in the description of the electronic structure of the cluster. Regarding the assignment of the transitions, peaks A and B have a character very close to HOMO/LUMO excitations, ranging from HOMO−2 to LUMO+4. Interestingly, their energy difference is attributed mainly to the different energy of the virtual orbitals, which are grouped in two close groups separated by about 0.5 eV (see Fig. 3). All these orbitals have large silver contribution (see also the molecular orbital plots in Fig. S1 and S2 of the ESI†) that is especially large in LUMO and LUMO+1. We can describe the character of these orbitals as Ag–S σ-bonds for the HOMO, HOMO−1 and HOMO−2, whereas those from LUMO and LUMO+4 mainly pertain to Ag atoms only. With this picture in mind, we can

 This journal is © the Owner Societies 2024

Open Access Article. Published on 07 June 2024. Downloaded on 9/30/2025 10:07:30 AM.
This article is licensed under a Creative Commons Attribution-NonCommercial 3.0 Unported Licence.

Table 1 Analysis of the spectral features of $Ag_{25}(DMBT)_{18}^-$. Label feature, calculated and experimental energy (eV), calculated molar absorption (M^{-1} cm^{-1}) and assignment

Excitation	Excitation E (eV)	Experimental E (eV)	ϵ	Assignment
A	1.90	1.88	33 555	56.61% HOMO−1 (32% Ag 5s, 21% S 3p, 8% Ag 5p) → LUMO+1 (29% Ag 5s, 15% Ag 5p, 4% S 3p, 1% Ag 4d); 30.54% HOMO (28% Ag 5s, 20% S 3p, 7% Ag 5p) → LUMO+1
B	2.46	2.51	61 256	21.50% HOMO−2 (31% Ag 5s, 18% S 3p, 7% Ag 5p, 5% Ag 4d) → LUMO+2 (25% Ag 5p, 23% Ag 5s, 6% S 3p, 1% Ag 4d); 15.26% HOMO → LUMO+4 (26% Ag 5p, 22% Ag 5s, 6% S 3p, 1% Ag 4d); 11.51% HOMO−2 → LUMO+4
C	3.16	3.22	102 811	24.56% HOMO−22 (38% S 3p, 6% Ag 4d, 2% Ag 5s) → LUMO+1; 16.32% HOMO−20 (27% S 3p, 3% Ag 5s) → LUMO+1
D	3.66	3.79	87 273	8.91% HOMO−23 (34% S 3p, 5% Ag 4d, 4% Ag 5s) → LUMO+3 (29% Ag 5p, 7% S 3p, 2% Ag 5s, 1% Ag 4d); 8.31% HOMO−22 → LUMO+2
E	4.06	4.07	97 827	10.19% HOMO−13 (34% S 3p, 2% C 2p, 1% Ag 4d) → LUMO+8 (28% Ag 5p, 9% Ag 5s, 1% C 2p); 8.89% HOMO−12 (32% S 3p, 1% C 2p) → LUMO+8
F	4.22	4.15	94 691	32.53% HOMO−16 (29% S 3p, 5% Ag 5s, 4% Ag 4d, 1% C 2p) → LUMO+8

attribute the A and B features to transitions from Ag–S σ-bonds to the metal core. B is more intense due to the largest metal contribution in the final virtual orbitals. C is the most intense band, whereas in the experiment it is more broadened as already noted. This feature is attributed to transitions starting from rather deep occupied orbitals (HOMO−20, HOMO−21) with major ligand character (Fig. S1, ESI†). The nature of the C band can also explain why it is so broadened in the experiment: the mainly ligand character of the occupied orbitals is conceivably more sensitive to their conformational freedom, which in solution is particularly relevant for the ligands but is much less important for the metal core.[66,67] The next E and F features are less pronounced, with the orbitals involved in such transition localized mainly on the ligands.

4.4. $Ag_{24}Pt(DMBT)_{18}^{2-}$

Here we focus on the first doped cluster of the series, namely $Ag_{24}Pt(DMBT)_{18}^{2-}$. Fig. 4 shows the scheme of the molecular orbital energy levels together with the main spectral features (A, B and C), whereas the main contributions in terms of electronic configurations are reported in Table 2. Fig. 2b illustrates that the theory reproduces remarkably well the spectral window here considered, with the position of the three peaks in quantitative agreement with experiment, and the largest deviation for peak C limited to only 0.15 eV. Furthermore, the intensity distribution is quite accurately predicted by theory, and it is also worth noting that the profile shape between the peaks follows very closely the experimental trend. The energy levels from Fig. 4 give a situation qualitatively like the previous pure silver cluster: the A and B bands again start from the same group of occupied orbitals (HOMO, HOMO−1 and HOMO−2) but arrive to two different groups of virtual orbitals, separated by about 0.3 eV (LUMO and LUMO+1 for feature A and LUMO+2 and LUMO+3 and LUMO+4 for feature B). Interestingly, in comparison with $Ag_{25}(DMBT)_{18}^-$, the nature of the transitions is the same but both transitions are blue shifted, which is a consequence of the larger HOMO/LUMO gap as well as the smaller separation between virtual states involved in features A and B. It is worth noting that the calculated shape of the peak C of the present cluster is in very good agreement with the experiment, at variance of previous Ag_{25} cluster where the experimental peak was strongly broadened. We attributed the strong broadening to a consequence of the ligand conformational freedom. Therefore it is interesting to argue if this different behavior could be ascribed to the Pt doping and/or to the charge of the cluster, since the rest of the system (such as the Ag geometry and the ligand nature) is the same. Indeed, the Pt–Ag bonds are much more 'directional' and stronger than Ag–Ag bonds, due to the role played by the Pt 5d orbitals, whereas in Ag the 4d orbitals are deeper in energy and play a very minor role in the chemical bond formed by Ag. Moreover, the larger charge of the Pt–Ag cluster should entail a larger 'pressure' by the solvent, which should also compress the ligands' degrees of freedom. This enhanced 'Pt–Ag bond directionality' together with a larger environmental pressure should inhibit the conformational freedom of the ligands giving a sharper peak.

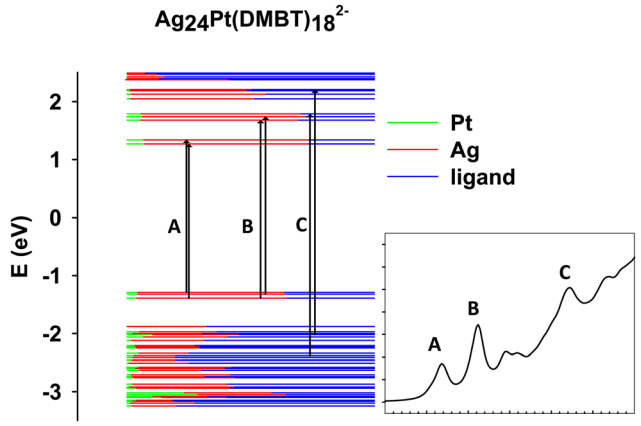


Fig. 4 Scheme with the most important occupied-virtual configurations involved in the transitions in $Ag_{24}Pt(DMBT)_{18}^{2-}$. The labels refer to specific features as reported in the inset. The color of the levels represent the nature of the molecular orbitals in terms of fragments (see legend).

In summary, the computational model describes properly the optical behavior, ascribing the observed differences to the presence of the Pt atom. The Pt contribution remains below 10% in all the orbitals considered, except for some that are rather deep, around −3 eV, and do not contribute appreciably to the spectral features. Incidentally, the Pt atom participates mainly with the 5d electrons, which are rather diffuse, thereby

Open Access Article. Published on 07 June 2024. Downloaded on 9/30/2025 10:07:30 AM.
This article is licensed under a Creative Commons Attribution-NonCommercial 3.0 Unported Licence.

Table 2 Analysis of the spectral features of $Ag_{24}Pt(DMBT)_{18}^{2-}$. Label feature, calculated and experimental energy (eV), calculated molar absorption (M^{-1} cm^{-1}) and assignment

Excitation	Excitation E (eV)	Experimental E (eV)	ϵ	Assignment
A	2.18	2.15	34 131	37.37% HOMO (28% Ag 5s, 20% S 3p, 3% Ag 4d, 3% Pt 6p, 2% Ag 5p) → LUMO+1 (26% Ag 5s, 19% Ag 5p, 6% Pt 5d); 18.90% HOMO−2 (31% Ag 5s, 18% S 3p, 6% Ag 5p, 2% Pt 6s) → LUMO
B	2.62	2.70	68 651	24.62% HOMO−2 → LUMO+2 (21% Ag 5p, 19% Ag 5s, 4% Pt 5d, 1% S 3p); 22.00% HOMO−1 → LUMO+3 (23% Ag 5s, 25% Ag 5p, 3% Pt 5d, 3% S 3p)
C	3.72	3.58	101 702	10.65% HOMO−13 (29% S 3p, 16% C 2p, 1% Pt 5d) → LUMO+4 (22% Ag 5p, 19% Ag 5s, 4% Pt 5d, 2% S 3p); 9.10% HOMO−6 (27% S 3p, 9% Pt 5d, 7% Ag 4d, 3% Ag 5s, 1% C 2p) → LUMO+8 (16% Ag 5p, 8% Ag 5s, 1% C 2p)

providing kind of an 'electron reservoir'. We can conclude that for this cluster the spectral difference with respect to the silver cluster can be rationalized in terms of the nature of the central atom.

4.5. $Au_{24}Pt(SC_4H_9)_{18}$

The last compound considered in this work consists of a neutral gold cluster protected by alkyl ligands and doped with Pt, $Au_{24}Pt(SC_4H_9)_{18}$. Fig. 5 shows the molecular-orbital energy levels, with the main features (A, B, C and D) analyzed in Table 3 in terms of leading electronic configurations. From the previous Fig. 2c, it appears that the theory reproduces quantitatively the peak A at low energy (2.2 eV). At higher energy the photoabsorption profile is not as highly structured as in the two silver-based clusters but is much smoother. Only weak shoulders are predicted to show up in the energy range 3.2–3.7 eV, which is in satisfactory agreement with experiment. For this cluster, the theoretical spectrum is blue shifted with respect to the experiment by few tenths of eV. The predicted feature D is unfortunately outside the experimental energy interval, and thus, we do not have an experimental counterpart for comparison. Also for this cluster it is worth noting that, despite a minor disagreement in the energy positions of features B and C, the calculated intensity profile resembles closely the experimental shape, which features a typical 'step' behavior. In the present work we did not consider the corresponding pure gold clusters, as they have already been the object of previous extensive experimental and theoretical studies,[48,64,68] and thus we can profitably compare the present results on the Au/Pt nanoalloy with the photoabsorption spectrum of $Au_{25}(SR)_{18}^-$ measured at room temperature[68] and the absorption spectrum we previously calculated at the TDDFT B3LYP HDA level.[49] Note that in ref. 49 the experimental R = $CH_2CH_2C_6H_5$ ligand was simplified as R = CH_3 in the calculations, but keeping the experimental geometry, in such a way that the alkyl ligand nature was preserved (important to describe properly the optical spectrum). This comparison indicates that Pt doping shifts the A feature to higher energy from 1.8 eV in $Au_{25}(SR)_{18}^-$ to 2.2 eV in $Au_{24}Pt(SC_4H_9)_{18}$ in both experiment and calculations. In the experimental $Au_{25}(SR)_{18}^-$ spectrum other less pronounced features appear at 2.75, 3.1 and 3.9 eV, all of them shifted at higher energy in $Au_{24}Pt(SC_4H_9)_{18}$ by about 0.5–0.6 eV on average. We conclude that Pt doping definitely promotes a blue shift of the spectral features by about 0.4–0.6 eV depending on the specific structure, in both Ag as well as Au clusters.

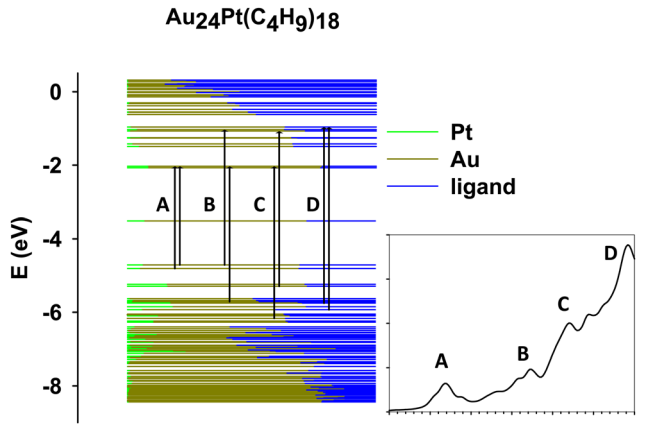


Fig. 5 Scheme with the most important occupied-virtual configurations involved in the transitions in $Au_{24}Pt(SC_4H_9)_{18}$. The labels refer to specific features as reported in the inset. The color of the levels represent the nature of the molecular orbitals in terms of fragments (see legend).

5. Conclusions

The photoabsorption spectra of three MPC compounds with different alloy nature and ligands: $Ag_{25}(DMBT)_{18}^-$, $Ag_{24}Pt(DMBT)_{18}^{2-}$ and $Au_{24}Pt(SC_4H_9)_{18}$, where DMBT is 2,4-dimethylbenzenethiolate and SC_4H_9 is *n*-butylthiolate, have been measured at low temperature (77 K) in order to better resolve single optical peaks and compare them with state-of-the-art theoretical simulations at the TDDFT level of theory using hybrid xc-functional and experimentally-derived geometries. For all three cases, we find an excellent match between theory and experiment, with typical deviations being less than 0.1 eV, occasionally reaching 0.2 eV. This result provides a stringent validation of the proposed computational protocol. In addition to validated accuracy, the calculations are analyzed to assign the relevant spectra features, ascribing them to specific transitions between occupied-virtual orbital pairs. It is found that doping by Pt has an important effect on the spectra, shifting the spectral features to higher energy by about 0.4 eV, for both silver and gold clusters. Future developments of the present work would be towards metal clusters containing atoms of different nature with respect to the present ones, as well as ligands different from thiols. This would help to trace more general conclusions regarding the transferability of the method. Moreover

 This journal is © the Owner Societies 2024

Open Access Article. Published on 07 June 2024. Downloaded on 9/30/2025 10:07:30 AM. This article is licensed under a Creative Commons Attribution-NonCommercial 3.0 Unported Licence.

Table 3 Analysis of the spectral features of $Au_{24}Pt(SC_4H_9)_{18}$. Label feature, calculated and experimental energy (eV), calculated molar absorption (M^{-1} cm^{-1}) and assignment

Excitation	Excitation E (eV)	Experimental E (eV)	ϵ	Assignment
A	2.20	2.16	12 804	34.51% HOMO−1 (17% Au 6s, 17% S 3p, 8% Au 5d, 5% Pt 6p) → LUMO+2 (29% Au 6s, 15% Au 6p, 9% Pt 5d, 2% S 3p); 25.04% HOMO (23% S 3p, 15% Au 6s, 11% Au 5d, 7% Pt 6p, 4% Au 6p) → LUMO+2
B	3.24	3.06	19 247	17.44% HOMO → LUMO+8 (25% Au 6p, 9% Au 6s, 6% S 3p, 1% C 2p, 1% H 2s); 15.88% HOMO−6 (30% S 3p, 11% Au 5d, 1% Pt 5d) → LUMO+2
C	3.70	3.40	40 118	16.24% HOMO−14 (20% S 3p, 18% Au 5d, 12% Au 6s) → LUMO+2; 14.65% HOMO−3 (16% Pt 5d, 14% Au 5d, 10% S 3p, 8% Au 6s) → LUMO+7 (30% Au 6p, 13% Au 6s, 3% S 3p)
D	4.42	—	75 502	8.05% HOMO−8 (17% Pt 5d, 16% Au 5d, 14% S 3p, 1% Au 6s) → LUMO+9 (28% Au 6p, 2% Au 6s, 2% S 3p); 6.91% HOMO−10 (26% S 3p, 17% Au 5d, 7% Au 6s, 4% Pt 5d, 1% Pt 7s) → LUMO+9

future inclusion of range-separated xc-functionals, necessary to describe charge transfer excitations, is under consideration.

Conflicts of interest

There are no conflicts of interest to declare.

Acknowledgements

Computational support from CINECA supercomputing center within the ISCRA program is gratefully acknowledged. The authors are grateful to the Stiftung Beneficentia for a generous grant employed to set up a computational server. Support from Trieste University within the FRA programme is gratefully acknowledged. Financial support from ICSC – Centro Nazionale di Ricerca in High Performance Computing, Big Data and Quantum Computing, funded by European Union – NextGenerationEU is gratefully acknowledged. Financial support from MIUR of Italy under the PRIN 2022 project COCAP funded by European Union – NextGenerationEU is gratefully acknowledged. Networking within the COST Action CA21101 ''Confined molecular systems: from a new generation of materials to the stars'' (COSY) supported by COST (European Cooperation in Science and Technology) is gratefully acknowledged. Experimental work was financially supported by the Italian Ministero dell'Università e della Ricerca (PRIN2022 ''ProNano4Bio'' grant 2022RSXC9X) and the University of Padova (Supporting Talent in Research – STARS ''TimeForResponse'' grant 166081). Tiziano Dainese is thanked for his help in the syntheses of the two silver clusters.

References

1 R. L. Whetten, J. T. Khoury, M. M. Alvarez, S. Murthy, I. Vezmar, Z. L. Wang, P. W. Stephens, C. L. Cleveland, W. D. Luedtke and U. Landman, *Adv. Mater.*, 1996, **8**, 428.
2 P. D. Jadzinsky, G. Calero, C. J. Ackerson, D. A. Bushnell and R. D. Kornberg, *Science*, 2007, **318**, 430.
3 J. Akola, M. Walter, R. L. Whetten, H. Häkkinen and H. Grönbeck, *J. Am. Chem. Soc.*, 2008, **130**, 3756.
4 M. W. Heaven, A. Dass, P. S. White, K. M. Holt and R. W. Murray, *J. Am. Chem. Soc.*, 2008, **130**, 3754.
5 H. Qian, W. T. Eckenhoff, Y. Zhu, T. Pintauer and R. Jin, *J. Am. Chem. Soc.*, 2010, **132**, 8280.
6 O. Lopez-Acevedo, H. Tsunoyama, T. Tsukuda, H. Häkkinen and C. M. Aikens, *J. Am. Chem. Soc.*, 2010, **132**, 8210.
7 C. Zeng, H. Qian, T. Li, G. Li, N. L. Rosi, B. Yoon, R. N. Barnett, R. L. Whetten, U. Landman and R. Jin, *Angew. Chem.*, 2012, **51**, 13114.
8 I. Dolamic, S. Knoppe, A. Dass and T. Bürgi, *Nat. Commun.*, 2012, **3**, 798.
9 Y. Negishi, C. Sakamoto, T. Ohyama and T. Tsukuda, *J. Phys. Chem. Lett.*, 2012, **3**, 1624.
10 A. Desireddy, B. E. Conn, J. Guo, B. Yoon, R. N. Barnett, B. M. Monahan, K. Kirschbaum, W. P. Griffith, R. L. Whetten, U. Landman and T. P. Bigioni, *Nature*, 2013, **501**, 399.
11 S. Mustalahti, P. Myllyperkiö, T. Lahtinen, K. Salorinne, S. Malola, J. Koivisto, H. Häkkinen and M. Pettersson, *J. Phys. Chem. C*, 2014, **118**, 18233.
12 A. Dass, S. Theivendran, P. R. Nimmala, C. Kumara, V. R. Jupally, A. Fortunelli, L. Sementa, G. Barcaro, X. Zuo and B. C. Noll, *J. Am. Chem. Soc.*, 2015, **137**, 4610.
13 A. Fernando, K. L. D. M. Weerawardene, N. V. Karimova and C. M. Aikens, *Chem. Rev.*, 2015, **115**, 6112.
14 W. Kurashige, Y. Niihori, S. Sharma and Y. Negishi, *Coord. Chem. Rev.*, 2016, **320–321**, 238.
15 R. Jin, C. Zeng, M. Zhou and Y. Chen, *Chem. Rev.*, 2016, **116**, 10346.
16 N. A. Sakthivel, S. Theivendran, V. Ganeshraj, A. G. Oliver and A. Dass, *J. Am. Chem. Soc.*, 2017, **139**, 15450.
17 M. Rambukwella, N. A. Sakthivel, J. H. Delcamp, L. Sementa, A. Fortunelli and A. Dass, *Front. Chem.*, 2018, **6**, 330.
18 T. Dainese, S. Antonello, S. Bogialli, W. Fei, A. Venzo and F. Maran, *ACS Nano*, 2018, **12**, 7057.
19 Z. Lei, J. J. Li, X. K. Wan, W. H. Zhang and Q. M. Wang, *Angew. Chem.*, 2018, **57**, 8639.
20 M. A. Abbas, P. V. Kamat and J. H. Bang, *ACS Energy Lett.*, 2018, **3**, 840.
21 N. A. Sakthivel, M. Shabaninezhad, L. Sementa, B. Yoon, M. Stener, R. L. Whetten, G. Ramakrishna, A. Fortunelli, U. Landman and A. Dass, *J. Am. Chem. Soc.*, 2020, **142**, 15799.
22 C. A. Hosier, I. D. Anderson and C. J. Ackerson, *Nanoscale*, 2020, **12**, 6239.

Open Access Article. Published on 07 June 2024. Downloaded on 9/30/2025 10:07:30 AM. This article is licensed under a Creative Commons Attribution-NonCommercial 3.0 Unported Licence.

23 T. Kawawaki, A. Ebina, Y. Hosokawa, S. Ozaki, D. Suzuki, S. Hossain and Y. Negishi, *Small*, 2021, 2005328.
24 J. V. Rival, P. Mymoona, K. M. Lakshmi Nonappa, T. Pradeep and E. S. Shibu, *Small*, 2021, 2005718.
25 T. Dainese, M. Agrachev, S. Antonello, D. Badocco, D. M. Black, A. Fortunelli, J. A. Gascón, M. Stener, A. Venzo, R. L. Whetten and F. Maran, *Chem. Sci.*, 2018, **9**, 8796.
26 M. Agrachev, M. Ruzzi, A. Venzo and F. Maran, *Acc. Chem. Res.*, 2019, **52**, 44.
27 M. Agrachev, W. Fei, S. Antonello, S. Bonacchi, T. Dainese, A. Zoleo, M. Ruzzi and F. Maran, *Chem. Sci.*, 2020, **11**, 3427.
28 E. Boisselier and D. Astruc, *Chem. Soc. Rev.*, 2009, **38**, 1759.
29 U. H. F. Bunz and V. M. Rotello, *Angew. Chem.*, 2010, **49**, 3268.
30 Y. Du, H. Sheng, D. Astruc and M. Zhu, *Chem. Rev.*, 2020, **120**, 526.
31 R. Jin, G. Li, S. Sharma, Y. Li and X. Du, *Chem. Rev.*, 2021, **121**, 567.
32 A. Tlahuice-Flores, *Phys. Chem. Chem. Phys.*, 2016, **18**, 27738.
33 C. M. Aikens, *Acc. Chem. Res.*, 2018, **51**, 3065.
34 K. L. D. M. Weerawardene and C. M. Aikens, *Phys. Chem. C*, 2018, **122**, 2440.
35 K. L. D. M. Weerawardene and C. M. Aikens, *J. Am. Chem. Soc.*, 2016, **138**, 11202.
36 G. Barcaro, L. Sementa, A. Fortunelli and M. Stener, *Phys. Chem. Chem. Phys.*, 2015, **17**, 27952.
37 A. Dass, T. Jones, M. Rambukwella, D. Crasto, K. Gagnon, L. Sementa, M. De Vetta, O. Baseggio, E. Aprà, M. Stener and A. Fortunelli, *J. Phys. Chem. C*, 2016, **120**, 6256.
38 O. Baseggio, M. De Vetta, G. Fronzoni, D. Toffoli, M. Stener, L. Sementa and A. Fortunelli, *Int. J. Quantum Chem.*, 2018, **118**, e25769.
39 H.-Ch Weissker, H. Barron Escobar, V. D. Thanthirige, K. Kwak, D. Lee, G. Ramakrishna, R. L. Whetten and X. López-Lozano, *Nat. Commun.*, 2014, **5**, 3785.
40 A. D. Becke, *J. Chem. Phys.*, 1993, **98**, 5684.
41 P. J. Stephens, F. J. Devlin, C. F. Chabalowski and M. J. Frisch, *J. Phys. Chem.*, 1994, **98**, 11623.
42 M. Medves, L. Sementa, D. Toffoli, G. Fronzoni, K. R. Krishnadas, T. Bürgi, S. Bonacchi, T. Dainese, F. Maran, A. Fortunelli and M. Stener, *J. Chem. Phys.*, 2021, **155**, 084103.
43 J. P. Perdew, K. Burke and M. Ernzerhof, *Phys. Rev. Lett.*, 1996, **77**, 3865.
44 R. Van Leeuwen and E. J. Baerends, *Phys. Rev. A*, 1994, **49**, 2421.
45 S. Linic, P. Christopher and D. B. Ingram, *Nat. Mater.*, 2011, **10**, 911.
46 O. Baseggio, G. Fronzoni and M. Stener, *J. Chem. Phys.*, 2015, **143**, 024106.
47 O. Baseggio, M. De Vetta, G. Fronzoni, M. Stener, L. Sementa, A. Fortunelli and A. Calzolari, *J. Phys. Chem. C*, 2016, **120**, 12773.
48 O. Baseggio, M. De Vetta, G. Fronzoni, M. Stener and A. Fortunelli, *Int. J. Quantum Chem.*, 2016, **116**, 1603.
49 M. Medves, L. Sementa, D. Toffoli, G. Fronzoni, A. Fortunelli and M. Stener, *J. Chem. Phys.*, 2020, **152**, 184102.
50 M. S. Bootharaju, C. P. Joshi, M. R. Parida, O. F. Mohammed and O. M. Bakr, *Angew. Chem., Int. Ed.*, 2016, **55**, 922.
51 X. Liu, J. Yuan, C. Yao, J. Chen, L. Li, X. Bao, J. Yang and Z. Wu, *J. Phys. Chem. C*, 2017, **121**, 13848.
52 W. Fei, S. Antonello, T. Dainese, A. Dolmella, M. Lahtinen, K. Rissanen, A. Venzo and F. Maran, *J. Am. Chem. Soc.*, 2019, **141**, 16033.
53 J. Hutter, M. Iannuzzi, F. Schiffmann and J. VandeVondele, *Wiley Interdiscip. Rev.: Comput. Mol. Sci.*, 2014, **4**, 15.
54 S. Grimme, J. Antony, S. Ehrlich and H. Krieg, *J. Chem. Phys.*, 2010, **132**, 154104.
55 G. Lippert, J. Hutter and M. Parrinello, *Theor. Chem. Acc.*, 1999, **103**, 124.
56 J. VandeVondele and J. Hutter, *J. Chem. Phys.*, 2007, **127**, 114105.
57 S. Goedecker, M. Teter and J. Hutter, *Phys. Rev. B*, 1996, **54**, 1703.
58 **https://www.scm.com/product/ams**.
59 E. J. Baerends, D. E. Ellis and P. Ros, *Chem. Phys.*, 1973, **2**, 41.
60 C. Fonseca Guerra, J. G. Snijders, G. Te Velde and E. J. Baerends, *Theor. Chem. Accounts*, 1998, **99**, 391.
61 M. Medves, G. Fronzoni and M. Stener, *J. Comput. Chem.*, 2022, **43**, 1923.
62 E. Van Lenthe, E. J. Baerends and E. J. J. G. Snijders, *J. Chem. Phys.*, 1993, **99**, 4597.
63 P. D'Antoni, M. Medves, D. Toffoli, A. Fortunelli, M. Stener and L. Visscher, *J. Phys. Chem. A*, 2023, **127**, 9244.
64 M. W. Heaven, A. Dass, P. S. White, K. M. Holt and R. W. Murray, *J. Am. Chem. Soc.*, 2008, **130**, 3754.
65 L. Sementa, G. Barcaro, O. Baseggio, M. De Vetta, A. Dass, E. Aprà, M. Stener and A. Fortunelli, *J. Phys. Chem. C*, 2017, **121**, 10832.
66 M. Monti, G. Brancolini, E. Coccia, D. Toffoli, A. Fortunelli, S. Corni, M. Aschi and M. Stener, *J. Phys. Chem. Lett.*, 2023, **14**, 1941.
67 M. Monti, M. F. Matus, S. Malola, A. Fortunelli, M. Aschi, M. Stener and H. Häkkinen, *ACS Nano*, 2023, **17**, 11481.
68 M. Zhu, C. M. Aikens, F. J. Hollander, G. Schatz and R. Jin, *J. Am. Chem. Soc.*, 2008, **130**, 5883.

 This journal is © the Owner Societies 2024

4.1.3 Damped Linear Response TDDFT with Range-Separated Functionals and Density Fitting

After establishing the computational efficiency and quantitative accuracy of the RI-accelerated Hybrid Diagonal Approximation (RI/HDA) for global hybrid exchange–correlation functionals, the present work extends the applicability of the method to the more general and demanding class of range-separated (RS) hybrid functionals. This development represents a necessary step to enable an accurate description of electronic excitations with pronounced long-range and charge-transfer character within an efficient TDDFT framework.

Range-separated functionals are known to overcome intrinsic limitations of global hybrids in the description of charge-transfer excitations, owing to their correct asymptotic treatment of the nonlocal exchange interaction. However, their application at the TDDFT level is computationally challenging, particularly when non-Gaussian basis sets are employed and when the nonlocal exchange kernel must be evaluated explicitly. Within this context, extending the RI/HDA strategy to RS kernels allows one to retain the favorable accuracy of range-separated TDDFT while maintaining a computational cost comparable to that of a hybrid DFT single-point calculation.

In this work, the RI/HDA formulation is generalized to RS exchange–correlation functionals within both the Casida and polTDDFT implementations available in the AMS/ADF suite. The method is assessed on two representative systems that exhibit charge-transfer excitations of increasing complexity: a prototypical model system commonly used for benchmarking charge-transfer transitions, and a realistic donor–acceptor–acceptor molecular triad for which high-quality experimental photoabsorption data are available. In both cases, the comparison with reference TDDFT calculations and experimental spectra demonstrates that the proposed approach accurately reproduces excitation energies and spectral profiles.

Overall, this study demonstrates that the RI/HDA scheme can be consistently extended to range-separated hybrid functionals without compromising accuracy, thereby broadening the scope of applicability of the method. The results confirm that polTDDFT combined with RI and RS hybrid functionals provides a reliable and computationally efficient strategy for the simulation of optical spectra in systems where charge-transfer effects play a dominant role, paving the way for future applications to larger and more complex molecular assemblies.

THE JOURNAL OF PHYSICAL CHEMISTRY A
A JOURNAL OF THE AMERICAN CHEMICAL SOCIETY

Open Access
This article is licensed under CC-BY 4.0

pubs.acs.org/JPCA
Article

Damped Linear Response TDDFT with Range-Separated Functionals and Density Fitting

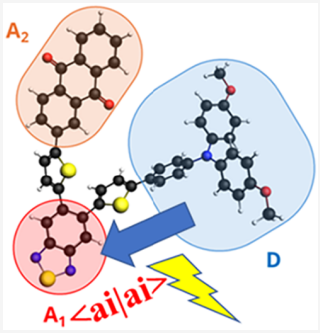
Published as part of The Journal of Physical Chemistry A special issue "Forty Years of Response Function Theory".

Pierpaolo D'Antoni, Daniele Toffoli, and Mauro Stener*

Cite This: https://doi.org/10.1021/acs.jpca.5c03798
Read Online

ACCESS | Metrics & More | Article Recommendations

ABSTRACT: The Resolution of the Identity (RI) technique has been employed to enhance the computational efficiency of Range-Separated (RS) exchange−correlation (xc-) functionals at the time-dependent density functional theory (TDDFT) level using the Hybrid Diagonal Approximation. RI has been implemented within the polTDDFT algorithm (a complex damped polarization method) as part of the AMS/ADF program suite. Comparison between the present TDDFT simulations and the Casida algorithm, for both the model ethylene−tetrafluoroethylene charge-transfer system and the experimental photoabsorption spectrum of a large donor−acceptor−acceptor triad, demonstrates the method's excellent accuracy and efficiency. The present method provides a reliable and computationally efficient tool to predict photoabsorption spectra in the presence of charge-transfer transitions and is suitable for applications to large systems with sizes up to several hundred atoms.



1. INTRODUCTION

One of the most direct and easily applicable experimental methods to probe the electronic structure of matter, both in general and for specific materials, is optical spectroscopy. Although the information contained in an electronic spectrum is very rich, it is often challenging to extract it without a robust and reliable theoretical model. Such a model enables, for instance, the assignment of experimental features to specific electronic transitions. For this reason, the availability of suitably accurate computational methods to support and rationalize experiments is of great importance for the scientific community.[1] Moreover, when the computational approach is accurate enough to be predictive, it can be employed for the rational design of new materials with targeted optical properties. This is particularly relevant in fields such as solar energy conversion and light harvesting, where developing materials with an increasingly high efficiency is crucial.

In this context, a reliable theoretical tool for solar cell materials must be able to describe the charge-transfer (CT) excitations, which are fundamental to generate the exciton, which may evolve into charge separation and ultimately lead to photocurrent generation.

From a theoretical point of view, the optimal compromise between accuracy and computational economy is currently offered by time-dependent density functional theory (TDDFT), which allows the calculation of systems containing up to a thousand atoms. In quantum chemistry, the most widely used implementation of TDDFT is that proposed by Casida.[2] In the Casida formulation, an eigenvalue equation is solved on the space of one-electron excitations, the number of which is the product of the number of occupied and unoccupied orbitals. In addition to Casida's approach, other TDDFT formulations and implementations are available.[3−11] More recently, a damped linear response TDDFT algorithm, which extracts the absorption spectrum from the average of the complex polarizability tensor[12−14] (also known as polTDDFT), has proven particularly suitable for application to very large systems,[15] and will be employed also in the present work.

In both DFT and TDDFT, accuracy remains a critical open challenge, as it is intimately connected with the choice of the exchange−correlation (xc-) functional: in DFT to solve Kohn−Sham equations, and in the response kernel of TDDFT when solving the TDDFT equations.[16] The quest to improve the accuracy and efficiency of xc-functionals and kernels is an active and ongoing field of research.[17,18] Hybrid xc-functionals for DFT and hybrid kernels for TDDFT, i.e., functionals including a variable fraction of the exact Hartree−Fock (HF) nonlocal exchange, often represent the best choice

Received: June 2, 2025
Revised: August 25, 2025
Accepted: September 18, 2025

Downloaded via UNIVERSITA STUDI TRIESTE on September 30, 2025 at 09:14:31 (UTC).
See https://pubs.acs.org/sharingguidelines for options on how to legitimately share published articles.

ACS Publications
© XXXX The Authors. Published by American Chemical Society

in terms of accuracy, at least with respect to simpler Generalized Gradient Approximation, GGA. Among hybrid xc-functionals, B3LYP[19,20] is the most popular. However, even hybrid functionals are known to fail in the description of CT excitations. This failure is well understood: since CT excitations involve a pair of occupied-virtual orbitals lying in different spatial regions, the kernel must contain the full nonlocal Fock exchange to recover the particle−hole interaction.[21]

From a computational point of view, for global hybrid and RS kernels, the HF nonlocal exchange is demanding when evaluating the matrix elements needed for the Casida equations. More precisely, matrix elements can be treated efficiently when Gaussian Type Orbitals (GTO) basis sets are employed, but become problematic with other basis sets, such as Slater Type Orbitals (STO) or Plane Waves (PW). A recently proposed approximate scheme, known as the Hybrid Diagonal Approximation[22] (HDA), addresses this issue by including the nonlocal exchange only in the diagonal terms of the response equations. This reduces the computational cost to that of a conventional GGA kernel, while retaining nearly the same accuracy as full hybrid TDDFT. More recently, an improved HDA implementation exploiting the Resolution of Identity (RI) technique, named fitted HDA, has proven extremely efficient[23] and gives almost quantitative agreement with respect to high-resolution low-temperature photoabsorption experiments for gold nanoalloys protected by thiol ligands.[24,25]

In the present work, we extended the previous fitted HDA implementation from global hybrid (like B3LYP) to RS functionals using STO basis set within the ADF engine of the AMS program suite.[26] For the moment, we focus on the RS CAMY-B3LYP functional.[27] The Review is organized as follows. First, we provide a short review of the HDA approximation in both the Casida and polTDDFT implementations. Then, we detail the RI method to calculate HDA integrals and describe its implementation within the AMS-ADF program. Finally, to assess the performance of the method, we applied it to two systems: the prototypical ethylene−tetrafluoroethylene adduct, often used to benchmark CT transitions, and a realistic donor−acceptor−acceptor triad exhibiting intramolecular CT excitations.

2. THEORETICAL METHOD AND IMPLEMENTATION

The present implementation of the Hybrid Diagonal Approximation (HDA)[22] is developed within the damped linear response complex polarizability algorithm (called polTDDFT). A brief summary of the HDA scheme is provided below, while a detailed derivation can be found in the literature. The linear response TDDFT equations within the Random Phase Approximation (RPA) take the standard form

$$\begin{pmatrix} A & B \\ B^* & A^* \end{pmatrix}\begin{pmatrix} X \\ Y \end{pmatrix} = \omega\begin{pmatrix} 1 & 0 \\ 0 & -1 \end{pmatrix}\begin{pmatrix} X \\ Y \end{pmatrix} \tag{1}$$

where the submatrices A and B take the following general form for hybrid kernels

$$A_{ia,jb} = \delta_{ij}\delta_{ab}(\varepsilon_a - \varepsilon_i) + \langle ajlib\rangle - \alpha\langle ajlbi\rangle + (1-\alpha)\langle a\left|\frac{\partial V_{XC}}{\partial\rho}j^*b\right|i\rangle \tag{2a}$$

$$B_{ia,jb} = \langle ablij\rangle - \alpha\langle ablji\rangle + (1-\alpha)\langle a\left|\frac{\partial V_{XC}}{\partial\rho}b^*j\right|i\rangle \tag{2b}$$

where in expressions 2a and 2b, the indices i, j refer to occupied orbitals and a, b refer to the virtual ones. α represents the fraction of nonlocal HF exchange in the xc-kernel and the Adiabatic Local Density Approximation, ALDA, is assumed in the last terms of both equations. The two-electron integrals in the last terms of eqs 2a and 2b correspond to the elements of the coupling matrix with the ALDA local part of the time-independent f_{xc} kernel, namely

$$\langle a\left|\frac{\partial V_{XC}}{\partial\rho}j^*b\right|i\rangle = \iint \varphi_a^*(\mathbf{r}_1)\varphi_j^*(\mathbf{r}_2)f_{xc}^{\mathrm{ALDA}}(\mathbf{r}_1,\mathbf{r}_2)\varphi_i(\mathbf{r}_1)\varphi_b(\mathbf{r}_2)\mathrm{d}\mathbf{r}_1\mathrm{d}\mathbf{r}_2 \tag{3}$$

A general definition of the kernel is given in eq (7.89) from the Ullrich book.[28]

In practice, HDA consists of approximate eqs 2a and 2b with the following ones

$$A_{ia,jb} = \delta_{ij}\delta_{ab}(\varepsilon_a - \varepsilon_i - \Delta_{ia}) + \langle ajlib\rangle + \langle a\left|\frac{\partial V_{XC}}{\partial\rho}j^*b\right|i\rangle \tag{4}$$

$$B_{ia,jb} = \langle ablij\rangle + \langle a\left|\frac{\partial V_{XC}}{\partial\rho}b^*j\right|i\rangle \tag{5}$$

where in expression 4, we introduced a diagonal corrective term

$$\Delta_{ia} = \alpha\langle ailai\rangle + \alpha\langle a\left|\frac{\partial V_{XC}}{\partial\rho}i^*a\right|i\rangle \tag{6}$$

So, actually, the hybrid correction is used only for the diagonal elements of matrix A, and it can be interpreted as a correction of the difference between the eigenvalues of the virtual-occupied KS orbitals. Although we refer to the original work for a more complete discussion and justification of HDA,[22] in practice, the main effect of the diagonal correction is to recover the too high energy of the virtual orbital, which is pushed up by the nonlocal Fock exchange.

Because the HDA modifies only orbital energy differences, it can be directly applied to the polTDDFT scheme, where the photoabsorption spectrum $\sigma(\omega)$ is discretized and computed in a limited number of points from the imaginary part of the dynamic polarizability $\alpha(\omega)$

$$\sigma(\omega) = \frac{4\pi\omega}{c}\mathrm{Im}[\alpha(\omega)] \tag{7}$$

In the following, we give a brief summary of the polTDDFT algorithm, while we refer the reader to the original literature for more details concerning the method and its implementation.[12−14] The complex dynamical polarizability is calculated by solving the following nonhomogeneous linear system

$$[\mathbf{S} - \mathbf{M}(\omega)]\mathbf{b} = \mathbf{d} \tag{8}$$

In eq 8, $\mathbf{S}$ is the overlap matrix between density fitting functions, $\mathbf{b}$ is the unknown vector containing the expansion coefficients $b_\mu(\omega)$ of the induced density $\rho_z^{(1)}$, $\mathbf{d}$ is the frequency-dependent vector corresponding to the known nonhomogeneous term, and finally, the elements of the frequency-dependent matrix $\mathbf{M}$ are

https://doi.org/10.1021/acs.jpca.5c03798
J. Phys. Chem. A XXXX, XXX, XXX−XXX

$$M_{\mu\nu} = \langle f_\mu | \chi_{KS}(\omega) K | f_\nu \rangle \tag{9}$$

In eq 9, χ_{KS} refers to the Kohn−Sham frequency-dependent dielectric function and K to the kernel. The original characteristic of the polTDDFT method is the introduction of a simple approximation, which enables the construction of $\mathbf{M}(\omega)$ as a linear combination of frequency-independent matrices $\mathbf{G}^k$ with frequency-dependent coefficients $s_k(\omega)$, with the following expression

$$\mathbf{M}(\omega) = \sum_k s_k(\omega)\mathbf{G}^k \tag{10}$$

With this idea, a set of matrices $\{\mathbf{G}^k\}$ is calculated and stored only once at the beginning, then the matrix $\mathbf{M}(\omega)$ is calculated very rapidly at each photon energy ω, as a linear combination of the $\{\mathbf{G}^k\}$ matrices with the following coefficients as the left-hand side of eq 11

$$s_k(\omega) = \frac{4(\varepsilon_a - \varepsilon_i)}{\omega^2 - (\varepsilon_a - \varepsilon_i)^2} \overset{\text{HDA}}{\Longrightarrow} s_k(\omega) = \frac{4(\varepsilon_a - \varepsilon_i - \Delta_{ia})}{\omega^2 - (\varepsilon_a - \varepsilon_i - \Delta_{ia})^2} \tag{11}$$

In order to apply the HDA to the polTDDFT, it is sufficient to correct the orbital energy differences with the same correction term (6) as already done for expression 4: $\varepsilon_a - \varepsilon_i - \Delta_{ia}$, so that the right-hand side of eq 11 is obtained.

Extending HDA to range-separated (RS) functionals requires modifying the Δ_{ia} term to reflect the RS exchange structure. In order to give an explicit expression for these corrections, it is convenient to recall the split of the Coulomb operator into a Short Range (SR) and a Long Range (LR) component

$$\frac{1}{r_{12}} = \text{SR} + \text{LR} = \frac{w(\gamma, r_{12})}{r_{12}} + \frac{1 - w(\gamma, r_{12})}{r_{12}} \tag{12}$$

where in (12) w is a switching function which goes to 1 as r_{12} goes to zero and goes to 0 as r_{12} goes to infinity, then the exchange is calculated at the DFT level for the SR part, and at the exact exchange level for the LR. The standard RS CAM-B3LYP[29] for GTO basis set employs the complementary error function erfc as w switching function; such a choice is essentially technical due to the possibility of integrating analytically. On the other hand, when STO basis functions are employed, as in the present case, it is more convenient to use an exponential switching, which can be integrated analytically for 2-center STO functions; in this case, the CAMY-B3LYP functional is obtained,[27] where Y refers to the Yukawa potential $\frac{\exp(-\gamma r_{12})}{r_{12}}$.

In practice, we efficiently calculate the correction as follows:

$$\Delta_{ia} = \left\langle ai \left| \frac{1 - \exp(-\gamma r_{12})}{r_{12}} \right| ai \right\rangle - \left\langle a \left| \frac{\partial V_X^Y}{\partial \rho} \right| i \right\rangle + \left\langle a \left| \frac{\partial V_{XC}^{\text{ALDA}}}{\partial \rho} \right| i \right\rangle \tag{13}$$

where the first term in eq 13 is the diagonal element calculated with the Long Range attenuated Yukawa potential, the second term is calculated with the Short Range DFT Yukawa functional, and the third term subtracts the ALDA kernel from the diagonal elements in order to avoid double counting.

While for the calculation of the second term, an efficient routine is already available in AMS, the first term is calculated with the Resolution of the Identity technique[23] as follows:

$$\left\langle ai \left| \frac{1 - \exp(-\gamma r_{12})}{r_{12}} \right| ai \right\rangle = \iint \frac{\varphi_a^*(\vec{r_1})\varphi_a(\vec{r_1})(1 - \exp(-\gamma r_{12}))\varphi_i^*(\vec{r_2})\varphi_i(\vec{r_2})}{r_{12}} \mathrm{d}\vec{r_1}\mathrm{d}\vec{r_2} \tag{14}$$

The numerator in eq 14 contains the product of the electron densities of orbitals φ_a and φ_i

$$\rho_a(\vec{r_1}) = \varphi_a^*(\vec{r_1})\varphi_a(\vec{r_1}) \tag{15}$$

$$\rho_i(\vec{r_2}) = \varphi_i^*(\vec{r_2})\varphi_i(\vec{r_2}) \tag{16}$$

They are developed as a linear combination of density fitting functions as follows:

$$\rho_a(\vec{r_1}) \cong \sum_{k=1}^{N_F} f_k(\vec{r_1})C_{ka} \quad \rho_i(\vec{r_2}) \cong \sum_{m=1}^{N_F} f_m(\vec{r_2})C_{mi} \tag{17}$$

Using expressions 15−17 to rewrite eq 14, we get

$$\left\langle ai \left| \frac{1 - \exp(-\gamma r_{12})}{r_{12}} \right| ai \right\rangle \cong \sum_{k=1}^{N_F}\sum_{m=1}^{N_F} \iint \frac{f_k(\vec{r_1})C_{ka}(1 - \exp(-\gamma r_{12}))f_m(\vec{r_2})C_{mi}}{r_{12}} \mathrm{d}\vec{r_1}\mathrm{d}\vec{r_2} \tag{18}$$

Introducing matrix $\boldsymbol{F}^Y$ with elements

$$F_{km}^Y = \iint \frac{f_k(\vec{r_1})(1 - \exp(-\gamma r_{12}))f_m(\vec{r_2})}{r_{12}} \mathrm{d}\vec{r_1}\mathrm{d}\vec{r_2} \tag{19}$$

It is worth noting that such a procedure is possible since an analytical expression for the one- and two-center integrals (19) is available for STO functions.[27] After computing $\boldsymbol{F}^Y$, the correct diagonal integrals are finally obtained

$$\left\langle ai \left| \frac{1 - \exp(-\gamma r_{12})}{r_{12}} \right| ai \right\rangle \cong \sum_{k=1}^{N_F}\sum_{m=1}^{N_F} C_{ak}^+ F_{km}^Y C_{mi} \tag{19a}$$

The C coefficients to be employed in eq 19a are extracted from the projection of the orbital density $\rho_a(\vec{r_1})$ on the set of fit functions f_p

$$\langle f_p | \rho_a \rangle = \sum_{k=1}^{N_F} \langle f_p | f_k \rangle C_{ka} = \sum_{k=1}^{N_F} S_{pk}^f C_{ka} = d_{pa} \tag{20}$$

where S^f is the overlap matrix between fitting function pairs. Solving the linear system (20) yields coefficients for virtual orbitals; a similar procedure holds for occupied orbitals, finally

$$\sum_{n=1}^{N_F} (S^f)_{kn}^{-1} d_{na} = C_{ka}, \quad \sum_{p=1}^{N_F} (S^f)_{mp}^{-1} d_{pi} = C_{mi} \tag{21}$$

so that we can rewrite eq 19

https://doi.org/10.1021/acs.jpca.5c03798
J. Phys. Chem. A XXXX, XXX, XXX−XXX

Table 1. Lowest Excitation Energies (E_{exc}) and Intensities in Terms of Oscillator Strength (f) of the Ethylene–Tetrafluoroethylene Adduct at a Distance of 5Å Calculated with Both Casida and polTDDFT Methods[a]

	Casida		POLTDDFT		
n° Excitation	E_{exc} (eV)	f	E_{exc} (eV)	f	Assignment
1	6.64	0.024	6.68	0.085	85% HOMO → LUMO+1 Ryd
2	6.76	$0.3\cdot10^{-4}$	6.96	0.055	60% HOMO → LUMO+3
3	**7.10**	**0.11**	**7.12**	**0.072**	**66% HOMO-1 → LUMO+1 Ryd CT**
4	**7.48**	**0.033**	**7.66**	**0.113**	**76% HOMO → LUMO CT**
5	7.55	0.22	7.46	0.161	89% HOMO-1 → LUMO
6	7.81	$0.7\cdot10^{-4}$	-	-	42% HOMO-1 → LUMO+6
7	7.92	0.053	8.18	0.097	41% HOMO → LUMO+4
8	8.00	0.037			67% HOMO-1 → LUMO+4
9	8.12	$0.3\cdot10^{-4}$	-	-	91% HOMO-2 → LUMO
10	8.32	0.38	8.46	0.203	73% HOMO → LUMO+2
11	8.34	$1\cdot10^{-3}$			55% HOMO-1 → LUMO+5
12	**8.39**	**0.015**			**96% HOMO-1 → LUMO+2 CT**
13	8.56	0.001			72% HOMO-1 → LUMO+5

[a]Assignment in terms of the dominant one-electron excited configuration. Calculated at the TDDFT level with CAMY-B3LYP XC-functional and TZP STO basis set. CT excitations are in bold.

$$\left\langle ai \left| \frac{1-\exp(-\gamma r_{12})}{r_{12}} \right| ai \right\rangle \cong \sum_{n=1}^{N_F}\sum_{p=1}^{N_F}\sum_{k=1}^{N_F}\sum_{m=1}^{N_F} d_{an}^{\dagger}(S^f)_{nk}^{-1}F_{km}^{Y}(S^f)_{mp}^{-1}d_{pi} \quad (22)$$

Moreover, the effect of the DFT SR kernel can be included since its matrix over the auxiliary density fitting basis is already available, since it is needed by the polTDDFT (see matrix $\boldsymbol{Z}$ in ref 12)

$$\boldsymbol{Q} = (\boldsymbol{S}^f)^{-1}(\boldsymbol{F}^{\boldsymbol{Y}} + \boldsymbol{Z})(\boldsymbol{S}^f)^{-1} \quad (23)$$

The final correction for the diagonal term is then obtained as follows:

$$\cong \boldsymbol{d}_a^{+}\boldsymbol{Q}\boldsymbol{d}_i \quad (24)$$

For the details of the implementation, we refer the reader to the previous work on the hybrid functionals, since that part is identical, only the matrix $\boldsymbol{F}$ is substituted by $\boldsymbol{F}^{\boldsymbol{Y}}$.

An important modification introduced in the present implementation concerns the normalization of the orbital densities, while expressions 15 and 16 are normalized; when expanded with auxiliary density fitting basis with expression 17, the densities are no more exactly normalized, unless a constraint is introduced in order to impose normalization. Unlike previous versions, we now impose that these densities integrate to unity over $\mathbb{R}^3$. This is achieved using a standard Lagrange multiplier approach. The usefulness of the imposition of the normalization constraint to the fitted density has been known for a long time in the context of the efficient calculation of the Hartree potential during the SCF cycles.[30] In matrix form, it consists of adding an "edge" to the overlap matrix with the normalization integrals of the fitting functions (last column and last row) and putting the value of the normalization constraint (1 in the present case) as the last new element of the known term (which now has dimension N + 1). This new matrix will be no more definite positive, so the Cholesky decomposition cannot be used; thus, the more general standard routine for symmetric linear systems must be chosen instead. We noticed that with this constraint, the agreement

https://doi.org/10.1021/acs.jpca.5c03798
J. Phys. Chem. A XXXX, XXX, XXX–XXX

between the polTDDFT results and a Casida reference is improved; therefore, starting with the AMS2025 version, this constraint is the default for both hybrid and RS polTDDFT fitted HDA calculations.

3. COMPUTATIONAL DETAILS

All of the DFT KS calculations reported in this work were performed employing a TZP basis of STO functions (included in the ADF database) and the CAMY-B3LYP hybrid xc-functional.[27] The auxiliary density fitting basis STO functions are taken from the POLTDDFT basis set database included in the AMS program.[31] The TDDFT calculations were performed with the polTDDFT algorithm.[12,13] The HDA density functional approximation[22] is the only available scheme for hybrid or RS functional within polTDDFT. The HDA has been implemented by exploiting the parallelization at the general Message Passing Interface (MPI) level. The imaginary part of the photon energy was set to 0.075 eV during the calculation of the polTDDFT spectra. All of the calculations were performed with a local developer version of the AMS code, which has already been distributed starting with the AMS2025.01 version. The coordinates of the systems considered in the present work have been taken from the literature.[32,33]

4. RESULTS AND DISCUSSION

The aim of the present work is the implementation of the RS functional within TDDFT, in the framework of the polTDDFT algorithm using the HDA approximation. Accordingly, the new method must be validated in two main directions. First, we assess whether the algorithm is capable of accurately describing charge-transfer (CT) excitations. Second, we evaluate its computational performance and scalability to ensure it can be applied to systems where conventional approaches are computationally prohibitive.

To address the first point, we consider in Section 4.1 the ethylene−tetrafluoroethylene adduct, which is a typical model to test CT excitation. The second point is discussed in Section 4.2, where we consider an extended system (TAA-th-BTD-th-AQ) comprising one donor and two acceptor fragments so that the CT excitations consist of intramolecular transitions between spatially separated orbitals.

4.1. Ethylene−Tetrafluoroethylene. The ethylene−tetrafluoroethylene adduct is a practical model used by many authors[21,32,34,35] to test the suitability of theoretical methods to describe CT excitations. In this work, our goal is to test the accuracy of the present implementation, so we will take the Casida results as a reference and will compare them with the new polTDDFT implementation, using the same basis set, exchange−correlation functional, and code (AMS) in both calculations. In this work, the distance between the two fragments has been set to 5 Å. It is convenient to start describing the Casida results, which are reported in Table 1 and Figure 1, while the orbitals involved in the excitations are reported in Figure 2. Notice that the polTDDFT method directly gives a continuous profile, while the Casida one gives excitation energies and oscillator strengths, which are reported in the figure as vertical bars. In order to facilitate the comparison between the Casida method and the polTDDFT, we have also reported in the figure the profile obtained by smoothing the Casida discrete excitations with Lorentzian functions with the same HWHM as the imaginary photon energy used in polTDDFT in order to have the same bandwidth in both methods. From Table 1 and Figure 1, it is worth noting that the most intense transitions, at 7.55 eV (f = 0.22) and 8.32 eV (f = 0.38), correspond to intramolecular $\pi \rightarrow \pi^*$ on ethylene and tetrafluoroethylene, respectively. The first excitation at 6.64 eV, which is rather weak (f = 0.024) but still visible on the scale of Figure 2, is an intramolecular transition $\pi \rightarrow$ Rydberg F 3s on tetrafluoroethylene. It is worth noting that RS functionals, besides giving a correct description

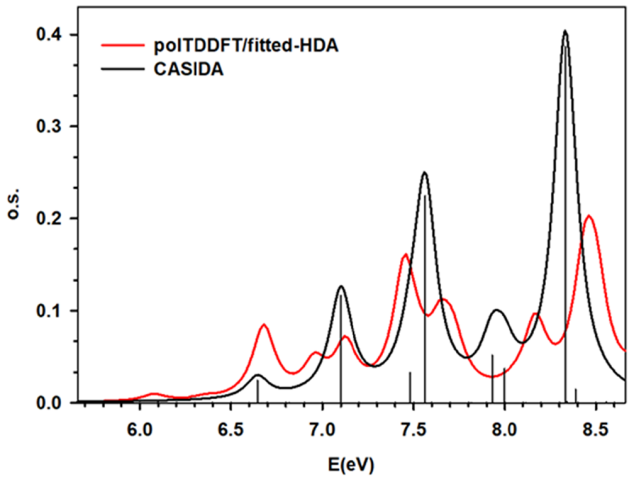


Figure 1. Calculated photoabsorption spectrum of the ethylene−tetrafluoroethylene model system at a distance of 5Å, absolute intensity (oscillator strength) on the vertical axis, excitation energy on the horizontal axis. Black vertical bar: discrete Casida excitations, black curve: smoothed Casida spectrum, red curve: polTDDFT.

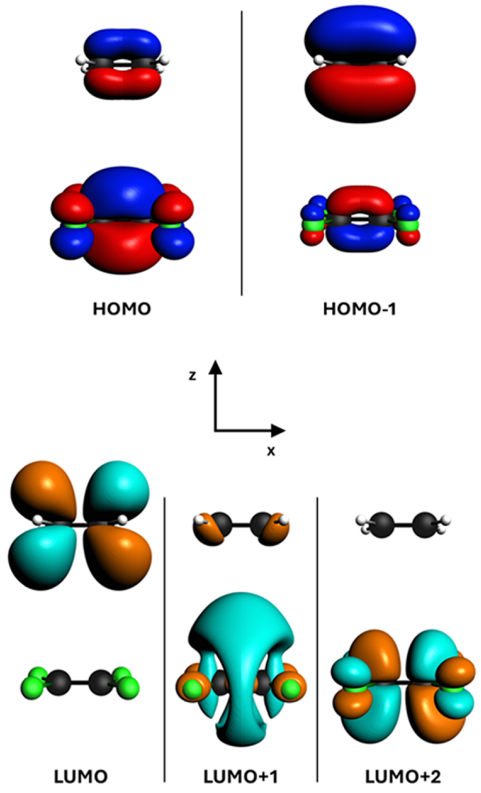


Figure 2. Occupied and virtual orbitals of the ethylene−tetrafluoroethylene model system involved in the most important excitations.

https://doi.org/10.1021/acs.jpca.5c03798
J. Phys. Chem. A XXXX, XXX, XXX−XXX

of the CT excitations, also display the correct behavior of the exchange at large distances and therefore properly support the Rydberg states. Moreover, such Rydberg states to be supported need that the basis set contains diffuse functions, as in the case of the presently employed TZP. The next visible excitation at 7.10 eV consists of a CT from the π orbital of ethylene to the Rydberg F 3s orbital of tetrafluoroethylene; the relatively high intensity (f = 0.11) is a consequence of the very diffuse Rydberg state. In fact, in general, CT transitions involving valence orbitals are rather weak, since the initial and final orbitals are localized in different spatial regions, so their electric dipole transition moment tends to zero as their separation increases. On the other hand, Rydberg orbitals are very diffuse, so they can be more effective than valence orbitals to overlap with moieties that are localized far away. In fact, as we will see later, the other CT that involves valence instead of Rydberg states is less intense by at least a factor of 2. The next transition at 7.48 eV is again a CT, but this time it is from tetrafluoroethylene $\pi \rightarrow$ ethylene π^*, with intensity f = 0.033, roughly three times weaker than the previous Rydberg CT. The following CT falls at 8.39 (f = 0.015) and corresponds to ethylene $\pi \rightarrow$ tetrafluoroethylene π^*; however, such a transition is very close in energy to the strong intramolecular one at 8.32 eV, which is 25 times more intense. In Figure 1, the comparison between the Casida and present polTDDFT implementation is presented as well, while both excitation energies and oscillator strengths are reported in Table 1 for a more quantitative comparison between the two approaches. The polTDDFT spectrum satisfactorily reproduces the main features of the Casida spectrum, although some discrepancies are present, in terms of energy shifts as well as intensity redistribution. Starting with the low energy region, the two excitations calculated by Casida at 6.64 and 7.10 eV are found at 6.68 and 7.12 eV, respectively, in the polTDDFT calculation, so we obtain an excellent energy match but a clear deterioration of the intensity, whose distribution is different. Actually, the polTDDFT profile gives a feature at 6.96 eV, which is not apparent in the Casida spectrum; however, from Table 1, a dark transition (with negligible oscillator strength) is found at 6.76 eV. So, we can rationalize the presence of this feature due to an incorrect redistribution of the oscillator strength between the two states: in Casida, one excited state brings all of the intensity, while in polTDDFT, the intensity is shared. This effect is typical when the excited states are very close to each other in energy; in fact, going to the limit of two degenerate states, it is possible to choose a unitary transformation that preserves their eigenvector nature but brings the intensity from one to the other. If the states are not exactly degenerate, a small perturbation/inaccuracy may strongly mix the states, changing the intensity distribution between the two states. Of course, this difficulty ascribed to polTDDFT is more critical for small systems, when the states are few and well separated in energy; however, when the system is larger, the density of excited states increases, they start to be almost degenerate, and polTDDFT will furnish an average description, even more practical than the Casida approach when the presence of many congested excited states prevents a simple analysis. Since polTDDFT has been designed suitably for applications to very large systems containing several hundreds of atoms, we believe that this does not represent a real limitation of the method. The next features at the Casida level fall at 7.48 and 7.55 eV, in polTDDFT, we assign them with the reverse order at 7.66 and 7.46 eV. Such an assignment is corroborated by 3 different arguments: first, the same dominant one-electron excited configuration, second, the intensity (which is also reversed), and third, by the following fragment analysis. In fact, with polTDDFT, it is possible to perform a fragment analysis splitting[36] of the spectrum into 4 components, according to the initial and final fragment. In the present situation, it is quite natural to split the system into two fragments corresponding to ethylene and tetrafluoroethylene in order to identify the CT region. In Figure 3, we report the total fragment analysis, and also the partial analysis according to the x or z active electric dipole component, since the y component is not active for these transitions. The CT regions in Figure 3 are filled in yellow and green for ethylene → tetrafluoroethylene and tetrafluoroethylene → ethylene, respectively; this corroborates attributing the polTDDFT peak at 7.66 eV to the CT Casida peak at 7.48 eV. Interestingly, the ethylene → tetrafluoroethylene CT shows up around 8.4 eV in the x dipole component and 7.2 eV in the z component: the former corresponds to the 8.39 eV peak in Casida (HOMO − 1 $\pi \rightarrow$ LUMO + 2 π^*) and the latter to the 7.1 eV peak in Casida (HOMO − 1 $\pi \rightarrow$ LUMO + 1 Ryd). Notice that while the $\pi \rightarrow \pi^*$ transitions are active with the x component, the $\pi \rightarrow$ F 3s Rydberg are active in the z dipole component due to the totally symmetric shape of the Rydberg orbital. Finally, the Casida peaks at 8.0 and 8.32 eV are shifted at higher energy by 0.2 eV in the polTDDFT result, but keeping the correct intensity distribution.

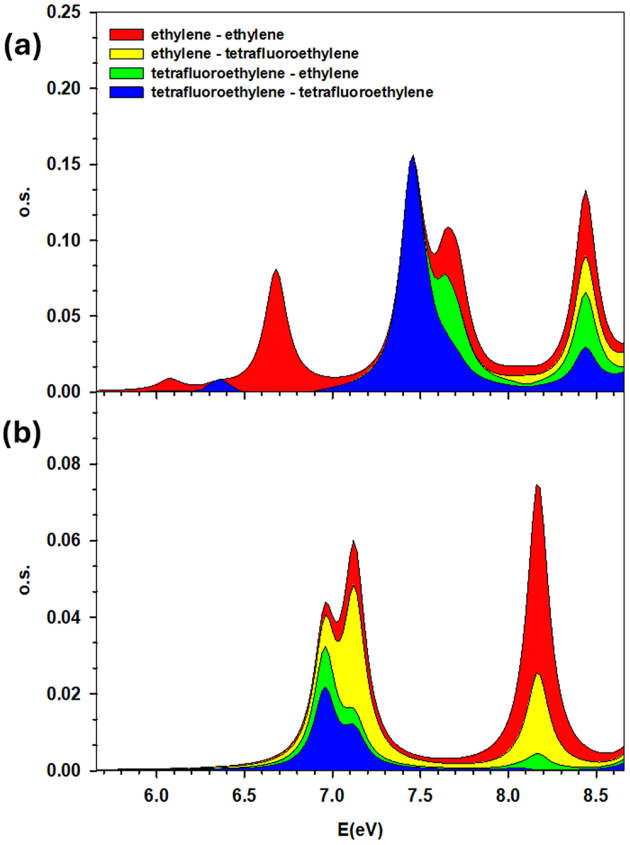


Figure 3. Fragment analysis of the spectrum of the ethylene−tetrafluoroethylene model system. (a) Upper panel: x component of transition moment electric dipole, (b) lower panel: z component of transition moment electric dipole.

https://doi.org/10.1021/acs.jpca.5c03798
J. Phys. Chem. A XXXX, XXX, XXX−XXX

We can conclude the analysis on this model system, saying that the present implementation of the polTDDFT RS CAMY-B3LYP functional is able to describe the CT transition, although some minor deterioration with respect to the Casida reference is found. The discrepancy in the energy is rather small, no more than 0.2 eV at most; more sensitive is the intensity, which is usually well reproduced, but in some instances (low energy part of the spectrum), more evident deviations are observed. Such still minor deterioration can be safely attributed to deficiencies of the density fitting basis set, which is optimized to reproduce the spectrum but has not yet been optimized to fit the densities as in previous eq 17. An analogous deterioration for the same problem has been observed for the fitted HDA with global hybrid functionals,[23] but such deficiency tends to strongly alleviate when the size of the system increases.[25] The systematic improvement of the accuracy as the size (or the number of electrons) increases has also been observed in different simplified TDDFT schemes, in particular the recent XsTD-DFT from de Wergifosse and Grimme.[37] In particular, for the XsTD-DFT scheme, a complete analysis on a set of 77 molecules and 4 different functionals has demonstrated that the excitation energy absolute deviations are decreasing as the number of electrons increases. The effect is quite prominent, starting with errors on the order of 1−2 eV for systems with less than 50 electrons, going down to 0.2 eV when 250 electrons are present. However, in the paper,[37] this interesting trend was identified but not explained. We can tentatively explain this behavior as follows: assume that the orbitals are all strongly delocalized; this means that in larger systems, the orbitals are in any case more flexible since they are contributed by more basis set functions. Since the present accuracy is governed by the accuracy of the two-electron integrals, the latter will be more accurate when the system is larger. Actually, this is a very interesting finding that deserves a deeper analysis in future work; in fact, if well understood, this may allow us to improve even more both accuracy and efficiency for very large systems.

So we are confident that the same improvement with system size should be expected for RS functionals as well, preventing the necessity to reoptimize the density fitting basis set when larger systems are taken into account. Although the polTDDFT method is much faster than the Casida one, for the present model system, the computational effort is negligible for both approaches, employing only a few seconds to complete the calculations; therefore, we defer the analysis of the computational economy to the next system, which is much larger and therefore more informative.

4.2. Electron-Donor−Acceptor−Acceptor Triad. In order to test the present implementation on a challenging system, we have selected a so-called electron-donor−acceptor−acceptor triad.[33] Such a system is built (see Figure 4) by three different fragments linked by a thiophene moiety: the first fragment is a Donor (D) and consists of a triarylamine (TAA), linked by thiophene (th) to the first Acceptor (A1) consisting of a benzothiadiazole (BTD) further linked by th to the second Acceptor (A2) consisting of an anthraquinone (AQ). Such a complex system is very interesting as a model of a molecular electronic circuit. The current is triggered by a bright CT transition by light absorption from D TAA to A1 BTD, followed by a nonradiative electron transfer from A1 BTD to A2 AQ. The so-obtained charge-separated system (hole in TAA and electron in AQ) promotes a strong geometrical relaxation such that D and A2 get much closer.

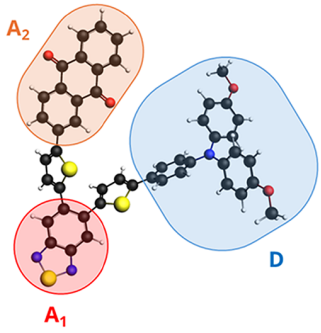


Figure 4. Geometry of the TAA-th-BTD-th-AQ electron-donor−acceptor−acceptor triad.

Finally, the hole−electron recombination between D and A2 takes place, and the electron returns in its initial state, closing this sort of molecular electronic circuit. Since our goal is to test the CT performance of this method, we focus only on the first step of the process, namely, the photoabsorption spectrum, which we compare with the experimental one to test if our approach is able to properly describe the CT excitation from D to A1. The experimental photoabsorption spectrum[33] is compared with present polTDDFT calculations in Figure 5,

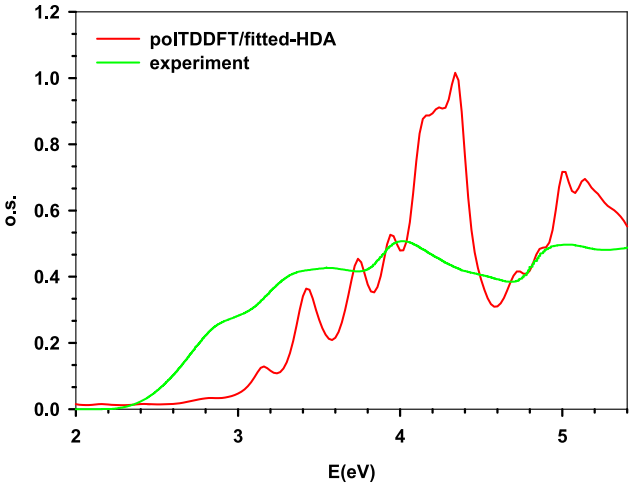


Figure 5. Calculated photoabsorption spectrum of the TAA-th-BTD-th-AQ electron-donor−acceptor−acceptor triad, absolute intensity (oscillator strength) on the vertical axis, excitation energy on the horizontal axis. Red curve: polTDDFT, green curve: experiment from ref 33.

while the analysis of the most relevant calculated spectral features is reported in Table 2 at both Casida as well as polTDDFT levels. Such analysis is performed in terms of leading one-electron excited configurations, so the molecular orbitals involved are reported in Figure 6. In the following, we will employ the polTDDFT to discuss the results. The lowest energy calculated peak is found at 3.16 eV, which is essentially contributed by HOMO → LUMO + 1, from Figure 6. Such a transition can be easily assigned to a CT excitation from D (TAA) to A1 (BTD). In the experiment,[33] such peaks are found at 415 nm, corresponding to 3.02 eV, in excellent agreement with the present calculation. Such a nice result confirms the suitability and the accuracy of the present scheme to describe CT excitation in large systems. The next transition is calculated at 3.42 eV and corresponds to the HOMO − 2 →

https://doi.org/10.1021/acs.jpca.5c03798
J. Phys. Chem. A XXXX, XXX, XXX−XXX

Table 2. Main Absorption Peaks Predicted by Both Casida and polTDDFT/fitted-HDA for TAA-th_BTD-th-AQ System[a]

	casida		POLTDDFT		a
absorption peak	E_{exc} (eV)	f	E_{exc} (eV)	f	assignment
A	2.98	0.27	3.16	0.13	72.44% HOMO → LUMO + 1
B	3.32	0.31	3.42	0.36	66.27% HOMO − 2 → LUMO
C	3.73	0.32	3.74	0.45	34.76% HOMO − 1 → LUMO + 1
					27.81% HOMO − 2 → LUMO + 1
D	3.54	0.49	3.94	0.53	83.28% HOMO → LUMO + 3
E	4.24	0.48	4.16	0.89	51.30% HOMO → LUMO + 4
F	4.38	0.25	4.24	0.91	37.67% HOMO → LUMO + 9
					14.57% HOMO → LUMO + 4
G	4.48	0.18	4.34	1.02	47.82% HOMO − 2 → LUMO + 2
					21.03% HOMO − 15 → LUMO
H			4.72	0.42	40.89% HOMO − 1 → LUMO + 3
					13.07% HOMO − 1 → LUMO + 2
I			4.88	0.49	49.75% HOMO − 2 → LUMO + 3
					15.39% HOMO − 8 → LUMO + 1
L			5.00	0.72	51.37% HOMO − 1 → LUMO + 4
M			5.14	0.70	39.42% HOMO − 1 → LUMO + 4
					11.61% HOMO − 2 → LUMO + 3

[a]For each one, we report the excitation energy, the oscillator strength, and the assignment. Assignment in terms of the dominant one-electron excited configuration.

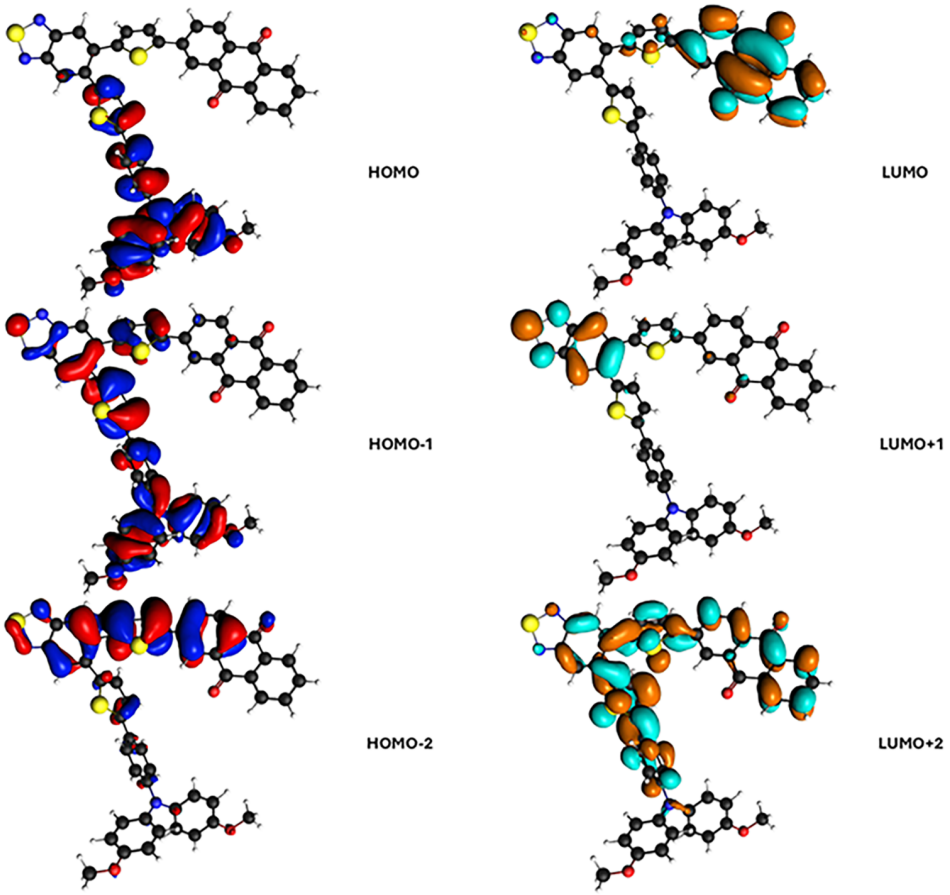


Figure 6. Occupied and virtual orbitals of the TAA-th-BTD-th-AQ electron-donor−acceptor−acceptor triad involved in the most important excitations.

LUMO excitation: from Figure 6, it can be ascribed to an A1 (BTD) to A2 (AQ) transition, but with strong involvement of the th linker, so with only minor CT character; in fact, its intensity is much larger than the first excitation. The experimental peak falls at 355 nm, corresponding to 3.49 eV; also, in this case, theory is in fairly nice agreement with the experiment. The next peak calculated at 3.74 eV displays a strongly mixed character (Table 2), which can be ascribed on

https://doi.org/10.1021/acs.jpca.5c03798
J. Phys. Chem. A XXXX, XXX, XXX−XXX

average to a BTD-th → BTD transition. We do not have a clear indication in the experiment for such a peak; however, the previous feature at 3.49 eV is rather flat at the maximum, so it is possible that these two transitions are both encompassed by the feature around 3.49 eV. Actually, in the assignment given in the experimental work, the feature at 3.49 is ascribed to a th → BTD transition, which is consistent with the present work.

Going to higher energies, we find four features very close to each other in energy, from 3.95 to 4.34 eV, which we can compare with the experimental maximum at 4.02 eV. All of these transitions display a rather high contribution of th in both initial and final orbitals. Then, a rather wide energy gap is found in both calculated and experimental spectra. The next features are found in the calculated spectrum from 4.72 to 5.14 eV, with the most intense being at 5.00 eV; in the experiment, the maximum is found at 5.04 eV, confirming the accuracy of the present theoretical model. For such a region, the inspection of the molecular orbitals involved suggests that the transitions are internal to acceptor fragments, namely, A1 (BTD → BTD) and A2 (AQ → AQ). This explains the higher intensity for this energy region. We can supplement this section with the fragment analysis reported in Figure 7. In the upper figure, we divided the molecule into 2 fragments: the first fragment corresponds to the TAA donor, while the second fragment includes all of the remaining moieties: BTD, both bridges, and AQ. It is well evident that the first peak corresponds to a CT from TAA (as previously mentioned). In order to specify better the involvement of the fragments, in the lower panel we split the molecule into 5 fragments (accordingly to their chemical nature: D, A1, A2, and the two th bridges), but we reported only the contributions from the donor D to any of the two acceptors A1 or A2 and from A1 to A2. From such analysis, the first peak is clearly ascribed to the TAA to BTD CT transfer, as we already did on the grounds of the localization of the molecular orbitals, corroborating previous discussion. We can conclude this section with a comparison between the Casida and the polTDDFT methods for such a larger system, in terms of accuracy as well as computational economy. From Table 2, it is well apparent that the agreement between Casida and polTDDFT is fairly nice in terms of excitation energies; usually, the disagreement is much less than 0.2 eV, with the only exception of the peak D, which is shifted by 0.4 eV. The intensity distribution is more difficult; a rather good agreement is obtained up to 4 eV, but above, the polTDDFT seems to overestimate the intensity. Actually, this is not really true because for such a system, the Casida method furnishes a very high density of states above 4 eV. While polTDDFT provides an average, the Casida gives several almost degenerate discrete transitions that should be properly summed up for a correct comparison with polTDDFT. For such reason, we do not report in Table 2 the Casida states above 4.48 eV. Regarding the computational economy, we ran the calculations up to 6 eV of excitation energy, using 20 cores on a single node of a cluster with an Intel Xeon 20-Core 4416 + 2.0Ghz CPU. The Casida TDDFT took 12 h and 25 min, while polTDDFT took 1 h and 22 min, so polTDDFT proved 9 times faster than Casida. Such a factor is larger as the system becomes larger and larger, so polTDDFT will be faster than Casida by more than 1 order of magnitude. Notice that for very large systems, like for example metal clusters, like Au_{25} protected by ligands, Casida calculations with global hybrid or RS functionals are not practicable at all if a spectrum up to 5 eV of excitation energy is requested; on the other hand, the polTDDFT with HDA approximation and RI technique can deal with such systems with modest efforts (2 days using 20 CPU on the same clusters).

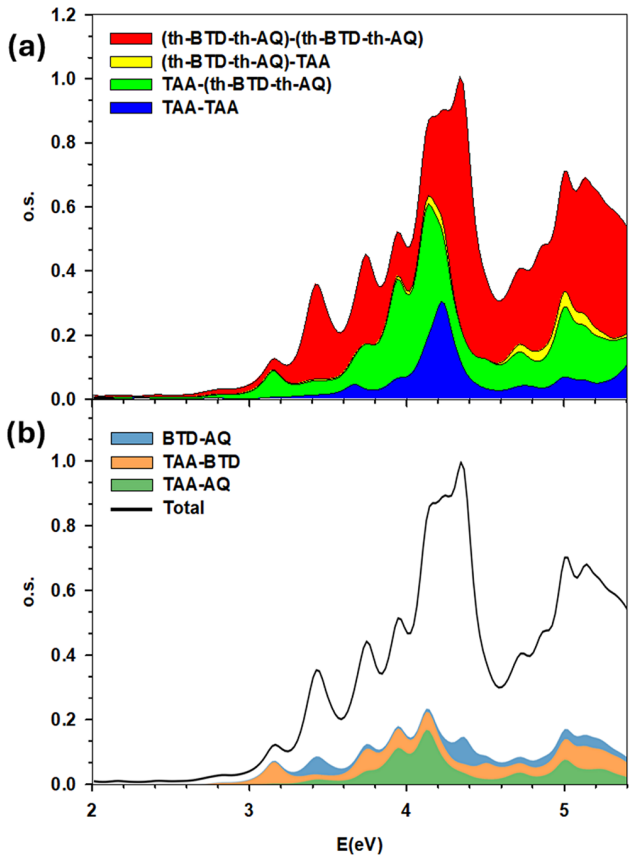


Figure 7. Fragment analysis of the spectrum of TAA-th-BTD-th-AQ electron-donor−acceptor−acceptor triad. In panel (a) the thiophene moiety is included in the fragments, while in panel (b) thiophene is not included.

Finally, we can conclude that the present implementation of the RS CAMY-B3LYP functional in polTDDFT has proven accurate and efficient also for the description of such a complex system, with an accuracy even better than in the previous section model system. The better performance on a larger system in terms of accuracy should be ascribed to the density fitting basis set: as the system under study increases its size, the deficiencies of the basis set become less and less important.

5. CONCLUSIONS

In this work, we implemented an RI technique to employ RS xc-functionals within the HDA approximation at the TDDFT theory level, solving the equations through the polTDDFT algorithm. Only the diagonal matrix elements of the RS kernel are computed, making the overall computational cost comparable to that of a DFT SCF single-point calculation with hybrid functionals. The method reliably describes CT excitations, as demonstrated for the ethylene/tetrafluoroethylene model system. Moreover, the comparison with respect to the experimental photoabsorption spectra of an electron-donor−acceptor−acceptor triad demonstrates the method's predictive accuracy and efficiency.

https://doi.org/10.1021/acs.jpca.5c03798
J. Phys. Chem. A XXXX, XXX, XXX−XXX

This result suggests that polTDDFT with the RI technique and global or RS hybrid xc-functionals represents a computationally efficient yet accurate approach, and it stands out as a promising tool for investigating large molecular systems, potentially comprising several hundred atoms, with a favorable trade-off between cost and precision.

■ ASSOCIATED CONTENT

Data Availability Statement

The data that support the findings of this study are available from the corresponding author upon reasonable request.

■ AUTHOR INFORMATION

Corresponding Author

Mauro Stener − *Dipartimento di Scienze Chimiche e Farmaceutiche, Università di Trieste, 34127 Trieste, Italy; IOM-CNR, Istituto Officina dei Materiali, 34149 Trieste, Italy;* orcid.org/0000-0003-3700-7903; Email: stener@units.it

Authors

Pierpaolo D'Antoni − *Dipartimento di Scienze Chimiche e Farmaceutiche, Università di Trieste, 34127 Trieste, Italy*

Daniele Toffoli − *Dipartimento di Scienze Chimiche e Farmaceutiche, Università di Trieste, 34127 Trieste, Italy;* orcid.org/0000-0002-8225-6119

Complete contact information is available at: https://pubs.acs.org/10.1021/acs.jpca.5c03798

Notes

The authors declare no competing financial interest.

■ ACKNOWLEDGMENTS

P.D.A. and M.S. are grateful to Erik van Lenthe and Stan van Gisbergen of SCM (Amsterdam) for fruitful discussions and technical assistance during the implementation within the AMS/ADF program. Computational support from CINECA supercomputing center within the ISCRA program is gratefully acknowledged. The authors are grateful to the Stiftung Beneficentia for a generous grant employed to set up a computational server. Support from Trieste University within the FRA program is gratefully acknowledged. Financial support from ICSC−Centro Nazionale di Ricerca in High Performance Computing, Big Data and Quantum Computing, funded by the European Union−NextGenerationEU is gratefully acknowledged. Financial support from MIUR of Italy under the PRIN 2022 project COCAP funded by European Union − NextGenerationEU is gratefully acknowledged.

■ REFERENCES

(1) Barone, V. The Virtual Multifrequency Spectrometer: A New Paradigm for Spectroscopy. *WIREs Comput. Mol. Sci.* **2016**, *6*, 86−110.

(2) Casida, M. E. *Recent Advances in Density Functional Methods*; Chong, D. P., Ed.; World Scientific: Singapore, 1995; p 155.

(3) Yabana, K.; Bertsch, G. F. Time-Dependent Local-Density Approximation in Real Time. *Phys. Rev. A* **1996**, *54*, 4484−4487.

(4) Marques, M. A. L.; Castro, A.; Bertsch, G. F.; Rubio, A. Octopus: A First-Principles Tool for Excited Electron−Ion Dynamics. *Comput. Phys. Commun.* **2003**, *151*, 60−78.

(5) Walker, B.; Saitta, A. M.; Gebauer, R.; Baroni, S. Efficient Approach to Time-Dependent Density-Functional Perturbation Theory for Optical Spectroscopy. *Phys. Rev. Lett.* **2006**, *96*, No. 113001.

(6) Grimme, S. A Simplified Tamm-Dancoff Density Functional Approach for the Electronic Excitation Spectra of Very Large Molecules. *J. Chem. Phys.* **2013**, *138*, No. 244104.

(7) Bannwarth, C.; Grimme, S. A Simplified Time-Dependent Density Functional Theory Approach for Electronic Ultraviolet and Circular Dichroism Spectra of Very Large Molecules. *Comput. Theor. Chem.* **2014**, *1040−1041*, 45−53.

(8) Zuehlsdorff, T. J.; Hine, N. D. M.; Spencer, J. R.; Harrison, N. M.; Riley, D. J.; Haynes, P. D. J. Linear-Scaling Time-Dependent Density-Functional Theory in the Linear Response Formalism. *J. Chem. Phys.* **2013**, *139*, 064104.

(9) Malola, S.; Lehtovaara, L.; Enkovaara, J.; Häkkinen, H. Birth of the Localized Surface Plasmon Resonance in Monolayer-Protected Gold Nanoclusters. *ACS Nano* **2013**, *7*, 10263−10270.

(10) Noda, M.; Ishimura, K.; Nobusada, K.; Yabana, K.; Boku, T. Massively-Parallel Electron Dynamics Calculations in Real-Time and Real-Space: Toward Applications to Nanostructures of More than Ten-Nanometers in Size. *J. Comput. Phys.* **2014**, *265*, 145−155.

(11) Iida, K.; Noda, M.; Ishimura, K.; Nobusada, K. J. First-Principles Computational Visualization of Localized Surface Plasmon Resonance in Gold Nanoclusters. *J. Phys. Chem. A* **2014**, *118*, 11317−11322.

(12) Baseggio, O.; Fronzoni, G.; Stener, M. A New Time Dependent Density Functional Algorithm for Large Systems and Plasmons in Metal Clusters. *J. Chem. Phys.* **2015**, *143*, No. 024106.

(13) Baseggio, O.; De Vetta, M.; Fronzoni, G.; Stener, M.; Fortunelli, A. A New Time-Dependent Density-Functional Method for Molecular Plasmonics: Formalism, Implementation, and the $Au_{144}(SH)_{60}$Case Study. *Int. J. Quantum Chem.* **2016**, *116*, 1603−1611.

(14) Baseggio, O.; Toffoli, D.; Fronzoni, G.; Stener, M.; Sementa, L.; Fortunelli, A. Extension of the Time-Dependent Density Functional Complex Polarizability Algorithm to Circular Dichroism: Implementation and Applications to Ag_8 and $Au_{38}(SC_2H_4c_6H_5)_{24}$. *J. Phys. Chem. C* **2016**, *120*, 24335−24345.

(15) Baseggio, O.; De Vetta, M.; Fronzoni, G.; Stener, M.; Sementa, L.; Fortunelli, A.; Calzolari, A. Photoabsorption of Icosahedral Noble Metal Clusters: An Efficient TDDFT Approach to Large-Scale Systems. *J. Phys. Chem. C* **2016**, *120*, 12773−12782.

(16) Kaur, J.; Ospadov, E.; Staroverov, V. N. What Is the Accuracy Limit of Adiabatic Linear-Response TDDFT Using Exact Exchange−Correlation Potentials and Approximate Kernels? *J. Chem. Theory Comput.* **2019**, *15*, 4956−4964.

(17) Becke, A. D. Perspective: Fifty Years of Density-Functional Theory in Chemical Physics. *J. Chem. Phys.* **2014**, *140*, No. 18A301.

(18) Mardirossian, N.; Head-Gordon, M. Thirty Years of Density Functional Theory in Computational Chemistry: An Overview and Extensive Assessment of 200 Density Functionals. *Mol. Phys.* **2017**, *115*, 2315−2372.

(19) Becke, A. D. Density-Functional Thermochemistry. III. The Role of Exact Exchange. *J. Chem. Phys.* **1993**, *98*, 5648−5652.

(20) Stephens, P. J.; Devlin, F. J.; Chabalowski, C. F.; Frisch, M. J. Ab Initio Calculation of Vibrational Absorption and Circular Dichroism Spectra Using Density Functional Force Fields. *J. Phys. Chem. A* **1994**, *98*, 11623−11627.

(21) Dreuw, A.; Weisman, J. L.; Head-Gordon, M. Long-range charge-transfer excited states in time-dependent density functional theory require non-local exchange. *J. Chem. Phys.* **2003**, *119*, 2943−2946.

(22) Medves, M.; Sementa, L.; Toffoli, D.; Fronzoni, G.; Fortunelli, A.; Stener, M. An Efficient Hybrid Scheme for Time Dependent Density Functional Theory. *J. Chem. Phys.* **2020**, *152*, No. 184104.

(23) D'Antoni, P.; Medves, M.; Toffoli, D.; Fortunelli, A.; Stener, M.; Visscher, L. A Resolution of Identity Technique to Speedup TDDFT with Hybrid Functionals: Implementation and Application to the Magic Cluster Series $Au_{8n+4}(SC_6H_5)_{4n+8}$ (n = 3−6). *J. Phys. Chem. A* **2023**, *127*, 9244−9257.

(24) Medves, M.; Sementa, L.; Toffoli, D.; Fronzoni, G.; Krishnadas, K. R.; Bürgi, T.; Bonacchi, S.; Dainese, T.; Maran, F.; Fortunelli, A.;

Stener, M. Predictive Optical Photoabsorption of $Ag_{24}Au(DMBT)_{18}^-$ via Efficient TDDFT Simulations. *J. Chem. Phys.* **2021**, *155*, No. 084103.
(25) D'Antoni, P.; Sementa, L.; Bonacchi, S.; Reato, M.; Maran, F.; Fortunelli, A.; Stener, M. Combined Experimental and Computational Study of the Photoabsorption of the Monodoped and Nondoped Nanoclusters $Au_{24}Pt(SR)_{18}$, $Ag_{24}Pt(SR)_{18}$, and $Ag_{25}(SR)_{18}$. *Phys. Chem. Chem. Phys.* **2024**, *26*, 17569−17576.
(26) Baerends, E. J.; Aguirre, N. F.; Austin, N. D.; Autschbach, J.; Bickelhaupt, F. M.; Bulo, R.; Cappelli, C.; van Duin, A. C. T.; Egidi, F.; Fonseca Guerra, C.; et al. The Amsterdam Modeling Suite. *J. Chem. Phys.* **2025**, *162*, No. 162501.
(27) Seth, M.; Ziegler, T. Range-Separated Exchange Functionals with Slater-Type Functions. *J. Chem. Theory Comput.* **2012**, *8*, 901−907.
(28) Ullrich, C. A. *Time-Dependent Density-Functional Theory Concepts and Application*; Oxford Graduate Texts: Oxford, 2012; p 142.
(29) Yanai, T.; Tew, D. P.; Handy, N. C. A new hybrid exchange−correlation functional using the Coulomb-attenuating method (CAM-B3LYP). *Chem. Phys. Lett.* **2004**, *393*, 51−57.
(30) Baerends, E. J.; Ellis, D. E.; Ros, P. Self-Consistent Molecular Hartree—Fock—Slater Calculations I. The Computational Procedure. *Chem. Phys.* **1973**, *2*, 41−51.
(31) Medves, M.; Fronzoni, G.; Stener, M. Optimization of Density Fitting Auxiliary Slater-Type Basis Functions for Time-Dependent Density Functional Theory. *J. Comput. Chem.* **2022**, *43*, 1923−1935.
(32) Kozma, B.; Tajti, A.; Demoulin, B.; Izsák, R.; Nooijen, M.; Szalay, P. G. A New Benchmark Set for Excitation Energy of Charge Transfer States: Systematic Investigation of Coupled Cluster Type Methods. *J. Chem. Theory Comput.* **2020**, *16*, 4213−4225.
(33) Larsen, C. B.; Wenger, O. S. Circular Photoinduced Electron Transfer in a Donor-Acceptor-Acceptor Triad. *Angew. Chem., Int. Ed.* **2018**, *57*, 841−845.
(34) Tawada, Y.; Tsuneda, T.; Yanagisawa, S.; Yanai, T.; Hirao, K. A long-range-corrected time-dependent density functional theory. *J. Chem. Phys.* **2004**, *120*, 8425−8433.
(35) Zhao, Y.; Truhlar, D. G. Density Functional for Spectroscopy: No Long-Range Self-Interaction Error, Good Performance for Rydberg and Charge-Transfer States, and Better Performance on Average than B3LYP for Ground States. *J. Phys. Chem. A* **2006**, *110*, 13126−13130.
(36) Sementa, L.; Barcaro, G.; Baseggio, O.; De Vetta, M.; Dass, A.; Aprà, E.; Stener, M.; Fortunelli, A. Ligand-enhanced optical response of gold nanomolecules and its fragment projection analysis: the case of $Au_{30}(SR)_{18}$. *J. Phys. Chem. C* **2017**, *121*, 10832−10842.
(37) de Wergifosse, M.; Grimme, S. The eXact integral simplified time-dependent density functional theory (XsTD-DFT). *J. Chem. Phys.* **2024**, *160*, No. 204110.



https://doi.org/10.1021/acs.jpca.5c03798
J. Phys. Chem. A XXXX, XXX, XXX−XXX

4.1.4 Dichroism of plasmonic chiral nanoalloys by rational design

While the previous works are primarily focused on the development and validation of efficient TDDFT-based methodologies, the present article illustrates the application of the polTDDFT framework to the investigation of chiro-optical properties in extended metallic nanostructures. In particular, this study exploits the ability of polTDDFT to treat large systems and dense manifolds of excited states in order to address a fundamental question in structural chiral plasmonics.

Chiral metallic nanowires represent an intriguing class of systems, as they simultaneously exhibit intrinsic chirality and pronounced plasmonic absorption features. From an intuitive standpoint, one would therefore expect a strong plasmon-enhanced Electronic Circular Dichroism (ECD) response. Surprisingly, previous investigations have shown that purely chiral gold nanowires, despite their intense plasmonic absorption, display a nearly vanishing ECD signal at the plasmon resonance. This apparent contradiction motivates the present work and provides the conceptual starting point of the study.

Through a detailed TDDFT analysis, it is demonstrated that the suppression of the plasmonic ECD originates from a nearly perfect destructive interference between iso-energetic excitation contributions of opposite chiro-optical character. Building on this understanding, the system is deliberately perturbed by introducing controlled alloying with silver atoms, with the aim of lifting the degeneracy responsible for the cancellation of the ECD signal. This strategy proves effective for selected classes of linear chiral nanowires, where silver substitution leads to a pronounced enhancement of the plasmonic ECD response.

Beyond reproducing the emergence or suppression of plasmonic dichroism, the study provides a microscopic interpretation of the phenomenon by correlating the presence of plasmon-enhanced ECD with the spatial structure of the induced electron density. In particular, a continuous curling pattern of the induced density along the nanowire axis is identified as a key signature of a strong chiro-optical plasmonic response. Overall, this work demonstrates how first-principles TDDFT simulations can be used not only to compute spectra, but also to validate and rationalize chemical and physical intuition, offering a deeper understanding of structure–property relationships in chiral plasmonic nanomaterials.

Check for updates

Received: 19 December 2023 | Revised: 13 February 2024 | Accepted: 19 February 2024

DOI: 10.1002/jcc.27359

RESEARCH ARTICLE

Journal of COMPUTATIONAL CHEMISTRY WILEY

Dichroism of plasmonic chiral nanoalloys by rational design

Pierpaolo D'Antoni[1] | Daniele Toffoli[1] | Giovanna Fronzoni[1] | Mauro Stener[1] | Luca Sementa[2] | Alessandro Fortunelli[2]

[1]Dipartimento di Scienze Chimiche e Farmaceutiche, Università di Trieste, Trieste, Italy

[2]CNR-ICCOM & IPCF, Consiglio Nazionale delle Ricerche, Pisa, Italy

Correspondence
Mauro Stener, Dipartimento di Scienze Chimiche e Farmaceutiche, Università di Trieste, Via Giorgieri 1, 34127 Trieste, Italy.
Email: stener@units.it

Alessandro Fortunelli, CNR-ICCOM, Via Moruzzi 1, 56124 Pisa, Italy.
Email: alessandro.fortunelli@cnr.it

Funding information
Beneficentia Stiftung; ICSC—Centro Nazionale di Ricerca in High Performance Computing, Big Data and Quantum Computing; Università degli Studi di Trieste

Abstract

Time-dependent density functional theory (TDDFT) simulations are conducted on a series of chiral gold/silver alloy nanowires to explore whether silver doping can produce an enhancement of circular dichroism at the plasmon resonance in these systems, and to identify the quantum-mechanical origin of the observed effects. We find a strong plasmonic dichroism when one or two helixes of gold atoms are substituted by silver in a linear chiral nanotube, whose pure gold counterpart does not display any plasmonic dichroism, and we rationalize this finding in terms of "decoupling" the destructive interference of excitations in the pure gold nanotube via alloying. However, further attempts to increase the plasmonic dichroism by considering multi-shell gold nanowires in which one entire shell is doped with silver did not produce the desired effect, but rather a decrease in circular dichroism. We show that this latter result is due to a more severe destructive interference in the dipole excitation contributions, and suggest that further amplification should be possible in principle by properly tuning simultaneously the nanowire structure and chemical ordering.

KEYWORDS
chiral metal clusters, plasmonic dichroism

1 | INTRODUCTION

Plasmons play a major role in nanotechnology since they can focus the electromagnetic field within a small region of space thus obtaining a high electromagnetic energy density.[1–3] This effect can potentially amplify the local field intensity by many orders of magnitude and is routinely exploited in enhanced spectroscopies like Surface Enhanced Raman spectroscopy,[4] allowing the study of even single-molecules.[5,6] Although the nature of the plasmon phenomenon is well established for extended systems as an electronic collective oscillation mode, for finite nano-sized systems such as nanoclusters and nanowires their physical nature is still discussed and not yet completely assessed.[7–11]

Besides photoabsorption, when the system is chiral (absence of symmetry planes and inversion symmetry), an Electronic Circular Dichroism (ECD) signal is expected, that is, the absorption coefficient is different when right or left circularly polarized light is employed in the experiment. The ECD response can be exploited in practice for extremely selective chiral sensing.[12] However, the ECD signal is governed by the electric-dipole/magnetic-dipole scalar product, according to the Rosenfeld equation (Equation 1)[13]:

$$R_{on} = Im(\langle 0|\boldsymbol{\mu}|n\rangle\langle n|\boldsymbol{m}|0\rangle), \quad (1)$$

so ECD is much weaker than absorption, typically by a factor of about $\approx 10^{-5}$. Therefore the ability of amplifying the ECD exploiting *plasmonic* effects is a very promising strategy to improve the efficiency of chiral sensing and has been the topic of active research in the last decades.[14–17] Plasmonic ECD can be conveniently classified into structural and induced[17]: structural plasmonic ECD is related to systems which are intrinsically chiral,[18] while induced plasmonic ECD is generated by a chiral arrangement of non-chiral subsystems. Induced plasmonic ECD is more accessible at the experimental level,[19] but the growing interest for structural chiral plasmonics is justified by its potential larger enhancing efficiency and to the availability of new

 © 2024 Wiley Periodicals LLC.

synthetic strategies based on new bottom-up advanced techniques. From the theoretical point of view, it is important to identify which is the most suitable method to computationally describe the plasmon. When the system size is below 2 nm, such as gold clusters, quantum confinement effects are important,[20] and a quantum mechanical approach is necessary. Moreover, being the plasmon a collective resonance, it is necessary to employ a method which allows configuration mixing like Time Dependent Density Functional Theory (TDDFT),[21] while simpler DFT is not suitable.[22] In the present work we are interested in alloy nanosystems, whose relative small size still allows for a TDDFT treatment. In a previous work[23] some of us have shown that linear chiral gold nanowires exhibit very intense plasmonic absorption but almost negligible ECD despite being chiral. Additionally, it was shown that if the nanowires are coiled around the lateral surface of a cylinder the ECD is dramatically more intense than in linear nanowires. An analysis based on Individual Component Map of Rotatory Strength (ICM-RS)[24] demonstrated that in linear nanowires the plasmonic ECD is drastically quenched by an almost perfect *totally* destructive interference among iso-energetic configurations present in the collective plasmonic excitation. Hence, it was suggested that a small "perturbation" of the nanowire may be able to remove this almost perfect destructive interference and produce an intense plasmonic ECD. Coiling the nanowires indeed represents a kind of perturbation of the system shape. In the present paper we further elaborate this line of research, investigate a different route, and demonstrate that alloying may also be a practical way to avoid destructive interference and achieve a *plasmonic ECD signal* even in strictly linear nanowires.

The article is organized as follows. In Section 2, we give a brief description of the computational method. In Section 3, we report the results and their discussion for two kinds of linear nanoalloys which differ by their chemical ordering. In the first class of linear nanoalloys one or more chains of coiling atoms are doped, whereas in the second class of linear nanowires one entire wall (or shell) is doped within a multiwall systems. Interestingly, we obtain a strong plasmonic ECD only for the former class of doped systems, and we rationalize our finding via an analysis of ICM plots and induced densities. Finally, Section 4 summarizes the conclusions of the present study.

2 | THEORETICAL METHOD AND COMPUTATIONAL DETAILS

The geometries of the systems considered in the present study were taken from our previous work on gold nanowires,[23] by only changing the nature of the element, that is, replacing gold atoms with silver ones while keeping the original coordinates, not allowing for geometrical relaxation. This choice is justified since gold and silver have an almost identical atomic radius, of 1.46 and 1.44 Å, respectively, and we are interested in fundamental phenomena in pure form, without complications due to structural effects.

Photoabsorption as well as ECD calculations were carried out with the complex polarizability TDDFT (pol-TDDFT) algorithm,[25,26] using the ADF engine of the AMS software.[27] Such method consists in a linear-response TDDFT formalism in the frequency domain.

The algorithm calculates the oscillator strength and the rotatory strength as:

$$f = \frac{2\omega\varepsilon}{3} Im[\bar{\alpha}] \; R = \frac{3\omega\varepsilon}{2c} Im[\bar{\beta}], \tag{2}$$

where, $Im[\bar{\alpha}]$ and $Im[\bar{\beta}]$ represent respectively the imaginary part of the polarizability and rotatory strength tensor averaged over all the orientations, ω is the photon energy, c is the speed of the light, and ε is the imaginary part of the photon energy chosen as 0.06 eV. We have chosen this value since it has been already employed in the previous works on gold nanowires,[22,23] this allows to compare consistently the present results with those ones. The calculations were done with the asymptotically corrected LB94 xc functional,[28] the TZP basis-set (with density fitting set appropriately optimized to be used with the pol-TDDFT[29]), and the scalar ZORA[30] approach. Such choice has proven as a convenient compromise between accuracy and computational economy: in particular both xc functional[31] and basis set performances[29] have been assessed in previous work.

Besides the calculation of photoabsorption and ECD, we also analyze the results using tools specifically developed to study plasmonic systems in previous work: the Individual Component Map of Oscillator Strength plots (ICM-OS)[32] and the Individual Component Map of Rotatory Strength plots (ICM-RS).[24]

2.1 | Nanoalloys structures and chemical ordering

The structures of the alloy nanowires considered in this work are reported in Figure 1.[23] Such structures were inspired by linear chiral nanowires produced experimentally.[33] In the present work, we used identical geometrical structures, but introducing a chemical substitution of a subset of gold atoms with silver ones. Note that we did not re-optimize the structures, this assumption being justified by the almost identical atomic radius of gold and silver, as well as their almost identical interatomic distance in the bulk. Starting from above and using the nomenclature adopted in the previous work,[23] Figure 1A ($Au_{122}Ag_{30}$) and Figure 1B ($Au_{90}Ag_{62}$) correspond to the (5,3)NT (NanoTube) where one or two gold wires were substituted by silver atoms respectively. The substitution were introduced in one or two of the five wires which, coiling around the longitudinal axis, constitute the (5,3)NT. In the case of Figure 1B ($Au_{90}Ag_{62}$) the two silver wires are chosen in order not to be adjacent, in fact there are only two possibilities to choose the two wires from five: adjacent or not adjacent. We took the non-adjacent chemical ordering in order to maximize the "perturbing" effects of alloying on destructive interference. In the other structures we explored the effect of alloying from a different perspective: instead of generating a coiling pattern on the exposed surface of the system, we alloyed different shells of a multi-shell system. For this reason we have taken the 7-1 Helical Multi Shell

1096987x, 2024, 19, Downloaded from https://onlinelibrary.wiley.com/doi/10.1002/jcc.27359 by Universita Di Trieste, Wiley Online Library on [30/09/2025]. See the Terms and Conditions (https://onlinelibrary.wiley.com/terms-and-conditions) on Wiley Online Library for rules of use; OA articles are governed by the applicable Creative Commons License

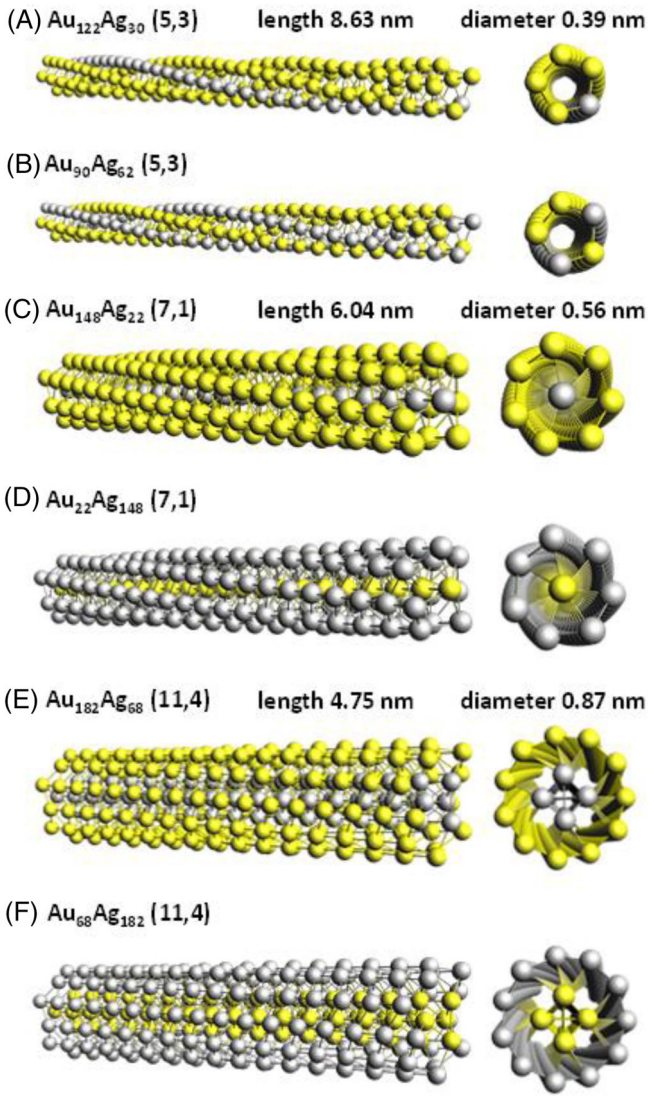


FIGURE 1 Structures of the nanoalloys considered in the present work. (5,3)NT: (A) $Au_{122}Ag_{30}$ and (B) $Au_{90}Ag_{62}$. 7-1 HMS (C) $Au_{148}Ag_{22}$ and (D) $Au_{22}Ag_{148}$. 11-4 HMS (E) $Au_{182}Ag_{68}$ and (F) $Au_{68}Ag_{182}$.

(HMS) and the 11-4 HMS. These systems consist of two shells: in 7-1 HMS seven nanowires are coiling around one linear chain of metal atoms which lies along the longitudinal axis of the system. In the 11-4 nanowire 11 wires are coiling around an achiral nanotube consisting of four linear wires. In present work, Figure 1C ($Au_{148}Ag_{22}$) and Figure 1D ($Au_{22}Ag_{148}$) correspond to the 7-1 HMS structure where the inner wire consists of silver and gold atoms respectively, and the atomic nature of the outer shell is opposite to the inner one. Figure 1E ($Au_{182}Ag_{68}$) and Figure 1F ($Au_{68}Ag_{182}$) instead correspond to the 11-4 HMS structure where the inner nanotube consists of silver and gold atoms, respectively, and the outer shell atomic nature is opposite to the inner one.

Note that in this study we do not investigate the dependence of plasmonic phenomena upon the size of the wires, which was the topic of a previous work.[22]

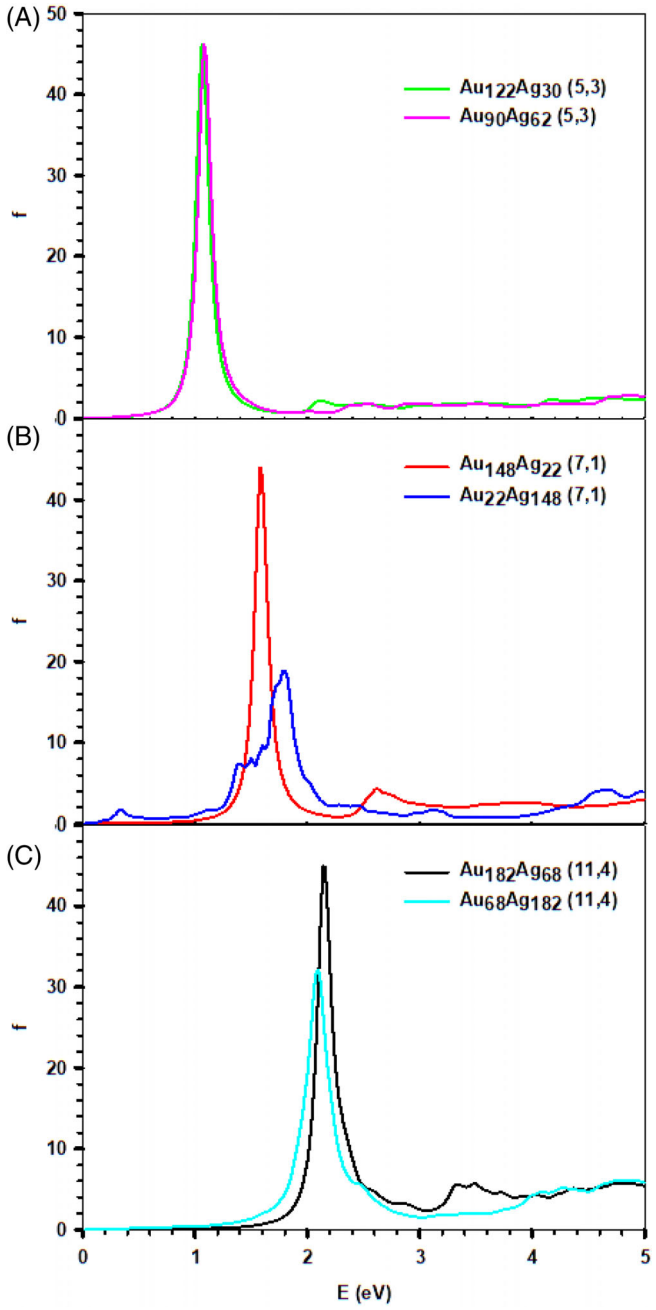


FIGURE 2 Photoabsorption for the series of linear chiral nanoalloys. (A) (5,3)NT $Au_{122}Ag_{30}$ and $Au_{90}Ag_{62}$. (B) 7-1 HMS $Au_{148}Ag_{22}$ and $Au_{22}Ag_{148}$. (C) 11-4 HMS $Au_{182}Ag_{68}$ and $Au_{68}Ag_{182}$.

3 | RESULTS AND DISCUSSION

3.1 | Nanoalloys plasmonic photoabsorption

In Figure 2, the calculated TDDFT photoabsorption spectra of all the systems defined in Section 2.1 are reported. All the calculated profiles display a very sharp and intense plasmonic peak whose energy is almost independent by the chemical ordering but changes with the structure. More precisely, the peak of (5,3)NT

1096987x, 2024, 19, Downloaded from https://onlinelibrary.wiley.com/doi/10.1002/jcc.27359 by Universita Di Trieste, Wiley Online Library on [30/09/2025]. See the Terms and Conditions (https://onlinelibrary.wiley.com/terms-and-conditions) on Wiley Online Library for rules of use; OA articles are governed by the applicable Creative Commons License

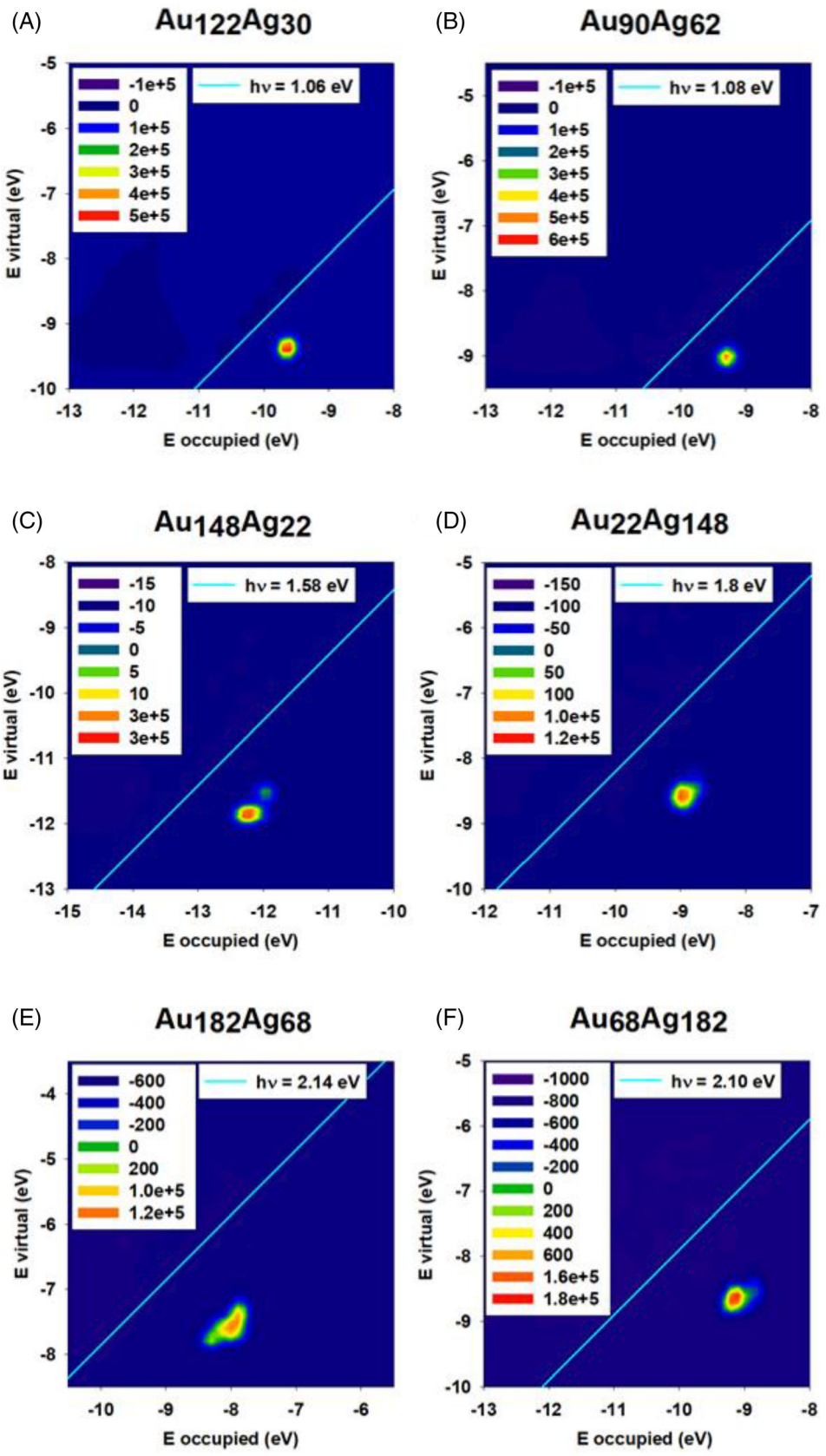


FIGURE 3 ICM-OS analysis of the longitudinal electric dipole component at plasmon energies for the nanoalloys: (A) $Au_{122}Ag_{30}$ at 1.06 eV, (B) $Au_{90}Ag_{62}$ at 1.08 eV, (C) $Au_{148}Ag_{22}$ at 1.58 eV, (D) $Au_{22}Ag_{148}$ at 1.80 eV, (E) $Au_{182}Ag_{68}$ at 2.10 eV, and (F) $Au_{68}Ag_{182}$ at 2.14 eV. The straight line corresponds to virtual-occupied pair energy difference equal to the excitation energy.

falls at 1.06 and 1.08 eV for $Au_{122}Ag_{30}$ and $Au_{90}Ag_{62}$, in 7-1 HMS the peak is at 1.58 and 1.80 eV for $Au_{148}Ag_{22}$ and $Au_{22}Ag_{148}$, finally in 11-4 HMS the plasmon lies at 2.14 and 2.10 eV for $Au_{182}Ag_{68}$ and $Au_{68}Ag_{182}$, respectively. The energies and the photoabsorption intensities of the plasmon resonances of the nanoalloys are quite close to those of the corresponding gold

1096987x, 2024, 19, Downloaded from https://onlinelibrary.wiley.com/doi/10.1002/jcc.27359 by Universita Di Trieste, Wiley Online Library on [30/09/2025]. See the Terms and Conditions (https://onlinelibrary.wiley.com/terms-and-conditions) on Wiley Online Library for rules of use; OA articles are governed by the applicable Creative Commons License

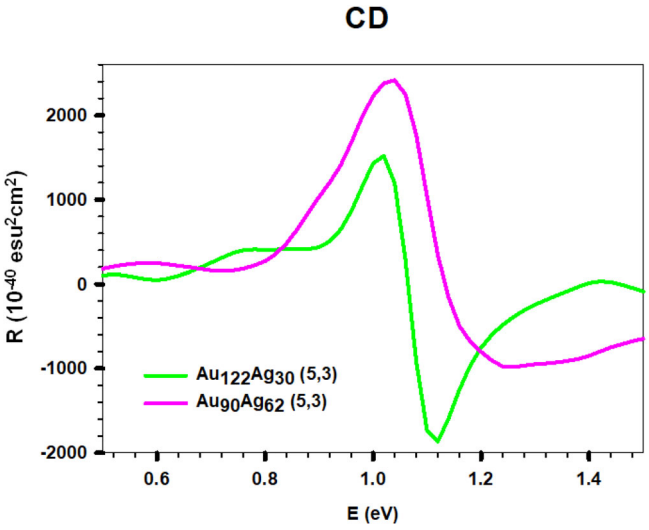
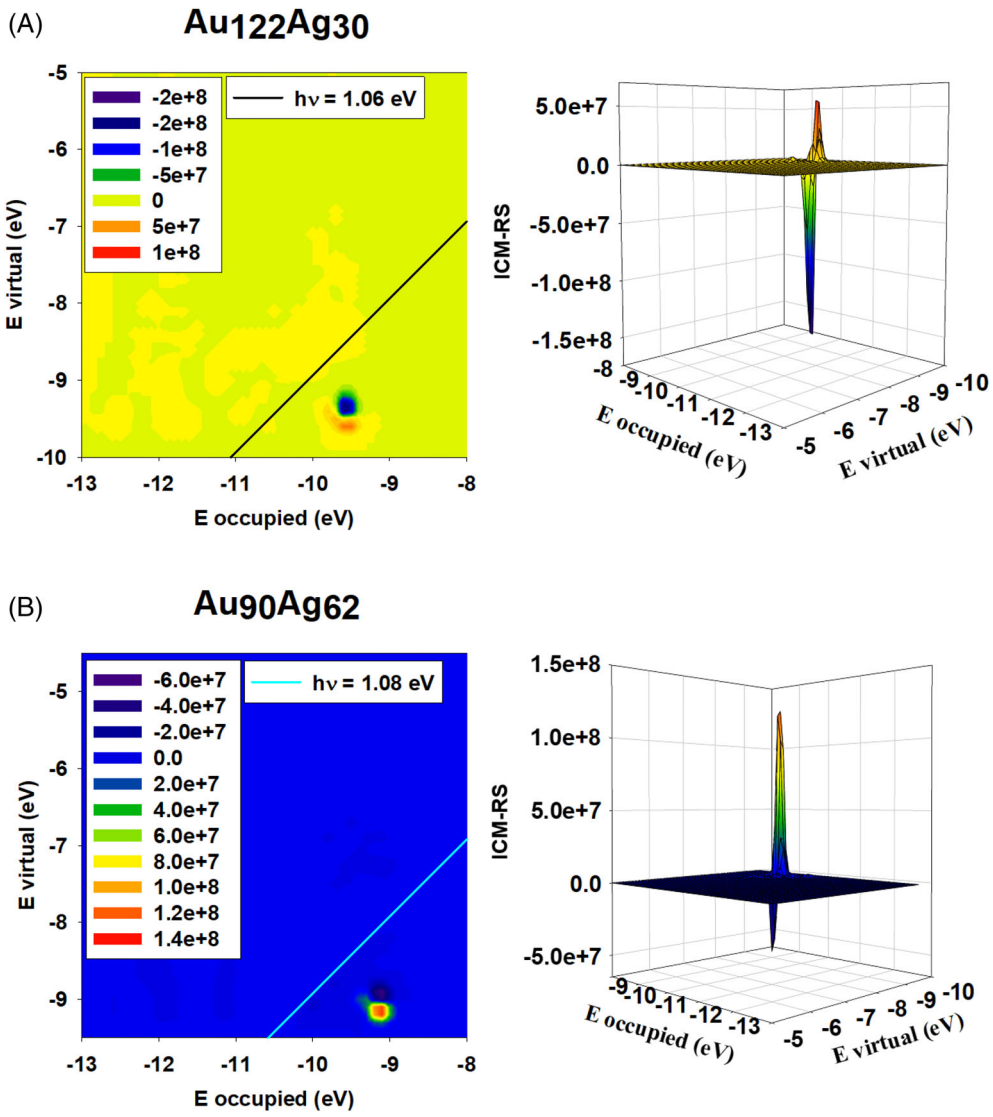


FIGURE 4 ECD for the linear chiral nanoalloys (5,3)NT $Au_{122}Ag_{30}$ and $Au_{90}Ag_{62}$. Rotator strength (R) is given in 10^{-40} esu^2 cm^2.

nanowires,[23] indicating that alloying has a negligible effect on the plasmonic resonance in absorption. Up to now we have ascribed the spectral features to plasmon resonances due to their sharp and intense peak. It is however desirable to confirm the plasmonic nature of such features via a more rigorous argument. To this end we employed the ICM-OS analysis, whose results are reported in Figure 3. In these plots, calculated at the energies corresponding to the maximum absorption and for the longitudinal dipole component, we report the energy of the occupied orbitals on the *x*-axis and the energy of the virtual ones on the *y*-axis. The "spots" correspond to the dipole contribution arising from the occupied-virtual pair excited configurations with orbital energies corresponding to the values of the *x* and *y* coordinates. The straight line corresponds to a virtual-occupied pair energy difference equal to the excitation energy. As it can be easily seen, all the spots are remarkably far (at least 1 eV) from the straight line, indicating a strong coupling between different configurations, confirming the plasmonic collective behavior of the peak.

FIGURE 5 On the left panel are shown the ICM-RS analysis of the longitudinal magnetic dipole component at plasmon energies for the (5,3)NT nanoalloys: (A) $Au_{122}Ag_{30}$ at 1.06 eV and (B) $Au_{90}Ag_{62}$ at 1.08 eV. In right panel the same plots are shown in 3D to better appreciate the destructive interference effect.



1096987x, 2024, 19, Downloaded from https://onlinelibrary.wiley.com/doi/10.1002/jcc.27359 by Universita Di Trieste, Wiley Online Library on [30/09/2025]. See the Terms and Conditions (https://onlinelibrary.wiley.com/terms-and-conditions) on Wiley Online Library for rules of use; OA articles are governed by the applicable Creative Commons License

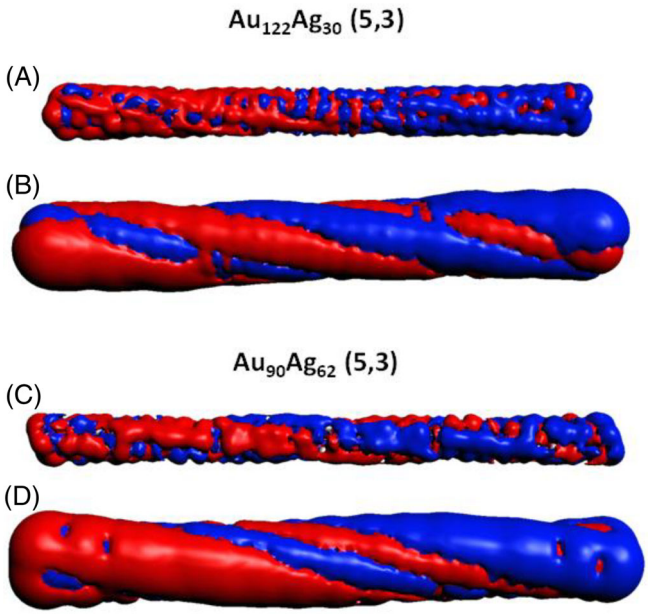


FIGURE 6 The induced density of the longitudinal component at plasmon energies for the (5,3)NT nanoalloys: (A, B) $Au_{122}Ag_{30}$ at 1.06 eV and (C, D) $Au_{90}Ag_{62}$ at 1.08 eV. The isosurface value is 0.03 electrons/Bohr^3 for (A and C) and 0.00003 electrons/Bohr^3 for (B and D).

3.2 | Nanoalloys plasmonic electronic circular dichroism of (5,3)NT

In Figure 4, we report the calculated TDDFT ECD of the two (5,3) NT nanoalloys. Surprisingly, it is immediately evident that a very intense ECD is calculated at the plasmon energy. It is worth noting that this finding is a genuine effect of alloying. Indeed, the pure gold (5,3)NT gave no ECD features at the plasmon resonance.[23] Morever the effect is quite strong, with a Rotator strength (R) amplified by a factor of about 20 as a consequence of alloying: from R around ±100 cgs 10^{-40} units of the background without plasmon enhancement of the pure gold nanowire[23] to R around ±2000 for the nanoalloys. Besides its intensity, it is apparent that such plasmonic ECD is also sensitive to the chemical ordering, as the spectral features are appreciably different in the two nanowires: the typical Cotton profile of $Au_{122}Ag_{30}$ is less positive than $Au_{90}Ag_{62}$ just below the plasmon energy, but is more negative above the plasmon. Moreover, also the curvature of the R profile is different just beyond the plasmon: $Au_{122}Ag_{30}$ displays a convex shape (corresponding to a negative second derivative) while $Au_{90}Ag_{62}$ gives a concave shape (positive second derivative), such behavior extending roughly from 1.0 to 1.5 eV. We believe that this finding is quite new and very promising in terms of potential applications and exploitations in the field of nanoscience. Indeed, the possibility to enhance ECD by alloying could be exploited to trigger ECD on presently inactive systems. Of course, taking complete control over the chemical ordering in such systems is challenging, but the potential chances it offers are so significant to trigger pursuing it. To the best of our knowledge, this is the first time

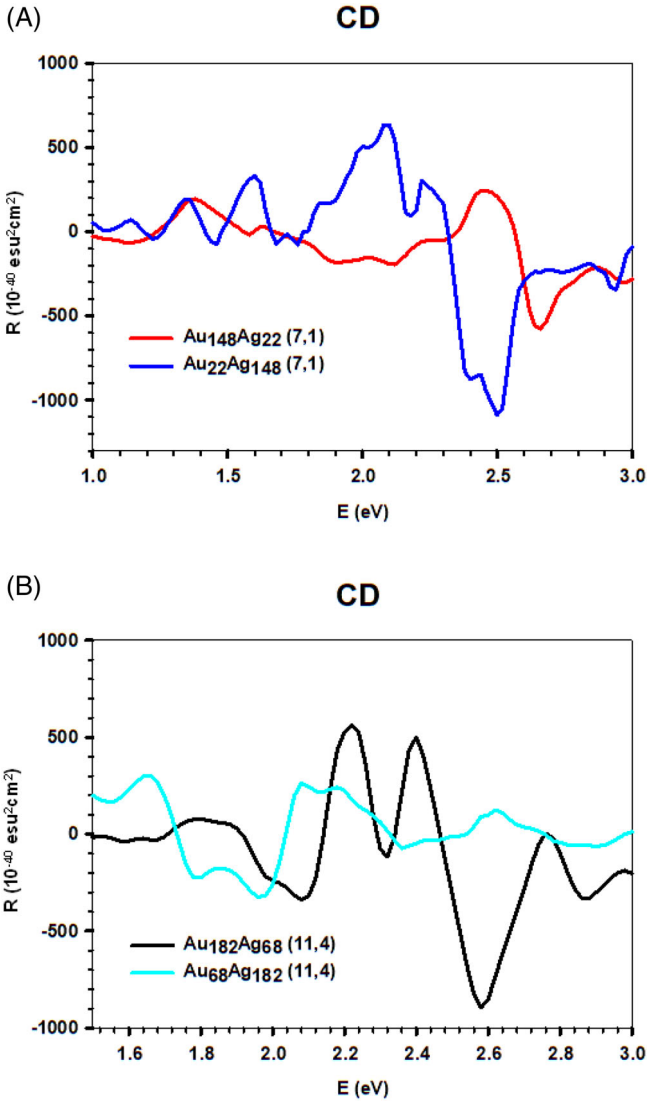


FIGURE 7 ECD for the linear chiral nanoalloys (A) 7-1 HMS $Au_{148}Ag_{22}$ and $Au_{22}Ag_{148}$, (B) $Au_{182}Ag_{68}$ and $Au_{68}Ag_{182}$. Rotator strength (R) is given in 10^{-40} esu^2 cm^2.

in which a chiral chemical ordered alloying is predicted to have such a dramatic effect on the ECD. It is clearly important from a scientific point of view to investigate the physical origin of this new effect, to understand better the mechanism lying behind it so as to suggest even more effective enhancements and finally reach a rational design of dichroic plasmonic nanoalloys. We have thus performed an ICM-RS analysis at the plasmon energies to better describe what happens in terms of electronic structure. The ICM-RS analysis is analogue to the ICM-OS one, but now the contributions of the excited configurations are weighted by the magnetic dipole transition moment, in order to split the total R in contributions from each one-electron excited pair. In the ICM-RS the electric dipole is used as an external field perturbation, the induced magnetic dipole is calculated by linear response. The ICM-RS analysis at the plasmon energies of $Au_{122}Ag_{30}$ and $Au_{90}Ag_{62}$ are reported in Figure 5. It is well apparent that both systems display a strong dichroism which is the sum of two contributions of opposite

1096987x, 2024, 19, Downloaded from https://onlinelibrary.wiley.com/doi/10.1002/jcc.27359 by Universita Di Trieste, Wiley Online Library on [30/09/2025]. See the Terms and Conditions (https://onlinelibrary.wiley.com/terms-and-conditions) on Wiley Online Library for rules of use; OA articles are governed by the applicable Creative Commons License

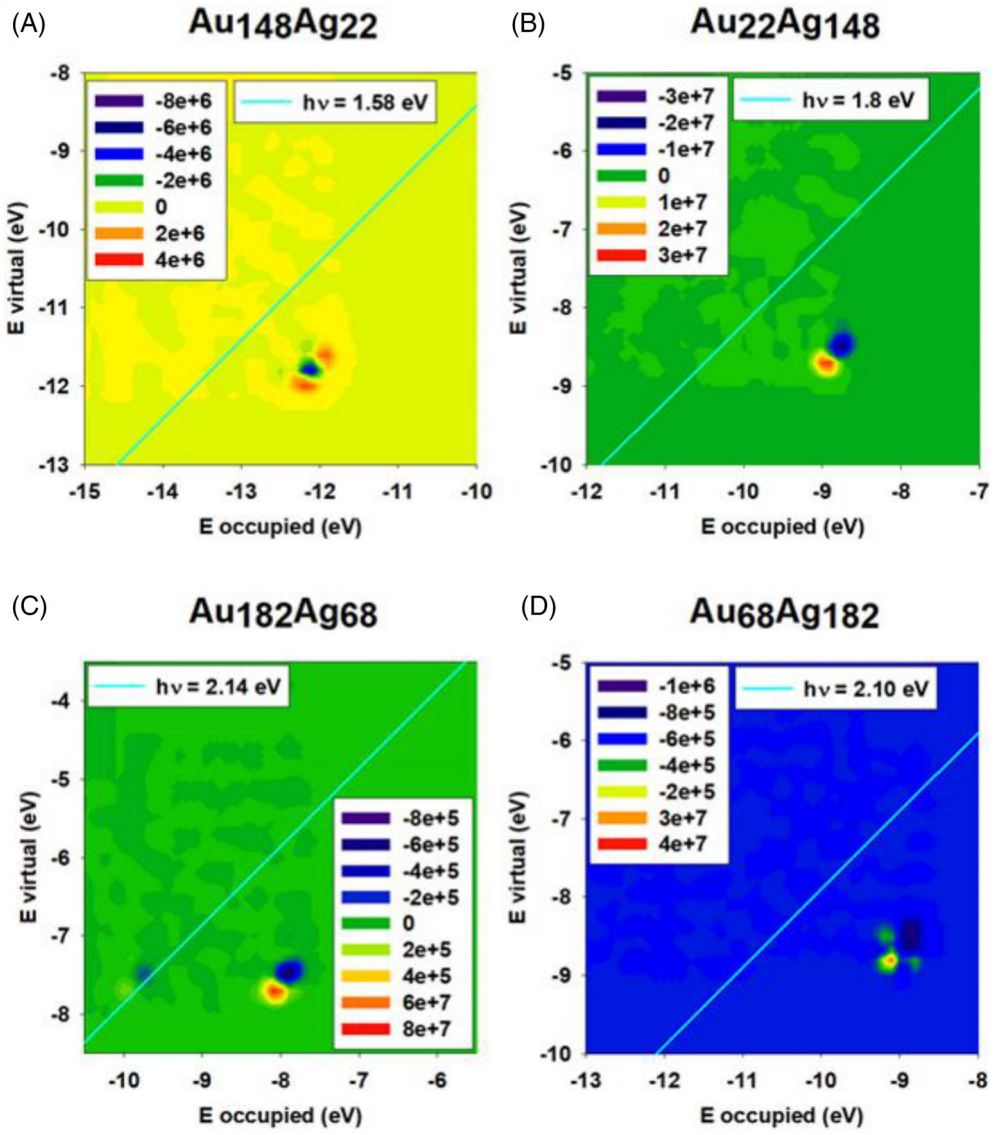


FIGURE 8 ICM-RS analysis of the longitudinal magnetic dipole component at plasmon energies for the 7-1 HMS (A) $Au_{148}Ag_{22}$ and (B) $Au_{22}Ag_{148}$ and the 11-4 HMS (C) $Au_{182}Ag_{68}$ and (D) $Au_{68}Ag_{182}$. The straight line corresponds to virtual-occupied pair energy difference equal to the excitation energy.

sign, so a *partially* destructive interference is taking place. It is interesting to compare this finding to the pure gold (5,3)NT considered previously,[23] also in that case two very strong contributions were present at the plasmon energies, but a *totally* destructive interference was observed, in fact there was basically no appreciable ECD at the plasmon energy. So, we have been able to find out that a proper chemical ordered alloying is effective to "decouple" the *totally* destructive interference by means of alloying the system with silver atoms. It is worth noting, especially in the 3D plots in the right panel of Figure 5, that a large amount of destructive interference is still present, so there is still room to increase the plasmon dichroism, at least in principle. For this reason, it would be important to design or explore additional strategies (besides alloying) to further reduce the amount of destructive interference. Another useful analysis in this context is the inspection of the induced density, as an effect of the external time-dependent perturbation. This analysis is somehow complementary to the ICM-RS, since it is in real-space and therefore more suitable to be visualized and suggest structural changes to improve plasmonic dichroism. In Figure 6, we have considered two different isosurface values, where the larger value of 0.03 electrons/Bohr^3 (Figure 6A,C) shows the localization of the density while the smaller value of 0.00003 electrons/Bohr^3 (Figure 6B,D) is useful to identify a more regular shape. From an inspection of Figure 6, we find the usual dipolar shape, typical of plasmon resonance, but also a curling of the density, especially in the plots with the smaller isosurface value. This finding suggests that, for example, a chiral disposition of protecting ligands around the nanowires should improve the dichroism, favoring a curly induced density. Such a procedure, however, could also quench the plasmon since protective ligands favor the oxidation of the metallic atoms, excluding their active role in the plasmon, so this mechanism might be more promising for larger multiwall nanotubes, which can maintain their plasmonic behavior even in the presence of a ligand shell. It is important to observe that, due to the Cotton profile of the plasmonic dichroism, a fast change in the induced density can be expected for small energy changes near the resonance. We have therefore analyzed the induced density at three very close energy

1096987x, 2024, 19, Downloaded from https://onlinelibrary.wiley.com/doi/10.1002/jcc.27359 by Universita Di Trieste, Wiley Online Library on [30/09/2025]. See the Terms and Conditions (https://onlinelibrary.wiley.com/terms-and-conditions) on Wiley Online Library for rules of use; OA articles are governed by the applicable Creative Commons License

points: at the maximum positive R, at the plasmon energy, at the maximum negative R. The relative density plots are reported in Figure S1 for $Au_{122}Ag_{30}$ and S2 for $Au_{90}Ag_{62}$ of the Supporting Information. Also in this case two isosurfaces are considered, to facilitate the shape assessment with the small isosurface. The induced density displays actually a phase inversion going through the plasmon, in line with the Cotton profile of the dichroism. Moreover, while the plots with larger isosurface value display a helicity, when the smaller isosurface is considered a very clear-cut helicity is found mainly in the higher energy tail of the plasmon.

A further helpful tool is the fragment analysis, as described in detail in Reference 34. This tool allows one to split the total photoabsorption in partial contributions according to the definition of fragments within the system under study. In practice, for present nanowires it is natural to consider them as built by two fragments: the gold fragment and the silver one. In this case the fragment analysis will assign four partial contributions rising from the four possible transitions: Au → Au, Au → Ag, Ag → Au, and Ag → Ag. Such analysis performed on the two (5,3)NT $Au_{122}Ag_{30}$ and $Au_{90}Ag_{62}$ are reported in Figures S3 and S4 of the Supporting information. Interestingly for $Au_{122}Ag_{30}$ it is evident (Figure S3) that the first plasmonic positive peak of dichoroism can be ascribed to a transition starting and arriving to gold (Au → Au), while the plasmonic negative peak is ascribed to a transition starting from gold and arriving to silver (Au → Ag). Apparently, contributions starting from the silver moiety do not play an important role. For the other nanowire $Au_{90}Ag_{62}$ the analysis (Figure S4) is not helpful since it seems that there is no specific fragment role, it is apparent that the ECD profile is dominated by the Au → Au partial contribution on both side of the plasmonic structure.

We can conclude this subsection saying that, for the first time, we predict theoretically that a dichroic plasmon can be triggered by means of proper alloying.

3.3 | Nanoalloys plasmonic electronic circular dichroism of 7-1 and 11-4 HMS

In Figure 7, the ECD of the 7-1 and 11-4 HMS nanoalloys are reported. In this case, at variance with the (5,3)NT, we observe a significantly smaller amplification of the ECD at the plasmon energy with respect to the pure nanowire considered in Reference 23. In detail, while the profiles for the 7-1 HMS is rather flat, a small effect can be found for the 11-4 HMS around 2 eV, although in any case it can be observed that the feature around 2.6 eV is larger than the plasmonic one. Moreover the 11-4 HMS response seems to be more sensitive to the chemical ordering than the 7-1 one. To rationalize this somewhat disappointing results, we produced the ICM-RS for the 7-1 HMS $Au_{148}Ag_{22}$, $Au_{22}Ag_{148}$ and 11-4 HMS $Au_{182}Ag_{68}$, $Au_{68}Ag_{182}$ in Figure 8. Once more, we found an almost *total* destructive interference, so in this case the alloying has not been effective in decoupling the contributions and giving rise to a significant plasmonic ECD. If we inspect the induced densities (reported in Figure 9) only for the smaller isosurface value, we find that for the gold exposed systems, Figure 9A,C, the induced density looks rather "granular," while for the silver exposed systems, Figure 9B,D, the density looks much more uniform. This is an effect of the different dynamical behavior of silver with respect to gold: for gold the localized 5d manifolds tends to quench the plasmon, while in silver the behavior is much more typical of a free-electron gas, less sensitive to the fine details of the atomic geometry. In Figures S5 and S6 of the SI we also report the plots obtained with a larger value of the isosurface. An interesting finding is that the curling shape of the induced density, although less evident than in the more active (5,3)NT, shows a kind of "breaking" or "interruption" in the middle of the nanoallys, while when strong plasmonic ECD is calculated (see Figure 6 for comparison) we do not have any "breaking" in the induced density plots. Finally it is important to comment why for (5,3)NT the alloying is efficient in triggering plasmonic dichroism, whereas for 7-1 and 11-4 HMS the alloying strategy fails.

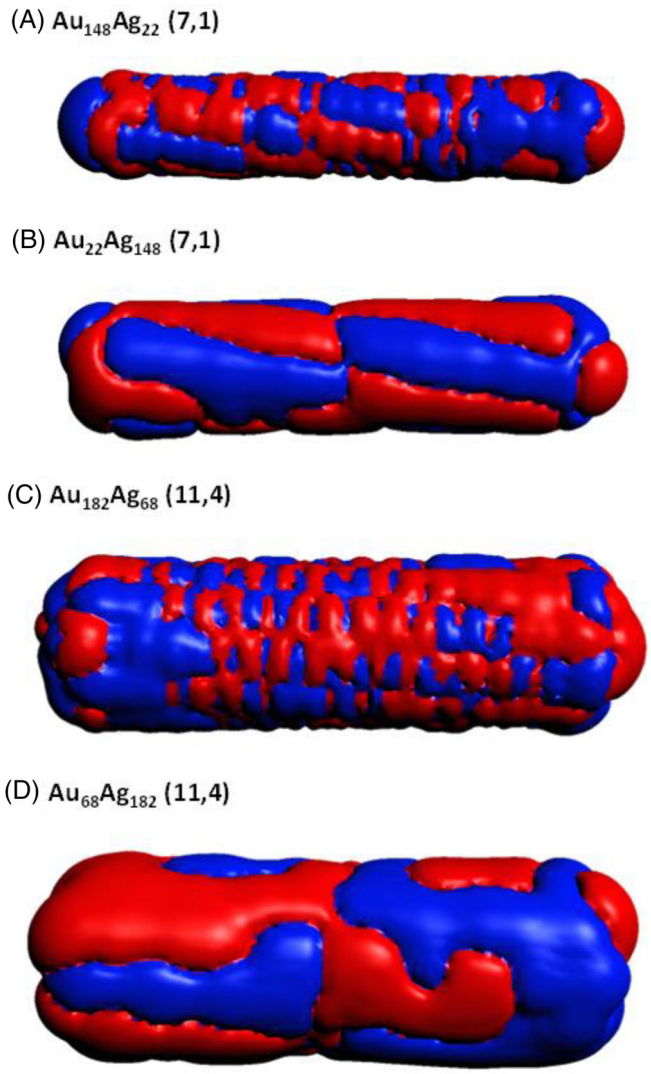


FIGURE 9 The induced density of the longitudinal component at plasmon energies for the 7-1 HMS (A) $Au_{148}Ag_{22}$ and (B) $Au_{22}Ag_{148}$ and the 11-4 HMS (C) $Au_{182}Ag_{68}$ and (D) $Au_{68}Ag_{182}$. The isosurface value is 0.00003 electrons/Bohr^3.

1096987x, 2024, 19, Downloaded from https://onlinelibrary.wiley.com/doi/10.1002/jcc.27359 by Universita Di Trieste, Wiley Online Library on [30/09/2025]. See the Terms and Conditions (https://onlinelibrary.wiley.com/terms-and-conditions) on Wiley Online Library for rules of use; OA articles are governed by the applicable Creative Commons License

In this respect it is worth noting that in (5,3)NT the alloying consists in doping by Ag one or two strings of atoms which are curling around the longitudinal axis of the system. In contrast, alloying in 7-1 and 11-4 HMS it consists in doping one or four *linear* strings of atoms (not curling) along the longitudinal direction. This suggests that, for doping to be effective in enhancing plasmonic dichroism, it must follow a helical arrangement. This requirement can be rationalized as follows: in pure linear chiral gold nanowires we do not observe plasmonic dichroism because the induced current does not follows the chiral atomic pattern, but rather it moves back and forth following a straight line path. Helical doping forces the induced current to follow a curling path, but this does not happen in 7-1 and 11-4 HMS because in these systems the doping arrangement is linear.

4 | CONCLUSIONS

Here, we have investigated the chiro-optical response of a series of chiral gold/silver alloy nanowires via time-dependent density functional theory (TDDFT) simulations. These systems are promising for chiro-optical sensor applications since they display strong plasmonic optical absorption peaks in a relatively small size. The main conclusion of our study is that by properly alloying silver into chiral gold nanowires, it is possible to trigger a strong plasmonic Electronic Circular Dichroism (ECD) signal, at variance with pure gold nanowire in which a total destructive interference results in a negligible ECD signal at the plasmon energy. A chiro-optically effective alloying is achieved by replacing one or two chains of gold atoms which curl around the axis of the (5,3)NT system. In contrast, alloying an entire single wall (shell) of even larger systems, such as the multiwall 7-1 and 11-4 HMS, is not effective in enhancing the ECD at the plasmon energy, producing less intense ECD peaks. An analysis based on the Individual Component Map of Rotatory Strength (ICM-RS) tool indicates that, whereas in the (5,3)NT system a partial decoupling of destructive contributions from iso-energetic excitations is induced by alloying, in the multiwall case a more significant destructive interference remains. Plots of the induced density further suggest that the plasmon ECD is strong when a curling shape of the density is achieved exhibiting no interruptions along the wire. Further possibilities to remove the phenomenon of destructive interference can then be envisaged from the present analysis, for example by properly adding ligand adsorbates along the helical patterns so as to obtain the desired decoupling of interfering excitations.

ACKNOWLEDGMENTS

Financial support from ICSC—Centro Nazionale di Ricerca in High Performance Computing, Big Data and Quantum Computing, funded by European Union—NextGenerationEU is gratefully acknowledged. This publication is based upon work networked within the COST Action CA21101 "Confined molecular systems: from a new generation of materials to the stars" (COSY) supported by COST (European Cooperation in Science and Technology). Computational support from CINECA supercomputing center within the ISCRA program is gratefully acknowledged. The authors are grateful to the Stiftung Beneficentia for the financial support to set up a computing server. Support from Trieste University within the FRA program is also acknowledged.

DATA AVAILABILITY STATEMENT

The data that support the findings of this study are available from the corresponding author upon reasonable request.

ORCID

Daniele Toffoli https://orcid.org/0000-0002-8225-6119
Mauro Stener https://orcid.org/0000-0003-3700-7903
Luca Sementa https://orcid.org/0000-0002-3951-2842
Alessandro Fortunelli https://orcid.org/0000-0001-5337-4450

REFERENCES

[1] C. Zhang, J. Z. Noguez, *Plasmonics* **2008**, *3*, 127.
[2] M. Rycenga, C. M. Cobley, J. Zeng, W. Li, C. H. Moran, Q. Zhang, D. Qin, Y. Xia, *Chem. Rev.* **2011**, *111*, 3669.
[3] N. Durante, A. Fortunelli, M. Broyer, M. Stener, *J. Phys. Chem. C* **2011**, *115*, 6277.
[4] J. Langer, D. Jimenez de Aberasturi, J. Aizpurua, R. A. Alvarez-Puebla, B. Auguié, J. J. Baumberg, G. C. Bazan, S. E. J. Bell, A. Boisen, A. G. Brolo, J. Choo, D. Cialla-May, V. Deckert, L. Fabris, K. Faulds, F. J. García de Abajo, R. Goodacre, D. Graham, A. J. Haes, C. L. Haynes, C. Huck, T. Itoh, M. Käll, J. Kneipp, N. A. Kotov, H. Kuang, E. C. le Ru, H. K. Lee, J. F. Li, X. Y. Ling, S. A. Maier, T. Mayerhöfer, M. Moskovits, K. Murakoshi, J. M. Nam, S. Nie, Y. Ozaki, I. Pastoriza-Santos, J. Perez-Juste, J. Popp, A. Pucci, S. Reich, B. Ren, G. C. Schatz, T. Shegai, S. Schlücker, L. L. Tay, K. G. Thomas, Z. Q. Tian, R. P. van Duyne, T. Vo-Dinh, Y. Wang, K. A. Willets, C. Xu, H. Xu, Y. Xu, Y. S. Yamamoto, B. Zhao, L. M. Liz-Marzán, *ACS Nano* **2020**, *14*, 28.
[5] M. Barbry, P. Koval, F. Marchesin, R. Esteban, A. G. Borisov, J. Aizpurua, D. Sánchez-Portal, *Nano Lett.* **2015**, *15*, 3410.
[6] L. Sementa, A. Marini, F. R. Negreiros, A. Fortunelli, *ACS Photonics* **2014**, *1*, 315.
[7] S. Bernadotte, F. Evers, C. R. Jacob, *J. Phys. Chem. C* **2013**, *117*, 1863.
[8] R. Zhang, L. Bursi, J. D. Cox, Y. Cui, C. M. Krauter, A. Alabastri, A. Manjavacas, A. Calzolari, S. Corni, E. Molinari, E. A. Carter, F. J. García de Abajo, H. Zhang, P. Nordlander, *ACS Nano* **2017**, *11*, 7321.
[9] R. Sinha-Roy, P. García-González, H. C. Weissker, F. Rabilloud, A. I. Fernández-Domínguez, *ACS Photonics* **2017**, *4*, 1484.
[10] J. H. Mokkath, U. Schwingenschlögl, *J. Chem. Phys.* **2016**, *144*, 134305.
[11] N. J. Halas, S. Lal, W. S. Chang, S. Link, P. Nordlander, *Chem. Rev.* **2011**, *111*, 3913.
[12] N. Kameta, M. Masuda, T. Shimizu, *Chem. Commun.* **2015**, *51*, 11104.
[13] J. J. Pelayo, I. Valencia, A. P. García, L. Chang, M. López, D. Toffoli, M. Stener, A. Fortunelli, I. L. Garzón, *Adv. Phys. X* **2018**, *3*, 1509727. https://doi.org/10.1080/23746149.2018.1509727
[14] N. Karimova, C. M. Aikens, *J. Phys. Chem. A* **2015**, *119*, 8163.
[15] L. Nguyen, M. Dass, M. F. Ober, L. V. Besteiro, Z. M. Wang, B. Nickel, A. O. Govorov, T. Liedl, A. Heuer-Jungemann, *ACS Nano* **2020**, *14*, 7454.
[16] J. M. Slocik, P. B. Dennis, A. O. Govorov, N. M. Bedford, Y. Ren, R. R. Naik, *ACS Biomater. Sci. Eng.* **2020**, *6*, 2612.
[17] Z. Hu, D. Meng, F. Lin, X. Zhu, Z. Fang, X. Wu, *Adv. Opt. Mater.* **2019**, *7*, 1801590.
[18] Z. Fan, A. O. Govorov, *Nanoletters* **2012**, *12*, 3283.
[19] C. Zeng, Y. Chen, C. Liu, K. Nobusada, N. L. Rosi, R. Jin, *Sci. Adv.* **2015**, *1*, e1500425.

1096987x, 2024, 19, Downloaded from https://onlinelibrary.wiley.com/doi/10.1002/jcc.27359 by Universita Di Trieste, Wiley Online Library on [30/09/2025]. See the Terms and Conditions (https://onlinelibrary.wiley.com/terms-and-conditions) on Wiley Online Library for rules of use; OA articles are governed by the applicable Creative Commons License

[20] S. Lu, L. Xie, K. Lai, R. Chen, L. Cao, K. Hu, X. Wang, J. Han, X. Wan, J. Wan, Q. Dai, F. Song, J. He, J. Dai, J. Chen, Z. Wang, G. Wang, *Natl. Sci. Rev.* **2021**, *8*, nwaa282.
[21] M. E. Casida, in *Recent Advances in Density-Functional Methods* (Ed: D. P. Chong), World Scientific, Singapore **1995**, p. 155.
[22] G. M. Piccini, R. W. A. Havenith, R. Broer, M. Stener, *J. Phys. Chem. C* **2013**, *117*, 17196.
[23] D. Toffoli, A. Russi, G. Fronzoni, E. Coccia, M. Stener, L. Sementa, A. Fortunelli, *J. Phys. Chem. Lett.* **2021**, *12*, 5829.
[24] L. Chang, O. Baseggio, L. Sementa, D. Cheng, G. Fronzoni, D. Toffoli, E. Aprà, M. Stener, A. Fortunelli, *J. Chem. Theory Comput.* **2018**, *14*, 3703.
[25] O. Baseggio, G. Fronzoni, M. Stener, *J. Chem. Phys.* **2015**, *143*, 024106.
[26] O. Baseggio, D. Toffoli, G. Fronzoni, M. Stener, L. Sementa, A. Fortunelli, *J. Phys. Chem. C* **2016**, *120*, 24335.
[27] G. te Velde, F. M. Bickelhaupt, E. J. Baerends, C. F. Guerra, S. J. A. van Gisbergen, J. G. Snijders, T. Ziegler, *J. Comput. Chem.* **2001**, *22*, 931.
[28] R. van Leeuwen, E. J. Baerends, *Phys. Rev. A* **1994**, *49*, 2421.
[29] M. Medves, G. Fronzoni, M. Stener, *J. Comput. Chem.* **2022**, *43*, 1923.
[30] F. Wang, T. Ziegler, E. van Lenthe, S. van Gisbergen, E. J. Baerends, *J. Chem. Phys.* **2005**, *122*, 204103.
[31] O. Baseggio, M. De Vetta, G. Fronzoni, D. Toffoli, M. Stener, L. Sementa, A. Fortunelli, *Int. J. Quantum Chem.* **2018**, *118*, e25769.
[32] S. Theivendran, L. Chang, A. Mukherjee, L. Sementa, M. Stener, A. Fortunelli, A. Dass, *J. Phys. Chem. C* **2018**, *122*, 4524.
[33] Y. Oshima, A. Onga, K. Takayanagi, *Phys. Rev. Lett.* **2003**, *91*, 205503.
[34] L. Sementa, G. Barcaro, O. Baseggio, M. De Vetta, A. Dass, E. Aprà, M. Stener, A. Fortunelli, *J. Phys. Chem. C* **2017**, *121*, 10832.

SUPPORTING INFORMATION

Additional supporting information can be found online in the Supporting Information section at the end of this article.

How to cite this article: P. D'Antoni, D. Toffoli, G. Fronzoni, M. Stener, L. Sementa, A. Fortunelli, *J. Comput. Chem.* **2024**, *45*(19), 1657. https://doi.org/10.1002/jcc.27359

1096987x, 2024, 19, Downloaded from https://onlinelibrary.wiley.com/doi/10.1002/jcc.27359 by Universita Di Trieste, Wiley Online Library on [30/09/2025]. See the Terms and Conditions (https://onlinelibrary.wiley.com/terms-and-conditions) on Wiley Online Library for rules of use; OA articles are governed by the applicable Creative Commons License

4.2 Additional Publications

4.2.1 Time-dependent quantum/continuum modeling of plasmon-enhanced electronic circular dichroism

In this work, we investigate whether the presence of a plasmonic nanoparticle (NP) can significantly modify molecular chiro-optical properties, focusing on the electronic circular dichroism (ECD) of chiral molecules in close proximity to a metal NP. In this work, a quantum description of the molecular system is coupled to a classical representation of the NP via a continuum model. Specifically, we analyze the plasmonic influence on the ECD response of peridinin (PID) and methyloxirane (MOX) using a computational approach that goes beyond simplified dipole models, providing an explicit description of the molecular electronic structure and its interaction with both an external pulse and the NP-induced polarization.

Our simulations show that PID exhibits a pronounced plasmon-induced enhancement of its ECD signal when the NP is placed at a distance of 1 nm and the external field is polarized perpendicular to the molecular axis. Under these conditions, the ECD feature around 4.2 eV is enhanced by approximately a factor of 20, while the peak at 2.9 eV undergoes a sign inversion accompanied by an increase in intensity. In contrast, no enhancement is observed for parallel polarization, regardless of the NP–molecule separation. These results identify PID as a plasmon-sensitive system when its electronic excitations are energetically aligned with the plasmon resonance and the geometry enables a constructive induced-field contribution.

MOX shows no appreciable plasmonic enhancement. This behavior is attributed to the large energy mismatch between molecular excitations and the plasmon resonance, which prevents effective coupling. Overall, the results demonstrate that plasmon-enhanced ECD is highly molecule- and geometry-dependent, requiring both favorable energetic alignment and efficient coupling between molecular and plasmonic degrees of freedom.

I personally collaborate with Leonardo Biancorosso to implement the new necessary features in AMS code and in writing the interface between AMS and WaveT. In a schematic way the work we performed could be summarized as follows:

- Allow the AMS input to read the fictisciouse coordinates at the surface of the Nanoparticle
- We calculate in AMS the transition potentials needed to account for the presence of the NP to the molecular excitations
- In the interface we translate the relevant AMS output (excitation coefficients, transition dipole moments and potentials) from atomic orbitals space, to molecular orbital space first and finally in the state space

The Journal of Chemical Physics

RESEARCH ARTICLE | DECEMBER 03 2024

Time-dependent quantum/continuum modeling of plasmon-enhanced electronic circular dichroism

L. Biancorosso ; P. D'Antoni ; S. Corni ; M. Stener ; E. Coccia

Check for updates

J. Chem. Phys. 161, 214104 (2024)
https://doi.org/10.1063/5.0235531

View Online
Export Citation

Articles You May Be Interested In

Femtosecond transient infrared and stimulated Raman spectroscopy shed light on the relaxation mechanisms of photo-excited peridinin

J. Chem. Phys. (March 2015)

Electronic circular dichroism from real-time propagation in state space

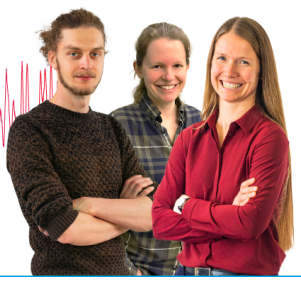
J. Chem. Phys. (February 2023)

Electronic circular dichroism spectra using the algebraic diagrammatic construction schemes of the polarization propagator up to third order

J. Chem. Phys. (February 2021)

30 September 2025 09:17:53

Webinar From Noise to Knowledge
May 13th – Register now
Zurich Instruments
Universität Konstanz



AIP Publishing

The Journal of Chemical Physics ARTICLE pubs.aip.org/aip/jcp

Time-dependent quantum/continuum modeling of plasmon-enhanced electronic circular dichroism

Cite as: J. Chem. Phys. 161, 214104 (2024); doi: 10.1063/5.0235531
Submitted: 28 August 2024 • Accepted: 13 November 2024 •
Published Online: 3 December 2024

View Online Export Citation CrossMark

L. Biancorosso,[1] P. D'Antoni,[1] S. Corni,[2,3] M. Stener,[1] and E. Coccia[1,a)]

AFFILIATIONS

[1] Dipartimento di Scienze Chimiche e Farmaceutiche, Università di Trieste, Via L. Giorgieri 1, 34127 Trieste, Italy
[2] Dipartimento di Scienze Chimiche, Università di Padova, Via F. Marzolo 1, 35131 Padova, Italy
[3] Istituto Nanoscienze-CNR, Via Campi 213/A, 41125 Modena, Italy

[a)] **Author to whom correspondence should be addressed:** ecoccia@units.it

ABSTRACT

In this work, we present a multiscale real-time approach to study the plasmonic effects of a metal nanoparticle (NP) on the electronic circular-dichroism (ECD) spectrum of a chiral molecule interacting with it. The method is based on the time-evolution of the molecule's time-dependent wavefunction, expanded in the eigenstates of a perturbed Hamiltonian. A quantum description of the molecular system is coupled to a classical representation of the NP via a continuum model. The method is applied to methyloxirane and peridinin at various distances (1, 3, and 5 nm) with respect to a gold NP surface. While no remarkable effect is observed for methyloxirane at any studied distance, an enhancement appears when the peridinin lies at 1 nm and the pulse is linearly polarized perpendicularly to the molecular axis, with the ECD signal centered at 4.1 eV increased by a factor of around 20. These results are rationalized looking at the gap between the plasmonic peak of the NP at around 2.5 eV and the molecular excitations: the smaller the gap between molecular and plasmonic excitations, the larger the plasmonic enhancement of the ECD signal. Moreover, ECD peaks are selectively enhanced due to the favorable coupling between the pulse polarization and the combined effect of electric and magnetic dipole moments. This approach allows one to go through the electronic structure and dynamics of chiral molecules for obtaining a realistic description of plasmon-mediated ECD spectra, e.g., paving the way to applications to molecules of biological relevance interacting with nanostructures of experimental interest.

Published under an exclusive license by AIP Publishing. https://doi.org/10.1063/5.0235531

30 September 2025 09:17:53

I. INTRODUCTION

The optical properties of a molecule can be dramatically modified by close metal nanoparticles (NPs) in the presence of an external electromagnetic perturbation.[1–6] Plasmonic effects from NPs are exploited to enhance weak molecular signals, with surface enhanced Raman scattering (SERS), namely being the most known plasmon-assisted spectroscopy:[7–10] the Raman signal is enhanced by several orders of magnitude thanks to the plasmonic response, making SERS an extremely sensitive technique.

In addition, the optical properties of chiral molecules can be enhanced by the coupling with plasmons. Among them, circular dichroism (CD) is central in many chemico-physical applications, being used to assign the absolute configuration of chiral compounds by distinguishing the response of the enantiomers of chiral molecules when interacting with left- and right-circularly polarized light.[11–18]

Plasmonic NPs with chiroptical properties can be classified into the following three classes:[19] (i) plasmonic systems with intrinsic chirality;[20–28] (ii) achiral plasmonic NPs coupled to a chiral molecule;[29–47] and (iii) chiral arrangement of achiral plasmonic NPs.[48–53] In this work, we focus on the second class of systems. The presence of the NP can affect the CD signal by determining two types of specific responses: enhancement of one or more molecular peak(s); promoting the appearance of a peak in correspondence to the plasmonic resonance.

The first feature is strictly related to the induced field generated by the NP, to its nature and shape, to the polarization direction of the

Published under an exclusive license by AIP Publishing

pulse, and to the energy gap between plasmon resonance and molecular excitations. The origin of this enhancement is the molecular response with respect to a total perturbation due to the external pulse and the induced field generated by the polarized NP.[30,54] Biological chiral molecules can be characterized by an absorption close to plasmon resonance, which is typically around 1–2.5 eV, permitting resonant coupling between the molecular and plasmon modes.

The second mechanism is interpreted as a chirality transfer to the NP, which then acquires a CD signal. In addition, this optical response depends on the geometry and shape of the NP. This second feature prevails when the molecular excitations are far from the plasmonic resonance.[30]

The enhanced sensitivity and response of chiral molecules in the presence of NPs have been thoroughly investigated in many experimental works,[35,55–61] and plenty of theoretical literature was dedicated to a dipole-like description of the chiral molecule,[30–43,45,46,57,62–65] usually within a master equation for the quantum states of the molecule. The magnitude of the enhancement in CD, which can vary from a few units to thousands, depends on several conditions, such as the nature of the chiral molecule, the size, shape, and nature of the NP, and the possible alignment of the molecule.[35,41,47,55–61,63] Giant enhancement of the order of 10^4 is usually due to magnetic and/or quadrupolar contributions.[63]

Modeling the plasmonic-enhanced CD spectrum within the quantum-chemistry framework, beyond a dipole-like representation of the molecule, is a fundamental step to support experimentalists in the prediction and rationalization of the recorded data. It is a challenging task for theory because a large and complex system, generically composed of a NP and a molecule, has to be properly simulated.

Limiting the discussion to the electronic CD (ECD), as an example, a full quantum real-time approach has been proposed in Ref. 66, applied to nanoscale metal–organic clusters.

We propose here to extend the recently published approach by some of the authors[67] based on the propagation of a time-dependent Schrödinger equation (TDSE) in the presence of an explicit electromagnetic field in length gauge[68,69] to account for the possible plasmonic effects of a metal NP on the ECD spectrum of a chiral molecule. The presented multiscale method is characterized by a quantum description of the chiral moiety, whereas the NP is treated according to a polarizable continuum model extended to nanoparticles (PCM-NPs).[6,70,71] Generally, one can compute the ECD spectrum by using the response of the time-dependent induced magnetic dipole to an electric-field perturbation or the response of the time-dependent electric dipole to a magnetic-field perturbation.[18] Here, we use the time-dependent magnetic dipole moment of the chiral molecule, which is computed on the basis of the molecular eigenstates of an effective Hamiltonian, accounting for the presence of the NP. Propagating TDSE in the state space permits to separate the electronic-structure problem from TDSE propagation, at variance with methods based on the direct time evolution of molecular orbitals.[72–74] Since the magnetic response of the NP is not included in the theory by construction, the computed plasmon-assisted spectra reported in this work only present molecular peaks possibly augmented by the plasmon. Details are given in Sec. II.

Molecular plasmonics has also been theoretically explored by parametrized quantum approaches based on density functional tight binding[75–77] for studying the absorption properties of large metal clusters[75,77] and the effect of quantum tunneling in the efficiency of electron energy transfer in a plasmonic chain composed of silver clusters.[76]

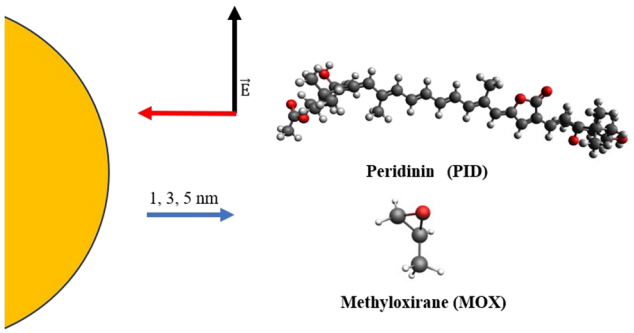


FIG. 1. Sketch representation of the NP + molecule (MOX and PID) system. The distance between the NP surface and the molecule is also reported (see Fig. 2 and main text for details). Code color: carbon black; oxygen red; hydrogen white; gold yellow.

In this article, we compute the ECD spectra of methyloxirane (MOX) and peridinin chromophore (PID) at various distances from an Au spherical NP of a radius of 2.5 nm (Fig. 1) to test the ability of our method to reproduce possible large plasmonic enhancements. We use density functional theory (DFT) and TDDFT for MOX and PID. MOX has been used to study surface-enhanced Raman optical activity,[78,79] while chiral properties of PID molecules have been studied both theoretically and experimentally in the context of the peridinin-chlorophyll-a protein (PCP),[80–83] and the enhancement of the optical properties of PCP in the presence of metal nanoparticles has been reported.[84–86]

The choice of MOX and PID in this work has been performed to answer these questions: can we discriminate by our approach "plasmon-sensitive" and "plasmon-insensitive" chiral molecules? Is this sensitiveness an absolute property of composite systems? Can we rationalize the possible plasmon enhancement of the ECD signal by analyzing the electron structure and dynamics of the spectroscopic target?

The goal is to verify the reliability of our method for understanding the microscopic reason of plasmon-induced changes in the ECD spectrum, such as enhancement and quenching of the signal, by means of a quantum description of the spectroscopic target.

The article is organized as follows: theory is presented in Sec. II; computational details are collected in Sec. III; results are shown and discussed in Sec. IV; conclusions are reported in Sec. V.

II. THEORY

A. Real-time propagation

In this work, we model the real-time magnetic response of the chiral molecule to an external electric field in the presence of a plasmonic NP. Our multiscale approach couples the nanostructure polarization based on the polarizable continuum model (PCM) to a quantum representation of the electronic degrees of freedom of the chiral molecule. We name the method hereafter time-dependent

30 September 2025 09:17:53

Published under an exclusive license by AIP Publishing

PCM-NP (TD-PCM-NP). Theory is formulated in time domain using the TDSE; atomic units are used.

The computational protocol is articulated in three main steps: (i) defining the basis for the time-dependent wavefunction $|\Psi(t)\rangle$; (ii) propagating TDSE in the state space in the presence of the nanostructure, treated at PCM level via the boundary-element method (BEM),[6,87] and of the external pulse; (iii) computing the plasmon-modified ECD spectrum.[67] Within BEM, the NP surface is discretized by a set N_T of (typically) triangular tesserae, on which apparent charges are located.[6] The time evolution of these charges describes the NP polarization induced by the external pulse and by the mutual interaction with the time-dependent electronic density of the quantum target.

TDSE in length gauge for TD-PCM-NP reads as

$$i\frac{d}{dt}|\Psi(t)\rangle = \hat{H}(t)|\Psi(t)\rangle, \tag{1}$$

with $\hat{H}(t)$ being the time-dependent Hamiltonian

$$\hat{H}(t) = \hat{H}_0 - \vec{\hat{\boldsymbol{\mu}}}\cdot\vec{E}_{ext}(t) + \mathbf{q}(t)\cdot\hat{\mathbf{V}}_{\mathrm{BEM}}. \tag{2}$$

where $\vec{\hat{\boldsymbol{\mu}}}$ is the dipole operator of the molecule, $\vec{E}_{ext}(t)$ is the external pulse, $\mathbf{q}(t)$ are the BEM charges,[71,88] and $\hat{\mathbf{V}}_{\mathrm{BEM}}$ is the operator associated with the molecular electrostatic potential calculated at the position of the charges on the NP surface. Both $\mathbf{q}(t)$ and $\hat{\mathbf{V}}_{\mathrm{BEM}}$ are vectors with N_T elements. $\hat{H}_0$ is the field-free electronic Hamiltonian

$$\hat{H}_0 = \hat{H}_{el} + \mathbf{q}_{GS}\cdot\hat{\mathbf{V}}_{\mathrm{BEM}}, \tag{3}$$

where $\hat{H}_{el}$ is the electronic Hamiltonian of the bare molecule, and the charges $\mathbf{q}_{GS}$ are obtained by a self-consistent calculation for the quantum ground-state (GS) in the presence of the polarizable NP.[89]

The time evolution of the charges in Eqs. (1) and (2) is obtained by the time-dependent PCM formulation in the integral equation formalism (IEF-PCM),[71,90] combined with a description of the dielectric function of the medium $\varepsilon(\omega)$ based on fitting the experimental data.[91] In the frequency domain, the charges $\mathbf{q}(\omega)$ are defined as[91]

$$\mathbf{q}(\omega) = \frac{1}{2\pi}f(\omega)\mathbf{F}(\omega), \tag{4}$$

with

$$f(\omega) = \frac{\varepsilon(\omega)-1}{\varepsilon(\omega)+1}, \tag{5}$$

and

$$\mathbf{F}(\omega) = -\left[\mathbf{A}\mathbf{D}^{*}\mathbf{q}(\omega) + \mathbf{S}^{-1}(2\pi\mathbf{I}+\mathbf{D}\mathbf{A})\mathbf{V}(\omega)\right], \tag{6}$$

being $\mathbf{A}$ a diagonal matrix with elements equal to the area of the tesserae, $\mathbf{D}$ and $\mathbf{S}$ matrices containing the Calderon projectors, $\mathbf{I}$ is the identity, and $\mathbf{V}$ the electrostatic potential.[91] The function $f(\omega)$ is fitted by a series of N Drude–Lorentz terms

$$f(\omega) = \frac{\varepsilon(\omega)-1}{\varepsilon(\omega)+1} \simeq \sum_{p=1}^{N}\frac{A_p}{\omega_p^2-\omega^2-i\gamma_p\omega}, \tag{7}$$

where A_p is related to the plasma frequency of the metal, γ_p is the relaxation time, and ω_p is the oscillator frequency.[71] Equation (7) allows one to rewrite the surface charges as a sum of pole-dependent charges

$$\mathbf{q}(\omega) = \sum_{p=1}^{N}\mathbf{q}_p(\omega), \tag{8}$$

and for each $\mathbf{q}_p(\omega)$ in Eq. (8), a time-dependent equation is then defined

$$\ddot{\mathbf{q}}_p(t) = -\omega_p^2\mathbf{q}_p(t) - \gamma_p\dot{\mathbf{q}}_p(t) + \frac{A_p}{2\pi}\mathbf{F}(t), \tag{9}$$

with $\mathbf{F}(t)$ being the Fourier transform of $\mathbf{F}(\omega)$. We refer to the original works (in particular Ref. 91 for this implementation) for further details.

In Eq. (1), $|\Psi(t)\rangle$ is defined as a linear combination of the N_{states} eigenstates of the effective field-free Hamiltonian $\hat{H}_0$, also containing the ground-state polarization of the molecule and the NP,

$$|\Psi(t)\rangle = \sum_{M=0}^{N_{\mathrm{states}}-1} C_M(t)|M\rangle, \tag{10}$$

where $C_M(t)$ are time-dependent coefficients, and $|M\rangle$ is the Mth eigenstate of the system, with eigenvalue E_M. The initial guess for the self-consistent calculation is provided by the eigenstates of H_{el}. In this work, such eigenstates are the Kohn–Sham DFT ground state and the (N_{states}-1) TDDFT eigenstates in the singly excited ansatz,[92,93] i.e.,

$$|M\rangle = \sum_{i}^{occ}\sum_{a}^{vir} d_{i,M}^{a}|\Phi_i^a\rangle, \tag{11}$$

where $|\Phi_i^a\rangle$ is the singly excited Slater determinant, with an electron promoted from the occupied orbital i to the virtual one a, while $d_{i,M}^{a}$ are the amplitudes of the expansion for the state $|M\rangle$.

The $|M\rangle$ states and the polarization charges, after the self-consistent step, are the starting point for the propagation of TDSE, according to Eq. (1). Without the NP, the Hamiltonian reduces to $\hat{H}(t) = \hat{H}_{el} - \vec{\hat{\boldsymbol{\mu}}}\cdot\vec{E}_{ext}(t)$, and the basis for $|\Psi(t)\rangle$ is simply given by the set of eigenstates of $\hat{H}_{el}$. From this point on, we no longer distinguish between eigenstates of the isolated molecule or of the molecule close to the NP, which will simply be referred to as $|M\rangle$ or $|L\rangle$.

Using TDDFT eigenstates within Casida's assignment ansatz[94] in TDSE propagation is an approach widely applied in several fields, such as, e.g., photochemistry,[95,96] high-harmonic generation spectroscopy,[97,98] Raman spectroscopy,[99] and strong-field ionization.[92] It is an alternative approach to real-time TDDFT (RT-TDDFT), which is undoubtedly a valuable tool for studying electronic dynamics in molecules and plasmonic systems.[72,73,100–106] However, the accuracy of photoinduced dynamics computed at the RT-TDDFT level could be affected by the choice of functional and the fact that the adiabatic approximation is typically used; this could lead to well-documented artifacts in the literature,[108–110] resulting in difficulty in correctly assigning the physical nature of the observed features in the dynamics itself, as in the case of a molecule close to an NP. On the other hand, a TDSE-based method is general since

30 September 2025 09:17:53

Published under an exclusive license by AIP Publishing

time propagation can be coupled to different levels of theory for the electronic structure, not limited to TDDFT eigenstates.[89,111,112]

In order to simulate a kick pulse, the external electric field $\vec{E}_{ext}(t)$ is given by a narrow linear Gaussian function

$$\vec{E}_{ext}(t) = \vec{E}_{max} t \exp\left(-\frac{(t-t_0)^2}{2\sigma^2}\right), \tag{12}$$

where t_0 is the center and σ the amplitude of the Gaussian function, respectively, and $\vec{E}_{max}$ is the maximum amplitude of the field. The choice of the pulse prevents numerical artifacts possibly affecting the Fourier transform of the time-dependent signal.

B. Excited-excited matrix elements in TDDFT

TD-PCM-NP, originally developed to study electron dynamics within molecular plasmonics,[110] has been extended here to the calculation of ECD spectra modified by plasmonic effects, using an in-house interface between the AMS package[112] and the WaveT code for propagation.[110] Such an interface has been recently proposed,[67,93] allowing one to simulate ECD spectra of isolated molecules using TDSE and DFT/TDDFT for the description of the molecular target. We emphasize here the novel implementation in the interface regarding the computation of a matrix element between excited states of a one-electronic operator $\hat{A}$ within DFT and TDDFT. Although the results reported in this paper concern a linear response, i.e., the pulse intensity is low enough, the dynamics were carried out using a full approach, that is, considering the entire matrix in the space of states, $\langle L|\hat{A}|M\rangle$. The need for the full DFT/TDDFT matrix comes from the practical solution of TDSE in Eq. (1) in the electronic basis

$$i\frac{\partial \mathbf{C}(t)}{\partial t} = \mathbf{H}(t)\mathbf{C}(t), \tag{13}$$

with the matrix representation at time t of $\hat{H}(t)$ in the basis of the eigenstates reading as

$$\begin{aligned}\mathbf{H}(t)_{LM} &= \langle L|\hat{H}(t)|M\rangle \\ &= E_M\delta_{LM} - \vec{E}_{ext}(t)\langle L|\vec{\hat{\mu}}|M\rangle + \mathbf{q}(t)\langle L|\hat{\mathbf{V}}_{\mathrm{BEM}}|M\rangle.\end{aligned} \tag{14}$$

From the inspection of Eq. (14), one sees that $\langle L|\vec{\hat{\mu}}|M\rangle$ and $\langle L|\hat{\mathbf{V}}_{\mathrm{BEM}}|M\rangle$ are ingredients in TDSE propagation. The full matrix for the magnetic dipole moment is required to compute the ECD spectrum, as specified in Sec. II C.

The molecular electrostatic potential $\hat{\mathbf{V}}_{BEM}$ in the basis of eigenstates $|M\rangle$, i.e., $\langle L|\hat{\mathbf{V}}_{BEM}|M\rangle$, which for each tessera T, is given by

$$\langle L|\hat{V}_{\mathrm{BEM}}(\mathbf{s}_T)|M\rangle = \langle L|\frac{1}{|\mathbf{s}_T - \mathbf{r}|}|M\rangle + V_{nuc}(\mathbf{s}_T)\delta_{LM}, \tag{15}$$

where $V_{nuc}(\mathbf{s}_T)$ is the nuclear contribution at the position $\mathbf{s}_T$ of the Tth tessera, and $\mathbf{r}$ is the electronic coordinate. Dependence of V_{BEM} and V_{nuc} on $\mathbf{s}_T$ is made explicit in Eq. (15). Further details about the nature of the charges $\mathbf{q}(t)$ are given in Ref. 71.

The approach proposed here to compute $\langle L|\hat{A}|M\rangle$, where $\hat{A}$ is an one-electron operator, is based on the frequency-dependent linear density matrix response[113–118]

$$\rho_M^{(1)} = \sum_{ia}\left[X_{i,M}^a\phi_i\phi_a^* + Y_{i,M}^a\phi_i^*\phi_a\right], \tag{16}$$

with $\rho_M^{(1)}$ being an element of the tensor space F, $N_{occ}xN_{vir} \otimes N_{vir}xN_{occ}$, with units tensors $\phi_i\phi_a^*$ and $\phi_i^*\phi_a$, being ϕ_i and ϕ_a occupied and virtual molecular orbitals. N_{occ} (N_{vir}) is the number of occupied (virtual) molecular orbitals. Starting from this formal definition one can arrange the terms $X_{i,M}^a\phi_i\phi_a^*$ and $Y_{i,M}^a\phi_i^*\phi_a$ in two arrays $\boldsymbol{\chi}^M$ and $\boldsymbol{\Upsilon}^M$ such that $\chi_i^{M,a} = X_{i,M}^a\phi_i\phi_a^*$ and $\Upsilon_i^{M,a} = Y_{i,M}^a\phi_i^*\phi_a$. We remark that $X_{i,M}^a$ and $Y_{i,M}^a$ in Eq. (16) are the elements of the usual TDDFT vectors $\mathbf{X}^M$ and $\mathbf{Y}^M$.[113,116] One can then write

$$\langle L|\hat{A}|M\rangle = \begin{pmatrix}\boldsymbol{\chi}^L & \boldsymbol{\Upsilon}^L\end{pmatrix}\begin{pmatrix}\hat{A} & 0\\ 0 & \hat{A}\end{pmatrix}\begin{pmatrix}\boldsymbol{\chi}^M\\ \boldsymbol{\Upsilon}^M\end{pmatrix}, \tag{17}$$

and, explicitly, one obtains

$$\langle L|\hat{A}|M\rangle = \sum_{ij}\sum_{ab}\left[X_{j,L}^{b*}X_{i,M}^a\langle ib|\hat{A}|aj\rangle + Y_{j,L}^{b*}Y_{i,M}^a\langle aj|\hat{A}|ib\rangle\right]. \tag{18}$$

where indices i and j run over occupied orbitals while indices a and b run over virtual ones.

If the operator $\hat{A}$ is symmetric, such as the electric dipole moment $\vec{\hat{\mu}}$ and the electrostatic potential $\hat{V}_{\mathrm{BEM}}(\mathbf{s}_T)$, then

$$\langle L|\hat{A}|M\rangle = \sum_{ij}\sum_{ab}\left[\langle ib|\hat{A}|aj\rangle\left(X_{j,L}^{b*}X_{i,M}^a + Y_{j,L}^{b*}Y_{i,M}^a\right)\right], \tag{19}$$

$$= \mathbf{X}^L\cdot\mathbf{A}\cdot\mathbf{X}^M + \mathbf{Y}^L\cdot\mathbf{A}\cdot\mathbf{Y}^M, \tag{20}$$

where the matrix $(\mathbf{A})_{ia,\,jb} = \langle ib|\hat{A}|aj\rangle$ has been defined. If the operator $\hat{A}$ is antisymmetric, such as the magnetic dipole moment $\vec{\hat{m}}$,[116,117] then

$$\langle L|\hat{A}|M\rangle = \sum_{ij}\sum_{ab}\left[\langle ib|\hat{A}|aj\rangle\left(X_{j,L}^{b*}X_{i,M}^a - Y_{j,L}^{b*}Y_{i,M}^a\right)\right], \tag{21}$$

$$= \mathbf{X}^L\cdot\mathbf{A}\cdot\mathbf{X}^M - \mathbf{Y}^L\cdot\mathbf{A}\cdot\mathbf{Y}^M. \tag{22}$$

According to Slater–Condor rules, the term $\langle ib|\hat{A}|aj\rangle$ simplifies to $\langle a|\hat{A}|b\rangle\delta_{ij} - \langle i|\hat{A}|j\rangle\delta_{ab}$, thus recovering the usual expressions in the molecular basis.[93]

In terms of excitation $(\mathbf{X}^{I(M)} + \mathbf{Y}^{I(M)})$ and deexcitation $(\mathbf{X}^{I(M)} - \mathbf{Y}^{I(M)})$, expressions in Eqs. (20) and (22) become, once the specific operators are made explicit

$$\begin{aligned}\langle L|\hat{V}_{\mathrm{BEM}}(\mathbf{s}_T)|M\rangle = \frac{1}{2}\big[&(\mathbf{X}^L + \mathbf{Y}^L)\cdot\mathbf{P}_{\mathrm{BEM}}(\mathbf{s}_T)\cdot(\mathbf{X}^M + \mathbf{Y}^M)\\ &+ (\mathbf{X}^L - \mathbf{Y}^L)\cdot\mathbf{P}_{\mathrm{BEM}}(\mathbf{s}_T)\cdot(\mathbf{X}^M - \mathbf{Y}^M)\big],\end{aligned} \tag{23}$$

$$\begin{aligned}\langle L|\hat{\mu}_\alpha|M\rangle = \frac{1}{2}\big[&(\mathbf{X}^L + \mathbf{Y}^L)\cdot\mathbf{D}_\alpha\cdot(\mathbf{X}^M + \mathbf{Y}^M) + (\mathbf{X}^L - \mathbf{Y}^L)\\ &\times\mathbf{D}_\alpha\cdot(\mathbf{X}^M - \mathbf{Y}^M)\big],\end{aligned} \tag{24}$$

30 September 2025 09:17:53

Published under an exclusive license by AIP Publishing

and

$$\langle L|\hat{m}_\alpha|M\rangle = \frac{1}{2}\left[(\mathbf{X}^L + \mathbf{Y}^L)\cdot\mathbf{M}_\alpha\cdot(\mathbf{X}^M - \mathbf{Y}^M) + (\mathbf{X}^L - \mathbf{Y}^L) \times \mathbf{M}_\alpha\cdot(\mathbf{X}^M + \mathbf{Y}^M)\right], \quad (25)$$

where $\alpha = x, y$, or z indicates the Cartesian component of the dipole, and being $\mathbf{D}_\alpha$, $\mathbf{M}_\alpha$, and $\mathbf{P}_{\mathrm{BEM}}(\mathbf{s}_T)$ the matrix representations of the corresponding operators. $\mathbf{P}_{\mathrm{BEM}}(\mathbf{s}_T)$ in Eq. (23) refers to the matrix representation of $\hat{V}_{\mathrm{BEM}}(\mathbf{s}_T)$ (one single tessera at position $\mathbf{s}_T$) in the molecular space, while $\hat{\mathbf{V}}_{\mathrm{BEM}}$ in Sec. II A is the vector representation of the potential operator with respect to the number of tesserae.

C. Computing the ECD spectrum

The induced magnetic dipole $\Delta\vec{m}(t)$ is defined as the difference between the time-dependent magnetic moment $\vec{m}(t)$ at time t and that at initial time $(t = 0)$, $\vec{m}(0)$, with $\vec{m}(t)$ provided by

$$\vec{m}(t) = \sum_{L,M} C_L^*(t)C_M(t)\langle L|\vec{\hat{m}}|M\rangle, \quad (26)$$

with $\langle L|\vec{\hat{m}}|M\rangle$ given by Eq. (25). The ECD spectrum is computed as the imaginary part of the following:[67,119]

$$P_{nl}^{ECD}(\omega) = -\frac{i}{2\pi\omega\vec{E}_{ext,n}(\omega)}\int_0^{+\infty} -\Delta\vec{m}_l(t)e^{i(\omega+i\Gamma)t}dt. \quad (27)$$

In Eq. (27), $\vec{E}_{ext,n}(\omega)$ is the Fourier transform of the nth component of the electric field of the external pulse, $\Delta\vec{m}_l(t)$ is the lth component of the induced magnetic dipole, and Γ is a damping parameter.[119,120]

III. COMPUTATIONAL DETAILS

Ground-state geometry of MOX and PID have been taken from Refs. 67 and 121, respectively. The time-domain ECD calculations have been performed with the WaveT package,[111] whose interface with AMS has been recently proposed for the electric and magnetic transition dipole moments.[67,93] Excitation energies and transition dipole moments are provided by the TDDFT calculation using the B3LYP functional and TZP basis set for MOX and CAM-B3LYP and TZP basis set for PID, and then employed as input parameters for the real-time propagation. For both MOX and PID, 150-fs dynamics have been carried out with a time step δt of 0.7 as. 20 (MOX) and 10 (PID) electronic excited states have been considered for the wavefunction expansion of Eq. (10). The equilibration procedure related to the effective Hamiltonian $\hat{H}_{NP}$ is implemented in WaveT.[89]

The external field is characterized by a maximum intensity equal to 10^4 W/cm^2 and a full width half maximum of 94 as for the Gaussian envelope [see Eq. (12)]. The value of the damping parameter Γ in Eq. (27) is 400 au for all the cases. The ECD spectrum in Eq. (27) has been computed with a post-processing tool implemented in WaveT, using the TDSE dynamics as input.

NP has a radius of 2.5 nm; 2704 tesserae have been used to discretize the NP surface. In our computed spectra, n and l components of Eq. (27) coincide.

IV. RESULTS AND DISCUSSION

In the present work, we have studied plasmonic effects of the NP on the ECD spectra of MOX and PID at various distances and pulse polarizations through the time-dependent multiscale method reported in Sec. II. The shortest distance selected for our simulations is 1 nm because we want to simulate a purely plasmon-driven physical effect by excluding any interaction of chemical type. Distances of 1 nm could be experimentally prepared by using, e.g., a molecular spacer.

We have rationalized the MOX and PID responses in terms of coupling between plasmon and molecular excitations, electric selection of excited states during the dynamics, interplay between electric and magnetic dipole moments, coupling with the pulse polarization, and the role of the induced field. Of course, all these ingredients are closely connected to each other; our theory and simulations have allowed us to dissect the role of each of them and, therefore, it represents an original approach to chiral plasmonics.

Since our methodology is not able, by construction, to determine plasmon peaks in the CD spectrum, our attention is exclusively focused on the possible enhancement of molecular peaks. In order

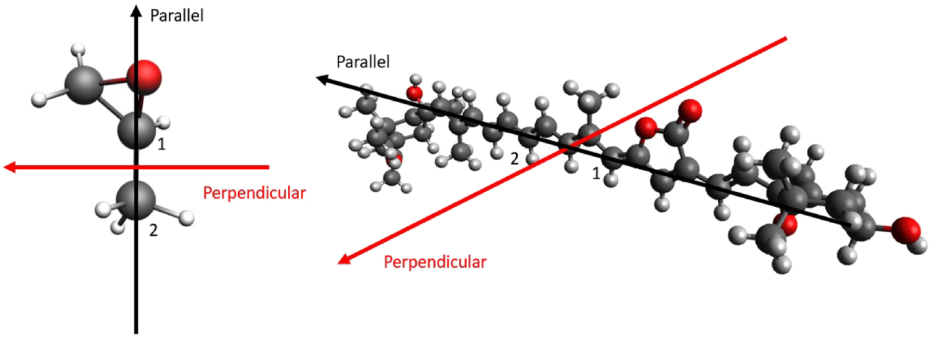


FIG. 2. Pulse polarization directions used in this work. MOX: "Parallel" is along the carbon–carbon bond; "perpendicular" is orthogonal to it. PID: "parallel" is parallel to the carbon chain; "perpendicular" is perpendicular to it. In both cases, "parallel" and "perpendicular" refer to the relative orientation with respect to the NP surface. Carbon atoms labeled as 1 and 2 define the two reference atoms, whose middle point is used for defining the distance with respect to the NP (see text). Components of the pulse polarization unit vector are: MOX "parallel" (−0.918, 0.092, −0.386); MOX "perpendicular" (0.100, 0.995, 0.000); PID "parallel" (−0.979, −0.183, −0.094); PID "perpendicular" (−0.146, 0.930, −0.289).

30 September 2025 09:17:53

Published under an exclusive license by AIP Publishing

to verify the reliability of the approach, we have selected two chiral molecules with different electronic and optical properties: MOX and PID (Fig. 1). In this context, we define the enhancement (quenching) at a given energy in the spectrum corresponding to an ECD peak when the ratio between the ECD signal with and without the NP is larger (smaller) than 1. For both molecules, the distance between the NP and the molecule is defined as the distance between the NP surface and the middle point of the vector connecting the reference carbon atoms (labeled 1 and 2), as shown in Fig. 2. We consider the pulse polarization to be tangential to the NP surface when it is parallel to the vector connecting these two atoms (labeled "Parallel"), while it is perpendicular to the NP surface when orthogonal to this vector (labeled "Perpendicular").

First, we have studied the NP effect on the ground state of MOX and PID before irradiating the system. The variation ΔE of the ground-state energy (formally a free-energy, but for metal nanoparticle polarization the entropic contribution is negligible) as a function of the NP distance is reported in Fig. 1 of the supplementary material. ΔE is defined as the difference between the ground-state energy of the bare molecule (Vac) and the ground-state energy of the molecule in the presence of the NP,

$$\Delta \mathrm{E} = E_{GS}^{Vac} - E_{GS}^{NP}. \tag{28}$$

ΔE accounts for both electronic and nuclear contributions to the electrostatic term in the ground-state energy. At 3 and 5 nm, the effect of the presence of the NP on the stabilization of the GS energy is minimal, while at 1 nm for both MOX and PID, a stabilization by 50 mKcal/mol is observed.

In Fig. 2 of the supplementary material, the differential projected density of states $\Delta\mathrm{PDOS}(t=0,\varepsilon)$[93] for the ground state of PID at 1 nm from the NP surface, i.e., at time $t = 0$, is reported

$$\Delta\mathrm{PDOS}(t=0,\varepsilon) = \mathrm{PDOS}^{NP}(t=0,\varepsilon) - \mathrm{PDOS}^{Vac}(t=0,\varepsilon). \tag{29}$$

The $\Delta\mathrm{PDOS}(t=0,\varepsilon)$ describes how the population of the molecular orbitals in the electronic ground state varies when the molecule interacts with the NP. In the PID case, HOMO-1 is largely depopulated in favor of LUMO and LUMO+1 at 1 nm, as shown in Fig. 2 of the supplementary material. This effect is completely negligible when PID is between 3 and 5 nm from the NP surface.

We then moved to rationalize the changes in the ECD spectrum due to the presence of the NP by looking first at the linear absorption spectra of the NP, MOX, and PID, reported in Fig. 3. Absorption spectra of MOX and PID have been computed by directly Fourier transforming the time-dependent induced electric dipole with no damping factor. The NP spectrum [panel (a) of Fig. 3] is computed as the imaginary part of the polarizability.[88] The plasmonic peak is clearly evident at around 2.5 eV. Using the same frequency scale, absorption spectra of bare MOX [panel (b) of Fig. 3] and bare PID [panel (c) of Fig. 3] for the two pulse polarization directions are also reported.

Excitation energies of MOX and PID after equilibration with the NP (see Sec. II) are not strongly modified with respect to the bare-molecule values, as seen in Tables 1–4 (MOX) and 9–12 (PID) of the supplementary material.

Values of Cartesian components of the electric and magnetic transition dipole moments for isolated MOX and PID and close to the NP are reported in Tables 1–16 of the supplementary material, together with their projection along the parallel and perpendicular direction (see Fig. 3). For the sake of simplicity, only the first ten transitions from the ground state are shown, even though simulations have been carried out including the full transition dipole matrices.

Electric and magnetic transition dipole moments of MOX and PID do not vary appreciably from the values of the isolated molecule when the NP is added at any distance (Tables 1–8 in the supplementary material). In Figs. 3 and 4 of the supplementary material, the absorption spectra of MOX and PID are reported in the presence of the NP. While MOX optical response is unaffected by the interaction with NP (as suggested by the behavior of the transition dipole moments in Tables 1–8 of the supplementary material), PID spectra show some appreciable differences, especially when the target molecule is placed at 1 nm from the NP. With a parallel pulse polarization, the very intense peak at 2.9 eV is partially quenched, while the other peaks do not significantly change with the variation of the distance. With a perpendicular pulse polarization, instead we observe an enhancement of the peak at 4.1 eV. These findings are due to the interaction between PID and NP during the dynamics. The latter result, indeed, is a peak enhancement of plasmonic nature: the corresponding transition dipoles alone are not sufficiently large to explain this intensity, which is instead easily understood if we consider the increase in the population of excited states due to the field induced by the NP, which adds up positively to the external one.[54,71] Indeed, the time-dependent population $|C_M(t)|^2$ of the excited states $(M > 0)$ is in the order of 10^{-8} for PID with a parallel pulse at all distances. For PID with perpendicular polarization at 1 nm, the population of the first three low-lying excitations is in the order 10^{-10}–10^{-11}, whereas the values of the populations without NP are in the range of 10^{-12}–10^{-13}. This result is clear evidence of the plasmonic effect on the electron dynamics, which in turn affects the PID optical response. However, plasmonic effects on a linear absorption spectrum are also not automatically observed in the ECD spectrum at the same frequencies, since in the latter case the magnetic transition dipole moment comes into play. The absolute value of the population depends on the applied pulse intensity.

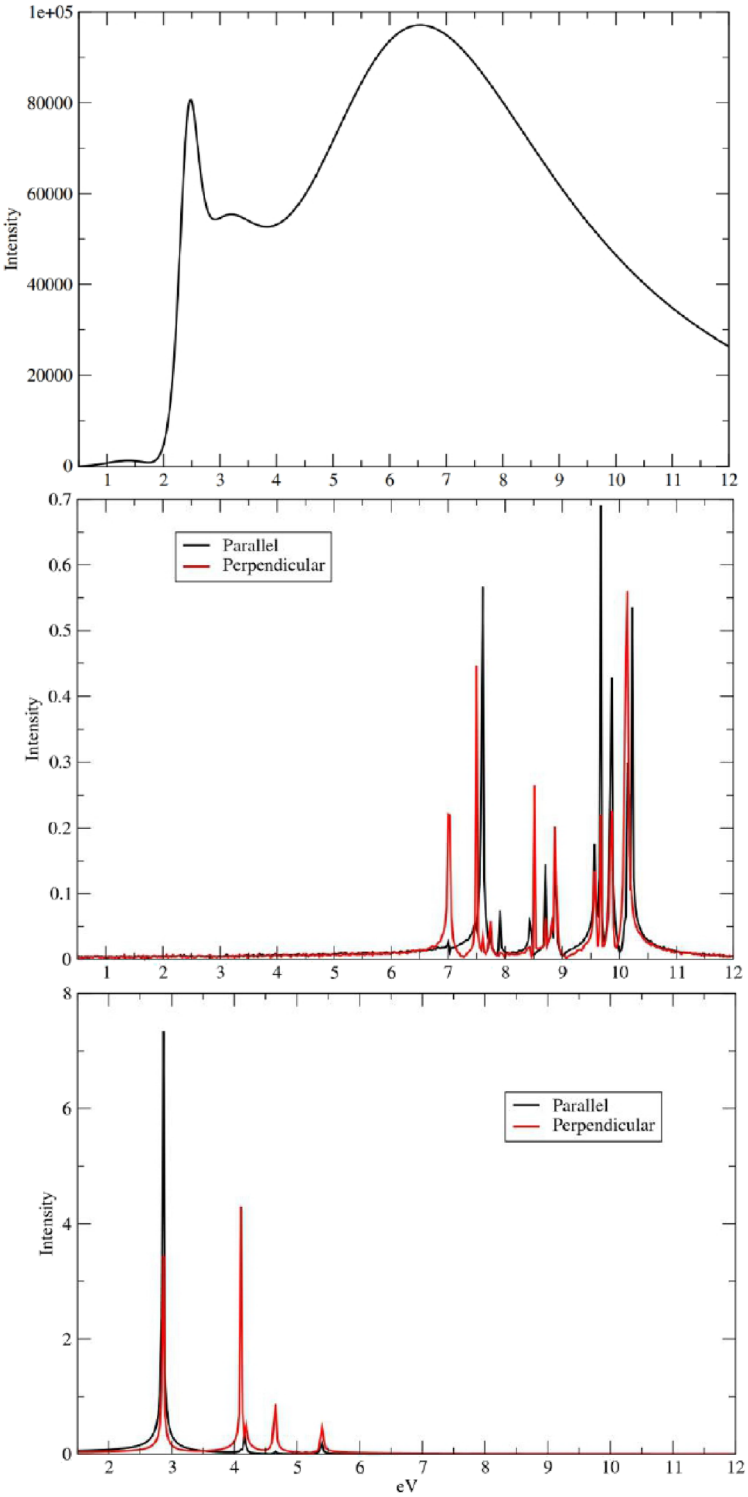
With these caveats in mind, peak positions in panels (b) and (c) of Fig. 3 can be used to be compared with the 2.5 eV plasmon. Considering both parallel and perpendicular pulse polarizations, MOX excited states are more than 4 eV higher than the plasmon energy, while the lowest PID excited states are much closer to the plasmon resonance.

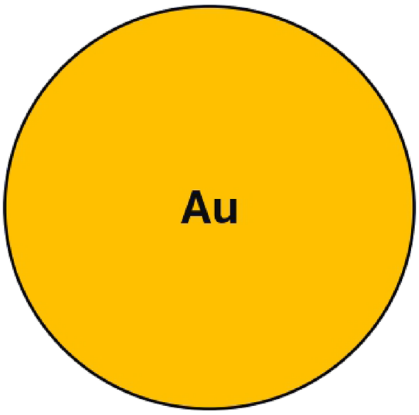
This preliminary analysis of the absorption spectra of MOX and PID is crucial to understand the ECD spectra collected here. Indeed, according to the theory reported in Ref. 30, enhancement is only expected when molecule and plasmon are in resonance or the gap is small enough. Moreover, the coupling between pulse polarization and molecular excitation and the geometric configuration of the composite system directly affect the intensity of the optical response of the chiral molecule.

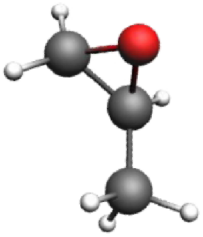
Comparison of ECD spectra of bare MOX is reported in Fig. 4: spectra obtained with parallel and perpendicular pulse polarizations show different features, but the intensity of peaks is characterized by the same order of magnitude. The effect of the NP is encoded in the spectra collected in Fig. 5. The general result is that the enhancement related to the induced field of the plasmonic excitation is not observed due to the gap between the electronic excitations of MOX

30 September 2025 09:17:53

Published under an exclusive license by AIP Publishing







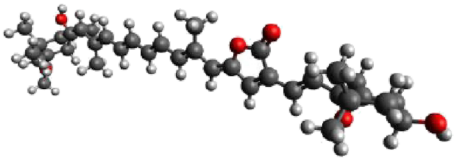


FIG. 3. (a) Absorption spectrum of the Au spherical NP of a radius of 2.5 nm, (b) absorption spectra of isolated MOX, and (c) PID. MOX and PID spectra are normalized to unity.

30 September 2025 09:17:53

Published under an exclusive license by AIP Publishing

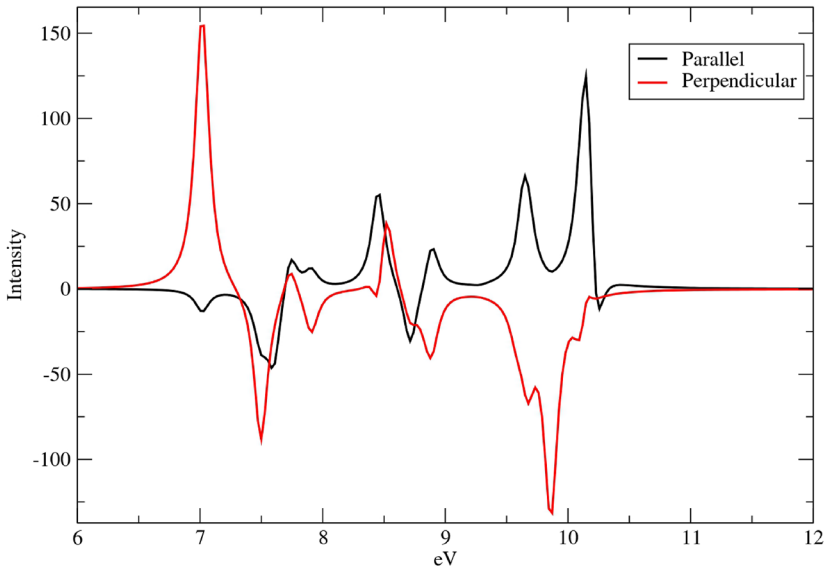


FIG. 4. ECD spectra of bare MOX with parallel and perpendicular pulse polarization with respect to the NP surface.

and the plasmon of the NP, making MOX insensitive to the gold NP of this size at the selected distances. Indeed, the difference between the plasmonic peak and the lowest MOX excitation is more than 4 eV, as already pointed out.

It is worth mentioning that the modulation of the bare-molecule ECD spectra is due to the combined effect of electric and magnetic dipole moments: the excited states playing a role are selected by the electric interaction in Eq. (2), thus affecting the time-dependent coefficients $C_M(t)$; such coefficients are responsible for the amplitude of the time-dependent magnetic moments, together with the magnetic transition dipole moments [see Eq. (26)]. In the presence of the NP, also the (possible) induced field has to be considered.

In detail, ECD spectra at 1, 3, and 5 nm are practically superimposed to the bare-molecule one for the parallel polarization, while tiny differences are found only at 1 nm for the perpendicular polarization, consistent with the change of the magnetic transition dipole moments. The spectra of the isolated molecule calculated compare pretty well with the reference ones in the literature, as it was also reported in Ref. 67.

In conclusion, no plasmonic enhancement is observed in the ECD spectra of MOX when distances of 1, 3, and 5 nm from the NP surface are considered.

The same computational protocol has been applied to PID. Parallel and perpendicular ECD spectra of the bare molecule of Fig. 6 are clearly distinguishable, but with different intensities. The

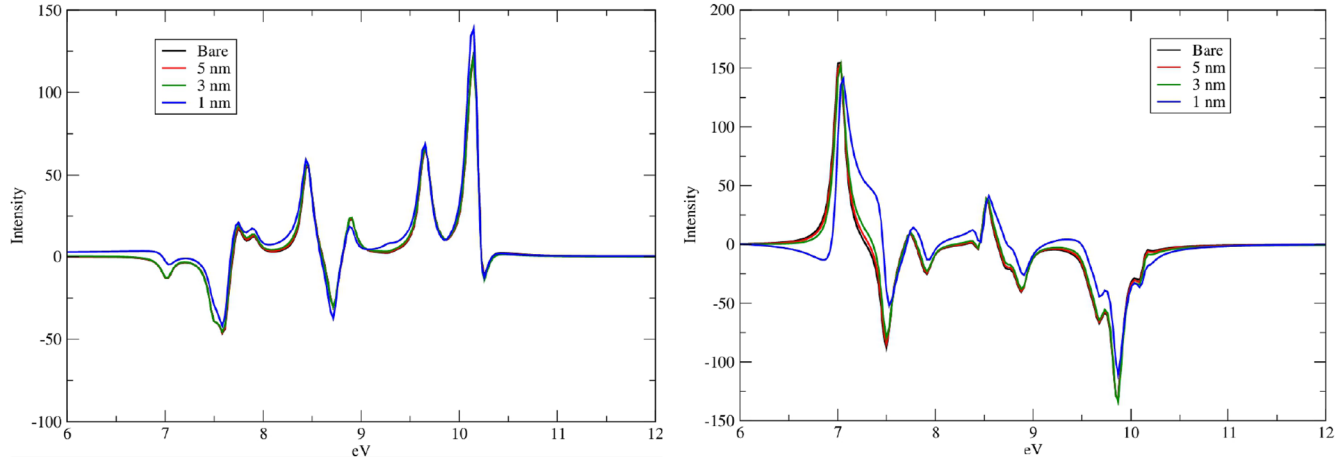


FIG. 5. ECD spectra of MOX at a distance *d* of 1, 3, and 5 nm from the NP surface for both pulse polarization directions, parallel (left panel) and perpendicular (right panel). Bare-molecule spectra are also reported for comparison.

30 September 2025 09:17:53

Published under an exclusive license by AIP Publishing

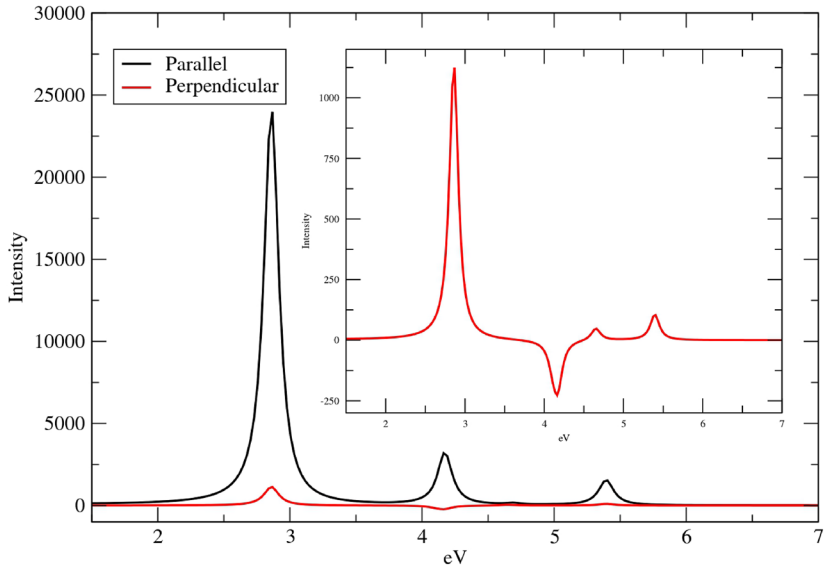


FIG. 6. ECD spectra of the bare PID with parallel and perpendicular pulse polarization with respect to the NP surface.

parallel spectrum shows an intense positive peak at around 2.9 eV and two other positive peaks centered at 4.2 and 5.4 eV. The perpendicular spectrum is much less intense, and it is mainly characterized by a positive peak at around 2.9 eV and a negative peak at 4.2 eV, whereas two other small and positive peaks appear at 4.6 and 5.4 eV.

Parallel and perpendicular ECD responses of PID behave in a totally different way when the gold NP is added, as shown in Fig. 7. In the parallel polarization spectra, shown in the left panel of Fig. 7, we observe at 1 nm a contained enhancement of the peak at 2.9 eV, whereas the other two peaks are unaffected. An analysis of the population of the excited states shows that the population of the first excited state (whose excitation is centered at 2.9 eV) at 1 nm is comparable to the ones at 3 and 5 nm and without NP. For this reason we do not observe important variations in the spectra at any distance.

ECD spectra calculated with the perpendicular polarization, reported in the panel of Fig. 7 (right), instead show a general much more intense response of PID with NP at 1 nm. In detail, a large enhancement of the structure centered at around 4.2 eV for the molecule at 1 nm is observed. The factor of this enhancement is around 20, which indicates a significant influence of the induced field. This interpretation is also supported by the value of the populations of the low-lying excited states, which are defined as $p_M = |C_M(t)|^2$, with C_M (t) given by Eq. (10). For this particular excitation, the increase in the population p_M is equal to a factor 10^3 at 1 nm with respect to the bare-molecule population for the

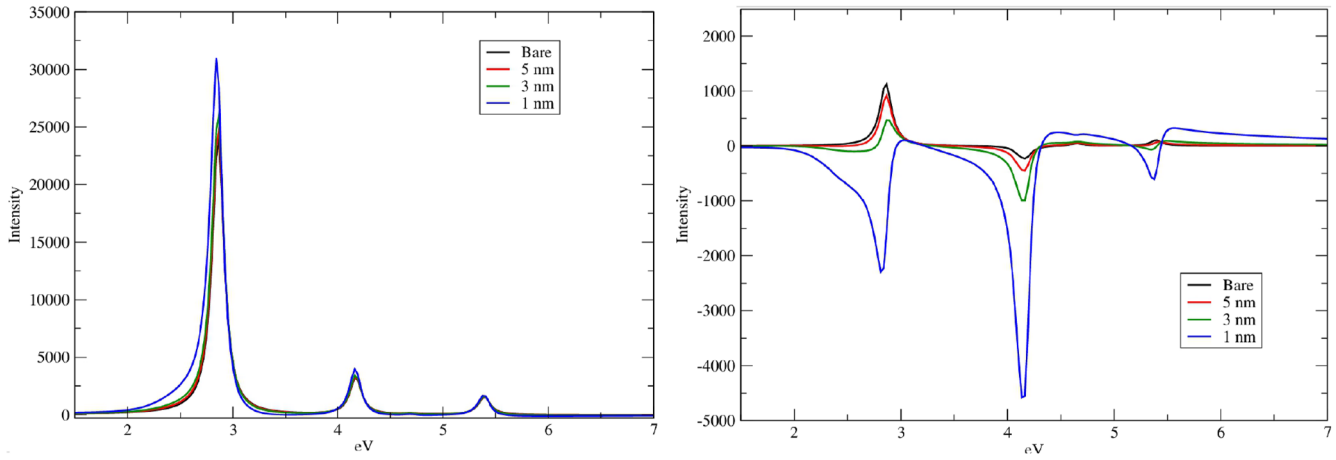


FIG. 7. ECD spectra of PID at a distance *d* of 1, 3, and 5 nm from the NP surface for both pulse polarization directions, parallel (left) and perpendicular (right). Bare-molecule spectra are also reported for comparison.

30 September 2025 09:17:53

Published under an exclusive license by AIP Publishing

same electronic state, which justifies the observed enhancement. The peak centered at 2.9 eV shows an enhancement of the peak as well, consequent to an increase of the population at 1 nm of a factor 10^3, but also a sign inversion in the intensity of the peak, which "hides" the enhancement in absolute value. The trend that brings to the sign inversion is already present at both 3 and 5 nm, for which one observes a decrease in the intensity of the peak if compared to the molecule without NP. Only at 1 nm to we observe a negative peak, though. A similar trend, characterized by an inversion of sign, can also be observed for the peak centered at 5.4 eV, although less pronounced. The observed sign flip could be interpreted in terms of a change of the induced density of the molecules due to the plasmonic field.

Enhancement observed for PID with perpendicular pulse polarization is robust against the value of the damping parameter Γ in Eq. (27). Indeed, the enhancement factor of the peak at 4.17 eV remains unchanged when a value of 200 or 600 a.u. is used, as reported in Fig. 5 of the supplementary material. Increasing the Γ value, e.g., 400 or 600 a.u., reduces the artifact of the smoothing procedure; for this reason, we are confident that the most accurate ECD spectra for PID with perpendicular pulse are those reported in Fig. 7 (Γ = 400 a.u.) and that in the left panel of Fig. 5 of the supplementary material (Γ = 600 a.u.).

By summarizing, the NP effect on PID is much more pronounced because of the smaller gap with the plasmon. However, a large enhancement of the ECD signal is only found for the perpendicular configuration. To the best of our knowledge, no experimental work has been dedicated to aligned PID molecules with Au NPs; therefore, we cannot get a direct comparison with published data. However, a large but not giant enhancement, as that found for PID, is in line with a pure electric dipole-driven mechanism.[30]

V. CONCLUSIONS

In this work, we have extended the TD-PCM-NP multiscale approach to the calculation of ECD spectra of chiral molecules close to a metal NP. We have studied the ECD response of MOX and PID in the presence of a spherical gold NP at various configurations. MOX and PID are described at the quantum level of theory, while the NP is a classically described continuous medium, whose polarization is simulated via the time evolution of BEM apparent surface charges. ECD spectra have been computed by Fourier transforming the molecular time-dependent magnetic dipole moment using TDSE based on B3LYP/TZP and CAM-B3LYP/TZP TDDFT calculations. This approach goes beyond a dipole-like representation of the chiral target, providing a realistic description of the electronic structure and dynamics of the molecule under the influence of an external pulse and of the coupled NP polarization.

We observe a large plasmonic-induced enhancement of the ECD signal for PID with the NP at 1 nm when the pulse is polarized perpendicularly to the molecular axis. In particular, the signal at around 4.2 eV is strongly affected by plasmonic effects; the enhancement factor is 20 at 1 nm. The peak at 2.9 eV is characterized by a change of sign and by an enhancement in absolute value.

Instead, no appreciable enhancement is observed when the pulse polarization is parallel to the axis at any of the considered distances. PID can therefore be defined as a plasmon sensitive molecule when the plasmon peak is located at 2.5 eV and the system configuration results in a positive contribution of the induced field, as in the perpendicular case.

Moreover, MOX shows no appreciable enhancement when the NP is close to it, up to the shortest distance investigated, i.e., 1 nm.

These results are easily rationalized in terms of the gap between plasmonic and molecular excitation and of the coupling of the pulse with the electric and magnetic dipoles of the molecule. If the gap is too large, plasmon effects are negligible, as in the case of MOX; instead, since the PID lowest excitations are close to the NP plasmon, the effect of the induced plasmon field is remarkable and determines an enhancement approximately of a factor 20 with a pulse polarization perpendicular to the NP surface. This effect decreases with the distance between NP and PID, as the amplitude of the induced field decreases.

This method paves the way to a quantum-chemistry systematic investigation of plasmon-assisted ECD molecular spectra, also of biological relevance, and to propose novel routes for experiments.

SUPPLEMENTARY MATERIAL

See the supplementary material for ground-state energy variation of MOX and PID in the presence of the NP. Differential PDOS for the ground state of MOX and PID, with and without NP. Electric and magnetic transition dipole moments for MOX and PID. Absorption spectra of MOX and PID as a function of the distance with the NP surface. ECD spectra for PID with Γ = 200 and 600 a.u.

ACKNOWLEDGMENTS

Financial support from ICSC—Centro Nazionale di Ricerca in High Performance Computing, Big Data, and Quantum Computing, funded by the European Union—NextGenerationEU is gratefully acknowledged.

AUTHOR DECLARATIONS

Conflict of Interest

The authors have no conflicts to disclose.

Author Contributions

L. Biancorosso: Data curation (lead); Investigation (lead); Methodology (equal); Software (equal); Visualization (equal); Writing – original draft (equal); Writing – review & editing (equal). **P. D'Antoni**: Methodology (equal); Software (equal); Writing – review & editing (equal). **S. Corni**: Formal analysis (equal); Methodology (equal); Software (equal); Writing – review & editing (equal). **M. Stener**: Formal analysis (equal); Methodology (equal); Software (equal); Writing – review & editing (equal). **E. Coccia**: Conceptualization (equal); Funding acquisition (equal); Investigation (equal); Methodology (equal); Software (equal); Supervision (equal); Validation (equal); Writing – original draft (equal); Writing – review & editing (equal).

30 September 2025 09:17:53

Published under an exclusive license by AIP Publishing

DATA AVAILABILITY

The data that support the findings of this study are available from the corresponding author upon reasonable request.

REFERENCES

[1] J. Gersten and A. Nitzan, "Spectroscopic properties of molecules interacting with small dielectric particles," J. Chem. Phys. **75**, 1139 (1981).
[2] R. P. Van Duyne, "Molecular plasmonics," Science **306**, 985 (2004).
[3] L. Novotny and B. Hecht, *Principles of Nano-Optics* (Cambridge University Press, Cambridge, 2012).
[4] A. Lauchner, A. E. Schlather, A. Manjavacas, Y. Cui, M. J. McClain, G. J. Stec, F. J. García de Abajo, P. Nordlander, and N. J. Halas, "Molecular plasmonics," Nano Lett. **15**, 6208 (2015).
[5] A. J. Wilson and K. A. Willets, "Molecular plasmonics," Annu. Rev. Anal. Chem. **9**, 27 (2016).
[6] B. Mennucci and S. Corni, "Multiscale modelling of photoinduced processes in composite systems," Nat. Rev. Chem. **3**, 315 (2019).
[7] D. Cialla, A. März, R. Böhme, F. Theil, K. Weber, M. Schmitt, and J. Popp, "Surface-enhanced Raman spectroscopy (SERS): Progress and trends," Anal. Bioanal. Chem. **403**, 27 (2012).
[8] S. Schlücker, "Surface-enhanced Raman spectroscopy: Concepts and chemical applications," Angew. Chem., Int. Ed. **53**, 4756 (2014).
[9] A. B. Zrimsek, N. Chiang, M. Mattei, S. Zaleski, M. O. McAnally, C. T. Chapman, A. I. Henry, G. C. Schatz, and R. P. Van Duyne, "Single-molecule chemistry with surface- and tip-enhanced Raman spectroscopy," Chem. Rev. **117**, 7583 (2017).
[10] P. Lafiosca, L. Nicoli, L. Bonatti, T. Giovannini, S. Corni, and C. Cappelli, "QM/classical modeling of surface enhanced Raman scattering based on atomistic electromagnetic models," J. Chem. Theory Comput. **19**, 3616 (2023).
[11] N. Berova, L. D. Bari, and G. Pescitelli, "Application of electronic circular dichroism in configurational and conformational analysis of organic compounds," Chem. Soc. Rev. **36**, 914–931 (2007).
[12] P. Lazzeretti, "General connections among nuclear electromagnetic shieldings and polarizabilities," Adv. Chem. Phys. **75**, 507 (1989).
[13] P. Lazzeretti, "Electric and magnetic properties of molecules," in *Handbook of Molecular Physics and Quantum Chemistry* (John Wiley & Sons, 2003), Vol. 3, p. 53.
[14] C. Diedrich and S. Grimme, "Systematic investigation of modern quantum chemical methods to predict electronic circular dichroism spectra," J. Phys. Chem. A **107**, 2524 (2003).
[15] T. D. Crawford, "*Ab initio* calculation of molecular chiroptical properties," Theor. Chem. Acc. **115**, 227 (2006).
[16] T. D. Crawford, M. C. Tam, and M. L. Abrams, "The current state of *ab initio* calculations of optical rotation and electronic circular dichroism spectra," J. Phys. Chem. A **111**, 12057 (2007).
[17] I. Warnke and F. Furche, "Circular dichroism: Electronic," Wiley Interdiscip. Rev.: Comput. Mol. Sci. **2**, 150 (2012).
[18] S. S. Andrews and J. Tretton, "Physical principles of circular dichroism," J. Chem. Educ. **97**, 4370 (2020).
[19] N. S. S. Nizar, M. Sujith, K. Swathi, C. Sissa, A. Painelli, and K. G. Thomas, "Emergent chiroptical properties in supramolecular and plasmonic assemblies," Chem. Soc. Rev. **50**, 11208 (2021).
[20] C. Gautier and T. Bürgi, "Chiral gold nanoparticles," ChemPhysChem **10**, 483 (2009).
[21] Z. Fan and A. O. Govorov, "Chiral nanocrystals: Plasmonic spectra and circular dichroism," Nano Lett. **12**, 3283 (2012).
[22] M. Hentschel, M. Schäferling, X. Duan, H. Giessen, and N. Liu, "Chiral plasmonics," Sci. Adv. **3**, e1602735 (2017).
[23] W. Ma, L. Xu, A. F. de Moura, X. Wu, H. Kuang, C. Xu, and N. A. Kotov, "Chiral inorganic nanostructures," Chem. Rev. **117**, 8041 (2017).
[24] G. Zheng, J. He, V. Kumar, S. Wang, I. Pastoriza-Santos, J. Pérez-Juste, L. M. Liz-Marzán, and K.-Y. Wong, "Discrete metal nanoparticles with plasmonic chirality," Chem. Soc. Rev. **50**, 3738 (2021).
[25] E. S. A. Goerlitzer, A. S. Puri, J. J. Moses, L. V. Poulikakos, and N. Vogel, "The beginner's guide to chiral plasmonics: Mostly harmless theory and the design of large-area substrates," Adv. Opt. Mater. **9**, 2100378 (2021).
[26] S. Wang, X. Liu, S. Mourdikoudis, J. Chen, W. Fu, Z. Sofer, Y. Zhang, S. Zhang, and G. Zheng, "Chiral Au nanorods: Synthesis, chirality origin, and applications," ACS Nano **16**, 19789 (2022).
[27] S. Both, M. Schäferling, F. Sterl, E. A. Muljarov, H. Giessen, and T. Weiss, "Nanophotonic chiral sensing: How does it actually work?," ACS Nano **16**, 2822 (2022).
[28] W. Wu and M. Pauly, "Chiral plasmonic nanostructures: Recent advances in their synthesis and applications," Mater. Adv. **3**, 186 (2022).
[29] J.-M. Ha, A. Solovyov, and A. Katz, "Postsynthetic modification of gold nanoparticles with calix[4]arene enantiomers: Origin of chiral surface plasmon resonance," Langmuir **25**, 153 (2009).
[30] A. O. Govorov, Z. Fan, P. Hernandez, J. M. Slocik, and R. R. Naik, "Theory of circular dichroism of nanomaterials comprising chiral molecules and nanocrystals: Plasmon enhancement, dipole interactions, and dielectric effects," Nano Lett. **10**, 1374 (2010).
[31] A. O. Govorov, "Plasmon-induced circular dichroism of a chiral molecule in the vicinity of metal nanocrystals. Application to various geometries," J. Phys. Chem. C **115**, 7914 (2011).
[32] J. M. Slocik, A. O. Govorov, and R. R. Naik, "Plasmonic circular dichroism of peptide-functionalized gold nanoparticles," Nano Lett. **11**, 701 (2011).
[33] N. A. Abdulrahman, Z. Fan, T. Tonooka, S. M. Kelly, N. Gadegaard, E. Hendry, A. O. Govorov, and M. Kadodwala, "Induced chirality through electromagnetic coupling between chiral molecular layers and plasmonic nanostructures," Nano Lett. **12**, 977 (2012).
[34] F. Lu, Y. Tian, M. Liu, D. Su, H. Zhang, A. O. Govorov, and O. Gang, "Discrete nanocubes as plasmonic reporters of molecular chirality," Nano Lett. **13**, 3145 (2013).
[35] B. M. Maoz, Y. Chaikin, A. B. Tesler, O. Bar Elli, Z. Fan, A. O. Govorov, and G. Markovich, "Amplification of chiroptical activity of chiral biomolecules by surface plasmons," Nano Lett. **13**, 1203 (2013).
[36] H. Zhang and A. O. Govorov, "Giant circular dichroism of a molecule in a region of strong plasmon resonances between two neighboring gold nanocrystals," Phys. Rev. B **87**, 075410 (2013).
[37] T. Wu, J. Ren, R. Wang, and X. Zhang, "Competition of chiroptical effect caused by nanostructure and chiral molecules," J. Phys. Chem. C **118**, 20529 (2014).
[38] R. Y. Wang, P. Wang, Y. Liu, W. Zhao, D. Zhai, X. Hong, Y. Ji, X. Wu, F. Wang, D. Zhang, W. Zhang, R. Liu, and X. Zhang, "Experimental observation of giant chiroptical amplification of small chiral molecules by gold nanosphere clusters," J. Phys. Chem. C **118**, 9690 (2014).
[39] T. J. Davis and D. E. Gomez, "Interaction of localized surface plasmons with chiral molecules," Phys. Rev. B **90**, 235424 (2014).
[40] D. Zhai, P. Wang, R. Y. Wang, X. Tian, Y. Ji, W. Zhao, L. Wang, H. Wei, X. Wu, and X. Zhang, "Plasmonic polymers with strong chiroptical response for sensing molecular chirality," Nanoscale **7**, 10690 (2015).
[41] M. C. di Gregorio, A. Ben Moshe, E. Tirosh, L. Galantini, and G. Markovich, "Chiroptical study of plasmon–molecule interaction: The case of interaction of glutathione with silver nanocubes," J. Phys. Chem. C **119**, 17111 (2015).
[42] T. Levi-Belenkova, A. O. Govorov, and G. Markovich, "Orientation-sensitive peptide-induced plasmonic circular dichroism in silver nanocubes," J. Phys. Chem. C **120**, 12751 (2016).
[43] W. Zhang, T. Wu, R. Wang, and X. Zhang, "Surface-enhanced circular dichroism of oriented chiral molecules by plasmonic nanostructures," J. Phys. Chem. C **121**, 666 (2017).
[44] S. Lee, J.-H. Kang, S. Yoo, and Q.-H. Park, "Robust numerical evaluation of circular dichroism from chiral medium/nanostructure coupled systems using the finite-element method," Sci. Rep. **8**, 8406 (2018).
[45] W. Wang, F. Wu, Y. Zhang, W. Wei, W. Niu, and G. Xu, "Boosting chiral amplification in plasmon-coupled circular dichroism using discrete silver nanorods as amplifiers," Chem. Commun. **57**, 7390 (2021).
[46] A. Carone, P. Mariani, A. Desert, M. Romanelli, J. Marcheselli, M. Garavelli, S. Corni, I. Rivalta, and S. Parola, "Insight on chirality encoding from small thiolated molecule to plasmonic Au@Ag and Au@Au nanoparticles," ACS Nano **16**, 1089 (2022).

30 September 2025 09:17:53

Published under an exclusive license by AIP Publishing

[47]M. Venturi, R. Adhikary, A. Sahoo, C. Ferrante, I. Daidone, F. Di Stasio, A. Toma, F. Tani, H. Altug, A. Mecozzi, M. Aschi, and A. Marini, "Plasmon-enhanced circular dichroism spectroscopy of chiral drug solutions," J. Chem. Phys. **159**, 154703 (2023).
[48]J. George and K. G. Thomas, "Surface plasmon coupled circular dichroism of Au nanoparticles on peptide nanotubes," J. Am. Chem. Soc. **132**, 2502 (2010).
[49]X. Shen, C. Song, J. Wang, D. Shi, Z. Wang, N. Liu, and B. Ding, "Rolling up gold nanoparticle-dressed DNA origami into three-dimensional plasmonic chiral nanostructures," J. Am. Chem. Soc. **134**, 146 (2012).
[50]M. J. Urban, P. K. Dutta, P. Wang, X. Duan, X. Shen, B. Ding, Y. Ke, and N. Liu, "Plasmonic toroidal metamolecules assembled by DNA origami," J. Am. Chem. Soc. **138**, 5495 (2016).
[51]X. Lan, X. Lu, C. Shen, Y. Ke, W. Ni, and Q. Wang, "Au nanorod helical superstructures with designed chirality," J. Am. Chem. Soc. **137**, 457 (2015).
[52]J. George, S. Kar, E. S. Anupriya, S. M. Somasundaran, A. D. Das, C. Sissa, A. Painelli, and K. G. Thomas, "Chiral plasmons: Au nanoparticle assemblies on thermoresponsive organic templates," ACS Nano **13**, 4392 (2019).
[53]J. Lu, Y. Xue, K. Bernardino, N.-N. Zhang, W. R. Gomes, N. S. Ramesar, S. Liu, Z. Hu, T. Sun, A. F. de Moura, N. A. Kotov, and K. Liu, "Enhanced optical asymmetry in supramolecular chiroplasmonic assemblies with long-range order," Science **371**, 1368 (2021).
[54]E. Coccia and S. Corni, "Role of coherence in the plasmonic control of molecular absorption," J. Chem. Phys. **151**, 044703 (2019).
[55]Y. Zhao, A. N. Askarpour, L. Sun, J. Shi, X. Li, and A. Alù, "Chirality detection of enantiomers using twisted optical metamaterials," Nat. Commun. **8**, 14180 (2017).
[56]I. Lieberman, G. Shemer, T. Fried, E. M. Kosower, and G. Markovich, "Plasmon-resonance-enhanced absorption and circular dichroism," Angew. Chem., Int. Ed. **47**, 4855 (2008).
[57]M. L. Nesterov, X. Yin, M. Schäferling, H. Giessen, and T. Weiss, "The role of plasmon-generated near fields for enhanced circular dichroism spectroscopy," ACS Photonics **3**, 578 (2016).
[58]L. A. Warning, A. R. Miandashti, L. A. McCarthy, Q. Zhang, C. F. Landes, and S. Link, "Nanophotonic approaches for chirality sensing," ACS Nano **15**, 15538–15566 (2021).
[59]I. Carmeli, I. Lieberman, L. Kraversky, Z. Fan, A. O. Govorov, G. Markovich, and S. Richter, "Broad band enhancement of light absorption in photosystem I by metal nanoparticle antennas," Nano Lett. **10**, 2069–2074 (2010).
[60]T. R. Leite, L. Zschiedrich, O. Kizilkaya, and K. M. McPeak, "Resonant plasmonic–biomolecular chiral interactions in the far-ultraviolet: Enantiomeric discrimination of sub-10 nm amino acid films," Nano Lett. **22**, 7343–7350 (2022).
[61]W. Ma, H. Kuang, L. Xu, L. Ding, C. Xu, L. Wang, and N. A. Kotov, "Attomolar DNA detection with chiral nanorod assemblies," Nat. Commun. **4**, 2689 (2013).
[62]B. M. Maoz, R. van der Weegen, Z. Fan, A. O. Govorov, G. Ellestad, N. Berova, E. W. Meijer, and G. Markovich, "Plasmonic chiroptical response of silver nanoparticles interacting with chiral supramolecular assemblies," J. Am. Chem. Soc. **134**, 17807 (2012).
[63]T. Wu, W. Zhang, R. Wang, and X. Zhang, "A giant chiroptical effect caused by the electric quadrupole," Nanoscale **9**, 5110 (2017).
[64]L. M. Kneer, E.-M. Roller, L. V. Besteiro, R. Schreiber, A. O. Govorov, and T. Liedl, "Circular dichroism of chiral molecules in DNA-assembled plasmonic hotspots," ACS Nano **12**, 9110 (2018).
[65]S. Adhikari and M. Orrit, "Optically probing the chirality of single plasmonic nanostructures and of single molecules: Potential and obstacles," ACS Photonics **9**, 3486 (2022).
[66]E. Makkonen, T. P. Rossi, A. H. Larsen, O. Lopez-Acevedo, P. Rinke, M. Kuisma, and X. Chen, "Real-time time-dependent density functional theory implementation of electronic circular dichroism applied to nanoscale metal–organic clusters," J. Chem. Phys. **154**, 114102 (2021).
[67]M. Monti, M. Stener, and E. Coccia, "Electronic circular dichroism from real-time propagation in state space," J. Chem. Phys. **158**, 084102 (2023).
[68]J. Mattiat and S. Luber, "Electronic circular dichroism with real time time dependent density functional theory: Propagator formalism and gauge dependence," Chem. Phys. **527**, 110464 (2019).
[69]J. Mattiat and S. Luber, "Comparison of length, velocity, and symmetric gauges for the calculation of absorption and electric circular dichroism spectra with real-time time-dependent density functional theory," J. Chem. Theory Comput. **18**, 5513 (2022).
[70]S. Corni and J. Tomasi, "Enhanced response properties of a chromophore physisorbed on a metal particle," J. Chem. Phys. **114**, 3739–3751 (2001).
[71]S. Pipolo and S. Corni, "Real-time description of the electronic dynamics for a molecule close to a plasmonic nanoparticle," J. Phys. Chem. C **120**, 28774 (2016).
[72]N. Tancogne-Dejean, M. J. T. Oliveira, X. Andrade, H. Appel, C. H. Borca, G. Le Breton, F. Buchholz, A. Castro, S. Corni, A. A. Correa, U. De Giovannini, A. Delgado, F. G. Eich, J. Flick, G. Gil, A. Gomez, N. Helbig, H. Hübener, R. Jestädt, J. Jornet-Somoza, A. H. Larsen, I. V. Lebedeva, M. Lüders, M. A. L. Marques, S. T. Ohlmann, S. Pipolo, M. Rampp, C. A. Rozzi, D. A. Strubbe, S. A. Sato, C. Schäfer, I. Theophilou, A. Welden, and A. Rubio, "Octopus, a computational framework for exploring light-driven phenomena and quantum dynamics in extended and finite systems," J. Chem. Phys. **152**, 124119 (2020).
[73]T. P. Rossi, M. Kuisma, M. J. Puska, R. M. Nieminen, and P. Erhart, "Kohn-Sham decomposition in real-time time-dependent density-functional theory: An efficient tool for analyzing plasmonic excitations," J. Chem. Theory Comput. **13**, 4779 (2017).
[74]S. A. Fischer, C. J. Cramer, and N. J. Govind, "Excited state absorption from real-time time-dependent density functional theory," J. Chem. Theory Comput. **11**, 4294 (2015).
[75]S. D'Agostino, R. Rinaldi, G. Cuniberti, and F. Della Sala, "Density functional tight binding for quantum plasmonics," J. Phys. Chem. C **122**, 19756 (2018).
[76]N. V. Ilawe, M. B. Oviedo, and B. M. Wong, "Effect of quantum tunneling on the efficiency of excitation energy transfer in plasmonic nanoparticle chain waveguides," J. Mater. Chem. C **6**, 5857 (2018).
[77]N. Asadi-Aghbolaghi, R. Rüger, Z. Jamshidi, and L. Visscher, "TD-DFT+TB: An efficient and fast approach for quantum plasmonic excitations," J. Phys. Chem. C **124**, 7946 (2020).
[78]T. Wu, X. Zhang, R. Wang, and X. Zhang, "Strongly enhanced Raman optical activity in molecules by magnetic response of nanoparticles," J. Phys. Chem. C **120**, 14795 (2016).
[79]X. Ren, W. Lin, Y. Fang, F. Ma, and J. Wang, "Raman optical activity (ROA) and surface-enhanced ROA (SE-ROA) of (+)-(R)-methyloxirane adsorbed on a Ag_{20} cluster," RSC Adv. **7**, 34376–34381 (2017).
[80]F. J. Kleima, M. Wendling, E. Hofmann, E. J. Peterman, R. van Grondelle, and H. van Amerongen, "Peridinin chlorophyll a protein: Relating structure and steady-state spectroscopy," Biochemistry **39**, 5184–5195 (2000).
[81]T. Polívka, R. G. Hiller, and H. A. Frank, "Spectroscopy of the peridinin–chlorophyll-a protein: Insight into light-harvesting strategy of marine algae," Arch. Biochem. Biophys. **458**, 111–120 (2007).
[82]D. Carbonera, G. Giacometti, U. Segre, E. Hofmann, and R. G. Hiller, "Structure-based calculations of the optical spectra of the light-harvesting peridinin–chlorophyll–protein complexes from *Amphidinium carterae* and *Heterocapsa pygmaea*," J. Phys. Chem. B **103**, 6349–6356 (1999).
[83]M. Pilch and M. Pawlikowski, "Circular dichroism (CD) study of peridinin–chlorophyll a protein (PCP) complexes from marine dinoflagellate algae: The tetramer approach," J. Chem. Soc., Faraday Trans. **94**, 227–232 (1998).
[84]I. Kaminska, J. Bohlen, S. Mackowski, P. Tinnefeld, and G. P. Acuna, "Strong plasmonic enhancement of a single peridinin–chlorophyll a–protein complex on DNA origami-based optical antennas," ACS Nano **12**, 1650–1655 (2018).
[85]M. K. Schmidt, A. O. Govorov, and S. Mackowski, "Plasmon induced modifications of the Förster energy transfer in reconstituted peridinin-chlorophyll-protein photosynthetic complex," MRS Online Proc. Libr. **1286**, 324 (2010).
[86]N. Czechowski, P. Nyga, M. K. Schmidt, T. H. Brotosudarmo, H. Scheer, D. Piatkowski, and S. Mackowski, "Absorption enhancement in peridinin–chlorophyll–protein light-harvesting complexes coupled to semicontinuous silver film," Plasmonics **7**, 115–121 (2012).
[87]U. Hohenester and A. Trügler, "MNPBEM: A Matlab toolbox for the simulation of plasmonic nanoparticles," Comput. Phys. Commun. **183**, 370 (2012).
[88]G. Dall'Osto, E. Coccia, C. A. Guido, and S. Corni, "Investigating ultrafast two-pulse experiments on single DNQDI fluorophores: A stochastic quantum approach," Phys. Chem. Chem. Phys. **22**, 16734 (2020).

30 September 2025 09:17:53

Published under an exclusive license by AIP Publishing

[89]M. Marsili and S. Corni, "Electronic dynamics of a molecular system coupled to a plasmonic nanoparticle combining the polarizable continuum model and many-body perturbation theory," J. Phys. Chem. C **126**, 8768 (2022).
[90]S. Corni, S. Pipolo, and R. Cammi, "Equation of motion for the solvent polarization apparent charges in the polarizable continuum model: Application to real-time TDDFT," J. Phys. Chem. A **119**, 5405 (2015).
[91]G. Dall'Osto, G. Gil, S. Pipolo, and S. Corni, "Real-time dynamics of plasmonic resonances in nanoparticles described by a boundary element method with generic dielectric function," J. Chem. Phys. **153**, 184114 (2020).
[92]P. Hoerner, M. K. Lee, and B. Schlegel, "Angular dependence of strong field ionization of N_2 by time-dependent configuration interaction using density functional theory and the Tamm-Dancoff approximation," J. Chem. Phys. **151**, 054102 (2019).
[93]P. Grobas Illobre, M. Marsili, S. Corni, M. Stener, D. Toffoli, and E. Coccia, "Time-resolved excited-state analysis of molecular electron dynamics by TDDFT and Bethe–Salpeter equation formalisms," J. Chem. Theory Comput. **17**, 6314 (2021).
[94]M. E. Casida, "Time-dependent density functional response theory for molecules," in *Recent Advances in Density Functional Methods: (Part I)* (World Scientific, 1995), pp. 155–192.
[95]E. Tapavicza, I. Tavernelli, and U. Rothlisberger, "Trajectory surface hopping within linear response time-dependent density-functional theory," Phys. Rev. Lett. **98**, 023001 (2007).
[96]E. Tapavicza, I. Tavernelli, U. Rothlisberger, C. Filippi, and M. E. Casida, "Mixed time-dependent density-functional theory/classical trajectory surface hopping study of oxirane photochemistry," J. Chem. Phys. **129**, 124108 (2008).
[97]E. Luppi and M. Head-Gordon, "Computation high-harmonic generation spectra H_2 and N_2 in intense laser pulses using quantum chemistry methods and time-dependent density functional theory," Mol. Phys. **110**, 909 (2012).
[98]C. F. Pauletti, E. Coccia, and E. Luppi, "Role of exchange and correlation in high-harmonic generation spectra of H_2, N_2, and CO_2: Real-time time-dependent electronic-structure approaches," J. Chem. Phys. **154**, 014101 (2021).
[99]G. Dall'Osto and S. Corni, "Time resolved Raman scattering of molecules: A quantum mechanics approach with stochastic Schroedinger equation," J. Phys. Chem. A **126**, 8088 (2022).
[100]F. Ding, W. Liang, C. T. Chapman, C. M. Isborn, and X. Li, "On the gauge invariance of nonperturbative electronic dynamics using the time-dependent Hartree-Fock and time-dependent Kohn-Sham," J. Chem. Phys. **135**, 164101 (2011).
[101]P. Wopperer, P. M. Dinh, P.-G. Reinhard, and E. Suraud, "Electrons as probes of dynamics in molecules and clusters: A contribution from time dependent density functional theory," Phys. Rep. **562**, 1 (2015).
[102]B. Peng, D. B. Lingerfelt, F. Ding, C. M. Aikens, and X. Li, "Real-time TDDFT studies of exciton decay and transfer in silver nanowire arrays," J. Phys. Chem. C **119**, 6421 (2015).
[103]J. J. Goings, P. J. Lestrange, and X. Li, "Real-time time-dependent electronic structure theory," Wiley Interdiscip. Rev.: Comput. Mol. Sci. **8**, e1341 (2018).
[104]A. Parise, A. Alvarez-Ibarra, X. Wu, X. Zhao, J. Pilmé, and A. de la Lande, "Quantum chemical topology of the electron localization function in the field of attosecond electron dynamics," J. Phys. Chem. Lett. **9**, 844 (2018).
[105]X. Li, N. Govind, C. Isborn, A. E. DePrince III, and K. Lopata, "Real-time time-dependent electronic structure theory," Chem. Rev. **120**, 9951 (2020).
[106]M. Jacobs, J. Krumland, A. M. Valencia, and C. Cocchi, "Pulse-induced dynamics of a charge-transfer complex from first principles," J. Phys. Chem. A **127**, 8794 (2023).
[107]S. Raghunathan and M. Nest, "Critical examination of explicitly time-dependent density functional theory for coherent control of dipole switching," J. Chem. Theory Comput. **7**, 2492 (2011).
[108]M. R. Provorse and C. M. Isborn, "Electron dynamics with real-time time-dependent density functional theory," Int. J. Quantum Chem. **116**, 739 (2016).
[109]F. Bedurke, T. Klamroth, and P. Saalfrank, "Many-electron dynamics in laser-driven molecules: Wavefunction theory vs. density functional theory," Phys. Chem. Chem. Phys. **23**, 13544 (2021).
[110]E. Coccia, J. Fregoni, C. A. Guido, M. Marsili, S. Pipolo, and S. Corni, "Hybrid theoretical models for molecular nanoplasmonics," J. Chem. Phys. **153**, 200901 (2020).
[111]E. Coccia and E. Luppi, "Time-dependent *ab initio* approaches for high-harmonic generation spectroscopy," J. Phys.: Condens. Matter **34**, 073001 (2021).
[112]R. Rüger, M. Franchini, T. Trnka, A. Yakovlev, E. van Lenthe, P. Philipsen, T. van Vuren, B. Klumpers, and T. Soini, *AMS 2022.1, SCM, Theoretical Chemistry* (Vrije Universiteit, Amsterdam, The Netherlands, 2022).
[113]R. McWeeny, *Methods of Molecular Quantum Mechanics* (Academic Press, 2016).
[114]F. Furche, R. Ahlrichs, C. Wachsmann, E. Weber, A. Sobanski, F. Vögtle, and S. Grimme, "Circular dichroism of helicenes investigated by time-dependent density functional theory," J. Am. Chem. Soc. **122**, 1717 (2000).
[115]F. Furche, "On the density matrix based approach to time-dependent density functional response theory," J. Chem. Phys. **114**, 5982 (2001).
[116]J. Autschbach, T. Ziegler, S. J. A. van Gisbergen, E. J. Baerends, and E. J. Baerends, "Chiroptical properties from time-dependent density functional theory. I. Circular dichroism spectra of organic molecules," J. Chem. Phys. **116**, 6930 (2002).
[117]J. Autschbach and T. Ziegler, "Calculating molecular electric and magnetic properties from time-dependent density functional response theory," J. Chem. Phys. **116**, 891 (2002).
[118]J. Autschbach, S. Patchkovskii, T. Ziegler, S. van Gisbergen, and E. Jan Baerends, "Chiroptical properties from time-dependent density functional theory. II. Optical rotations of small to medium sized organic molecules," J. Chem. Phys. **117**, 581 (2002).
[119]S. Pipolo, S. Corni, and R. Cammi, "The cavity electromagnetic field within the polarizable continuum model of solvation: An application to the real-time time dependent density functional theory," Comput. Theor. Chem. **1040–1041**, 112 (2014).
[120]D. Varsano, L. A. Espinosa-Leal, X. Andrade, M. A. L. Marques, R. di Felice, and A. Rubio, "Towards a gauge invariant method for molecular chiroptical properties in TDDFT," Phys. Chem. Chem. Phys. **11**, 4481 (2009).
[121]S. Knecht, C. M. Marian, J. Kongsted, and B. Mennucci, "On the photophysics of carotenoids: A multireference DFT study of peridinin," J. Phys. Chem. B **117**, 13808–13815 (2013).

30 September 2025 09:17:53

Published under an exclusive license by AIP Publishing

4.2.2 How Adsorption Geometry Dictates Chiroptical Properties: A Computational Study of L-Cysteine on Au(111) Cluster Models

In this study, polarizable time-dependent density functional theory (polTDDFT) combined with an efficient Hybrid Diagonal Approximation implemented via Resolution of Identity (RI–HDA) is employed to investigate the electronic circular dichroism of L-cysteine-functionalized gold cluster models. The work serves as an application of recently developed hybrid TDDFT methodologies to metal–ligand systems of realistic size, enabling the exploration of chirality transfer mechanisms beyond purely molecular models.

By systematically varying ligand adsorption sites, molecular orientations, and intermolecular interactions, the study assesses how local structural arrangements modulate the induced chiroptical response of the metal cluster. A fragment projection analysis is used to disentangle metal-centered, ligand-centered, and charge-transfer contributions to the ECD spectra, providing a detailed interpretation of the electronic origin of the observed signals.

While the systems investigated are not plasmonic in nature, the results highlight the role of metal–ligand coupling in shaping chiroptical properties and demonstrate the robustness and flexibility of the polTDDFT/RI–HDA framework for analyzing complex hybrid nanostructures.

My contribution to this work was primarily methodological and technical. In particular, I provided support for the use of the polTDDFT framework within the AMS/ADF suite, including guidance on the setup and interpretation of the calculations employing the RI–HDA approximation and on the post-processing tools used for fragment-based analysis of the ECD spectra.

The pubblication has been recently accepted to be published on *The Journal of Physical Chemistry C*

THE JOURNAL OF PHYSICAL CHEMISTRY C
A JOURNAL OF THE AMERICAN CHEMICAL SOCIETY

pubs.acs.org/JPCC

Article

How Adsorption Geometry Dictates Chiroptical Properties: A Computational Study of L-Cysteine on Au(111) Cluster Models

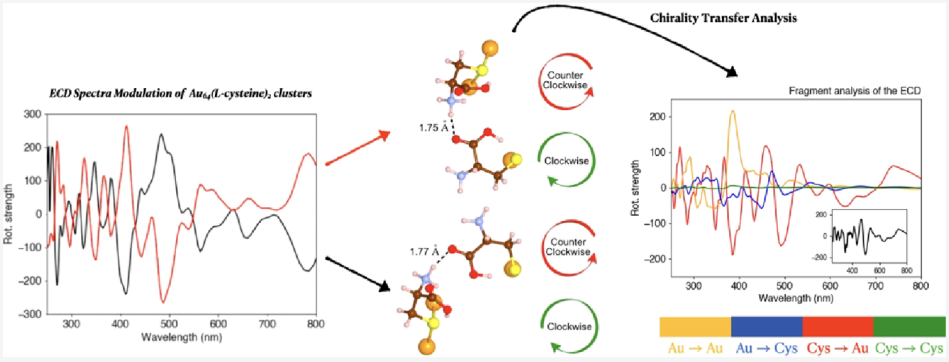
Mary Tabut,* Pierpaolo D'Antoni, Daniele Toffoli,* Mauro Stener, Caroline Salzemann, and Monica Calatayud

Cite This: https://doi.org/10.1021/acs.jpcc.5c07107

Read Online

ACCESS | Metrics & More | Article Recommendations | Supporting Information

Downloaded via UNIVERSITA STUDI TRIESTE on December 29, 2025 at 09:46:12 (UTC).
See https://pubs.acs.org/sharingguidelines for options on how to legitimately share published articles.



ABSTRACT: Understanding chirality transfer in metal nanoclusters is crucial for developing advanced materials with tailored optical properties. This study investigates the chiroptical properties of gold clusters functionalized with L-cysteine using time-dependent density functional theory. By exploring different ligand adsorption configurations, molecular orientations, and intermolecular interactions, we systematically analyze their influence on electronic circular dichroism (ECD) spectra. The results reveal that ligand-induced chirality transfer dominates the ECD response, with hydrogen bonding and molecular orientation playing a significant role in modulating the optical activity. In addition, fragment analysis confirms that metal−ligand interactions strongly contribute to the observed chiroptical effects, demonstrating that controlling ligand arrangement on the gold cluster surface is essential for tuning induced circular dichroism.

INTRODUCTION

Chirality plays a fundamental role in numerous chemical and biological processes, and its manifestation in nanoscale materials has accumulated significant attention in recent years. In particular, chirality transfer mechanisms in plasmonic and nanostructured systems have been extensively studied due to their implications in asymmetric catalysis, enantioselective sensing, and optoelectronic applications.[1−3] Among these materials, gold nanoclusters (AuNCs) have emerged as particularly promising candidates for exploring chiroptical effects, as they exhibit size-dependent electronic transitions and strong ligand interactions that can be tuned for specific applications.[4−6]

Thiolate-protected gold nanoclusters (RS-AuNCs) are of particular interest for their unique chiroptical properties, which arise from their distinct structural configurations and ligand arrangements. A well-known example is the $Au_{38}(SR)_{24}$ cluster, which features a bi-icosahedral core surrounded by a chiral ligand shell.[7−11] Despite the achirality of the metal core and ligands, this structure induces significant circular dichroism (CD) signals, a phenomenon known as induced chirality. This work demonstrates how the chiral information from the ligand shell can influence the electronic structure of the entire nanocluster. The relationship between ligand chirality and the electronic transitions of the gold core is further explored through electronic circular dichroism (ECD) spectroscopy.[12] Research has shown that the adsorption of chiral thiolates onto gold clusters leads to notable ECD signals, indicating a strong coupling between the ligand's chirality and the cluster's electronic transitions.

In this study, we investigate the chiroptical properties of L-cysteine-functionalized gold (111) cluster models, $Au_{64}(Cys)_2$. L-cysteine, a naturally occurring chiral amino acid, is an ideal model ligand due to its well-defined stereochemistry and strong affinity for metal surfaces. While numerous studies have

Received: October 16, 2025
Revised: December 6, 2025
Accepted: December 8, 2025

ACS Publications
© XXXX American Chemical Society

explored cysteine derivatives for nanoparticle functionalization, the specific effects of pH and molecular form on optical activity remain less understood. In our work, we focus on the specific acidic form of L-cysteine [$NH_3^+CH(CH_2SH)COOH$]. However, we adapted our model to represent the chemisorbed state of cysteine on the Au(111) surface, where adsorption typically leads to S−H bond cleavage and formation of a thiolate (Au−S) species. For this reason, the [$NH_3^+CH(CH_2S^-)COOH$] form of the molecule was chosen as the relevant adsorbed species under acidic conditions. Importantly, this form of the molecule not only allows potential intermolecular interactions between the amino and carboxylic groups of two neighboring molecules but also plays an important role in the way the molecules interact with the gold surface. These effects have been extensively studied in our previous work using periodic surfaces at the density functional theory (DFT) level of theory.[13]

Building on this, we move from periodic models to finite clusters to study the chiroptical response of these systems. Au-thiolate clusters have been extensively studied both experimentally[6,14] and theoretically, from small to larger cluster sizes,[15−17] focusing on various ligand effects and structural influences on the chiroptical properties. They have provided valuable insights into chirality transfer mechanisms and the enhancement of optical activity in gold nanoclusters. Notably, Monti et al. demonstrated that solvent interactions, including hydrogen bonding, significantly influence the ECD response of glutathione-protected $[Au_{25}(GSH)_{18}]^{-1}$ nanoclusters, highlighting the active role of the solvent in modulating optical activity.[15]

However, a comprehensive analysis of chirality transfer mechanisms and ECD behavior, particularly in relation to molecular orientation, adsorption sites, and intermolecular interactions, is still lacking. To fill these gaps, we employ state of the art time-dependent density functional theory (TD-DFT) to systematically investigate the ECD spectra of L-cysteine-functionalized gold clusters. Our simulations take into account variations in ligand adsorption, molecular orientation, and hydrogen bonding, providing detailed insights into how these factors influence the electronic and optical properties of the clusters across the near UV (250 nm) to near-infrared (800 nm) wavelength range.

The calculated ECD spectra are further analyzed using a fragment projection method, which helps determining the contributions of specific molecular orbitals to the observed transitions. Our findings demonstrate a strong chirality transfer from the L-cysteine ligands to the metal cluster, and emphasize the importance of controlling the surface arrangement of chiral molecules in tuning induced circular dichroism.

COMPUTATIONAL METHODS AND CLUSTER MODEL

All cluster geometries presented in this paper were designed based on the corresponding optimized periodic systems extracted from ref 13. The optimized geometries of the periodic systems were obtained from Density functional theory (DFT) calculations performed using the Vienna Ab initio Simulation Package (VASP), version 6.4.0.[18,19] The Perdew−Burke−Ernzerhof (PBE) generalized gradient approximation (GGA) was employed as the exchange-correlation functional,[20] with van der Waals interactions incorporated via the Grimme-D3 method.[21,22] The periodic systems were constructed for the Au(111) surface, where a slab model of four atomic layers thick was used, from which the bottom two layers were fixed to simulate bulk properties, and the top two layers were fully relaxed during optimization process. A plane-wave basis set with an energy cutoff of 450 eV was applied,[19] and core electrons were treated using projector-augmented wave (PAW) pseudopotentials.[23] The valence electrons considered in the calculations correspond to 11 for Au, 6 for S, 1 for H, 4 for C, 6 for O, and 5 for N atoms. Periodic boundary conditions were enforced, with a 15 Å vacuum region along the z-axis to prevent interactions between periodic images. The Au(111) facet was modeled using a p(4 × 4) supercell, and the Brillouin zone was sampled with a 3 × 3 × 1 k-point mesh generated by the Monkhorst−Pack scheme.[24] Self-consistent field calculations were converged with a threshold of 10^{-6} eV.

The cluster model used for this study is presented in Figure 1. All clusters were cut out from their corresponding optimized slabs using the VESTA program, version 3.9.0,[25] see below.

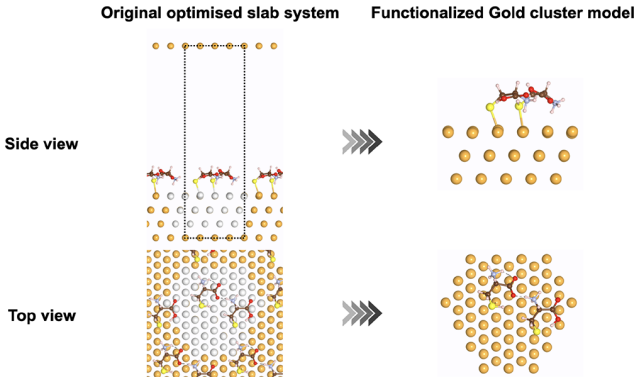


Figure 1. Computational model of the functionalized gold cluster: (Left) Top and side views of the optimized slab model used as the foundation for designing the clusters shape. (Right) Top and side views of the L-cysteine-functionalized gold cluster.

This approach ensures a well-defined local environment consistent with surface adsorption and allows the focus on the molecular surface arrangements rather than in the gold substrate itself. Our study focuses on the investigation of various factors that can affect the chirality transfer mechanism. Therefore, in designing these systems, particular attention was given to the shape of the gold cluster to ensure that it did not introduce any artifacts or undesired chiral influences on the calculated ECD spectra. The gold cluster is composed of the first three layers of the Au(111) surface (for a total of 64 gold atoms), and 2 molecules of L-cysteine adsorbed to the surface, comprising a total of 92 atoms. From the top view of the slab (Figure 1 (Left)), we can see that a particular attention was paid to place the adsorbed molecules as close to the center as possible to avoid side effects that could alter the ECD response.

The optical response of the finite systems was calculated at the polarizable TDDFT (polTDDFT) level of theory.[26,27] For all systems investigated, no further geometry optimization was performed.

The Hybrid Diagonal Approximation (HDA)[28] was employed to facilitate the TDDFT calculations using the B3LYP hybrid functional.[29,30] This functional was selected based on a systematic comparison against various GGA and hybrid functionals, which identified B3LYP as the most suitable compromise for simultaneously describing the electronic response of both the gold clusters and the organic ligands (see Figure S3 for details). In the present work we employed a much more efficient implementation of the HDA (fitted HDA) which

https://doi.org/10.1021/acs.jpcc.5c07107
J. Phys. Chem. C XXXX, XXX, XXX−XXX

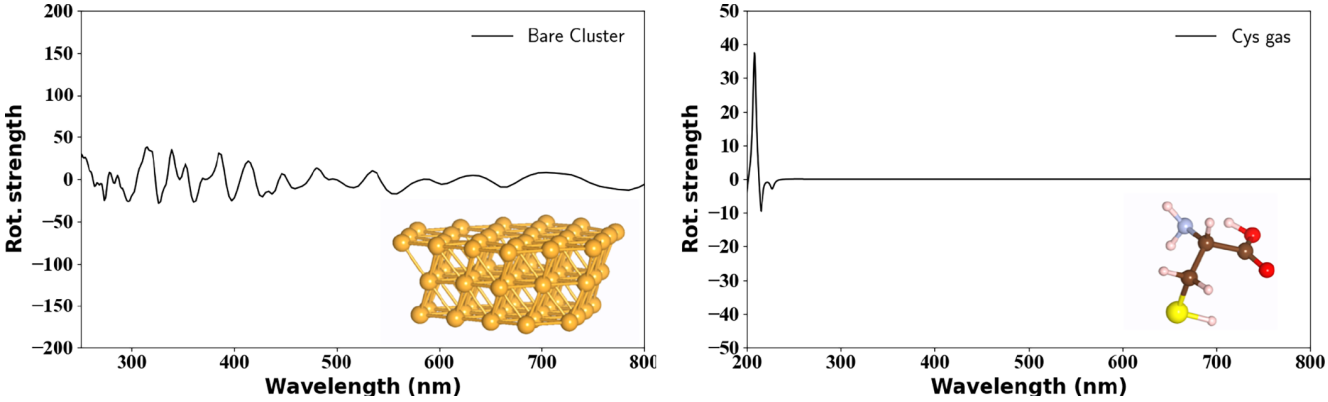


Figure 2. Calculated ECD spectra of the bare gold cluster (left) and the gas cysteine molecule (right).

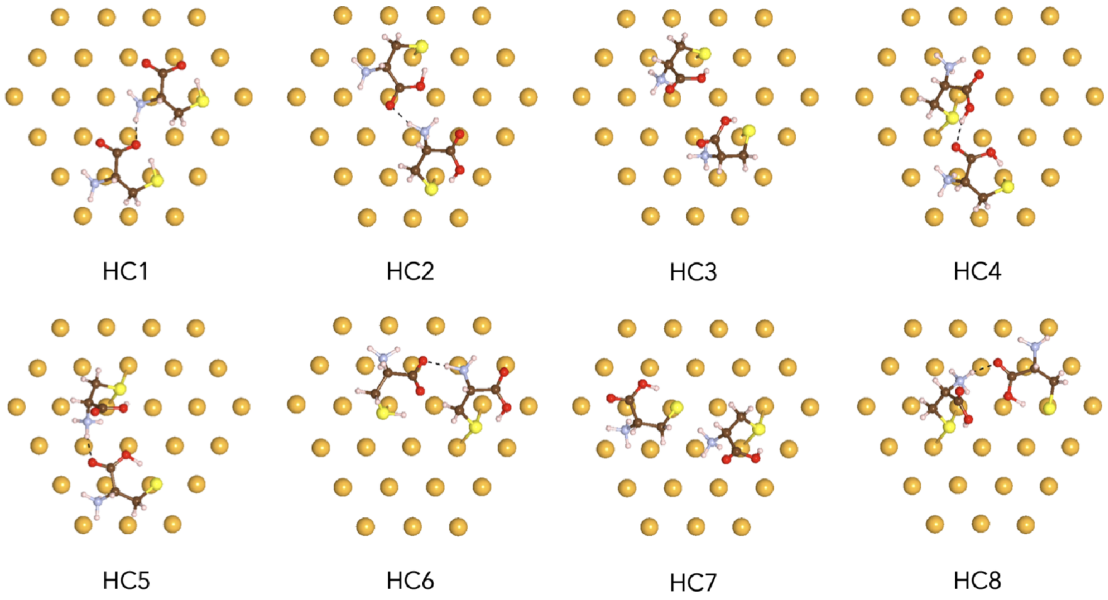


Figure 3. Top views of all clusters investigated in this study. Only the first layer of the gold atoms is represented for clarity. Au atoms are depicted as dark yellow spheres, while S, C, N, O, and H atoms of the cysteine ligands are represented in yellow, brown, blue, red, and white, respectively.

allows the treatment of large systems at a reasonable computational cost.[31] For organic molecules and gold atoms near cysteine molecules, a Slater Type Orbitals (STO) Triple Zeta plus Polarization (TZP) basis set was used with fitting functions optimized for polTDDFT.[32] The remaining gold atoms in the clusters were described using a Double Zeta plus Polarization (DZP) basis set. The simulated ECD spectra were calculated using the Amsterdam Density Functional (ADF) engine within the AMS code. All calculations were carried out at the scalar relativistic level within the Zero-Order Regular Approximation (ZORA) to incorporate relativistic effects, which are crucial for heavy elements such as gold. The ECD spectra were obtained from the imaginary part of the optical rotation tensor, following the formalism detailed in refs 26,27. The photon energies were computed with an imaginary part of ω_i = 0.060 eV, resulting in Lorentzian broadening of the profiles with the same half-width at half-maximum (HWHM).

To bring insight into the nature of the interactions, a fragment analysis of the spectra was investigated. Using this methodology we were able to separate the contributions from metallic atoms and organic molecules on the optical response, enabling a fragment projection analysis as described in refs 33,34.

RESULTS AND DISCUSSION

To ensure the accuracy of the model, in Figure 2, we present an example of the calculated ECD spectrum for the bare gold cluster. The spectrum shows a rather weak signal in the near UV/visible region of interest (250 to 800 nm), with a maximum intensity of 40 $M^{-1}\cdot cm^{-1}$ in absolute value, showing that the cluster itself does not contribute significantly to any chiral optical activity within this range of energy. This is a critical observation, as it establishes a baseline that confirms that any significant ECD activity in the functionalized systems cannot exist without the transfer of chirality from the ligands to the metallic cluster.

In addition, the ECD spectrum calculated for L-cysteine in the gas phase displays a similar chiral response (Figure 2), but only in the UV region around 200 nm, which aligns well with experimental data.[35] Notably, there is no significant ECD activity in the rest of the spectral range explored in this study, further emphasizing the need for a physicochemical interaction between the gold cluster and the organic ligand to observe a chiral response for such systems.

In Figure 3, we illustrate the eight configurations selected for this study, labeled HC1 to HC8. These systems were selected to

https://doi.org/10.1021/acs.jpcc.5c07107
J. Phys. Chem. C XXXX, XXX, XXX−XXX

cover a range of factors that influence their chiroptical properties, including molecular orientation, adsorption site and the presence of intermolecular interactions between the NH_3^+ and COO^- groups.

As previously stated, the configurations were carefully selected from a previous study,[13] which focused on the stability of self-assembled monolayers of the acidic form of L-cysteine on the gold (111) surface. In that work, we investigated how variations in surface arrangement affect the structural stability of the system. In contrast, the present study shifts the focus toward understanding how these same properties influence the optical activity, with particular emphasis on chiroptical responses. Table 1 summarizes the differences in structural properties for all

Table 1. Summary of Structural Properties for the $Au_{64}(cys)_2$ Conformations[a]

system	H bond (Å)	adsorption site (S_1/S_2)	S···H bond (S_1/S_2)	molecular orientation
HC1	yes (1.619)	top/top	yes/yes	clockwise/clockwise
HC2	yes (1.779)	top/top	no/no	clockwise/counterclockwise
HC3	no	top/top	no/no	clockwise/counterclockwise
HC4	yes (1.691)	bridge/top	no/no	clockwise/clockwise
HC5	yes (1.752)	bridge/top	no/no	counterclockwise/clockwise
HC6	yes (1.542)	bridge/top	no/yes	clockwise/clockwise
HC7	no	bridge/top	no/no	clockwise/counterclockwise
HC8	yes (1.766)	bridge/top	no/no	clockwise/counterclockwise

[a]The table reports hydrogen bond presence (and length), adsorption site, presence of SH bonds, and molecular orientation for all cluster.

$Au_{64}(cys)_2$ conformations, while the selected electronic features, such as total dipole moment and charge transfer are detailed in Table 1 of Supporting Information.

Photoabsorption Spectra. The calculated UV photoabsorption spectra for the eight gold cluster−ligand complexes are shown in Figure 4. Each spectrum features a prominent absorption band in the UV range (200−400 nm), followed by a gradual decrease in oscillator strength toward the visible and near-infrared region (400−800 nm). Such behavior is characteristic of small gold nanoclusters, where localized surface plasmon

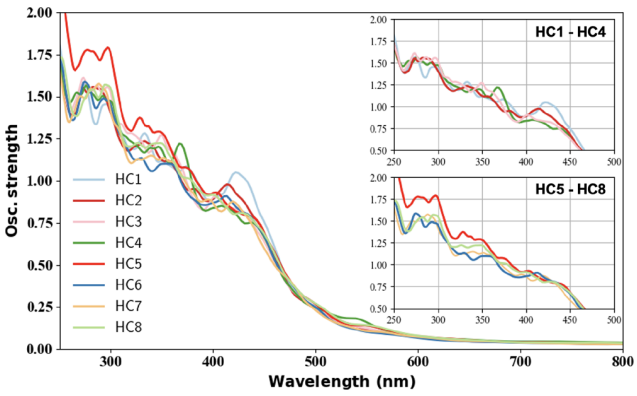


Figure 4. Photoabsorption spectra of all protected gold clusters investigated (HC1 to HC8). Inserts show a zoom between 250 and 500 nm.

resonances are generally weak and the absorption is dominated by ligand-to-metal charge transfer and metal-centered transitions. The rapid drop in intensity beyond 500 nm further supports the notion that purely plasmonic effects do not play a major role in these systems. This finding aligns with expectations, as the ECD technique is highly sensitive to model size, and the dimensions of our clusters are too small to support plasmonic behavior. The fact that the functionalized gold clusters investigated in this study do not show plasmonic resonance behavior permits us to assess other ways of tuning the chiroptical properties of hybrid systems defined by a chiral molecule at the surface of an achiral nanoparticle, or in this study, small metallic clusters.

Among the complexes, HC5 (red curve) shows the strongest absorption at shorter wavelengths (~200−350 nm), suggesting a particularly strong charge-transfer interaction between the ligand and the cluster core. HC1 (light blue curve) also show distinct behavior with a stronger absorption at 425 nm. By contrast, the rest of the set of complexes appears more uniform, indicating fewer structural or electronic differences. Subtler variations in peak positions and intensities across the other complexes likely arise from differences in binding mode, or local geometry at the cluster surface.

Effect of Molecular Orientation. In the present study, we begin by analyzing the influence of the molecular orientation of the ligands. This is examined by comparing the orientation of the ligands onto the surface, which can be defined either in a "clockwise" or "counterclockwise" orientation. The terms "clockwise" and "counterclockwise" refer to the carbon skeleton arrangement of the cysteine molecules relative to their adsorption on the gold surface, where the backbone path is defined from the SH group to the COOH group from a top view: in the "clockwise" orientation, the cysteine backbone follows a right-handed turn, while in the "counterclockwise" orientation, it follows a left-handed turn.

We first compare systems HC5 and HC8, which both feature one cysteine in a clockwise orientation and the other in a counterclockwise orientation (see Table 1). However, the specific cysteine molecules adopting these orientations differ between the two systems. In HC5, the cysteine molecule adsorbed on the bridge site adopts a "counterclockwise" orientation, while the cysteine molecule adsorbed on the top site adopts a clockwise orientation. In contrast, in HC8, the molecular orientations are reversed: the cysteine on the bridge site adopts a clockwise orientation, and the cysteine on the top site adopts an counterclockwise orientation. This results in a complete inversion of the global molecular orientation between HC5 and HC8, creating an enantiomeric molecular arrangement. To further investigate the impact of changes in molecular orientation, we then examine systems HC4 and HC5. These systems differ more subtly: in HC4, one cysteine adopts a clockwise orientation and the other a counterclockwise orientation, while in HC5, both cysteine molecules are oriented in the clockwise direction (see Figure S1).

The calculated spectra of HC5 and HC8 shown in Figure 5 reveal several distinct spectral features across all the energy range explored (from 250 to 800 nm). At first glance we see a complete mirror image spectra when comparing these two systems. In the higher-energy region (250−400 nm), both spectra display alternating positive and negative peaks with comparable intensities, but opposite signs. In the intermediate region (400−600 nm), a dominant feature appears near 500 nm in both systems; once again, its sign is inverted. Finally, in the lower-

https://doi.org/10.1021/acs.jpcc.5c07107
J. Phys. Chem. C XXXX, XXX, XXX−XXX

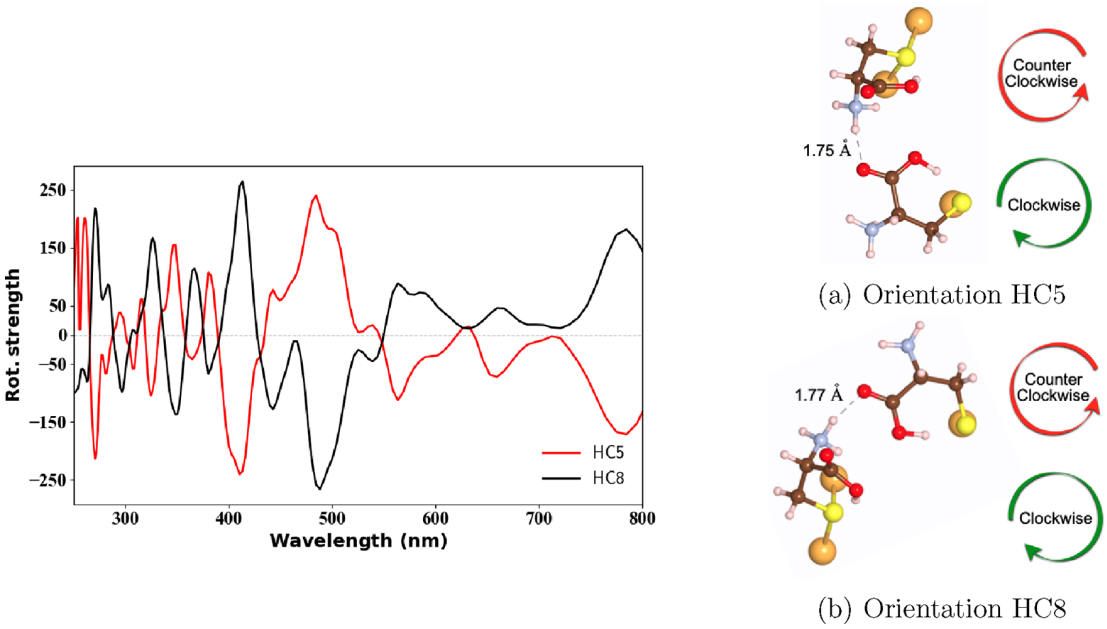


Figure 5. Calculated ECD spectra of gold clusters HC5 (red) and HC8 (black). (a, b) Illustrate the structural configurations of the cysteine ligands in HC5 and HC8, respectively, highlighting the influence of molecular orientation (backbone chain adopting a clockwise or counterclockwise arrangement) on the observed ECD signals.

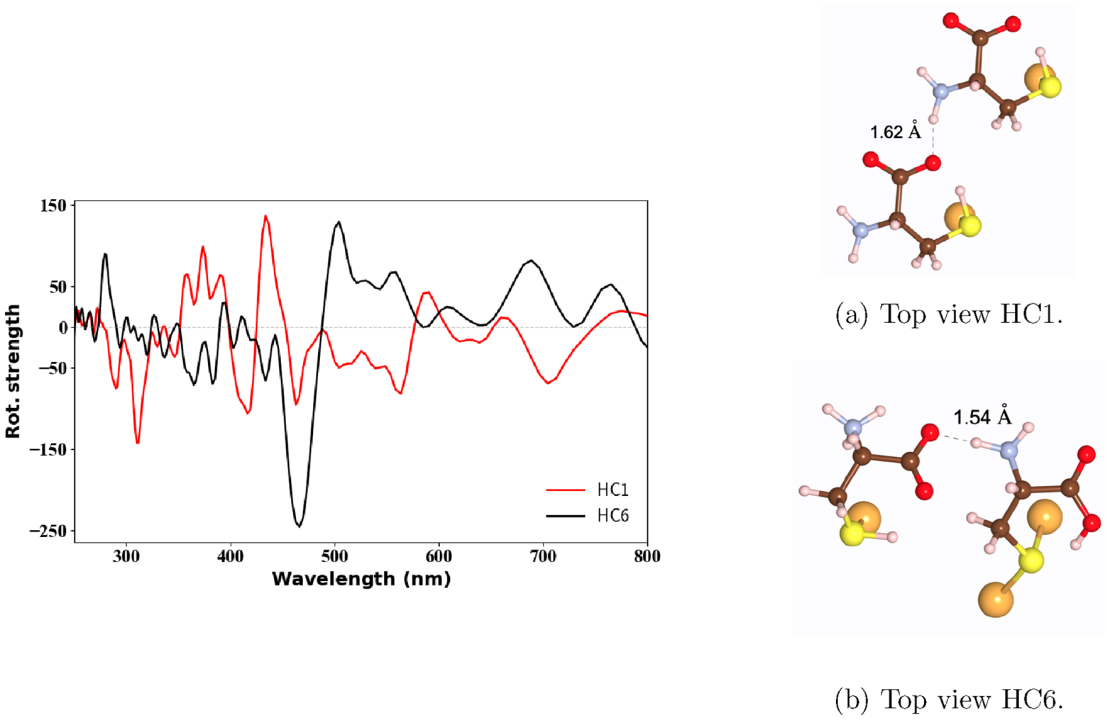


Figure 6. Calculated ECD spectra of gold clusters HC1 (red) and HC6 (black). (a, b) Illustrate the structural configurations of the cysteine ligands in HC1 and HC6, respectively, highlighting the influence of molecular adsorption (top or bridge) on the observed ECD signals.

energy range (600−800 nm), the signals are less pronounced, yet still exhibit opposite polarity of the bands. Such sign inversions are closely tied to the molecular arrangement of the cysteine ligands on the gold cluster. Although HC5 and HC8 share similar hydrogen-bonding distances (1.75 Å in HC5 vs 1.77 Å in HC8), and comparable charge transfer from the ligands to the gold surface (HC5:0.614 |e|; HC8:0.605 |e|), their global ligand orientations differ, creating an enantiomeric molecular arrangement that can be observed by the opposite direction of their permanent dipole moment vectors (see Table S1 available in the Supporting Information).

It is important to note that the permanent dipole moment itself does not directly dictate chiroptical properties; rather, the relevant factors are the electric and magnetic transition dipole moments associated with electronic excitations. However, the permanent dipole moment can serve as an indicator of the global

https://doi.org/10.1021/acs.jpcc.5c07107
J. Phys. Chem. C XXXX, XXX, XXX−XXX

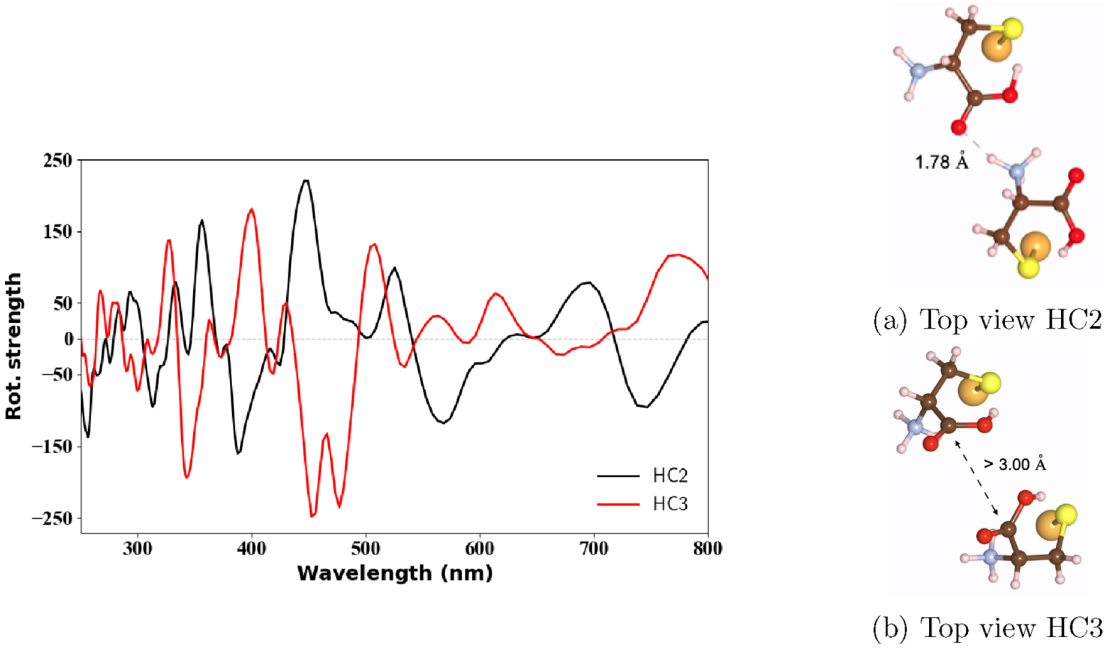


Figure 7. Calculated ECD spectra of gold clusters HC2 (black) and HC3 (red). (a, b) Illustrate the structural configurations of the cysteine ligands in HC2 and HC3, respectively, highlighting the influence of hydrogen bonding on the observed ECD signals.

molecular geometry. If changes in orientation lead to a drastic chiral inversion—i.e., producing an enantiomeric configuration—then the ECD signals become inverted accordingly. This phenomenon has been widely discussed in studies on plasmonic and molecular chirality, where even subtle geometric rearrangements can induce significant shifts or sign inversions in ECD spectra. In the present systems, the orientation of cysteine ligands fully changes the chiral environment to the point of inverting the entire ECD spectra.

A similar observation arises when comparing HC4 and HC5 (Figure S1). In that case, the top-position ligand remains the same, but the bridge-position ligand is inverted and reoriented into a "clockwise" orientation in HC4. Interestingly, in that case, the overall dipole moment does not invert; yet, certain regions of the ECD spectrum (particularly around 400−500 nm) exhibit nearly perfect sign inversion, underscoring how specific transitions can be highly sensitive to local structural changes. Outside this spectral region, the sign does not invert entirely, indicating that only certain electronic states, and their associated transition moments, are significantly perturbed.

Effect of Adsorption Site. Next, we investigate the effect of the adsorption site by comparing systems HC1 and HC6. These two configurations feature different adsorption sites (top/top vs top/bridge) but exhibit similar types of interactions between the cysteine molecules, including the formation of an SH bond and intermolecular interactions between the COO^- and NH_3^+ groups. Additionally, both systems present the same molecular orientation. The specific adsorption site of the ligands on a metallic surface also modulates local electronic environments, affecting the electric and magnetic transition dipole moments in subtle yet impactful ways. The corresponding ECD spectra of systems HC1 and HC6 is shown in Figure 6.

In HC1, both cysteine ligands occupy top (T) adsorption sites on the gold cluster (TT), maintaining an intermolecular hydrogen bond of 1.62 Å. In contrast, HC6 places one cysteine in a top site and the other in a bridge site (TB), shortening the hydrogen bond distance to 1.54 Å. This change in adsorption site disrupts the more symmetrical arrangement found in HC1 and modifies the local electronic environment around each ligand.

A comparison of the ECD spectra (Figure 6) shows that both systems feature multiple peaks in the energetic region of interest, but their intensities and signs differ in several key areas. More pronounced differences appear between 350 and 600 nm, where a clear sign inversion occurs but is shifted: HC1 shows a strong positive band around 420 nm, while HC6 displays a prominent negative feature near 460 nm. This shift in both wavelength and sign suggests that moving one ligand from a top to a bridge site alters the orientation and energies of the electronic transitions, likely by changing the ligand−metal bonding network and redistributing frontier molecular orbitals. In the 500−600 nm region, a clear sign inversion is observed, but with differences in intensities, with the ECD signal arising from system HC6 being twice as intense as for system HC1.

Beyond 600 nm, the rotational strengths gradually decrease, but still showcase shifted sign inversion. Overall, transitioning from a TT (HC1) to a TB (HC6) configuration breaks the higher symmetry present in HC1, thereby reshaping the chiroptical response. Notably, the intense peaks near 420 nm in HC1 and 460 nm in HC6 not only highlight this sensitivity but also differ markedly in magnitude, with the 460 nm peak in HC6 reaching nearly twice the intensity of the 420 nm peak (approximately 250 versus 150 in absolute values). The sign inversion observed between 500 and 600 nm also comes with a significant difference in intensity, with system HC6 showing twice the intensity of HC1. This difference in intensities is likely correlated to the electronic density being more spread out when the ligand is adsorbed into a bridge position rather than a top one.

Effect of Intramolecular Interactions. And finally, we explore the role of intermolecular interactions, specifically hydrogen bonding, on the chiroptical properties by analyzing systems HC2 and HC3 (also HC7 and HC8, see Figure S2). These systems are designed to probe how the presence and

https://doi.org/10.1021/acs.jpcc.5c07107
J. Phys. Chem. C XXXX, XXX, XXX−XXX

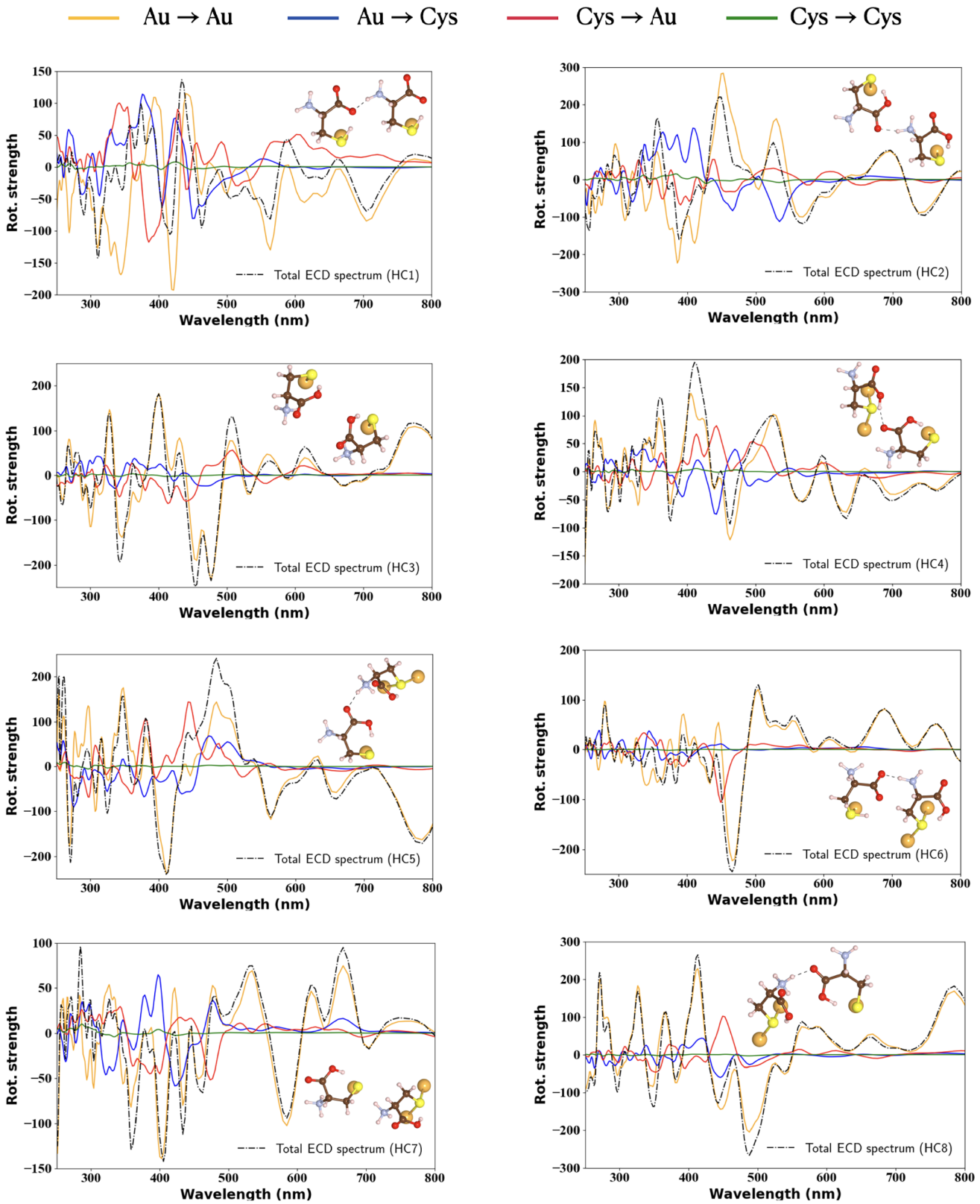


Figure 8. Fragment analysis of the calculated ECD spectrum for conformations HC1−HC8. Contributions from the gold and cysteine molecular orbitals (initial → final states) to the chiroptical response are delineated with distinct colored lines, while the overall spectrum is depicted by a dashed black line.

strength of hydrogen bonds between the cysteine molecules influence the chiroptical response.

Both HC2 and HC3 systems exhibit similar dipole moment vectors and total energies. However, they differ in the nature of

https://doi.org/10.1021/acs.jpcc.5c07107
J. Phys. Chem. C XXXX, XXX, XXX−XXX

the intermolecular interactions between the ligands. Specifically, HC2 displays a hydrogen bond of 1.78 Å, while HC3 shows no direct interaction between the two ligands, with the minimum distance between them exceeding 3 Å. Both systems exhibit similar absorption profiles, indicating that their electronic transitions involving the metallic core remain largely unchanged; however, their ECD spectra reveals differences, particularly in the wavelength regions between 350 and 500 nm, where HC2 shows distinct sign inversions with similar intensities in the rotational strength compared to HC3, as shown in Figure 7.

This inversion suggests that even subtle intermolecular interactions, such as a simple hydrogen bond, can significantly influence the chiroptical response. It is known that hydrogen bonds can highly influence the relative stability of adsorbed layers, in this study we also show that H-bonds can also modulate the electronic structure, thereby shaping the optical response of protected gold clusters.

Systems HC7 and HC8 have also been compared and the corresponding spectra can be found in Figure S2. These 2 systems showcase the same adsorption sites (top-bridge in this case) but HC7 is oriented such as no intermolecular bond is observed between the 2 ligands, in contrast with HC8. Their ECD spectra also present sign inversions between 350 and 600 nm but with significant differences in intensities, with HC8 having a much more intense ECD response than HC7.

Fragment Analysis. Overall, in all cases, the most relevant spectral region lies below 600 nm, where the most intense peaks and the clearest sign inversions occur. Notably, this behavior can be directly linked to the photoabsorption spectra in Figure 4, where the first absorption signal gradually emerges after around 600 nm. Since an ECD signal is still present beyond this threshold, it is interesting to determine its origin. Therefore, to further evaluate the mechanism of chirality transfer from the organic molecule to the gold cluster, we analyzed the contributions of gold (fragment 1) and cysteine (fragment 2) molecular orbitals to the spectral features. Using the fragment analysis tool in AMS, we identified which molecular orbitals participate in the transitions observed in the overall ECD spectrum. The fragment analysis spectra for all systems are presented in Figure 8.

Across all eight conformations (HC1−HC8), the fragment analysis of the calculated ECD spectra reveals that the dominant contributions generally arise from metal−metal (Au → Au) transitions (yellow lines). By contrast, transitions involving only the cysteine orbitals (Cys → Cys) (green lines) are negligible, which aligns well with the fact that organic molecules typically absorb at higher energies (below 200 nm) and their occupied molecular orbitals lie significantly lower than those of gold. Nevertheless, there is clear evidence of chirality transfer between the organic ligands and the metal cluster in every system, as indicated by the Au → Cys (blue lines) and Cys → Au (red lines) components. These transitions correspond to ligand-to-metal charge transfer (LMCT) contributions, in which electron density is transferred from the ligand orbitals to the gold cluster. Conversely, transitions where the electron density remains primarily on the metal atoms are considered metal-centered excitations. Interestingly, these transitions involving both gold and cysteine no longer contribute to the overall ECD spectra after 600 nm, leaving only the gold MOs to be at the origin of the optical activity. It is important to keep in mind that while the Au−Au contributions appear dominant in this spectral region, the bare gold cluster itself is intrinsically achiral. Their chiral response arises entirely from the perturbation induced by the attached chiral ligands, representing the effect of chirality transfer from the ligand to the cluster.

In HC3, HC6 and HC8, 3 systems that do not present significant resemblance, the ECD signal is dominated by strong Au → Au transitions, whereas in other systems, the metal−ligand coupling plays a more substantial role. Notably, HC1 exhibits a pronounced ligand-to-metal contribution, particularly around 370 nm, where Cys → Au transitions drive an intense positive band. At lower energies, the interplay of Au → Au, Au → Cys, and Cys → Au components can either dampen or enhance the net rotational strength; for instance, at 450 nm, these contributions nearly cancel each other out, yielding a near-zero signal. By contrast, HC5 and HC8, which feature a complete inversion of the ECD response compared to other systems, show that this reversal is predominantly due to metal-centered (Au → Au) transitions. The Au → Cys and Cys → Au terms largely cancel one another over most of the spectral range, resulting in negligible ligand−metal influence beyond 500 nm. Finally, comparing HC2 (with a strong hydrogen bond) and HC3 (no H-bond) demonstrates that intermolecular interactions can intensify chirality transfer; in HC2, the ligand orbitals contribute more significantly to the overall ECD than in HC3, highlighting how hydrogen bonding can amplify metal−ligand coupling and thus modulate the chiroptical properties. This is however contrasted by comparing HC7 and HC8 were the H bond seems to have no direct effect on the shape nor intensity of the Au → Cys and Cys → Au contributions.

CONCLUSIONS

In summary, this study provides a comprehensive computational exploration of the chiroptical properties of L-cysteine-functionalized gold(111) cluster models using time-dependent density functional theory (TD-DFT). Our findings highlight the critical role of ligand orientation, adsorption site, and intermolecular interactions in modulating the electronic circular dichroism response. The analysis of molecular configurations confirms that ligand-induced chirality transfer is the primary mechanism governing chiroptical behavior, with structural and electronic factors playing a significant role. Furthermore, fragment projection analysis emphasizes the contributions of ligand-to-metal charge transfer and metal-centered transitions in shaping the overall optical activity.

ASSOCIATED CONTENT

Supporting Information

The Supporting Information is available free of charge at https://pubs.acs.org/doi/10.1021/acs.jpcc.5c07107.

Characterization data for all systems; the structural and electronic analysis of all systems investigated in this study; and the additional ECD spectra discussed in the text (PDF)

AUTHOR INFORMATION

Corresponding Authors

Mary Tabut − *CNRS, Laboratoire de Chimie Théorique, LCT and CNRS, MONARIS, CNRS-UMR 8233, Sorbonne Université, F-75005 Paris, France;* orcid.org/0009-0005-4253-8030; Email: mary.tabut@sorbonne-universite.fr

Daniele Toffoli − *Department of Chemical and Pharmaceutical Sciences, University of Trieste, 34127 Trieste, Italy;* orcid.org/0000-0002-8225-6119; Email: toffoli@units.it

https://doi.org/10.1021/acs.jpcc.5c07107
J. Phys. Chem. C XXXX, XXX, XXX−XXX

Authors

Pierpaolo D'Antoni − *Department of Chemical and Pharmaceutical Sciences, University of Trieste, 34127 Trieste, Italy*

Mauro Stener − *Department of Chemical and Pharmaceutical Sciences, University of Trieste, 34127 Trieste, Italy;* orcid.org/0000-0003-3700-7903

Caroline Salzemann − *CNRS, MONARIS, CNRS-UMR 8233, Sorbonne Université, F-75005 Paris, France;* orcid.org/0009-0005-2308-7107

Monica Calatayud − *CNRS, MONARIS, CNRS-UMR 8233, Sorbonne Université, F-75005 Paris, France;* orcid.org/0000-0003-0555-8938

Complete contact information is available at: https://pubs.acs.org/10.1021/acs.jpcc.5c07107

Notes

The authors declare no competing financial interest.

■ ACKNOWLEDGMENTS

This research received partial funding from the French National Research Agency (ANR) through the project ANR-22-CE09-0007. We gratefully acknowledge financial support from the Initiative Sciences et Ingénierie Moléculaires (iSiM) at Sorbonne Université. This project was provided with computing HPC and storage resources by GENCI at IDRIS thanks to the grant 2025-802131 on the supercomputer Jean Zay CSL/V100 partition. Financial support from ICSC—Centro Nazionale di Ricerca in High Performance Computing, Big Data and Quantum Computing, funded by European Union—NextGenerationEU is gratefully acknowledged.

■ REFERENCES

(1) Chen, H.; Hao, C. Recent Advances in Chiral Gold Nanomaterials: From Synthesis to Applications. *Molecules* **2025**, *30*, 829.

(2) Warning, L. A.; Miandashti, A. R.; McCarthy, L. A.; Zhang, Q.; Landes, C. F.; Link, S. Nanophotonic approaches for chirality sensing. *ACS Nano* **2021**, *15*, 15538−15566.

(3) Carone, A.; Mariani, P.; Désert, A.; Parola, S. Colloidal Assemblies of Chiral Plasmonic Nanoparticles Induce Tunable Circular Dichroism Response. *Adv. Opt. Mater.* **2023**, *11*, No. 2300119.

(4) Wang, S.; Liu, X.; Mourdikoudis, S.; Chen, J.; Fu, W.; Sofer, Z.; Zhang, Y.; Zhang, S.; Zheng, G. Chiral Au nanorods: synthesis, chirality origin, and applications. *ACS Nano* **2022**, *16*, 19789−19809.

(5) Zheng, Y.; Wang, Q.; Sun, Y.; Huang, J.; Ji, J.; Wang, Z.; Wang, Y.; Chen, H. Chiral active surface growth via glutathione control. *Adv. Opt. Mater.* **2023**, *11*, No. 2202858.

(6) Khalfaoui-Hassani, N.; Tabut, M.; Awe, N. H.; Desmarets, C.; Toffoli, D.; Stener, M.; Goubet, N.; Calatayud, M.; Salzemann, C. The intriguing role of L-cysteine in the modulation of chiroplasmonic properties of chiral gold nano-arrows. *Nanoscale* **2025**, *17*, 3973−3982.

(7) Román-Velázquez, C. E.; Noguez, C.; Garzón, I. L. Circular dichroism simulated spectra of chiral gold nanoclusters: a dipole approximation. *J. Phys. Chem. B* **2003**, *107*, 12035−12038.

(8) Qian, H.; Eckenhoff, W. T.; Zhu, Y.; Pintauer, T.; Jin, R. Total structure determination of thiolate-protected Au38 nanoparticles. *J. Am. Chem. Soc.* **2010**, *132*, 8280−8281.

(9) Lopez-Acevedo, O.; Tsunoyama, H.; Tsukuda, T.; Hakkinen, H.; Aikens, C. M. Chirality and electronic structure of the thiolate-protected Au38 nanocluster. *J. Am. Chem. Soc.* **2010**, *132*, 8210−8218.

(10) Barrabés, N.; Zhang, B.; Bürgi, T. Racemization of chiral Pd2Au36 (SC2H4Ph) 24: doping increases the flexibility of the cluster surface. *J. Am. Chem. Soc.* **2014**, *136*, 14361−14364.

(11) Baseggio, O.; Toffoli, D.; Fronzoni, G.; Stener, M.; Sementa, L.; Fortunelli, A. Extension of the time-dependent density functional complex polarizability algorithm to circular dichroism: Implementation and applications to Ag8 and Au38 (SC2H4C6H5) 24. *J. Phys. Chem. C* **2016**, *120*, 24335−24345.

(12) Karoń, K.; Łapkowski, M.; Dobrowolski, J. C. ECD spectroelectrochemistry: A review. *Spectrochimica Acta Part A: Molecular and Biomolecular Spectroscopy* **2021**, *250*, No. 119349.

(13) Tabut, M.; Stishenko, P. V.; Calatayud, M. Modeling the self-assembly of L-cysteine molecules on the Au (111) surface: A lattice model approach. *Surf. Sci.* **2025**, *757*, No. 122740.

(14) Longo, E.; Orlandin, A.; Mancin, F.; Scrimin, P.; Moretto, A. Reversible chirality control in peptide-functionalized gold nanoparticles. *ACS Nano* **2013**, *7*, 9933−9939.

(15) Monti, M.; Matus, M. F.; Malola, S.; Fortunelli, A.; Aschi, M.; Stener, M.; Häkkinen, H. What contributes to the measured chiral optical response of the glutathione-protected Au25 nanocluster? *ACS Nano* **2023**, *17*, 11481−11491.

(16) Monti, M.; Brancolini, G.; Coccia, E.; Toffoli, D.; Fortunelli, A.; Corni, S.; Aschi, M.; Stener, M. The conformational dynamics of the ligands determines the electronic circular dichroism of the chiral Au38 (SC2h4Ph) 24 cluster. *J. Phys. Chem. Lett.* **2023**, *14*, 1941−1948.

(17) Baghdasaryan, A.; Martin, K.; Lawson Daku, L. M.; Mastropasqua Talamo, M.; Avarvari, N.; Bürgi, T. Ligand exchange reactions on the chiral Au 38 cluster: CD modulation caused by the modification of the ligand shell composition. *Nanoscale* **2020**, *12*, 18160−18170.

(18) Kresse, G.; Furthmüller, J. Efficiency of ab-initio total energy calculations for metals and semiconductors using a plane-wave basis set. *Computational materials science* **1996**, *6*, 15−50.

(19) Kresse, G.; Furthmüller, J. Efficient iterative schemes for ab initio total-energy calculations using a plane-wave basis set. *Phys. Rev. B* **1996**, *54*, 11169.

(20) Perdew, J. P.; Burke, K.; Ernzerhof, M. Generalized gradient approximation made simple. *Physical review letters* **1996**, *77*, 3865.

(21) Rosa, M.; Corni, S.; Di Felice, R. Waals effects at molecule-metal interfaces. *Phys. Rev. B* **2014**, *90*, No. 125448.

(22) Grimme, S.; Antony, J.; Ehrlich, S.; Krieg, H. A consistent and accurate ab initio parametrization of density functional dispersion correction (DFT-D) for the 94 elements H-Pu. *J. Chem. Phys.* **2010**, *132*, 154104.

(23) Blöchl, P. E. *Projector augmented-wave method. Physical review B* **1994**, *50*, 17953.

(24) Monkhorst, H. J.; Pack, J. D. Special points for Brillouin-zone integrations. *Phys. Rev. B* **1976**, *13*, 5188.

(25) Momma, K.; Izumi, F. VESTA 3 for three-dimensional visualization of crystal, volumetric and morphology data. *Journal of applied crystallography* **2011**, *44*, 1272−1276.

(26) Baseggio, O.; Toffoli, D.; Fronzoni, G.; Stener, M.; Sementa, L.; Fortunelli, A. Extension of the Time-Dependent Density Functional Complex Polarizability Algorithm to Circular Dichroism: Implementation and Applications to Ag8 and Au38(SC2H4C6H5)24. *J. Phys. Chem. C* **2016**, *120*, 24335−24345.

(27) Baseggio, O.; Fronzoni, G.; Stener, M. A new time dependent density functional algorithm for large systems and plasmons in metal clusters. *J. Chem. Phys.* **2015**, *143*, No. 024106.

(28) Medves, M.; Sementa, L.; Toffoli, D.; Fronzoni, G.; Fortunelli, A.; Stener, M. An efficient hybrid scheme for time dependent density functional theory. *J. Chem. Phys.* **2020**, *152*, 184104.

(29) Becke, A. D. Density-functional thermochemistry. III. The role of exact exchange. *J. Chem. Phys.* **1993**, *98*, 5648−5652.

(30) Stephens, P. J.; Devlin, F. J.; Chabalowski, C. F.; Frisch, M. J. Ab initio calculation of vibrational absorption and circular dichroism spectra using density functional force fields. *J. Phys. Chem.* **1994**, *98*, 11623−11627.

(31) D'Antoni, P.; Medves, M.; Toffoli, D.; Fortunelli, A.; Stener, M.; Visscher, L. A resolution of identity technique to speed up TDDFT with hybrid functionals: Implementation and application to the magic cluster series Au8 n+ 4 (SC6H5) 4 n+ 8 (n= 3−6). *J. Phys. Chem. A* **2023**, *127*, 9244−9257.

(32) Medves, M.; Fronzoni, G.; Stener, M. Optimization of density fitting auxiliary Slater-type basis functions for time-dependent density functional theory. *J. Comput. Chem.* **2022**, *43*, 1923−1935.
(33) Sementa, L.; Barcaro, G.; Baseggio, O.; De Vetta, M.; Dass, A.; Aprà, E.; Stener, M.; Fortunelli, A. Ligand-enhanced optical response of gold nanomolecules and its fragment projection analysis: the case of Au30 (SR) 18. *J. Phys. Chem. C* **2017**, *121*, 10832−10842.
(34) Pelayo, J. J.; Valencia, I.; García, A. P.; Chang, L.; López, M.; Toffoli, D.; Stener, M.; Fortunelli, A.; Garzón, I. L. Chirality in bare and ligand-protected metal nanoclusters. *Advances in Physics: X* **2018**, *3*, 1509727.
(35) Huang, H.; Hu, L.; Sun, Y.; Liu, Y.; Kang, Z.; MacFarlane, D. R. Preparation of chiral graphene oxides by covalent attachment of chiral cysteines for voltammetric recognition of tartrates. *Microchim. Acta* **2019**, *186*, 298.



https://doi.org/10.1021/acs.jpcc.5c07107
J. Phys. Chem. C XXXX, XXX, XXX−XXX

5 Conclusions

The research activity presented in this PhD thesis has been primarily devoted to the development, implementation, and application of advanced computational approaches for the simulation of optical and chiroptical properties of complex systems of large size. Rather than focusing on a specific class of materials or on a single spectroscopic observable, this work has been driven by a broader objective: extending the practical reach of time-dependent density functional theory (TDDFT) to regimes where both physical reliability and computational efficiency are essential.

Within this perspective, the core contribution of this thesis lies in the development and optimization of the RI–HDA framework within the polarization-based TDDFT (polTDDFT) formalism. Building upon established theoretical foundations, this work has addressed one of the main bottlenecks limiting the use of hybrid TDDFT methods for extended molecular and nanoscale systems, namely the computational cost associated with the calculation of exact exchange within the Hybrid Diagonal Approximation. By introducing a resolution-of-identity strategy for the evaluation of the HDA correction, a substantial reduction in computational effort has been achieved, enabling the treatment of systems that would otherwise be computationally inaccessible within a hybrid functional framework [177, 178].

Standing on the shoulders of existing theoretical and algorithmic advances, this thesis has sought not only to improve numerical efficiency, but also to preserve the physical reliability of the computed spectra. The performance of the fitted RI–HDA approach has been assessed on representative systems of increasing size and complexity, showing that the essential spectral features obtained from full hybrid TDDFT calculations are retained while achieving a significant gain in computational efficiency. In this way, the RI–HDA strategy developed here constitutes a general and scalable computational framework for the investigation of optical and chiroptical properties in large-scale systems.

A further major contribution of this work is the extension of the RI–HDA framework to Range-Separated hybrid functionals. Range-separated schemes are known to play a crucial role in the accurate description of charge-transfer excitations and long-range electronic effects, which are often central in chiroptical phenomena. However, their high computational cost has traditionally restricted their application to relatively small systems. By adapting and validating the fitted RI–HDA approach in combination with range-separated functionals such as CAMY-B3LYP, this thesis has significantly broadened the scope of applicability

of polTDDFT, making it possible to address complex molecular systems where long-range effects are essential to reproduce and interpret experimental optical responses [185].

Alongside this methodological and algorithmic development, the computational tools constructed in this work have been employed to address concrete physical questions, serving both as validation cases and as opportunities to extract physical insight. In this spirit, the study of chiral gold and alloyed nanowires, investigated through polTDDFT calculations of their plasmonic ECD response, has provided a clear example of how advanced TDDFT-based approaches can be used to rationalize non-trivial spectroscopic behavior [186]. Despite the simultaneous presence of chirality and plasmonic character, these systems were found to exhibit a strongly quenched ECD signal at the plasmon resonance. A detailed analysis of the excited-state manifold revealed that this behavior originates from destructive interference among nearly isoenergetic electronic excitations, highlighting the collective nature of the plasmonic response and its sensitivity to symmetry and electronic coupling.

The same computational framework was then applied to ligand-protected metal systems, where chirality is induced by the adsorption of chiral molecules on an otherwise achiral metallic substrate. In the investigation of L-cysteine–functionalized gold clusters, carried out in collaboration with M. Tabut and co-workers, the interplay between molecular orientation, adsorption geometry, and intermolecular interactions was systematically analyzed by means of polTDDFT calculations and fragment-resolved spectral analysis [187]. These studies demonstrated that the chiroptical response does not arise as a simple additive contribution of metal and ligands, but rather emerges from subtle metal–ligand electronic coupling and symmetry breaking at the interface.

In addition, this thesis has contributed to the development and application of multiscale computational strategies for chiroptical spectroscopy. Through a collaborative effort combining complementary expertise, a hybrid approach was developed in which a quantum-mechanical TDDFT description of a chiral molecular system was coupled to a continuum representation of a metallic nanoparticle within a PCM framework. This strategy, developed in collaboration with L. Biancorosso and co-workers, enabled the investigation of plasmon-enhanced chiroptical effects in a computationally affordable yet physically meaningful manner [188]. In this context, the technical contributions presented in this thesis were instrumental in enabling a genuinely multiscale study, bridging molecular electronic structure and nanoscale electromagnetic response within a unified computational framework.

Taken together, the works presented in this thesis outline a coherent research path in which algorithmic development, computational efficiency, and physical interpretation proceed hand in hand. Despite the diversity of the systems investigated, a common physical theme emerges: chiroptical signals are governed by delicate interference effects among electronic excitations, which can be either suppressed or enhanced depending on symmetry, electronic structure, and coupling across different length scales. The computational approaches developed here

are specifically designed to capture such effects in large and complex systems, where simpler models or lower-level approximations would fail.

In conclusion, the main outcome of this PhD project has been the construction, validation, and dissemination of computational frameworks and algorithmic tools for the simulation of optical and chiroptical properties of complex systems. Beyond the specific case studies presented, this work provides transferable approaches that extend the applicability polTDDFT to new classes of problems.

Bibliography

(1) Papadopoulos, P. Friedrich Siebert and Peter Hildebrandt, vibrational spectroscopy in life science. *Colloid and Polymer Science* **2008**, *286*, DOI: 10.1007/s00396-007-1816-4.

(2) Slund, A.; Rigler, R.; Widengren, J. *Single Molecule Spectroscopy in Chemistry, Physics and Biology*; Springer Series in Chemical Physics, 96; Springer: 2010.

(3) Laane, J. Frontiers of molecular spectroscopy. *Elsevier* **2009**.

(4) Quack, M. In *Handbook of High-Resolution Spectroscopy*, Quack, M., Merkt, F., Eds.; Wiley: Chichester, 2011; Vol. 1, pp 659–722.

(5) Barone, V. The virtual multifrequency spectrometer: a new paradigm for spectroscopy. *WIREs Computational Molecular Science* **2016**, *6*, 86–110.

(6) Ryczkowski, J. IR spectroscopy in catalysis. *Catalysis Today* **2001**, *68*, IR Spectroscopy in Catalysis, 263–381.

(7) Baron, A. Q. Introduction to high-resolution inelastic x-ray scattering. *arXiv preprint arXiv:1504.01098* **2015**.

(8) Hippert, F.; Geissler, E.; Hodeau, J. L.; Lelièvre-Berna, E.; Regnard, J.-R. *Neutron and X-ray Spectroscopy*; Springer Science & Business Media: 2006.

(9) Ullrich, C. A.; Vignale, G. Theory of the Linewidth of Intersubband Plasmons in Quantum Wells. *Phys. Rev. Lett.* **2001**, *87*, 037402.

(10) Weissker, H.-C.; Serrano, J.; Huotari, S.; Bruneval, F.; Sottile, F.; Monaco, G.; Krisch, M.; Olevano, V.; Reining, L. Signatures of Short-Range Many-Body Effects in the Dielectric Function of Silicon for Finite Momentum Transfer. *Phys. Rev. Lett.* **2006**, *97*, 237602.

(11) Autschbach, J.; Ziegler, T. Calculating molecular electric and magnetic properties from time-dependent density functional response theory. *The Journal of Chemical Physics* **2002**, *116*, 891–896.

(12) Becke, A. D. Density-functional thermochemistry. III. The role of exact exchange. *The Journal of Chemical Physics* **1993**, *98*, 5648–5652.

(13) Lee, C.; Yang, W.; Parr, R. G. Development of the Colle-Salvetti correlation-energy formula into a functional of the electron density. *Phys. Rev. B* **1988**, *37*, 785–789.

(14) Stephens, P. J.; Devlin, F. J.; Chabalowski, C. F.; Frisch, M. J. Ab initio calculation of vibrational absorption and circular dichroism spectra using density functional force fields. *The Journal of physical chemistry* **1994**, *98*, 11623–11627.

(15) Yanai, T.; Tew, D. P.; Handy, N. C. A new hybrid exchange–correlation functional using the Coulomb-attenuating method (CAM-B3LYP). *Chemical physics letters* **2004**, *393*, 51–57.

(16) Peach, M. J.; Helgaker, T.; Sałek, P.; Keal, T. W.; Lutnæs, O. B.; Tozer, D. J.; Handy, N. C. Assessment of a Coulomb-attenuated exchange–correlation energy functional. *Physical Chemistry Chemical Physics* **2006**, *8*, 558–562.

(17) Casida, M. E. In *Recent Advances in Density Functional Methods*, Chong, D. P., Ed.; World Scientific: 1995, pp 155–192.

(18) Baerends, E. J.; Ellis, D.; Ros, P. Self-consistent molecular Hartree—Fock—Slater calculations I. The computational procedure. *Chemical Physics* **1973**, *2*, 41–51.

(19) {Fonseca Guerra}, C.; Snijders, J.; Velde, G.; Baerends, E. Towards an order-N DFT method. *Theoretical Chemistry Accounts* **1998**, *99*, Journal OCT 139LF THEOR CHEM ACC, 391–403.

(20) van Gisbergen, S.; Snijders, J.; Baerends, E. Implementation of time-dependent density functional response equations. *Computer Physics Communications* **1999**, *118*, 119–138.

(21) Software for Chemistry & Materials Properties Module — ADF Documentation, https://www.scm.com/tools/properties/, Accessed: 2025-11-05, 2025.

(22) Ahlrichs, R.; Bär, M.; Häser, M.; Horn, H.; Kölmel, C. Electronic structure calculations on workstation computers: The program system turbomole. *Chemical Physics Letters* **1989**, *162*, 165–169.

(23) Hirata, S.; Head-Gordon, M. Time-dependent density functional theory within the Tamm–Dancoff approximation. *Chemical Physics Letters* **1999**, *314*, 291–299.

(24) Casida, M. E.; Wesołowski, T. A. Generalization of the Kohn–Sham equations with constrained electron density formalism and its time-dependent response theory formulation. *International journal of quantum chemistry* **2004**, *96*, 577–588.

(25) Neugebauer, J. Couplings between electronic transitions in a subsystem formulation of time-dependent density functional theory. *The Journal of chemical physics* **2007**, *126*.

(26) Ruger, R.; Van Lenthe, E.; Lu, Y.; Frenzel, J.; Heine, T.; Visscher, L. Efficient calculation of electronic absorption spectra by means of intensity-selected time-dependent density functional tight binding. *Journal of chemical theory and computation* **2015**, *11*, 157–167.

(27) Niehaus, T. A.; Suhai, S.; Della Sala, F.; Lugli, P.; Elstner, M.; Seifert, G.; Frauenheim, T. Tight-binding approach to time-dependent density-functional response theory. *Physical Review B* **2001**, *63*, 085108.

(28) Domínguez, A.; Aradi, B.; Frauenheim, T.; Lutsker, V.; Niehaus, T. A. Extensions of the time-dependent density functional based tight-binding approach. *Journal of Chemical Theory and Computation* **2013**, *9*, 4901–4914.

(29) Trani, F.; Scalmani, G.; Zheng, G.; Carnimeo, I.; Frisch, M. J.; Barone, V. Time-dependent density functional tight binding: new formulation and benchmark of excited states. *Journal of Chemical Theory and Computation* **2011**, *7*, 3304–3313.

(30) Porezag, D.; Frauenheim, T.; Köhler, T.; Seifert, G.; Kaschner, R. Construction of tight-binding-like potentials on the basis of density-functional theory: Application to carbon. *Physical Review B* **1995**, *51*, 12947.

(31) Seifert, G.; Porezag, D.; Frauenheim, T. Calculations of molecules, clusters, and solids with a simplified LCAO-DFT-LDA scheme. *International journal of quantum chemistry* **1996**, *58*, 185–192.

(32) Grimme, S. A simplified Tamm-Dancoff density functional approach for the electronic excitation spectra of very large molecules. *The Journal of chemical physics* **2013**, *138*.

(33) Bannwarth, C.; Grimme, S. A simplified time-dependent density functional theory approach for electronic ultraviolet and circular dichroism spectra of very large molecules. *Computational and Theoretical Chemistry* **2014**, *1040*, 45–53.

(34) Rüger, R.; van Lenthe, E.; Heine, T.; Visscher, L. Tight-binding approximations to time-dependent density functional theory — A fast approach for the calculation of electronically excited states. *The Journal of Chemical Physics* **2016**, *144*, 184103.

(35) Havenridge, S.; Rüger, R.; Aikens, C. M. Analytical excited state gradients for time-dependent density functional theory plus tight binding (TDDFT + TB). *The Journal of Chemical Physics* **2023**, *158*, 224103.

(36) Yabana, K.; Bertsch, G. Time-dependent local-density approximation in real time. *Physical Review B* **1996**, *54*, 4484.

(37) Marques, M. A.; Castro, A.; Bertsch, G. F.; Rubio, A. octopus: a first-principles tool for excited electron–ion dynamics. *Computer Physics Communications* **2003**, *151*, 60–78.

(38) Castro, A.; Marques, M. A.; Varsano, D.; Sottile, F.; Rubio, A. The challenge of predicting optical properties of biomolecules: what can we learn from time-dependent density-functional theory? *Comptes Rendus Physique* **2009**, *10*, 469–490.

(39) López-Lozano, X.; Barron, H.; Mottet, C.; Weissker, H.-C. Aspect-ratio-and size-dependent emergence of the surface-plasmon resonance in gold nanorods–an ab initio TDDFT study. *Physical Chemistry Chemical Physics* **2014**, *16*, 1820–1823.

(40) Walker, B.; Saitta, A. M.; Gebauer, R.; Baroni, S. Efficient Approach to Time-Dependent Density-Functional Perturbation Theory<? format?> for Optical Spectroscopy. *Physical review letters* **2006**, *96*, 113001.

(41) Walker, B.; Gebauer, R. Ultrasoft pseudopotentials in time-dependent density-functional theory. *The Journal of chemical physics* **2007**, *127*.

(42) Rocca, D.; Gebauer, R.; Saad, Y.; Baroni, S. Turbo charging time-dependent density-functional theory with Lanczos chains. *The Journal of Chemical Physics* **2008**, *128*.

(43) Baseggio, O.; Fronzoni, G.; Stener, M. A new time dependent density functional algorithm for large systems and plasmons in metal clusters. *The Journal of Chemical Physics* **2015**, *143*.

(44) Baseggio, O.; De Vetta, M.; Fronzoni, G.; Stener, M.; Sementa, L.; Fortunelli, A.; Calzolari, A. Photoabsorption of icosahedral noble metal clusters: an efficient TDDFT approach to large-scale systems. *The Journal of Physical Chemistry C* **2016**, *120*, 12773–12782.

(45) Malola, S.; Lehtovaara, L.; Enkovaara, J.; Hakkinen, H. Birth of the localized surface plasmon resonance in monolayer-protected gold nanoclusters. *Acs Nano* **2013**, *7*, 10263–10270.

(46) Noda, M.; Ishimura, K.; Nobusada, K.; Yabana, K.; Boku, T. Massively-parallel electron dynamics calculations in real-time and real-space: Toward applications to nanostructures of more than ten-nanometers in size. *Journal of Computational Physics* **2014**, *265*, 145–155.

(47) Iida, K.; Noda, M.; Ishimura, K.; Nobusada, K. First-principles computational visualization of localized surface plasmon resonance in gold nanoclusters. *The Journal of Physical Chemistry A* **2014**, *118*, 11317–11322.

(48) Valiev, M.; Bylaska, E. J.; Govind, N.; Kowalski, K.; Straatsma, T. P.; Van Dam, H. J. J.; Wang, D.; Nieplocha, J.; Aprà, E.; Windus, T. L., et al. NWChem: A comprehensive and scalable open-source solution for large scale molecular simulations. *Computer Physics Communications* **2010**, *181*, 1477–1489.

(49) Whetten, R. L.; Khoury, J. T.; Alvarez, M. M.; Murthy, S.; Vezmar, I.; Wang, Z.; Stephens, P. W.; Cleveland, C. L.; Luedtke, W.; Landman, U. Nanocrystal gold molecules. *Advanced materials* **1996**, *8*, 428–433.

(50) Sandomirskiĭ, V. Dependence of the forbidden-band width of semiconducting films on their thickness and temperature. *Soviet Journal of Experimental and Theoretical Physics* **1963**, *16*, 1630.

(51) Stasenko, A. Dependence of Forbidden energy gap in Cadmium Sulfide films on film thickness. *SOVIET PHYSICS SOLID STATE, USSR* **1968**, *10*, 186–+.

(52) Of Sciences, T. R. S. A. They added colour to nanotechnology: Popular Science Background to the Nobel Prize in Chemistry 2023 Illustration © Johan Jarnestad / The Royal Swedish Academy of Sciences, https://www.nobelprize.org/uploads/2023/12/popular-chemistryprize2023-3.pdf.

(53) Bloch, F. Quantum mechanics of electrons in crystal lattices. *Z. Phys* **1928**, *52*, 555–600.

(54) Fröhlich, H. Die spezifische wärme der elektronen kleiner metallteilchen bei tiefen temperaturen. *Physica* **1937**, *4*, 406–412.

(55) Borrelli, N. In *Semiconductor Nanocrystals: From Basic Principles to Applications*; Springer: 2003, pp 1–51.

(56) Efros, A. L.; Brus, L. E. Nanocrystal quantum dots: from discovery to modern development. *ACS nano* **2021**, *15*, 6192–6210.

(57) Murray, C.; Norris, D. J.; Bawendi, M. G. Synthesis and characterization of nearly monodisperse CdE (E= sulfur, selenium, tellurium) semiconductor nanocrystallites. *Journal of the American Chemical Society* **1993**, *115*, 8706–8715.

(58) LaMer, V. K.; Dinegar, R. H. Theory, production and mechanism of formation of monodispersed hydrosols. *Journal of the american chemical society* **1950**, *72*, 4847–4854.

(59) Peng, X.; Manna, L.; Yang, W.; Wickham, J.; Scher, E.; Kadavanich, A.; Alivisatos, A. P. Shape control of CdSe nanocrystals. *Nature* **2000**, *404*, 59–61.

(60) Milliron, D. J.; Hughes, S. M.; Cui, Y.; Manna, L.; Li, J.; Wang, L.-W.; Paul Alivisatos, A. Colloidal nanocrystal heterostructures with linear and branched topology. *Nature* **2004**, *430*, 190–195.

(61) Jin, R.; Li, G.; Sharma, S.; Li, Y.; Du, X. Toward active-site tailoring in heterogeneous catalysis by atomically precise metal nanoclusters with crystallographic structures. *Chemical reviews* **2020**, *121*, 567–648.

(62) Nozik, A. J. Quantum dot solar cells. *Physica E: Low-dimensional Systems and Nanostructures* **2002**, *14*, 115–120.

(63) Gao, J.; Nguyen, S. C.; Bronstein, N. D.; Alivisatos, A. P. Solution-processed, high-speed, and high-quantum-efficiency quantum dot infrared photodetectors. *ACS photonics* **2016**, *3*, 1217–1222.

(64) Abdellatif, A. A.; Younis, M. A.; Alsharidah, M.; Al Rugaie, O.; Tawfeek, H. M. Biomedical applications of quantum dots: overview, challenges, and clinical potential. *International journal of nanomedicine* **2022**, 1951–1970.

(65) Lu, H.; Carroll, G. M.; Neale, N. R.; Beard, M. C. Infrared quantum dots: progress, challenges, and opportunities. *ACS nano* **2019**, *13*, 939–953.

(66) Heaven, M. W.; Dass, A.; White, P. S.; Holt, K. M.; Murray, R. W. Crystal structure of the gold nanoparticle [N (C8H17) 4][Au25 (SCH2CH2Ph) 18]. *Journal of the American Chemical Society* **2008**, *130*, 3754–3755.

(67) Dolamic, I.; Knoppe, S.; Dass, A.; Bürgi, T. First enantioseparation and circular dichroism spectra of Au38 clusters protected by achiral ligands. *Nature communications* **2012**, *3*, 798.

(68) Desireddy, A.; Conn, B. E.; Guo, J.; Yoon, B.; Barnett, R. N.; Monahan, B. M.; Kirschbaum, K.; Griffith, W. P.; Whetten, R. L.; Landman, U., et al. Ultrastable silver nanoparticles. *Nature* **2013**, *501*, 399–402.

(69) Du, Y.; Sheng, H.; Astruc, D.; Zhu, M. Atomically precise noble metal nanoclusters as efficient catalysts: a bridge between structure and properties. *Chemical reviews* **2019**, *120*, 526–622.

(70) Fernando, A.; Weerawardene, K. D. M.; Karimova, N. V.; Aikens, C. M. Quantum mechanical studies of large metal, metal oxide, and metal chalcogenide nanoparticles and clusters. *Chemical reviews* **2015**, *115*, 6112–6216.

(71) Jadzinsky, P. D.; Calero, G.; Ackerson, C. J.; Bushnell, D. A.; Kornberg, R. D. Structure of a thiol monolayer-protected gold nanoparticle at 1.1 A resolution. *science* **2007**, *318*, 430–433.

(72) Akola, J.; Walter, M.; Whetten, R. L.; Häkkinen, H.; Grönbeck, H. On the structure of thiolate-protected Au25. *Journal of the American Chemical Society* **2008**, *130*, 3756–3757.

(73) Qian, H.; Eckenhoff, W. T.; Zhu, Y.; Pintauer, T.; Jin, R. Total structure determination of thiolate-protected Au38 nanoparticles. *Journal of the American Chemical Society* **2010**, *132*, 8280–8281.

(74) Lopez-Acevedo, O.; Tsunoyama, H.; Tsukuda, T.; Hakkinen, H.; Aikens, C. M. Chirality and electronic structure of the thiolate-protected Au38 nanocluster. *Journal of the American Chemical Society* **2010**, *132*, 8210–8218.

(75) Zeng, C.; Qian, H.; Li, T.; Li, G.; Rosi, N. L.; Yoon, B.; Barnett, R. N.; Whetten, R. L.; Landman, U.; Jin, R. Total structure and electronic properties of the gold nanocrystal Au36 (SR) 24. *Angewandte Chemie International Edition* **2012**, *51*, 13114–13118.

(76) Negishi, Y.; Sakamoto, C.; Ohyama, T.; Tsukuda, T. Synthesis and the Origin of the Stability of Thiolate-Protected Au130 and Au187 Clusters. *The Journal of Physical Chemistry Letters* **2012**, *3*, 1624–1628.

(77) Mustalahti, S.; Myllyperkio, P.; Lahtinen, T.; Salorinne, K.; Malola, S.; Koivisto, J.; Hakkinen, H.; Pettersson, M. Ultrafast electronic relaxation and vibrational cooling dynamics of Au144 (SC2H4Ph) 60 nanocluster probed by transient mid-IR spectroscopy. *The Journal of Physical Chemistry C* **2014**, *118*, 18233–18239.

(78) Agrachev, M.; Fei, W.; Antonello, S.; Bonacchi, S.; Dainese, T.; Zoleo, A.; Ruzzi, M.; Maran, F. Understanding and controlling the efficiency of Au 24 M (SR) 18 nanoclusters as singlet-oxygen photosensitizers. *Chemical Science* **2020**, *11*, 3427–3440.

(79) Toffoli, D.; Russi, A.; Fronzoni, G.; Coccia, E.; Stener, M.; Sementa, L.; Fortunelli, A. Circularly polarized plasmons in chiral gold nanowires via quantum-mechanical design. *The Journal of Physical Chemistry Letters* **2021**, *12*, 5829–5835.

(80) Oshima, Y.; Onga, A.; Takayanagi, K. Helical gold nanotube synthesized at 150 K. *Physical review letters* **2003**, *91*, 205503.

(81) Saito, R.; Fujita, M.; Dresselhaus, G.; Dresselhaus, u. M. Electronic structure of chiral graphene tubules. *Applied physics letters* **1992**, *60*, 2204–2206.

(82) Léonard, F.; Tersoff, J. Novel length scales in nanotube devices. *Physical Review Letters* **1999**, *83*, 5174.

(83) Rubio, A.; Corkill, J. L.; Cohen, M. L. Theory of graphitic boron nitride nanotubes. *Physical Review B* **1994**, *49*, 5081.

(84) Tenne, R.; Homyonfer, M.; Feldman, Y. Nanoparticles of layered compounds with hollow cage structures (inorganic fullerene-like structures). *Chemistry of materials* **1998**, *10*, 3225–3238.

(85) Zhu, M.; Aikens, C. M.; Hollander, F. J.; Schatz, G. C.; Jin, R. Correlating the crystal structure of a thiol-protected Au25 cluster and optical properties. *Journal of the American Chemical Society* **2008**, *130*, 5883–5885.

(86) Lin, D.; Zheng, M.; Xu, W. W. Structural predictions of thiolate-protected gold nanoclusters via the redistribution of Au–S "staple" motifs on known cores. *Physical Chemistry Chemical Physics* **2020**, *22*, 16624–16629.

(87) Xu, W. W.; Wang, E.; Zeng, X. C. Unveiling Complex Structural Features of Thiolate-Protected Gold Nanoclusters: From Internal Core to External "Staple" Motifs and Overall Charge States. *Accounts of Materials Research* **2024**, *5*, 1134–1145.

(88) Jiang, D.-e.; Tiago, M. L.; Luo, W.; Dai, S. The "staple" motif: A key to stability of thiolate-protected gold nanoclusters. *Journal of the American Chemical Society* **2008**, *130*, 2777–2779.

(89) Weerawardene, K. D. M.; Aikens, C. M. Origin of photoluminescence of Ag25 (SR) 18–nanoparticles: ligand and doping effect. *The Journal of Physical Chemistry C* **2018**, *122*, 2440–2447.

(90) Weerawardene, K. D. M.; Aikens, C. M. Theoretical insights into the origin of photoluminescence of Au25 (SR) 18–nanoparticles. *Journal of the American Chemical Society* **2016**, *138*, 11202–11210.

(91) Dass, A.; Jones, T.; Rambukwella, M.; Crasto, D.; Gagnon, K. J.; Sementa, L.; De Vetta, M.; Baseggio, O.; Aprà, E.; Stener, M., et al. Crystal structure and theoretical analysis of green gold Au30 (S-t Bu) 18 nanomolecules and their relation to Au30S (S-t Bu) 18. *The Journal of Physical Chemistry C* **2016**, *120*, 6256–6261.

(92) Baseggio, O.; De Vetta, M.; Fronzoni, G.; Toffoli, D.; Stener, M.; Sementa, L.; Fortunelli, A. Time-dependent density-functional study of the photoabsorption spectrum of Au25 (SC2H4C6H5) 18 anion: Validation of the computational protocol. *International Journal of Quantum Chemistry* **2018**, *118*, e25769.

(93) Weissker, H.-C.; Escobar, H. B.; Thanthirige, V.; Kwak, K.; Lee, D.; Ramakrishna, G.; Whetten, R.; López-Lozano, X. Information on quantum states pervades the visible spectrum of the ubiquitous Au144 (SR) 60 gold nanocluster. *Nature communications* **2014**, *5*, 3785.

(94) Medves, M.; Sementa, L.; Toffoli, D.; Fronzoni, G.; Krishnadas, K. R.; Bürgi, T.; Bonacchi, S.; Dainese, T.; Maran, F.; Fortunelli, A., et al. Predictive optical photoabsorption of Ag24Au (DMBT) 18- via efficient TDDFT simulations. *The Journal of Chemical Physics* **2021**, *155*.

(95) Linic, S.; Christopher, P.; Ingram, D. B. Plasmonic-metal nanostructures for efficient conversion of solar to chemical energy. *Nature materials* **2011**, *10*, 911–921.

(96) Bok, H.-M.; Shuford, K. L.; Kim, S.; Kim, S. K.; Park, S. Multiple surface plasmon modes for gold/silver alloy nanorods. *Langmuir* **2009**, *25*, 5266–5270.

(97) D'Antoni, P.; Toffoli, D.; Fronzoni, G.; Stener, M.; Sementa, L.; Fortunelli, A. Dichroism of plasmonic chiral nanoalloys by rational design. *Journal of Computational Chemistry* **2024**, *45*, 1657–1666.

(98) Wagnière, G. H. *On chirality and the universal asymmetry: reflections on image and mirror image*; John Wiley & Sons: 2007.

(99) Kondepudi, D. K.; Durand, D. J. Chiral asymmetry in spiral galaxies? *Chirality: The Pharmacological, Biological, and Chemical Consequences of Molecular Asymmetry* **2001**, *13*, 351–356.

(100) Dogic, Z.; Fraden, S. Smectic phase in a colloidal suspension of semiflexible virus particles. *Physical review letters* **1997**, *78*, 2417.

(101) Berova, N.; Nakanishi, K.; Woody, R. *Circular Dichroism. Principles and Applications 2nd Edition*, 2000.

(102) Stephens, P. J. Theory of vibrational circular dichroism. *The Journal of Physical Chemistry* **1985**, *89*, 748–752.

(103) Riehl, J. P.; Richardson, F. S. Circularly polarized luminescence spectroscopy. *Chemical Reviews* **1986**, *86*, 1–16.

(104) Kumar, J.; Thomas, K. G.; Liz-Marzán, L. M. Nanoscale chirality in metal and semiconductor nanoparticles. *Chemical Communications* **2016**, *52*, 12555–12569.

(105) Pelayo, J. J.; Valencia, I.; García, A. P.; Chang, L.; López, M.; Toffoli, D.; Stener, M.; Fortunelli, A.; Garzón, I. L. Chirality in bare and ligand-protected metal nanoclusters. *Advances in Physics: X* **2018**, *3*, 1509727.

(106) Dreaden, E. C.; Alkilany, A. M.; Huang, X.; Murphy, C. J.; El-Sayed, M. A. The golden age: gold nanoparticles for biomedicine. *Chemical Society Reviews* **2012**, *41*, 2740–2779.

(107) Liu, J.; Chen, L.; Cui, H.; Zhang, J.; Zhang, L.; Su, C.-Y. Applications of metal–organic frameworks in heterogeneous supramolecular catalysis. *Chemical Society Reviews* **2014**, *43*, 6011–6061.

(108) Gansel, J. K.; Thiel, M.; Rill, M. S.; Decker, M.; Bade, K.; Saile, V.; Von Freymann, G.; Linden, S.; Wegener, M. Gold helix photonic metamaterial as broadband circular polarizer. *science* **2009**, *325*, 1513–1515.

(109) Jensen, T. R.; Malinsky, M. D.; Haynes, C. L.; Van Duyne, R. P. Nanosphere lithography: tunable localized surface plasmon resonance spectra of silver nanoparticles. *The Journal of Physical Chemistry B* **2000**, *104*, 10549–10556.

(110) Wu, W.; Njoki, P. N.; Han, H.; Zhao, H.; Schiff, E. A.; Lutz, P. S.; Solomon, L.; Matthews, S.; Maye, M. M. Processing core/alloy/shell nanoparticles: tunable optical properties and evidence for self-limiting alloy growth. *The Journal of Physical Chemistry C* **2011**, *115*, 9933–9942.

(111) Gomez-Grana, S.; Fernandez-Lopez, C.; Polavarapu, L.; Salmon, J.-B.; Leng, J.; Pastoriza-Santos, I.; Perez-Juste, J. Gold nanooctahedra with tunable size and microfluidic-induced 3D assembly for highly uniform SERS-active supercrystals. *Chemistry of Materials* **2015**, *27*, 8310–8317.

(112) Kumar, J.; Thomas, K. G.; Liz-Marzán, L. M. Nanoscale chirality in metal and semiconductor nanoparticles. *Chemical Communications* **2016**, *52*, 12555–12569.

(113) Ma, W.; Xu, L.; de Moura, A. F.; Wu, X.; Kuang, H.; Xu, C.; Kotov, N. A. Chiral inorganic nanostructures. *Chemical reviews* **2017**, *117*, 8041–8093.

(114) Ben-Moshe, A.; Maoz, B. M.; Govorov, A. O.; Markovich, G. Chirality and chiroptical effects in inorganic nanocrystal systems with plasmon and exciton resonances. *Chemical Society Reviews* **2013**, *42*, 7028–7041.

(115) Gautier, C.; Bürgi, T. Chiral gold nanoparticles. *ChemPhysChem* **2009**, *10*, 483–492.

(116) Srivastava, S.; Santos, A.; Critchley, K.; Kim, K.-S.; Podsiadlo, P.; Sun, K.; Lee, J.; Xu, C.; Lilly, G. D.; Glotzer, S. C., et al. Light-controlled self-assembly of semiconductor nanoparticles into twisted ribbons. *Science* **2010**, *327*, 1355–1359.

(117) Hughes, J. F.; Skaletsky, H.; Brown, L. G.; Pyntikova, T.; Graves, T.; Fulton, R. S.; Dugan, S.; Ding, Y.; Buhay, C. J.; Kremitzki, C., et al. Strict evolutionary conservation followed rapid gene loss on human and rhesus Y chromosomes. *Nature* **2012**, *483*, 82–86.

(118) Shopsowitz, K. E.; Qi, H.; Hamad, W. Y.; MacLachlan, M. J. Free-standing mesoporous silica films with tunable chiral nematic structures. *Nature* **2010**, *468*, 422–425.

(119) Liu, S.; Han, L.; Duan, Y.; Asahina, S.; Terasaki, O.; Cao, Y.; Liu, B.; Ma, L.; Zhang, J.; Che, S. Synthesis of chiral TiO2 nanofibre with electron transition-based optical activity. *Nature communications* **2012**, *3*, 1215.

(120) Maoz, B. M.; van der Weegen, R.; Fan, Z.; Govorov, A. O.; Ellestad, G.; Berova, N.; Meijer, E.; Markovich, G. Plasmonic chiroptical response of silver nanoparticles interacting with chiral supramolecular assemblies. *Journal of the American Chemical Society* **2012**, *134*, 17807–17813.

(121) Dryzun, C.; Avnir, D. On the abundance of chiral crystals. *Chemical Communications* **2012**, *48*, 5874–5876.

(122) Funston, A. M.; Novo, C.; Davis, T. J.; Mulvaney, P. Plasmon coupling of gold nanorods at short distances and in different geometries. *Nano letters* **2009**, *9*, 1651–1658.

(123) Ding, B.; Deng, Z. H, Yan, S. Cabrini, RN Zuckermann, J. Bokor. *J. Am. Chem. Soc* **2010**, *132*, 3248–3249.

(124) Querejeta-Fernández, A.; Chauve, G.; Methot, M.; Bouchard, J.; Kumacheva, E. Chiral plasmonic films formed by gold nanorods and cellulose nanocrystals. *Journal of the American Chemical Society* **2014**, *136*, 4788–4793.

(125) Chen, C.-L.; Zhang, P.; Rosi, N. L. A new peptide-based method for the design and synthesis of nanoparticle superstructures: construction of highly ordered gold nanoparticle double helices. *Journal of the American Chemical Society* **2008**, *130*, 13555–13557.

(126) Schaaff, T. G.; Knight, G.; Shafigullin, M. N.; Borkman, R. F.; Whetten, R. L. Isolation and selected properties of a 10.4 kDa gold: glutathione cluster compound. *The Journal of Physical Chemistry B* **1998**, *102*, 10643–10646.

(127) Li, Y.; Yu, D.; Dai, L.; Urbas, A.; Li, Q. Organo-soluble chiral thiol-monolayer-protected gold nanorods. *Langmuir* **2011**, *27*, 98–103.

(128) Weight, B. M.; Li, X.; Zhang, Y. Theory and modeling of light-matter interactions in chemistry: current and future. *Phys. Chem. Chem. Phys.* **2023**, *25*, 31554.

(129) Kazuma, E.; Kim, Y. Mechanistic Studies of Plasmon Chemistry on Metal Catalysts. *Angew. Chem. Int. Ed.* **2019**, *58*, 4800.

(130) Zhang, Z.; Zhang, C.; Zheng, H.; Xu, H. Plasmon-driven catalysis on molecules and nanomaterials. *Acc. Chem. Res.* **2019**, *52*, 2506.

(131) Zhang, Y.; He, S.; Guo, W.; Hu, Y.; Huang, J.; Mulcahy, J. R.; Wei, W. D. Surface-Plasmon-Driven Hot Electron Photochemistry. *Chem. Rev.* **2018**, *118*, 2927.

(132) Brongersma, M. L.; Halas, N. J.; Nordlander, P. Plasmon-induced hot carrier science and technology. *Nat. nanotech.* **2015**, *10*, 25.

(133) Coccia, E.; Fregoni, J.; Guido, C. A.; Marsili, M.; Corni, S. Hybrid theoretical models for molecular nanoplasmonics. *J. Chem. Phys.* **2020**, *153*, 200901.

(134) Schlücker, S. Surface-enhanced raman spectroscopy: concepts and chemical applications. *Angew. Chem. Int. Ed.* **2014**, *53*, 4756.

(135) Lu, F.; Tian, Y.; Liu, M.; Su, D.; Zhang, H.; Govorov, A. O.; Gang, O. Discrete Nanocubes as Plasmonic Reporters of Molecular Chirality. *Nano Lett.* **2013**, *13*, 3145.

(136) Swearer, D. F.; Robatjazi, H.; Martirez, J. M. P.; Zhang, M.; Zhou, L.; Carter, E. A.; Nordlander, P.; Halas, N. J. Plasmonic Photocatalysis of Nitrous Oxide into N_2 and O_2 Using Aluminum–Iridium Antenna–Reactor Nanoparticles. *ACS Nano* **2019**, *13*, 8076.

(137) Zrimsek, A. B.; Chiang, N.; Mattei, M.; Zaleski, S.; McAnally, M. O.; Chapman, C. T.; Henry, A. .-.; Schatz, G. C.; Duyne, R. P. V. Single-Molecule Chemistry with Surface- and Tip-Enhanced Raman Spectroscopy. *Chem. Rev.* **2017**, *117*, 7583.

(138) Dulkeith, E.; Ringler, M.; Klar, T. A.; Feldmann, J.; Javier, A. M.; Parak, W. J. Gold Nanoparticles Quench Fluorescence by Phase Induced Radiative Rate Suppression. *Nano Lett.* **2005**, *5*, 585.

(139) Dong, J.; Zhang, Z.; Zheng, H.; Sun, M. Recent progress on plasmon-enhanced fluorescence. *Nanophotonics* **2015**, *4*, 472.

(140) Kim, S.; Jin, J.; Kim, Y.-J.; Park, I.-Y.; Kim, Y.; Kim, S.-W. High-harmonic generation by resonant plasmon field enhancement. *Nature* **2008**, *453*, 757.

(141) Sivis, M.; Duwe, M.; Abel, B.; Ropers, C. Nanostructure-enhanced atomic line emission. *Nature* **2012**, *485*, p. E1.

(142) Raschke, M. B. High-harmonic generation with plasmonics: feasible or unphysical? *Ann. Phys. (Berlin)* **2013**, *525*, p. A40.

(143) Blanco, M.; Hernandez-Garcia, C.; Chacon, A.; Lewenstein, M.; Flores-Arias, M. T.; Plaja, L. Phase matching effects in high harmonic generation at the nanometer scale. *Opt. Express* **2017**, *25*, 14974.

(144) Nesterov, M. L.; Yin, X.; Schäferling, M.; Giessen, H.; Weiss, T. The role of plasmon-generated near fields for enhanced circular dichroism spectroscopy. *Acs Photonics* **2016**, *3*, 578.

(145) Govorov, A. O. Plasmon-Induced Circular Dichroism of a Chiral Molecule in the Vicinity of Metal Nanocrystals. Application to Various Geometries. *J. Phys. Chem. C* **2011**, *115*, 7914.

(146) Linic, S.; Aslam, U.; Boerigter, C.; Morabito, M. Photochemical transformations on plasmonic metal nanoparticles. *Nat. Mater.* **2015**, *14*, 567.

(147) Zhan, C.; Chen, X. .-.; Yi, J.; Li, J. .-.; Wu, D.-Y.; Tian, Z.-Q. From plasmon-enhanced molecular spectroscopy to plasmon-mediated chemical reactions. *Nat. Rev. Chem.* **2018**, *2*, 216.

(148) García-Etxarri, A.; Dionne, J. A. Surface-enhanced circular dichroism spectroscopy mediated by nonchiral nanoantennas. *Phys. Rev. B* **2013**, *87*, 235409.

(149) Davis, T. J.; Gomez, D. E. Interaction of localized surface plasmons with chiral molecules. *Phys Rev. B* **2014**, *90*, 235424.

(150) Hendry, E.; Carpy, T.; Johnston, J.; Popland, M.; Mikhaylovskiy, R. V.; Lapthorn, A. J.; Kelly, S. M.; Barron, L. D.; Gadegaard, N.; Kadodwala, M. Ultrasensitive detection and characterization of biomolecules using superchiral fields. *Nat. nanotechnol.* **2010**, *5*, 783.

(151) Tullius, R.; Karimullah, A. S.; Rodier, M.; Fitzpatrick, B.; Gadegaard, N.; Barron, L. D.; Rotello, V. M.; Cooke, G.; Lapthorn, A.; Kadodwala, M. "Superchiral" spectroscopy: detection of protein higher order hierarchical structure with chiral plasmonic nanostructures. *J. Am. Chem. Soc.* **2015**, *137*, 8380.

(152) Pilot, R.; Signorini, R.; Durante, C.; Orian, L.; Bhamidipati, M.; Fabris, L. A review on surface-enhanced Raman scattering. *Biosensors* **2019**, *9*, 57.

(153) Yu, H.; Peng, Y.; Yang, Y.; Li, Z. Y. Plasmon-enhanced light–matter interactions and applications. *Npj Comput. Mater.* **2019**, *5*, 45.

(154) Li, J. F.; Li, C. Y.; Aroca, R. F. Plasmon-enhanced fluorescence spectroscopy. *Chem. Soc. Rev.* **2017**, *46*, 3962.

(155) Messiah, A. *Quantum mechanics*; Courier Corporation: 2014.

(156) McWeeny, R. Methods of molecular quantum mechanics / R. McWeeny, eng, London [etc, c1992.

(157) Marques, M. A.; Maitra, N. T.; Nogueira, F. M.; Gross, E. K.; Rubio, A. *Fundamentals of time-dependent density functional theory*; Springer: 2012; Vol. 837.

(158) Ullrich, C. *Time-Dependent Density-Functional Theory: Concepts and Applications*; Oxford Graduate Texts; OUP Oxford: 2012.

(159) Koch, W.; Holthausen, M. C. *A chemist's guide to density functional theory*; John Wiley & Sons: 2015.

(160) Heisenberg, W. In *Original Scientific Papers Wissenschaftliche Originalarbeiten*; Springer: 1985, pp 382–396.

(161) Born, M.; Jordan, P. Zur quantenmechanik. *Zeitschrift für Physik* **1925**, *34*, 858–888.

(162) Born, M.; Heisenberg, W.; Jordan, P. Zur quantenmechanik. II. *Zeitschrift für Physik* **1926**, *35*, 557–615.

(163) Ceperley, D. M.; Alder, B. J. Ground state of the electron gas by a stochastic method. *Physical review letters* **1980**, *45*, 566.

(164) Vosko, S. H.; Wilk, L.; Nusair, M. Accurate spin-dependent electron liquid correlation energies for local spin density calculations: a critical analysis. *Canadian Journal of physics* **1980**, *58*, 1200–1211.

(165) Becke, A. D. Density-functional exchange-energy approximation with correct asymptotic behavior. *Physical review A* **1988**, *38*, 3098.

(166) Lee, C.; Yang, W.; Parr, R. G. Development of the Colle-Salvetti correlation-energy formula into a functional of the electron density. *Physical review B* **1988**, *37*, 785.

(167) Perdew, J. P.; Burke, K.; Ernzerhof, M. Generalized gradient approximation made simple. *Physical review letters* **1996**, *77*, 3865.

(168) Van Leeuwen, R.; Baerends, E. J. Exchange-correlation potential with correct asymptotic behavior. *Phys. Rev. A* **1994**, *49*, 2421–2431.

(169) Adamo, C.; Barone, V. Toward reliable density functional methods without adjustable parameters: The PBE0 model. *J. Chem. Phys.* **1999**, *110*, 6158–6170.

(170) Chai, J.-D.; Head-Gordon, M. Long-range corrected hybrid density functionals with damped atom–atom dispersion corrections. *Phys. Chem. Chem. Phys.* **2008**, *10*, 6615–6620.

(171) Davidson, E. R. The iterative calculation of a few of the lowest eigenvalues and corresponding eigenvectors of large real-symmetric matrices. *Journal of Computational Physics* **1975**, *17*, 87–94.

(172) Sleijpen, G. L. G.; van der Vorst, H. A. A Jacobi–Davidson Iteration Method for Linear Eigenvalue Problems. *SIAM Journal on Matrix Analysis and Applications* **1996**, *17*, 401–425.

(173) Baseggio, O.; Fronzoni, G.; Stener, M. A new time-dependent density functional algorithm for large systems and plasmons in metal clusters. *The Journal of Chemical Physics* **2015**, *143*, DOI: 10.1063/1.4926841.

(174) Hirata, S.; Head-Gordon, M. Time-dependent density functional theory for radicals: an improved description of excited states with substantial double excitation character. *Chemical Physics Letters* **1999**, *302*, 375–382.

(175) Chibueze, C. S.; Visscher, L. Restricted open-shell time-dependent density functional theory with perturbative spin-orbit coupling. *The Journal of Chemical Physics* **2024**, *161*, 094112.

(176) Medves, M.; Sementa, L.; Toffoli, D.; Fronzoni, G.; Fortunelli, A.; Stener, M. An efficient hybrid scheme for time-dependent density functional theory. *The Journal of Chemical Physics* **2020**, *152*, DOI: 10.1063/1.5141934.

(177) D'Antoni, P.; Medves, M.; Toffoli, D.; Fortunelli, A.; Stener, M.; Visscher, L. A resolution-of-identity technique to speed up TDDFT with hybrid functionals: implementation and application to gold thiolate clusters. *The Journal of Physical Chemistry A* **2023**, *127*, 9244–9257.

(178) D'Antoni, P.; Sementa, L.; Bonacchi, S.; Reato, M.; Maran, F.; Fortunelli, A.; Stener, M. Combined experimental and computational study of the photoabsorption of monodoped and nondoped nanoclusters Au24Pt(SR)18, Ag24Pt(SR)18, and Ag25(SR)18. *Physical Chemistry Chemical Physics* **2024**, *26*, 17569–17576.

(179) Mahan, G. D.; Subbaswamy, K. R. *Local Density Theory of Polarizability*; Springer: 2013.

(180) Sementa, L.; Barcaro, G.; Baseggio, O.; De Vetta, M.; Dass, A.; Aprà, E.; Stener, M.; Fortunelli, A. Ligand-enhanced optical response of gold nanomolecules and its fragment projection analysis: the case of Au30 (SR) 18. *The Journal of Physical Chemistry C* **2017**, *121*, 10832–10842.

(181) Theivendran, S.; Chang, L.; Mukherjee, A.; Sementa, L.; Stener, M.; Fortunelli, A.; Dass, A. Principles of Optical Spectroscopy of Aromatic Alloy Nanomolecules: Au36–x Ag x (SPh-t Bu) 24. *The Journal of Physical Chemistry C* **2018**, *122*, 4524–4531.

(182) Baseggio, O.; Toffoli, D.; Fronzoni, G.; Stener, M.; Sementa, L. Extension of the time-dependent density functional complex polarizability algorithm to circular dichroism: Implementation and applications to Ag8 and Au38 (SC2H4C6H5) 24. *The Journal of Physical Chemistry C* **2016**, *120*, 24335–24345.

(183) Autschbach, J.; Ziegler, T. Calculating molecular electric and magnetic properties from time-dependent density functional response theory. *The Journal of chemical physics* **2002**, *116*, 891–896.

(184) Chang, L.; Baseggio, O.; Sementa, L.; Cheng, D.; Fronzoni, G.; Toffoli, D.; Aprà, E.; Stener, M.; Fortunelli, A. Individual component map of rotatory strength and rotatory strength density plots as analysis tools of circular dichroism spectra of complex systems. *Journal of Chemical Theory and Computation* **2018**, *14*, 3703–3714.

(185) D'Antoni, P.; Toffoli, D.; Stener, M. Damped linear response TDDFT with range-separated functionals and density fitting. *The Journal of Physical Chemistry A* **2025**, *129*, 9453–9463.

(186) D'Antoni, P.; Toffoli, D.; Fronzoni, G.; Stener, M.; Sementa, L.; Fortunelli, A. Dichroism of plasmonic chiral nanoalloys by rational design. *Journal of Computational Chemistry* **2024**, *45*, 1657–1666.

(187) Tabut, M.; D'Antoni, P.; Toffoli, D.; Stener, M.; Salzemann, C.; Calatayud, M. How Adsorption Geometry Dictates Chiroptical Properties: A Computational Study of l-Cysteine on Au (111) Cluster Models. *The Journal of Physical Chemistry C* **2025**.

(188) Biancorosso, L.; D'Antoni, P.; Corni, S.; Stener, M.; Coccia, E. Time-dependent quantum-continuum modeling of plasmon-enhanced electronic circular dichroism. *The Journal of Chemical Physics* **2024**, *161*, DOI: 10.1063/5.0226870.

UNIVERSITÀ
DEGLI STUDI
DI TRIESTE

La borsa di dottorato è cofinanziata con risorse dell'Unione europea, NextGeneration EU - Piano Nazionale di Ripresa e Resilienza, Missione 4 – Componente 1 – Investimento 3.4 CUP J93C22000540006